Republic of Iraq
Ministry of Higher Education
and Scientific Research
Al-Nahrain University
College of Science
Department of Physics

Preparation of Painting Material from Li-Ni Ferrite with Isovalent Substitution

A Dessirtation

Submitted to the College of Science / Al-Nahrain University as a partial fulfillment of requirments for the Degree of Ph.D of Science in Physics

By

Sadeq Hani Lafta

M.Sc. Applied Physics/ Dep. of Applied Science /University of Technology

Supervised by

Dr.Emad K. Alshakerji
(Prof.)

Dr.Ali M.Musa
(Prof.)

Jan 2016 Safar 1437

Supervisors Certification

We certify that this Dessirtation entitled "**Preparation of Painting Material from Li-Ni Ferrite with Isovalent Substitution**" was prepared by "**Sadeq Hani Lafta**" under our supervision at the College of Science/Al-Nahrain University as a partial fullfilment of the requirments for the Degree of Ph.D. of Science in Phyics.

Signature :

Name : **Dr.Emad K. Al-shakarchi**
Title: **Proffesor**
Adress: **College of Science/ Al-Nahrain University**
Date: **-2016**

Signature :

Name : **Dr. Ali M. Musa**
Title: **Proffesor**
Adress: **Department of Applied Science/ University of Technology**
Date: **-2016**

In view of the avilable recommendations, I forward this thesis for debate by examing committee.

Signature :

Name: **Alaa Jabbar Ghazai**
Title: **Assistant Proffesor**
Adress: **Head of Physics Department**
Date: **-2016**

Committee Certification

We the examining committee that we have read this dissertation entitled "**Preparation of Painting material from Ni-Li Ferrite with Isovalent Substitution**" and examined the student "**Sadeq Hani Lafta**" in its contents and that in our opinion, it is accepted for the Degree of Ph.D. of Science in Physics.

Signature :
Name: **I.K.Jasim**
Title: **Proffessor**
Adress: **College of Education for Pure Science/ Tikrit University**
Date: **2016**
(Chairman)

Signature :
Name: **Kadhum J.Kadhum**
Title: **Assistant Proffesor**
Adress: **College of Science/ Al-Mustansyria University**
Date: **2016**
(Member)

Signature :
Name: **Sabah M.Ali**
Title: **Assistant Proffesor**
Adress: **College of Education for Pure Science/ Kirkuk University.**
Dare: **2016**
(Member)

Signature :
Name: **Muthafar F.Al-Hill**
Title: **Assistant Proffesor**
Adress: **College of Science/ Baghdad University**
Date: **2016**
(Member)

Signature :
Name: **Alaa Jabbar Ghazai**
Title: **Assistant Proffesor**
Adress: **College of Science/Al-Nahrain University**
Date: **2016**
(Member)

Signature :
Name: **Emad K.Al-Shakarchi**
Title: **Proffesor**
Adress: **College of Sci./ Al-Nahrain Uni.**
Date: **2016**
(Member)

Signature :
Name: **Ali M.Musa**
Title: **Proffesor**
Adress: **Department of Applied Science/ University of Tehnology**
Date: **2016**
(Member)

I, herby certify upon the decision of the examined committee.

Signature :
Name: **Hadi M.A.Abood**
Title : **Assistant Proffesor**
Adress: **Dean of College Sscience/Al-Nahrain University**
Date: **2016**

Acknowledgments

After thanking Allah and my family I would like to express my great thanks:

Firstly to my supervisors, big brothers,

Prof. Imad K.Al-Shakarchi and Prof. Ali M.Musa

who were a resource of guidance, academic and technical support and advices.

Secondly to Iraqi Government /Ministry of Higher Education to its research scholarship grant.

Thirdly to A.G.Farle Group especially prof. M.farle, prof. Dr.Erni and Dr. Joerg Hippler

for their advice and help in performing main analysis in University of Duisburg-Essen.

Fourthly to My friends and colleagues within the Department particularly Mr.Natheer, R. Salikhov

Thanks to Dr.Sabah M.ALI and Dr.Muthafer F.Al-Hilli

for their supporting

Finally I would like to thank my family; mam to her prayer for me and my wife for her patience and support.

To all of them and to each one I forget to mention here,

I must say

Thank you

Abstract:

Nano Li-Ni ferrite samples having the structure $Li_{0.5-0.5x}Ni_xFe_{2.-0.5x}O_4$ were prepared by hydrothermal method in two sets from metal chlorides, ferrous sulfate and NaOH. Each set implicated varying x through 0, 0.1, 0.3 to 1.0. The samples were without and with adding Fe^{2+}. The ratio of Fe^{3+}/ Fe^{2+} was kept at 1.7. The preparation temperature was 155 °C and pH was equal to 11. All composition was prepared except that for x=0 without Fe^{2+} which cannot be prepared under used experimental conditions. Samples showed dominant spinel ferrite phase beyond x=0.3 for set one and pure phase at x=0.3 with Fe^{2+} addition. Lattice constant of set two is slightly lower than set one and both are slightly lower than theoretical values. The crystallite size gets minimum at x=0.5 for set one and roughly maximum at x=0 for set two.

Fourier Transformation Infrared (FTIR) spectrums tetrahedral showed peak shift to higher frequency with increasing Ni^{2+} concentration. Particles shapes were: rods (often hematite) average diameter 40 nm, spherical (nanocube ferrite in origin) sizing around 20nm.

Hysteresis Loops have S-shape like to superparamagnetic one. Generally the prepared samples have lower coercivety H_c, higher saturation magnetization M_s compared to these in literatures. Both sets give maximum susceptibility at x=0.5. These results are explained based on composition, cations distribution, cation interactions and particle size.

Resonance microwave absorption by using Ferromagnetic Resonance (FMR) test showed that the maximum imaginary susceptibility χ'' is at x=0.5 for set one besides high values of 0.7 and 0.9, with largest linewidth of about 950 G at x=0.7. Set two showed max absorption (χ'') and linewidth at x=0.9. Powders were then mixed with Novalac epoxy by 39.7 %wt. Shortcut-FMR test with no field showed that high absorption to microwave field for frequencies larger than 19 GHz. The explanation of that set two samples have larger absorption than set one is based on hopping conductivity and magnetic parameters (M_s and H_c) variation.

Transmission line method by using vector network analyzer in X-band and Ku-band showed that return (reflection) loss RL got minimum at x=0.3 in for set one in X-band whereas that happen at x=0.3 and x=0.5 for set two. Adding Fe^{2+} lowered the minimum by a factor of more than 1.5. The insertion losses IL in X-band ranging from -4.5 to -7 dB. RL and IL in Ku-band have same behavior but their values are lower. RL got minimum at

x=0.5 with value of about near to -18dB whereas it was around -12dB by adding Fe^{2+}. Average IL in Ku-band -6dB. Thickness effect is abstracted by enhancing RL and IL but shifting the minimum of peaks to lower frequency. 2mm thick has RL<-27dB and IL<-19dB.

Contents

List of symbols meaning

symbol	meaning
A_s	Stiffness constant
A	absorbance
a_o	Lattice constant
T_c	Curi temperature
T_N	Neel temperature
T_B	Blocking Temperature
T	temperature
Tr	Trivalent cation
M	magnetization
M_s	Saturation magnetization
M_r	Remanence magnetization
M_A	Moment of A cation normalized to Bohr magneton
M_B	Moment of B cation normalized to Bohr magneton
Mu	Multiple internal reflection
K_1	First order crystalline anisotropy constant
K_2	Second order crystalline anisotropy constant
K_{eff}	Effective anisotropy constant
K	anisotropy constant
K_B	Boltzmann constant
λ_s	Magnetostriction constant
λ	Microwave wavelegth
u	u-parameter in spinel structure
d_{M-O}	+2 cation – oxygen bond length
R	Reflection
r_A	Tetrahedral site radius
r_B	Octahedral site raduis
r_o	Oxygen anion radius
r_c	Critical particle size for superparamqgnetic
r	Charge displacement
r	reflectivity
Di	Divalent cation
D	Grain diameter
D_o	Flux density
d_L	Absorber layer thickness
d_s	Thickness of material
d	Crystalline planes spacing
dm	Particle size
d^n	Electronic state of the ion with n unpaired electron
μ_a	Average dipole magnetic moment
μ	Permeability
μ_r	Relative permeability
μ_i	Initial permeability
μ_{max}	Maximum permeability
μ'	ac-permeability
μ_o	Vacuum permeability
μ^w	Wall permeability

μ^R	**Rotation permeability**
μ_B	**Bohr magneton**
μ^*	**Imaginary magnetic permeability**
μ'	**Real magnetic permeability**
μ''	**Imaginary magnetic permeability**
α_f	**Fraction of A caations**
$\alpha_1\alpha_2\alpha_3$	**Direction cosine of moment**
α	**Ferromagnetic resonance damping factor**
N_A	**Avogadro number**
n_d	**Number of magnetic dipole moment per unit volume**
n	**Refractive index**
β_f	**Fraction of B moment**
β	**Crystalline FWHM of X-ray differaction peak**
H_c	**Coercivity of sample**
B	**Magnetic flux density**
H	**Magnetic field intensity**
H_o	**Maximum magnetic field intensity**
γ_e	**Wall energy**
γ_p	**Propagation constant**
γ	**Gyroscopic ratio**
ξ	**Wall thickness**
f_r	**Resonance frequency**
f_c	**Crtical frequency**
V	**Particle volume**
ε^*	**Complex dielectric constant**
ε'	**Real dielectric constant**
ε''	**Imaginary dielectric constant**
ε_∞	**Dielectric constant at infant frequency**
ε_o	**Vacuum dielectric constant**
ε_s	**Static dielectric constant**
ε_r	**Relative dielectric constant**
σ	**Electric conductivity of material**
σ_o	**Electric conductivity of material at 0K**
ω	**Angular frequency**
ω_o	**Resonance angular frequency**
ω_m	**Max frequency correspond saturation magnetization**
j	**Imaginary unit**
P_z	**Polarization of material**
P_{out}	**Output microwave power**
P_{in}	**Input microwave power**
P_T	**Transmitted microwave power**
E	**Electric field intensity**
E_o	**Maximum electric field intensity**
E_p	**Activation energy of conduction**
t	**time**
τ	**Relaxation time**
δ_{in}	**Degree of inversion in spinel structure**
δ	**loss phase angle**

δ	**Penetration depth**
δ_m	**Magnetic loss phase angle**
δ_h	**Hysteresis loss angle**
δ_e	**Eddy loss angle**
δ_r	**Residual loss angle**
W	**Absorbed power**
c	**Speed of light**
ρ	**Electrical resistivity**
χ_e^*	**Ferromagnetic resonance complex susceptibility**
χ_e'	**Ferromagnetic resonance real susceptibility**
χ_e''	**Ferromagnetic resonance imaginary susceptibility**
h	**Magnetic field of microwave**
ΔH	**Ferromagnetic resonance linewidth**
$\Delta\omega$	**Ferromagnetic angular frequency linewidth**
Q	**Quality factor**
η	**Material impedance**
Z_o	**Free space impedance**
S_{11},S_{12}	**Scattering parameters**
x	**Molar ratio**
h k l	**Miller indices**
θ	**Differaction angle**
υ_1, υ_2	**Infrared band of tetrahedral and octahedral**

List of some abbreviation meaning

Abbreviation	Meaning
MW	**Microwave**
FMR	**Ferromagnetic Resonance**
SE	**Shield Effectiveness**
RL	**Reflection Loss**
IL	**Insertion Loss**
MUT	**Material Under Test**
VNA	**Vector Network Analyzer**
SC	**Shortcut**
EDX	**Electron Dispersive x-ray analysis**
TEM	**Transmission Electron Microscope**
SEM	**Scanning Electron Microscope**
dx	**x-ray density**
XRD	**X-ray Diffraction**
JCPDS	**Joint Committee of powder Diffraction Standard**
RF	**Radio Frequency**
FWHM	**Full Width Half Maximum**
RAM	**Radar Absorbing Materials**
EM	**Electromagnetic Wave**
CA	**Circuit Analog**
EXAFS	**Extended x-ray absorption fine structure**
EMI	**Electromagnetic Interference**
FTIR	**Fouroer Transformation of Infrared**

List of Figures

List of Tables

Chapter 1: Introduction

1.1. Introduction

Among the fast developments and huge production in electrical and electronic devices, in continuous domestic, industrial, commercial and military applications in recent years, electromagnetic (EM) radiation has become a specific type of environ pollution [1]. It is estimated that approximately 3% of the total world electricity energy generated is consumed in communication. On other hand, EM radiation has been proved to be harmful to human tissues and organs severely in the range 0.5-3 GHz. Table (1.1) illustrate the radio and microwave spectrums and their applications.

Table (1.1) RF and MW spectrums with some of their applications. HF:High Freq., VHF: Very High Freq., UHF: Ultra High Freq. [1].

Band	Frequency	Wavelength	Application
Radio wave	0-3MHz	Mm-100 m ⇩	Transmission line, Radio broadcast, Communication, Experimental, hockey tokay etc.
HF	3-30 MHZ	10-1 m ⇩	
VHF	30-300 MHZ		
UHF	300MHz-3GHz	1m-10cm	
L Band	1-2 GHz		Satellite, GPS etc., mobile
S Band	2-4 GHz		Satellite, Wi-Fi, BT, mobile
C Band	4-8 GHz		Satellite , MW relay
X Band	8-12 GHz		Radar
Ku Band	12-18 GHz		Satellite TV, Police radar
K Band	18-26.5 GHz	1cm	MW backhaul
Ka Band	26.5-40 GHz		MW backhaul
Q Band	30-50 GHz		MW backhaul
U Band	40-60 GHz		Experimental, radar
V Band	50-75 GHz		New WLAN, 802.11 ad/WiGIg
E Band	60-90 GHz		MW backhaul
W Band	75-110 GHz		Automotive radar
F Band	90-140 GHz		Experimental, radar
D Band	110-170 GHz		Experimental, radar
EHF	170-300	1mm	

Due to various previous reasons, it is of great importance to study and prepare some effective microwave absorbing materials in civil and military utilization. When thickness and frequency bandwidth are required, spinel and hexaferrites have clear advantages.

Some researchers have indicated that solid-state reaction method which produces micron-sized ferrite has a good absorption at low-frequency microwave. But further application of this material is restricted by some inherent disadvantages. However, nano-sized ferrites with high quality usually have microwave absorption in high frequency region [2].

The interaction of material with the incident microwave, in general, is determined by two basic parameters: complex permittivity and complex magnetic permeability. The former express ability of material to be electrically polarized while the latter show the ability of material to be magnetized. The reason behind dielectric and magnetic losses is the lag of materials response to the external field.

The imaginary parts ε'' and μ'' represent the dielectric and magnetic losses, respectively. They vanish at zero frequency or infinite frequency. The dielectric losses are shared by conduction losses as well as polarization (relaxation losses), i.e. higher conductivity leads to a larger losses. Larger conductivity also means a stronger skin effect that in turn means more reflection. Magnetic losses result from the ferromagnetic resonance at high frequency, among other mechanisms such as hysteresis loss, eddy current loss and the magnetic after-effect (relaxations) at low frequency [3].

Generally, there are two types of absorbers; resonant absorbers and broadband absorbers (impedance matching or resonant absorbers). The resonant absorbers are frequency dependent and related to desired resonance of the material at a particular wavelength. Different types of resonant absorbers are the Salisbury screen, the Jaumann absorber, the Dallenbach layer and circuit analog (CA) absorbers. Broadband absorbers are independent of a particular frequency and can therefore be effective across a broad spectrum [4]. Many conductive and magnetic materials have been tried for absorption including carbon, metals and conducting polymers [5].

1.2. Ferrites

1.2.1. Chemical View

A ferrite is a material containing mostly iron and oxygen. The simplest form is magnetite (Fe_3O_4= $FeO.Fe_2O_3$=$Fe^{2+}O^{2-}.2Fe^{3+}3O^{2--}$). Other ferrite materials are produced by substituting divalent (transition elements: Mn, Ni, and Co ions and metals such as Cu, Zn, Mg, Cd and Ge or a combination of these) [6-9] and trivalent metal ions (A1, Cr, Ga and Mn) instead of Fe^{2+} and Fe^{3+} respectively. Other valencies (+1, +4, +5, and +6)

of metal ions such as Li^{+1} and Ti^{+3} can be substituted into the lattice by the appropriate change in the Fe^{2+}/Fe^{3+} ratio for charge compensation. The other condition except charge compensation is that the substituting ionic radii must within the range 0.5 - 1.0 $^{\circ}$A. Forming spinel fulfils the conditions of overall cation-to-anion ratio of 3/4, a total cation valency of 8, and relatively small cation radii [10].

General chemical spinel structure is AB_2O_4, or ($M[Fe_2]O_4$) where A (or M) represents any +2 cation. For the three types of ferrites: spinel, garnet, hexaferrite, the magnetic and electrical properties depend on chemical composition and crystal structure [7-15].

1.2.2. Spinel Structure

The spinel lattice has unit cell illustrated in Fig.1.1. Due two valence of cations, two sites are available:

1. A site: it is a tetrahedral site surrounded by four O^{-2} ions at corners of a tetrahedron.
2. B site: it is an octahedral site surrounded by six O^{-2} ions at corners of an octahedron.

Unit cell has 8 sites of 64 tetrahedral (or A) sites are filled with total charge= (+2)x8=+16. Also 16 of 32 octahedral sites (or B) are filled with total charge=(+3)x16=+48 as shown in Fig.1.1 [6,10].

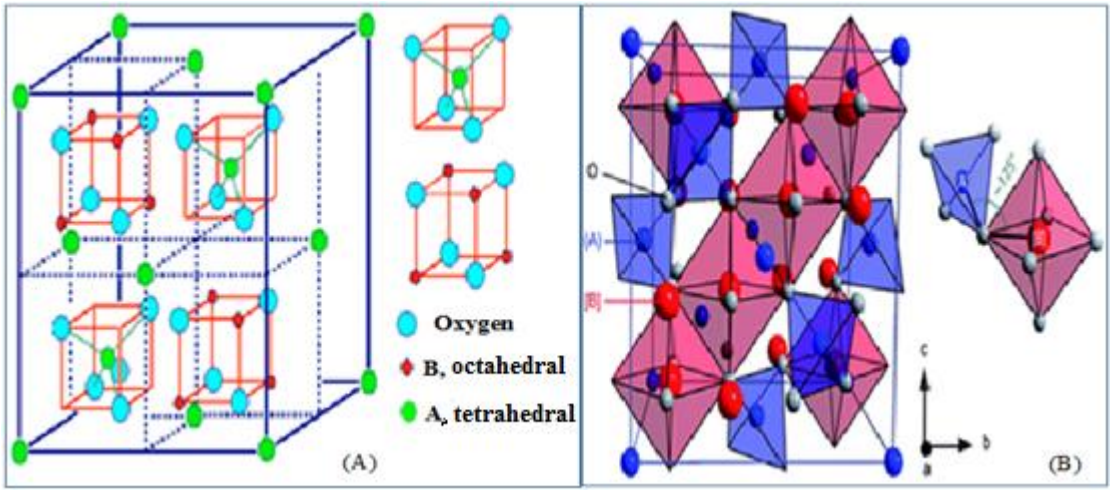

Fig. 1.1. Spinel ferrite unit cell. (A) cation sites, (B) tetrahedral and octahedral inside unit cell.

So the unit cell contains 8 formula units AB_2O_4 implemented 32 oxygen (total charge=(-2)x32=-64), where O anions form closed pack cube and cations takes interstitial sites due to their larger radii (0.13 Å)[12-15]. It is convenient to divide the unit cell into eight cubes of edge a/2 to show the

arrangement of the A and B sites The space group is Fd3m [15, 17]. Spinel structure has three types:

• Normal spinel if M (or A) occupies the tetrahedral site ($M[Fe_2]O_4$).

• Inverse spinel where M (or A) is in the octahedral site ($Fe[MFe]O_4$). 8 of 16 B-site occupy octa-site and the other 8 occupy tetra-site.

• Mixed spinel is mixed of normal and inverse ($((M_i+M_j)_{1-x}Fe_{2+x}O_4$) where M_i and M_j two metals or more and x varies between -0.3 and 0.3.

The distribution of ions between the two types of sites depends on a precise balance of contributions, such as the ionic radii magnitude, their electronic configuration and the electrostatic energy of the lattice [7-10].

The large oxygen ions are packed quite close together in a face-centered cubic arrangement, and the much smaller metal ions (radii from about 0.07 to 0.08 nm) occupy the spaces between them [9, 12].

According to the Coulombic energy of charged ions and their influence on the polarization of anions, large divalent ions favor tetrahedral occupancy and large trivalent ions favor octahedral occupancy. Practical applications use mixed type. There can exist an atomic stoichiometry where there are exactly 3 metal atoms for every 4 oxygen atoms [14]. The spinel lattice can stand a high concentration of cation vacancies designated as D. This tendency to form cation vacancies increases as x increases from 0 to a more positive value by the combination of excess α-Fe_20_3 with rhombohedral structure dissolving into a ferrite spinel structure. Increased temperature and decreased atmospheric oxygen tend to reduce the cation vacancy content [15,16]. Further, there are two tetrahedral voids and one octahedral void for each O atom, i.e. 64 tetrahedral and 32 octahedral voids [6]. Cation vacancies play an extremely important role in the ferrite's sintering kinetics and magnetic properties [16]. In the simple and ideal fcc oxygen basis, the presence of cations in some voids causes shrinkage of unoccupied voids, while maintaining the cubic overall symmetry. Ferrites lattice constant and some properties are shown in Table (1.2).

The lattice constant of ferrites is dependent on the metal-ion content, varying with different metal ions from a cube side of about 8.3 Å to 8.5 Å [16]. The detailed O atoms positions are determined by u-parameter. It reflects a modification of the structure to be suitable for differences in the radius ratio of cations A and B sites. The u-parameter is a number defines oxygen displacement from its ideal position. It has a value of 0.375 for ideal close-packed arrangement of O atoms.

Table (1.2). Some spinel ferrites properties at room temperature [13]. a_o: lattice cons. T_c: Curi Temperature. M_s: magnetization saturation. K_1: anisotropy cons. λ_s: magnetostriction cons. ρ: electric resistivity.

Ferrite	a_o (Å)	T_c (°K)	M_s (M A/m)	K_1 (kJ/m^3)	λ_s (10^{-6})	ρ (Ω.m)
$MgFe_2O_4$	8.36	713	0.18	-3	-6	10^3
$Li_{0.5}Fe_{2.5}O_4$	8.33	943	0.33	-8	-8	10^5
$MnFe_2O_4$	8.52	575	0.50	-3	-5	10^4
Fe_3O_4	8.40	860	0.48	-13	40	10^{-3}
$CoFe_2O_4$	8.39	790	0.45	290	-110	10^3
$NiFe_2O_4$	8.34	865	0.33	-7	-25	10^4
γ-Fe_2O_3	8.34	985	0.43	-5	-5	-

For the majority of the known spinel ferrites u is varied between (0.375 and 0.385). It is given by [13]:

$$u = \frac{\frac{1}{4}R^2 - \frac{2}{3} + \left(\frac{11}{48}R^2 - \frac{1}{18}\right)^{1/2}}{2R^2 - 2} \qquad \text{..... (1.1)}$$

where R= (B-O)/(A-O), R-O= < r_B + R_0 > and B-O=<r_A+R_0> are average bond lengths [18]. The increasing in u is return to excess of O^{-2} ions around tetrahedral sites, these were forced to move in the [111] direction because (A) cation is always larger than the ideal close-packed space, but without changing the symmetry. The u parameter are given corresponding to the unit cell parameter as in Table 1.3 [13].

The cations average radii have a direct effect on the cell parameter a, while the ratio between the tetrahedral and octahedral cation radii determines mainly the u value. The distance from oxygen nucleus to its nearest metal ion nucleus is [14]:

$$\mathbf{d_{M-O} = (a_0 \sqrt{3}) / 8} \qquad \text{..... (1.2)}$$

where a_0 is the lattice parameter of spinel unit cell. The ideal radii of the tetrahedral sites r_A and the ideal radii of the octahedral sites r_B in terms of r_0 (the radius of the oxygen anion) are given by [14]:

$$\mathbf{r_A = (a_0 \sqrt{3} - r_0)/8} \qquad \text{..... (1.3)}$$

$$\mathbf{r_B = (a_0 - r_0)/4} \qquad \text{..... (1.4)}$$

1.2.3. Cation Distribution in Spinels

In many cases, cation distribution for mixed ferrites is represented by [14]:

$$(Di_{1-\delta_{in}}Tr_{\delta_{in}})[Di_{\delta_{in}}Tr_{2-\delta_{in}}]O_4 \qquad \ldots\ldots\ldots (1.5)$$

where δ_{in} is the degree of inversion, the square brackets indicate the octahedral site occupancy. The cations in parentheses are located in the tetrahedral sites, Di denotes a divalent cation, and Tr denotes a trivalent one. The cation has a zero value for the normal and one for the inverse distributions, respectively. The inverse will be (Tr)[D Tr]O_4 and for normal will be (Di)[Tr]O_4 [14].

The compound $NiFe_2O_4$ is a soft magnet and its cation distribution is 80% inverse with a net moment of $2.3\mu_B$. While the theoretical value is $4\mu_B$ [10, 17]. The experimental cation distribution of selected ferrites is given in Table 1.3.

Table 1.3. Cation distribution, lattice parameter (a) and (u) value for several spinels [10].

	Distribution	a (Å)	u
Normal	**(Cd)[Fe_2]**	**8.7050**	**0.3935**
	(Zn)[Fe_2]	**8.4432**	**0.3865**
Inverse	**(Fe)[CoFe]**	**8.3500**	**0.381**
	(Fe)[CuFe]*	**8.3690**	**0.380**
	(Fe^{3+})[$Fe^{2+}Fe^{3+}$]	**8.3940**	**0.3798**
	(Fe)[Li0.5Fe1.5]	**8.3300**	**0.3820**
	(Fe)[NiFe]	**8.3390**	**0.3823**
Mixed	**($Mg_{1-\delta}Fe_\delta$)[$Mg_\delta Fe_{2-\delta}$]**	**8.3600**	**0.3820(δ=0.1)**
	($Mn_{1-\delta}Fe_\delta$)[$Mn_\delta Fe_{2-\delta}$]	**8.5110**	**0.3865(δ=0.85)**
	($Mo_{1-\delta}Fe_\delta$)[$Mo_\delta Fe_{2-\delta}$]	**8.5010**	**0.3751(δ=0.5)**
***Below 760 ºC, this spinel has tetragonal deformation, with a=8.7 ºA and c=8.22 ºA**			

Usually the preparation conditions determine the degree of inversion, especially the cooling rate after sintering. Cation types and their distribution are the main factors which influence the physical properties of spinels [10]. To be in a minimum lattice energy, due to distortion, smaller ionic radii of (0.225-0.4 Å) must occupy tetrahedral sites, while the bigger (0.4-0.73 Å) must occupy octahedral sites. While trivalent cations are usually smaller than divalent ions, a tendency to form inverse arrangement would be expected in 2+ and 3+ valancies like $NiFe_2O_4$ spinels. Different

cation combinations can form a spinel structure such as any three cations with a total charge +8 to balance -8 of the O^{-2} anions.

When u > 0.379, the normal distribution is more stable, while the lower u-values, the inverse arrangement possesses a higher Madelung constant which determines the electrostatic potential of a single ion in a crystal [2].

The distribution of cations over A and B sites is determined by their ionic radius, electronic configurations and electrostatic energy in the spinel lattice [11, 12].

Hund's rules state that 'the electron states with the greatest (2S + 1) are most stable, and of those, the most stable is that with the greatest L'. So there is a tendency to the high spin state, i.e., with the highest number of unpaired electron spins. For d1, d2 and d3 cations in octahedral sites, the lower energy triplet is occupied by unpaired electrons; the d3 state (V^{2+}, Cr^{3+} and Mn^{4+}) has the highest stabilization energy. Ni^{2+} with the d8 configuration (the triplet occupied by six paired electrons and the doublet by two unpaired electrons) will also be particularly stable in octahedral coordination.

The kinetics of cation redistribution are more complex and can be significantly affected by the presence of Fe^{2+}. When a substantial concentration of divalent Fe is present in an inverse spinel, the redistribution kinetics are independent of the cation vacancy concentration, grain size and O stoichiometry [17,18].

In most cases, the direct determination of cation distribution in spinels cannot be reliably established by x-ray diffraction, because the x-ray scattering factors for most of the transition-metal cations are very similar. Neutron diffraction analysis is better, since the scattering factors of transition metals for neutrons are quite different. Mossbauer spectroscopy and EXAFS (extended x-ray absorption fine structure) seems to overcome the disadvantages of XRD [10].

1.3. Ferrimagnetism Properties

The magnetism in ferrites is related to:

(i) Unpaired 3d electrons,
(ii) Superexchange between adjacent metal ions (cations)
(iii) Nonequivalence in number of A and B cations.

For free atom the total magnetic moment containing 3d electrons is the sum of the electron spin and orbital moments. In ferrite, the orbital magnetic moment is vanished by the electronic fields which is caused by

O^{-2} ions about the metal ion. The atomic magnetic moment (μ_a) then equals the moment of the electron spin and is equivalent to ($\mu_a = \mu_B . n$) where μ_B is a Bohr magnetron unit and n is the number of unpaired electrons [20].

Cations which have magnetic moments in ferrites form magnetic sublattices and have different crystallographic environments since the values of A and B moments are different. The magnetic moment inside its sublattice is often ferromagnetic. When different sublattices are coupled collinear antiferromagnetically, a net magnetic moment is produced, due to different numbers of magnetic ions in different sublattices and the nature of the superexchange interaction [6,19,20]. The representation of cations moments is illustrated in Fig. (1.2).

The spontaneous magnetization at zero Kelvin reaches the value:

$$\mathbf{M = MA + MB = \alpha_f n_d \mu_A + \beta_f n_d \mu_B = \chi H} \quad \text{..... (1.6)}$$

where n_f is the ions number per unit volume, α_f is the fraction of A ions, β_f is the fraction of B ions ($\beta_f = 1 - \alpha_f$), μ_A is the average magnetic moment of A-ion along magnetic field direction at some temperature and μ_B is the average moment of B-ion [20].

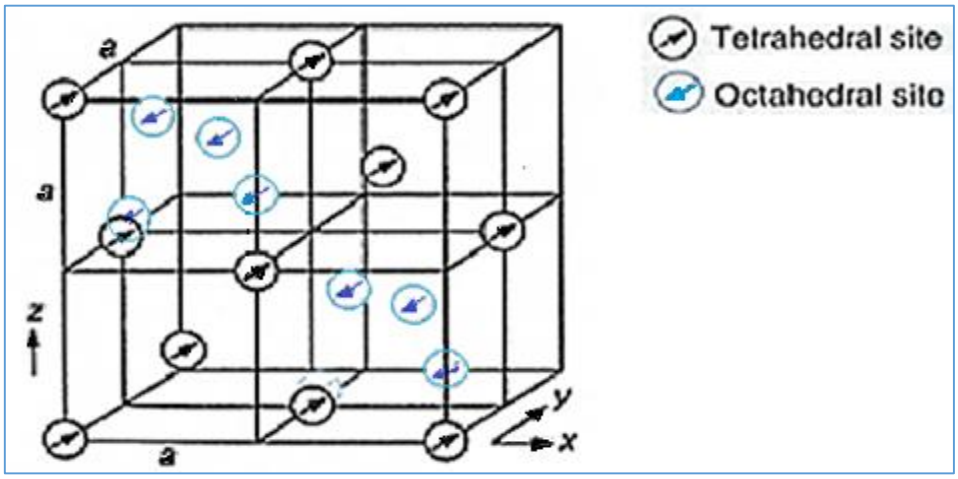

Fig.1.2. The magnetic structure of a ferrimagnetic inverse spinel [20].

Indirect exchange interaction (superexchange) occurs between adjacent metal ions separated by oxygen ions. The interaction strength is proportion to the angle of Me-O-Me (90°→180°) and inversely to the metals ions separation (bond length). So ion size is very much effective parameter in the magnetic properties [19]. In ferrites, the A-B interaction is the only important one since the angle between them is about 125° whereas the B-B is neglected because the angle is 90°. This interaction is a type of the magnetic ion dependent, so it may be antiparallel alignment of moments if

the two ions both have ≥ 5(3d) electrons, or ≤ 4(3d) electrons. Parallel alignment occurs if one ion has ≤4 electrons and the second has ≥5 electrons. The common ferrite ions (Mn^{2+}, Fe^{2+}, Ni^{2+}, Co^{2+}) have more than five 3d electrons, so the moments of A and B sites are aligned antiparallel. The occupied B-sites are twice as A-sites, thus the B site will be the dominator resulting in ferrimagnetism [21, 22].

As example of the theoretical magnetization, the $Mn^{2+}Fe^{2+}{}_3O^{2-}{}_4$ corresponds to $5\mu_B$, Fe_3O_4 has $4\mu_B$, the compound $Ni^{2+}Fe^{3+}{}_2O^{2-}{}_4$ has $2\mu_B$, and $Li^{1+}{}_{0.5}Fe^{3+}{}_{2.5}O^{2-}{}_4$ has $2.5\mu_B$ magnetic moment [50]. Usually spinel ferrites are called ferrospinel to distinguish them from other nonmagnetic spinels [9].

Nickel ferrite ($NiFe_2O_4$) and lithium ferrite ($LiFe_5O_8$) are ferrimagnetic ferrites, which possess both inverse spinel at room temperature, high permeability and resistivity. They have their own crystal parameters and physical properties due to different elements present in the materials. The inverse spinel structure and its formula can be written as $Fe^{3+}[Ni^{2+}Fe^{3+}]O_4$ and $Fe^{3+}[Li^{+0.5}Fe^{3+}{}_{1.5}]O_4$ respectively. Ni ferrite has a=8.340Å, Ms=3200G, and T_N=585 ˚C. The effect of cation distribution and addition of cations with valence (2+) on its magnetic properties was discussed before. According to the Néel model, the ferrimagnetism of ferrite comes from a mechanism of superexchange, in which different magnetic cation occuping sublattices are anti-aligned with each other in the presence of an external magnetic field and producing a net magnetism [50].

The substitutions who modify magnetic properties of Ni ferrites such as: Al (reduces the magnetization); Co^{2+} (reduces the anisotropy, because the sign of the anisotropy of Co compensates for the anisotropy of Fe); Mn (reduces the loss tangent, i.e. the dielectric losses); Zn (increases the magnetization, unfortunately T_N is reduced). These materials are lossy due to the orbital state of Ni, a relaxing ion (spin-lattice interaction). The magnetization of pure Ni ferrite is 3200G, T_N=570°C. If the ferrite contains ions with an orbitally degenerate cubic ground state such as the rare-earth ions or L-state transition metal ions, the linewidth might increase by several orders of magnitude due to magnon-phonon (spin-orbit) relaxation processes [11,13].

Li ferrites are the most frequently used microwave spinels. They have a lower cost, high T_N and a square hysteresis loop. $Li^{1+}{}_{0.5}\ Fe^{3+}{}_{2.5}O^{2-}{}_4$ has $4\pi Ms \approx 3600G$, $T_N \approx 645°C$ which are both higher than that of nickel ferrite.

It contains only S state Fe^{3+} ions, as a result it has a low linewidth ΔH_{FMR} < 10G. It's much lower than the value of nickel ferrite (40-80G) and comparable to that of yttrium iron garnet YIG ($Y_3Fe_5O_8$). This belongs to only S state in Fe^{3+} ions in this material. Adding of Ti^{4+} tends to reduce the magnetization, while Zn^{2+} increases $4\pi Ms$ [13,19].

Li ferrite also has low cost compared to YIG and so it can be used for microwave applications [50]. Li ferrite exists in two states: ordered and disordered states. In the ordered phase, the Li^+ and Fe^{3+} ions are ordered in a 1:3 molar ratio in the octahedral sites of the cubic structure. The disordered phase of Li ferrite has a disordered face centered cubic structure where the Li^+ and Fe^{3+} ions are randomly located in the octahedral interstices. The disordered phase is produced with quenching. Slow cooling allows redistribution and ordering of the ions in the cubic lattice and provides the condition for reversion to ordered phase. The lattice parameters for the ordered and disordered phase are 8.337Å and 8.333Å, respectively [50]. Both nickel ferrite and lithium ferrite are usually used only at low frequency bands (C or X band) and external magnets are needed to magnetically bias the material due to their intrinsic small cubic anisotropy [13].

1.3.1 B-H Loop

Magnetic material response (soft/hard) to an applied field is measured by the B-H (or M-H) loop, it is the characteristic curve of a magnetic material. B represents magnetic induction in Tesla produced by magnetic material. H is the applied field in A/m. B and H can be related according to equations [8]:

$$\mathbf{B = \mu_o (H + Ms)} \qquad \text{……. (1.7)}$$

where Ms is saturation magnetization having B unit, μ_o is the vacuum permeability having a value of $4\pi.10^{-7}$ H/m.

The B-H characteristic curves and important magnetic parameters of soft and hard magnetic materials are shown in Fig.1.3. These magnetic parameters are the tool to characterize the magnetic materials. *Saturation Magnetization Ms* is the maximum value of magnetic induction. At this point, almost all the magnetic domains align along the direction of applied field [15]. *Remanence magnetization (Mr or Br)* means when the applied field approaches zero, magnetic material still retains some of its induction

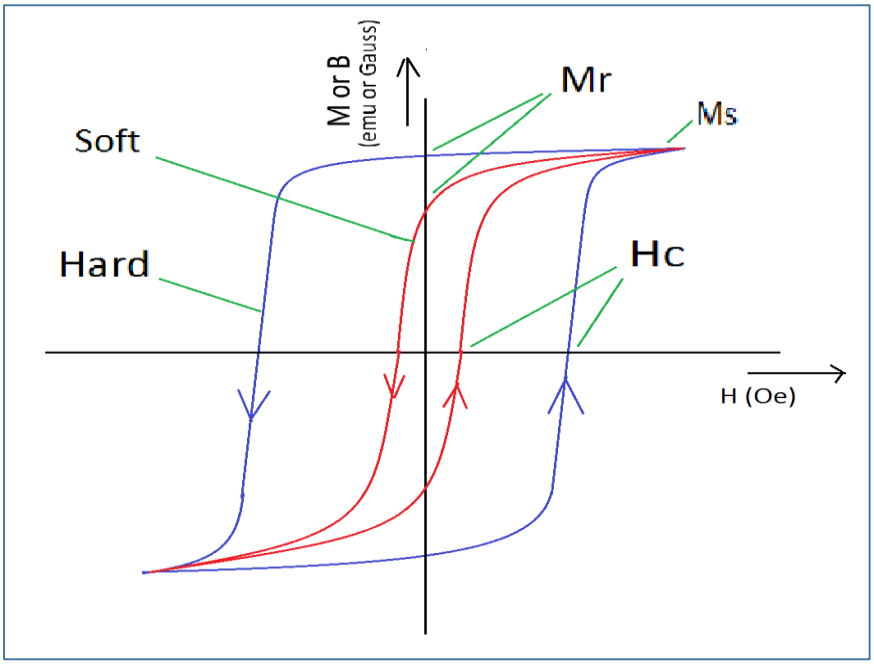

Fig. 1.3. M-H loop (B-H loop) [8].

called remanence magnetization. It is mainly due to the resistance offered by domain walls against the direction of applied field. *Coercive Force or coercivity (H_c)* is the largest of applied field required to fully demagnetize the ferrite (all reversed domains are in same direction). Many factors give rise to these field strengths such as granular inclusions and porosity, grain boundaries, lamellar precipitates and wall surface tension [20]. Soft ferrites has very low coercivity (≤100Oe) as compared to hard ferrites (≤400Oe). *Hysteresis Loss* means lag behind. It results from that anisotropy causes the second reversal does not coincide with its first reversal. It is proportional to the total area inside the loop. Hard ferrites have larger area than soft one. *Permeability* is the ratio of reached flux density (B) to an applied field (H). Actually, it is the slope of line, which connects the origin and any point of B-H curve by [9]:

$$\mu = B/H \quad \ldots\ldots\ldots\ldots \quad (1.8)$$

Permeability is the degree of magnetization that a material obtains in response to an applied magnetic field and measured by ($H{\bullet}m^{-1}$ or $N{\bullet}A^{-2}$) in (SI) and dimensionless in (cgs). Vacuum Permeability has exact value $\mu_0 = 4\pi\times10^{-7}$ $H{\bullet}m^{-1}$ [20]. It depends upon composition, sintered density and working temperature. Under the applied field, permeability initially increases and reaches its maximum value (saturation point). Later it decreases with further increasing of magnetic field (H) as shown in Fig. 1.4a.

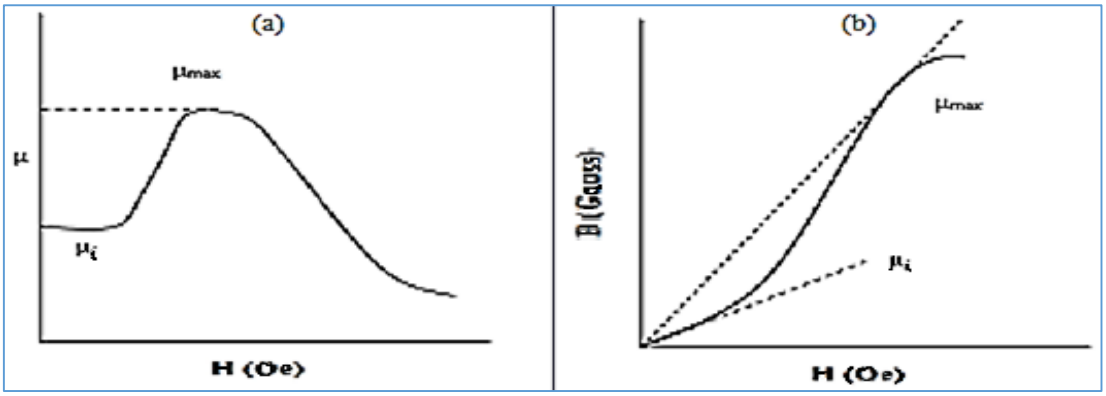

Fig. 1.4 (a) Initial and maximum permeability as function of magnetic field, (b) Determination of initial and maximum permeability [138].

In general, permeability can be classified in three different categories maximum permeability, differential permeability and initial permeability. *Maximum Permeability* is $\mu_{max} = B_{max}/H$, in B-H curve, it is the slope of line starting from origin to the point of saturation flux density. *Differential Permeability* (μ_d =dB/dH) is the slope of the line at any point on B-H curve. It helps to understand the variation in permeability. *Initial* permeability is the property that defines how quickly the domains align with applied field. It is denoted by μ_i and given by the slope of linear portion in Fig 1.4b. i.e. $\mu_i = \lim_{H\to 0}(B/H)$ [15].

Two mechanisms are in the phenomenon of permeability; spin rotation in the magnetic domains and wall displacement. For a spherical grain with diametral and spherically bulging walls, the intrinsic rotational permeability (μ^R) and 180° wall permeability (μ^w) may be written [15]:

$$\boldsymbol{\mu^R = 1 + \frac{2\pi M_S^2}{K}}, \quad \boldsymbol{\mu^W = 1 + \frac{3}{4}\pi M_S^2 \frac{D}{\gamma_e}} \qquad \textbf{..... (1.9)}$$

where D is the grain diameter and γ_e is the wall energy. The intrinsic properties, M_s (magnetic saturation) and K (anisotropy constant) are more important, as only becoming significant when K is very small [20,22].

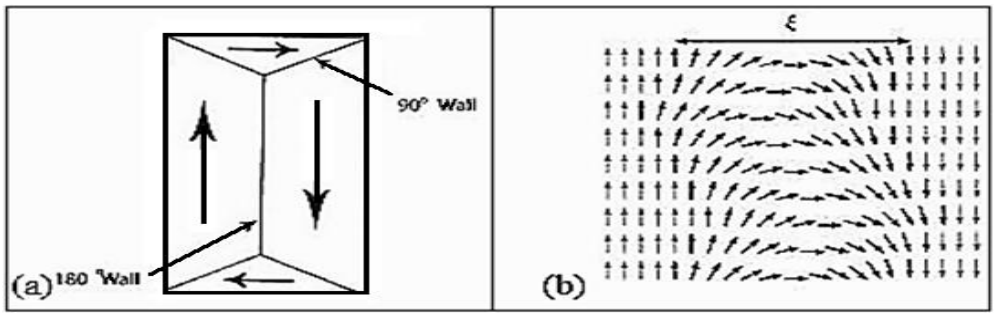

Fig. 1.5. The 180º and 90º wall. a) Over all. b) Micro presentation. ξ is wall thickness[145].

One can write the factors affecting permeability as follows:

1. Composition: high permeability can be obtained by the composition to produce minimum magnetocrystalline anisotropy and magnetostriction constant [16,21].
2. Pores density: pores prevents domain wall motion by pinning.
3. Grain size: the number of domain walls increases when grain size is larger, and permeability becomes higher due to a superior magnetizing process by the movement of domain walls.
4. Inclusions: also act as pinning site and prevent domain walls movement.
5. Defect: the permeability is reduced by the crystal imperfection, such as defect, dislocation, because it can decrease the domain wall mobility or increase the induced magnetic anisotropy.

Except for Li and Mg, the addition of alkali and alkaline earth metals decreases the permeability with increasing metal content. The substitution of (i) monovalent and divalent ions and (ii) trivalent and quadravalent ions for a ferrite have an indirect effect on properties. Fe^{2+} content on octahedral sites is decreased for (i) group (such as Li^{1+} and Ni^{2+}) and increased for (ii) group (such as Ti^{4+}, Sn^{4+}, Ge^{4+}, V^{4+} and Al^{3+}) additives, where Fe^{2+} contributes a positive anisotropy [20].

Permeability is not a constant, it can vary with the position in the medium, the frequency of the field applied, humidity, temperature, and other parameters. In a nonlinear medium, the permeability can depend on the strength of the magnetic field. Permeability as a function of frequency can take on real or complex values. In ferromagnetic materials, the relationship between B and H exhibits both non-linearity and hysteresis and depends also on the history of the material [23].

Pure lithium ferrite possesses poor squareness and, because of its high Curie temperature, has high coercivity. With the addition of Ni, Zn or Mn to Li ferrite the squareness ratio is improved considerably. The squareness is improved for Li-Ni ferrite with ferrous ferrite produced by sintering at high temperature. [20].

1.3.2. Magnetic Anisotropy

The ion spins are not free to rotate but are bound to a specific crystallographic direction to minimize the internal energy. This is due to the interaction of magnetic ions with electrostatic fields. The magnetocrystalline anisotropy possesses the crystal symmetry of the material. Magnetostriction anisotropy is related to magnetization direction

change due to mechanical stress. Shape anisotropy is mainly due to demagnetization fields which originate on the surface of the sample and from internal surfaces such as inclusions, pores, grain boundaries, second phase etc. The major effect of these demagnetization fields is reducing the remanent induction and increasing the coercivity which reduces squareness ratio [20, 22].

The magnetic anisotropies play an important role in a variety of magnetic properties, for example in domain structure, magnetization processes, shape of the hysteresis loop, permeability magnitudes, hysteresis losses and coercivity.

For spinels which have cubic symmetry, the magnetocrystalline anisotropy energy, E_a, is written [20]:

$$E_a = K_1\left(\alpha_1^2\alpha_2^2 + \alpha_2^2\alpha_3^2 + \alpha_3^2\alpha_1^2\right) + K_2\alpha_1^2\alpha_2^2\alpha_3^2 \quad \text{..... (1.10)}$$

where K_1 and K_2 are the first- and second-order magnetocrystalline anisotropy constants respectively and the α_1, α_2 and α_3 are the direction cosines of the moment of ion relative to the three crystal directions. In most ferrites (at -40 to 80°C), K_2 can be neglected compared to K_1. The produced field due to crystalline anisotropy is $H_k=2k_1/\mu_0 M_s$ where M_s is the saturation magnetization [19].

The Co^{2+}, Ni^{2+} and Fe^{2+} ions play a major role in ferrites magnetic properties. That is due to the orbital angular momentum in octahedral sites is not fully quenched by the crystal field [20].

1.4.3. Snoek's Law

Available frequency decreases with increase in permeability. It is good to enlarge anisotropic magnetic field, to extend permeability to higher frequencies. This relationship was pointed out by Snoek [15,22]. The relation between permeability of cubic crystal and anisotropic magnetic field H_A, is given by $\mu' - 1 = (2M_s/3\mu_0)(1/H_A)$. Here μ' is the real part of complex μ. If $H_A = f_r/(\gamma/2\pi)$ is substituted in previous equation, it becomes $fr\,(\mu' - 1) = (\gamma/3\pi\mu_0)M_s = 2x10^{10}M_s$, when M_s is constant, i.e. [15,24]:

$$\mu' f_r = \text{constant} \quad \text{..... (1.11)}$$

So if ferrites ac-permeability (μ') becomes smaller the resonance frequency (f_r) will be higher and vice versa. At resonance frequency ferrite losses its magnetic nature i.e. initial permeability approaches towards zero. [128]. Spinels can be adapted for 3-30 GHz applications by selecting the

proper chemical composition. However, spinel ferrites exhibit the well-known Snoek's limitation, i.e. spinel ferrite of a high permeability has a low natural resonance frequency, due to the cubic magnetocrystalline anisotropy [11]. When μ′ is constant, the associated frequency is called relaxation frequency [25].

1.3.4. Nanomagnetism

The structural, electrical and magnetic properties of nanoscale materials are not the same as they are in bulk size. Preparing nanoferrite opens a new and exciting research field, with promising applications in the electronic technology and biotechnology [15].

The variation of H_c due to particle size is shown in Fig.1.6 implemented the meaning of r_c. The equilibrium domain configuration occurs when the magnetostatic energy balances domain wall energy. Below r_c more energy is required to create domain-wall compared to the external magnetostatic energy of single domain state, that leads to a single domain state. For spherical particle r_c is [15]:

$$r_c = 18\frac{\sqrt{A_s K_{eff}}}{\mu_0 Ms^2} \quad \text{..... (1.12)}$$

where A_s is exchange stiffness constant (characteristic of a ferromagnetic material and depends on crystal structure, typical 10^{-11} J/m), K_{eff} is the anisotropy constant and μ_0 is vacuum permeability, M is the magnetization. Magnetite has r_c of 28 nm at room temperature [26].

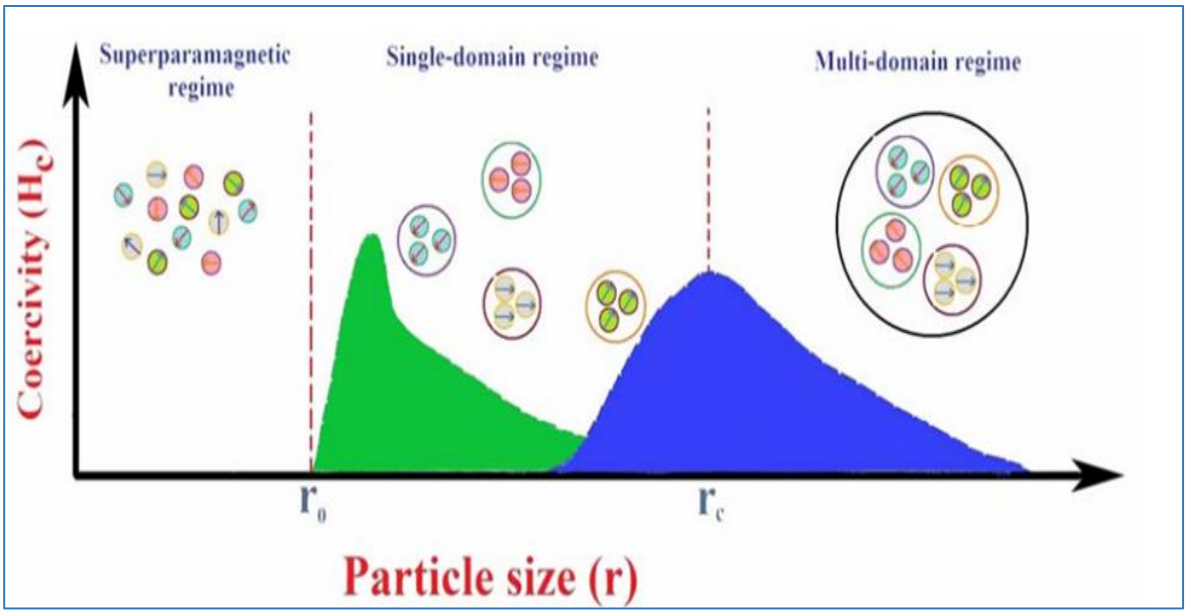

Fig. 1.6. Coercivity H_c as a function of particle size [27].

The transition temperature from ferromagnetic to superparamagnetic called the blocking temperature T_B is given by [27]:

$$T_B = \frac{K_{eff}\,V}{25\,K_B} \qquad \text{..... (1.13)}$$

where V is particle volume, K_B Boltzmann constant.

Minimizing magnetic particle size in multi-domain materials leads to formation of single domain particles (without domain wall) and produces superparamagnetism behavior. The thermal energy (K_BT) is sufficient to overcome the magnetic anisotropy energy barrier ($K_{eff.}V$), and to invert magnetic spin direction. In other word superparamagnetism happens when thermal energy or an external field can easily move the magnetic moments of the nanoparticle away from the easy axis which is the preferred crystalline axes for the magnetic moment to point along. Particles will be similar to paramagnetic atoms, but with a large magnetic moments, and in each nanoparticle magnetic order is still clear. Superparamagnetic materials can be easily magnetized and lose magnetization by external magnetic field applying and removing respectively. The value of critical radius r_c of about few tens of nanometer depends on shape, temperature and crystalline magnetic anisotropy [15, 26, 27].

Superparamagnetic particles display anhystertic but sigmoidal(S-shape) M-H curve. The particles in blocked state below T_B but above T_B the phase is superparamagnetic state. The classical Langevin model for paramagnetic is applicable:

$$M = M_s\left(cosh(\frac{\mu_B H}{K_B T}) - \frac{1}{\mu_B \mathrm{H}/\mathrm{K_B T}}\right) \qquad \text{..... (1.14)}$$

Superparamagnetic particles have no remnant magnetization after removing the field. Hence similar NMP's often exhibit different magnetic behavior because of different sample pre-history preparation and processing method producing different particle size, shape, and crystal defect morphology presence and particle-particle interaction and particle-matrix interactions [26].

1.4 Microwave Shielding

The term shielding usually refers to surrounding completely an electronic product or a portion of that product and preventing the EM emission from an outside source to spoil its electronic performance. So Shielding by electromagnetic interference (EMI) is the process by which a

certain level of attenuation for undesirable radiation is extended using a strategically designed EM shield to protect electronic device [6,10]. Sometimes this process is called suppression when it deals with decreasing or filtering stray EM.

EMI troubles always affect most electronic systems in daily activity, military applications and space investigation, because of the following reasons:

- The increasing of electronic devices in various life environments in small area gives a good chance for EMI;
- Size reduction of components in reduced electronic systems increases the possibility of EMI;
- New digital technology is in favor of EMI.

EMI has been found also harmful to human health. It may cause serious diseases like cancer [10,28]. The safe limit for microwave radiations according to World Health Organization and the International Commission on Non-Ionizing Radiation Protection guidelines is about 2.5 mW/cm^2 or less [1]. For all these reasons, active shielding materials are required to eliminate the EMI effects [28].

The whole microwave spectrum is used in the communication age, beginning from the quasimicrowave band (1GHz) for wireless telecommunications and electronic measuring equipment up to hundreds GHz. The problem of the interference between various sources, shielding for environmental EM radiation troubles, prevention of reflections and multiple reflections, and other applications requires efficient shield, inexpensive, lightweight, as thin as possible, a broad frequency range of work, and independent of the incident angle and polarization absorbers of electromagnetic EM radiation properties[19].

The EM radiation shielders are even reflection or absorption type. The forming of antireflection multilayers coating is gradually varying electromagnetic parameters to match the impedance between air and substrate. The zero reflection condition is determined by both μ and ε. The incident wave should vanish by absorbing layers before reaching the substrate. The absorber thickness is inversely proportional to the absorbed frequency and then imaginary part of the permeability.

Pure ferrites or as composites are the favorite for this application due to the possibility of modifying μ and ε independently [19]. Ferrites are used as microwave absorbers because they can absorb the MW energy around

FMR frequency. So they are used as EM absorbers to shield rooms and chambers used for EM compatibility testing of new products and devices at MW frequencies. Typically plastoferrite plates can be produced for EM absorbing applications. The EM properties of composites can be effectively tuned simply by varying the volume fractions of the constituent phases. In addition, an interaction effect between the properties of the constituent phases may also be observed in some composites [25].

The operating frequency range of mobile phones is 1-2GHz, at this frequency the typical size of the ferrite is 7mm square and 2mm thickness. The typical thickness in the 300MHz band is about 5-6mm for this absorber. A broadband RF absorbers can be made of planar hexaferrites for the 1-20GHz range. Sintered Ni-Zn ferrite absorbers are widely used in VHF/UHF band [19]. Composites of nanomagnetic materials can be utilized as broadband shields application. Iron nanoparticles in an oxide matrix have been synthesized by reaction milling, giving ΔH_{FMR} of 2.2-3.2.kG at 9.8GHz. The 8-10nm size of iron particles is below skin depth. The magnetization is high, the shape anisotropy is negligible, and the dielectric properties can be controlled by the oxide matrix [19].

Losses in ferrites depend essentially on hysteresis losses at low frequencies, conductivity (or eddy current) losses, and relaxation-resonance losses at high frequencies; their modeling is complex [10].

Ferrite nanoparticles in combination with carbon nanotubes can efficiently absorb microwave. CNT/$CoFe_2O_4$ spinel nanocomposite, the microwave absorption (2–18 GHz) was enhanced. Carbon nanotubes CNT, contribute to dielectric losses while Co ferrite is associated with magnetic losses, both isolated mechanisms are poor absorbers [25].

1.5. Aims of The Project

The nano ferrite has taken a great scientific attention due to characteristic properties. This makes the main objective of this project is to prepare a low cost nano Li-Ni ferrite by hydrothermal method. The second aim is preparing microwave absorber material or composite from nano Li-Ni ferrite with epoxy as shielding for electronic components, devices, and equipment from microwave stray signals. These objectives should also achieve requirements of low or minimum cost and that the product can be applied very easily to a variety of components such as printed circuit boards, coaxial wave guide, low-pass/high pass or pass band filters and antennas.

The objectives and requirements are transformed to tasks through surveying the methods of preparation of nano ferrite and characterization of nano Ni-Li ferrite with and without epoxy composite structurally, magnetically and their absorption for microwave. Analysis and discussing the results were done for examining the ability of applying these material and comparing the results with literatures.

1.6. Literature Review

Previous works in ferrites and MW absorbers will be divided into three branches:

1. Li-Ni Ferrites

Jiang et al. [29] prepared polyaniline (PANI)–Li Ni ferrite composite. They showed saturation magnetization is (M_s=9.7emu/g) and coercivity (Hc=128.7 Oe). The results of TGA, FTIR and UV–VIS spectra indicated that LiNi ferrite particles improve the thermal stability of composite and there are interactions between ferrite particles and PANI. TEM study showed that composite presented the core-shell structure. The composite under applied magnetic field exhibited ferromagnetic hysteretic loops.

S.A.Mazen and T.A.Elmosalami [30] prepared Li Ni ferrites by traditional ceramic method and studied the Ni content effect on structural properties. The lattice parameter was determined for each composition and found to be nearly constant over the whole range of Ni concentration (=0.83 nm±0.01). The analysis of IR spectra indicates the presence of splitting in the absorption band due to the presence of small amounts of Fe^{+2} ions in the ferrite system.

Muthafar F. Al-Hilli et al [31] prepared europium-doped Li–Ni ferrites by ceramic method and studied microstructure, electrical properties and Hall coefficient. Samples were p-type semiconductors. The dielectric loss was calculated from the AC conductivity in MHz range and found that it increased with firing temperature. They [32] studied samarium doping on structural analysis, magnetic and electrical properties Li-Ni ferrites. Hall measurement confirmed p-type conductivity behavior for Sm-doped. The dielectric constant was found to decrease rapidly at lower frequencies than at higher frequencies while the dielectric constant increased with Sm content. The decrease in ε with frequency agrees with Deby's type relaxation process. The maximum in ε was observed when the hopping frequency was equal to the external electric field frequency. The variation in tanδ with frequency showed a similar nature to that of ε with frequency.

The magnetization under applied magnetic field for the samples exhibited a clear hysteretic behavior. The SEM studies showed that the domain walls may tend to be trapped (pinned) by non-magnetic inclusions, precipitates and voids. The saturation magnetization increases with the sintering temperature, while the coercivity was found to decrease. The main charge transport mechanism was hopping of halls between Ni^{+2} and Ni^{+3}. They [33] studies gadolinium substituted Li–Ni ferrites with the formula $(Li_{0.5}Fe_{0.5})_{0.5}Ni_{0.5}Gd_yFe_{2-y}O_4$, (where $0 \leq y \leq 0.1$) which were prepared by chemical solid reaction technique. The effect of sintering temperature on the microstructure was investigated. The results exhibited spinel phase formation with variation in lattice parameters those were associated with the substitution of large size of Gd^{+3} ions. The SEM micrographs showed that the high content of Gd^{3+} ions might prevent grain growth while the effect of sintering temperature on grain size was significant.

Saafan et al. [34] prepared Co–Ni–Li ferrites by citrate precursor method. Saturation magnetization and remnant magnetization were found to increase with adding Li^{1+} ions up to x=0.15 and then decreased again, while coercivity decreased monotonically with increasing Li^{1+} ions. The change in magnetic properties by adding Li^{1+} ions was explained as depending on many factors such as crystallite size, measured density, porosity, expected cation distribution, A–B exchange interactions, and magnetocrystalline anisotropy.

Pathan et al. [35] used auto combustion method to prepare Co-Li-Ni-Zn ferrites having the general formula $Li_{0.5}Ni_{0.25-x/2}Co_{x/2}Zn_{0.5}Fe_2O_4$ with different Co content. The dielectric parameters were meiasured in the frequency range 20Hz – 1MHz, showing normal dielectric behavior of spinel ferrites. The frequency dependence of loss tangent (tan δ) was found to display a peak at certain frequency. The dielectric properties were explained in terms of Fe^{2+} concentration. Saafan and Assar[36], The ac conductivity and dielectric properties of spinel ferrite nanoparticles of $Li_{0.1}(Ni_{1-x}Zn_x)_{0.8}Fe_{2.1}O_4$ frequency and temperature by using a complex impedance technique. The ac conductivity of the samples was increased with increasing temperature, ensuring the semiconducting behavior of both nano and bulk samples, The significant decrease in ac conductivity σ_{ac}, dielectric constant, and dielectric losses of as-prepared nanosamples compared to their bulk counterparts was correlated to the small size of the grain compared to the grain boundary size.

Maisnam et al. [37] prepared Li-Ni-Mn ferrites by ball milled with distilled water, dried and calcined at 850°C and sintered by microwave furnace at 1050^0C for 30 minutes in air. Saturation magnetization value has been found to be slightly reduced with microwave sintering. The rapid rise in the dielectric constant with temperature has been significantly shifted to higher temperature. Maisnam [38] studied the significant changes in the structural, microstructural, magnetic and electrical properties of microwave sintered Li Ni Mn ferrites over the conventionally prepared one. Microwave sintering was the reason to reduce the evaporation of lithia or oxygen during sintering of lithium based ferrites further resulting in reduction in formation of ferrous ions. That has deep effect on the magnetic and electrical properties of the final product. Saturation magnetization value has been found to be slightly reduced with microwave sintering. Low dielectric constant values were measured in the composition prepared by microwave sintering. Increase in activation energy obtained in the sample sintered using microwave field offers greater resistance to the thermal activation of the polarizable charges. The rapid rise in the dielectric constant with temperature has been significantly shifted to higher temperature.

Chappel et al. [39] prepared $LiNi_{1-y}Fe_yO_2$ samples by solid state reaction method. They got products having single-phase. From AC magnetic susceptibility and magnetisation measurements, they determined the role of the extra 3d cations in lithium site. The relative distribution of the Ni and Fe ions in the layers was also derived and is in good agreement with Mössbauer data. Bhatu et al. [40] studied the structural and elastic properties of $Li_{0.5(1-x)}Ni_xFe_{2.5-0.5x}O_4$ (x = 0.0-1.0) spinel ferrite. The X-ray diffraction data was used to determine the lattice constant, X-ray density, distributions of cations among the tetrahedral and octahedral sites of spinel lattice, anion parameters, site radii, ionic radii, bond angle and bond length. The nature and change in the position of IR bands have been explained on the basis of cations involved in the system. The force constants have been used to calculate elastic moduli like bulk modulus, rigidity modulus, Young's modulus, Poisson's ratio, Debye temperature and corrected to zero porosity. The observed variation of elastic constants with nickel substitution has been explained on the basis of interatomic bond strength. The Debye temperature obtained from elastic constant data was higher than

that of the XRD analysis, mainly due to existence of peaks in the vibrational spectra at lower frequencies.

The dielectric properties of Li-Ni-Cd ferrites as a function of frequency in the range 100 Hz- 1 MHz were reported by Kharabe et al. [41]. It was found that the dielectric constant decreases with frequency rise that is explained on the basis of Maxwell-Wagner type of interfacial polarization in accordance with Koop's phenomenological theory. Dielectric constant was roughly inversely proportional to the square root of resistivity. Kharabe et al. [42] reported the structural and electrical properties of $Li_{0.5}Ni_{0.75-x/2}Cd_{x/2}Fe_2O_4$ (where x = 0. 0.1, 0.3, 0.5, 0.7, 0.9) ferrite. The temperature dependent on dc resistivity showed that the conduction takes place by hopping mechanism. The dc resistivity at room temperature showsed decrease with Cd content up to 0.3 and then it is enhanced with further increase in Cd contents. The variation of Seebeck coefficient with temperature reveals that the samples with x =0, 0.5, and 0.7 show p-type conduction whereas the samples with substitution level x = 0.1, 0.3 and 0.9 show transition from n-type to p-type charge carriers. The average grain diameter was found to increase while the Curie temperature decreases linearly with cadmium content.

2. Li ferrites, Ni ferrites and their substituted ferrites

Sankaranarayanan [43] prepared Lithium ferrite nanoparticles with size of about 10 nm by a citrate precursor method at a relatively low temperature of 200°C. The particles were examined by XRD and they showed broadened. The sample decomposed at 200 °C has the β-$LiFe_5O_8$ type (a disordered type of spinel) structure which on annealing at 350 ^{0}C transformed to the α-$LiFe_5O_8$ type (an ordered type spinel) structure as shown by both IR spectra and XRD studies. Magnetization curves indicate a particle size distribution consisting of both ferromagnetic particles and a superparamagnetic fraction. The value of $4\pi M_s$ was 2000G this means the particles could be useful for applications in certain low magnetization ferrofluids.

Ridgley [44] found that under 1 atmosphere of oxygen, lithium ferrite loses both oxygen and lithium oxide in increasing amounts with increasing temperature above about 950 to 1000°C. These losses affected structural and magnetic properties. Venudhar [45] prepared different lithium–cobalt mixed ferrites compositions by the double sintering technique, the final sintering temperature was 1100 ^{0}C. The dielectric constant was found to

decrease continuously with increasing a cobalt content. This had been explained on the basis of the availability of Fe ions on the octahedral sites. The dielectric constant also decreases with increasing frequency for all the samples under study. The reduction in the dielectric constant at higher frequencies has been explained on the basis of the fact that beyond a certain frequency of the externally applied electric field, the electronic exchange between the ferrous and ferric ions cannot follow the frequency of the alternating field.

Fua et al [46] prepared Li ferrites by microwaved-induced combustion process. The product showed the formation of lithium ferrite had saturation magnetization (M_s) of 13 emu/g, whereas upon annealing at 650 °C for 2 hr, the saturation magnetization increased to 71 emu/g. A high purity lithium ferrite was obtained when it was annealed at 650 °C for 2 hr, and had particle size ranged from 50 to 80 nm. The $Li_{0.5}Fe_{2.5}K_xMn_xO_4$ powders ($0 < x < 1.0$) with small and uniformly sized particles were successfully synthesized by microwave-induced combustion by same group [47]. The resultant powders annealed at 650 °C for 2h structural and magnetic properties were investigated. The results revealed that Mn content are strongly influenced the magnetic properties and Curie temperature of Mn-substituted lithium ferrite powder. The substituting an appropriate amount of Mn for Fe in the $Li_{0.5}Fe_{2.5}K_xMn_xO_4$ specimens markedly improved the complex permeability and loss tangent. They [48] studied the effect of adding Al and Cr to Li ferrites. The results revealed that saturation magnetization and Curie temperature of $Li_{0.5}Fe_{2.5-x}M_xO_4$ are strongly affected by different metal ions substitution. The results revealed that the lattice constant decreases linearly with increasing in Cr content in $Li_{0.5}Fe_{2.5-0.5x}Cr_xO_4$ specimens. Moreover, they [49]measured the magnetic properties of Cr-substituted lithium ferrite that is strongly affected by Cr content. The saturation magnetization, remanent magnetization, and coercivity decrease monotonously with increasing in Cr content.

NING LI [50] employed direct liquid injection of chemical vapor deposition (DLI-CVD) has been utilized for epitaxial growth of nickel ferrite ($NiFe_2O_4$), lithium ferrite ($LiFe_5O_8$) were obtained in the temperature range of (500-800) ºC on both MgO(100) and $MgAl_2O_4$(100). Magnetic measurements reveal an increase in the saturation magnetization for the films with increasing in growth temperature. Nickel ferrite films deposited on $MgAl_2O_4$ (100) at 800 ºC exhibit saturation magnetization

very close to the bulk value of 300 emu/cm^3. Out-of-plane FMR measurement showed the narrowest FMR line width of ~160 Oe for films deposited at 600˚C. Epitaxial growth of lithium ferrite films on MgO(100) was observed at the temperature range of (500-800)˚C. The grown films also showed an increase in the saturation magnetization with increasing deposition temperature.

Singhal et al. [51] prepared nano Li ferrite through aerosol route. The obtained particle size of the samples was about ~10 nm through TEM that increases up to ~ 80 nm on annealing at 1200 ^{o}C. The unit cell parameter calculated through XRD confirms the formation of α-$LiFe_5O_8$. Cation distribution obtained from the X-ray, magnetic confirms that the three fifth of the iron atom goes in to the octahedral site. Tehrani [52] intserted nonmagnetic dopants Zn and Cu to nickel ferrite nanocrystals, $Ni_{1-x}M_xFe_2O_4$ ($0 \leq x \leq 1$, M= {Cu, Zn}). Basically, these dopings cause a rearrangement of Fe^{+3} ions into the two preexisting octahedral and tetrahedral sites. In the case of Cu doping, the Jahn-Teller effect also emerges, which they identify through the FTIR spectroscopy of the samples. They showed an increase in the lattice parameters of the doped samples, besides a superparamagnetic behavior of the doped samples was shown, while the Jahn-Teller effect precludes a similar behavior in the $CuFe_2O_4$ nanocrystals. Khan et al. [53] investigated the impacts of terbium (Tb) contents on magnetic, ferromagnetic resonance, electrical and dielectric properties of $Ni_{1-x}Tb_xFe_2O_4$ ferrites. It was found that the increasing of Tb content produces decrease in the coercivity and saturation magnetization which may be attributed to spin canting. Magnetic dynamics of the samples was studied by ferromagnetic resonance in X band (9.5 GHz) at room temperature. The incorporation of Tb sufficiently lowers the FMR line-width. The decrease in FMR line-width is attributed to the reduction of super-exchange interactions. The DC resistivity and activation energy were higher for the substituted samples. The dielectric constant, dielectric losses (tanδ) and AC-conductivity decreased on account of doping. The dielectric data are explained on the basis of space charge polarization.

Carta et al. [54] studied the structural and magnetic properties of nanocrystalline manganese, cobalt, and nickel spinel ferrites dispersed in a highly porous SiO_2 aerogel matrix. The cation distribution between the octahedral and tetrahedral sites of the spinel structure was investigated by

X-ray absorption spectroscopy. The analysis of both the X-ray absorption near edge structure and the extended X-ray absorption fine structure indicates that the degree of inversion of the spinel structure increases in the series Mn, Co, and Ni spinel, in accordance with the values commonly found in the corresponding bulk spinels. The fitting of EXAFS data indicates that the degree of inversion in nanosized ferrites was 0.20 for $MnFe_2O_4$, 0.68 for $CoFe_2O_4$, and 1.00 for $NiFe_2O_4$. Magnetic characterization supported these findings.

Singh et al. [55] prepared $Zn_{0.5}Li_{1-2x}Mg_xFe_2O_4$ for ($0 < x < 0.5$) by sol-gel auto combustion technique. The dielectric properties in the frequency range (10 Hz-10 MHz) in the temperature range (310-473 K) had been tested. The effect of temperature, frequency and composition on dielectric constant, dielectric loss (tanδ) and conductivity has been discussed in terms of hopping of charge carriers ($Fe^{+2} \leftrightarrow Fe^{+3}$). The occurrence of peak in the dielectric losses (tanδ) spectra was found to be temperature and composition dependent. The electrical modulus formulism has also been employed to study the relaxation dynamics of charge carriers and the results indicate the presence of non-Debye type of relaxation in these ferrites. The absence of hysteresis and non-attainment of saturation magnetization (even at 8 kOe) suggests the super paramagnetic behaviour of these ferrites. Lee et al. [56] prepared Ni-ferrite by coprecipitation method in a microwave-hydrothermal reaction. The effect of formation conditions on the ferrites (pH, temperature, and time) was studied. The ferrite phase began to form at a relatively low temperature (120 °C) in a short-holding time (30 min). The crystallization of single-phase ferrite was promoted with an increase in annealing temperature and time. Under the same conditions, the sample prepared by the conventional hydrothermal method did not show the ferrite phase in XRD.

Faraz [57]synthesized the mixed Li-ferrites with dopants Mn^{2+} and Cd^{2+} by co-precipitation method. The nanoparticles size was in the range (17–36)nm. The dopant by incorporating Cd^{2+} raised the lattice parameter from 8.3 Å to 8.7 Å. This increase is due to difference in cations radii. The dc resistivity (ρ_{dc}) and drift mobility confirmed a semiconducting-like behavior. A small amount of Cd^{2+} causes an increase in saturation magnetization (Ms) and remanence (Mr) values. As x increased up to x=0.3, Ms increasesed, while further incorporation of Cd^{2+} decreased magnetization. This is due to canted spin. The decrease in Curie

temperature with increase in Cd^{2+} is due to interaction between tetrahedral (A) and octahedral (B) lattice sites.

Obi et al.[58] fabricated $Ni_{0.27}Zn_xFe_{2.73-x}O_4$ for (x = 0.03-0.1) thin films with high real permeability in the GHz range by the spin spray process onto glass substrates in the presence of external magnetic field of 360 Oe. These films exhibit high permeabilities that exceeded the Snoek limit for bulk NiZn-ferrite films and those previously reported for spin spray deposited ferrites. The NiZn-ferrite film at x =0.06 had magnetic losses, having ($\tan\delta$=0.027) from 1 to 1.5 GHz. A high ferromagnetic resonance (FMR) frequency of (2.7 GHz), while at (x = 0.1) the film exhibited a high μ' of 50 and $\mu'' > 50$ at 1 GHz. These properties are ideal for microwave applications such as antennas, inductors and electromagnetic interference (EMI) suppression in the GHz range. Bhise [59] synthesized substituted $Co_xZn_{0.8-x}Fe_2O_4$ (x=0.2, 0.5 and 0.6) ferrite with Nickle by sol-gel auto combustion method. The powders were sintering at 400^{o}C and 700^{o}C for 2hrs to densify properly. The XRD analyzed phase structure. The FTIR spectra confirmed that synthesis material was ferrite. The saturation magnetization increasesd with increasing Co-Zn concentration. Ferrite resistivity was decreased due to variation in concentration of Co and Zn.

Yusoff [60] used the complex scattering parameters (S_{11}*; S_{21}*; S_{12}* and S_{22}*) for measuring microwave permittivity; permeability and absorption characteristics of an undoped and doped samples (1 wt% CuO and MgO) for $(Li_{0.5}Fe_{0.5})_{0.7}Zn_{0.3}Fe_2O_4$ (LiZn ferrite) using a VNA by means of coaxial two-port and short-S_{11} techniques in the frequency range of 0.3–13.51 GHz. The addition of CuO and MgO has been found to increase the reflectivity and transmittivity relative to the pure LiZn ferrite. The dielectric constant and losses decrease with oxide addition but the change in the magnetic permeability was minimal. The ferrites exhibited magnetic resonance due to domain wall movement in the low-frequency regime. The ferrites showed a low-frequency matching condition when the complex relative dielectric permittivity equals that of the complex relative magnetic permeability $\mu_r^*=\varepsilon_r^*$: The matching frequency was found to increase but with a smaller matching thickness for the doped samples. The second matching condition at higher frequency, which occurs due to a geometrical cancellation of the incident and reflected waves at the surface of the absorbers, can only be seen for the LiZn/MgO sample.

Gupta [61] fabricated lithium ferrite substituted by Co and Mn –polymer composite films of thickness ~80 μm. The substituted lithium ferrite powders with general composition of $Li_{0.5-x/2}Co_xMn_{0.1}Fe_{2.4-x/2}O_4$ at x=0.0, 0.2, 0.4 and 0.6, were prepared by citrate-route. The composite films required lower processing temperature ~100°C. Cavity-perturbation technique was employed to measure the complex permittivity, and the complex permeability, of the composite films at X-band microwave frequencies (8–12 GHz). The dispersion in the complex permittivity of ferrite composite films was found to be significant. The maximum value of ε″ was observed for the film at x=0.6 and 75% volume loading of ferrite component. The permeability (μ′) of films was found to decrease with an increase in frequency as well as the volume loading of ferrite component in composite films. The single-phase of the substituted lithium ferrite powders for compositions (x=0.0, 0.2, 0.4 and 0.6) was confirmed by XRD pattern.

Folgueras et al. [62] presented the processing and characterization of EM radiation absorbing paints and sheets based on magnetic and dielectric materials dispersed in polymeric matrices. Two different paint formulations containing carbonyl iron and/or polyaniline, using polyurethane as matrix, were prepared. Silicone sheets were also produced with polyaniline conducting polymer as filler. Measurements of the electric permittivity and magnetic permeability of the materials were also carried out. Simulations of the silicone sheets were performed in order to correlate the electromagnetic parameters with the material thickness. The paints absorbed 60 to 80% of the incident EM radiation and the silicone sheets absorbed 90%, indicating the material's radar absorbing potential.

Fazio et al. [63] prepared nano lithium-substituted Mn-Zn ferrites $Li_{0.5x}Mn_{0.4}Zn_{0.6-x}Fe_{2+0.5x}O_4$ by the sol-gel autocombustion method. XRD analysis confirmed that samples has monophasic that is spinel phase. The saturation magnetization increases while the cell parameter of the cubic phase decreases with Li concentration. Magnetic permeability and dielectric permittivity of all samples were measured at room temperature as a function of frequency. Reflection loss calculations showed that the prepared samples are good absorbers in microwave range.

Mazen and Abu-Elsaad [64] prepared polycrystalline ferrites, $Li_{0.5-0.5x}Mn_xFe_{2.5-0.5x}O_4$, with (x = 0.0-1.0) by using ceramic method. The lattice parameter was found to increase with increasing Mn^{2+} substitution. IR

spectra of the samples were recorded from 200 to 1000 cm^{-1}. The two primary bands corresponding to tetrahedral υ_A and octahedral υ_B were observed at about 575 cm^{-1} and 370 cm^{-1}, respectively. Young's modulus (E), rigidity modulus (G), bulk modulus (B), Debye temperature (θ_D), and mean sound velocity (Vm) were calculated from the transverse (Vt) and longitudinal (V_l) wave velocities. The variation of elastic moduli with composition is interpreted in terms of binding forces between the atoms. AC conductivity and dielectric properties of the samples were measured at room temperature and over 100Hz–1MHz. The electrical conduction could be explained with the electron hopping model.

Cadieu and Rani [65] synthesized Li-ferrite films by PLD from bulk targets onto sapphire substrates. The substrate temperatures approached 1000 °C and the growth mode was predominant (333). A similar growth mode was reported for Ni-ferrite films grown sapphire substrates. The films were 4–8 μm thick and were grown at deposition rates of 3–5 Å/s at oxygen partial pressures of 200–400 mTorr. Magnetic measurements were made by using SQUID and 9.5 GHz FMR on the as deposited films. Li-ferrite films with XRD intensity ratios of I(333)/I(311)= 10.3 for films made in (200mTorr) oxygen and (14.5) for films made in (400mTorr) oxygen exhibited coercivities of (100Oe) for SQUID measurements. Li-ferrite films made in 400 mTorr oxygen exhibited symmetric FMR absorption lines with a derivative peak-to-peak linewidth of (335Oe) for the in-plane static field configuration. The FMR profiles for the perpendicular-to-plane field configuration were highly distorted. The magnetization versus field measurements yielded saturation flux density $4\pi Ms$ of 3.6–4.0 kG which are in the same range as for bulk Li-ferrite. The in-plane FMR line widths were significantly larger than expected for bulk single crystals or large grain size, dense polycrystals.

Rendale et al. [66] synthesized $Li_xMg_{0.7-2x}Zn_{0.3}Fe_{2+x}O_4$ ferrites by the sucrose precursor method. The cosubstitution of lithium and iron ions caused a decrease in the lattice parameter obeying Vegard's law. The variation in force constant with bond length showed an unexpected trend on both A and B sites of the lattice. Magnetic hysteresis studies revealed a reduction in magnetization due to Mg^{2+} concentration increasing. AC susceptibility showed the possibility of presence of superparamagnetic particles in the samples. The Curie tmperature decreased with the increase in magnesium concentration. Kwon [67] investigated the crystallographic

and magnetic properties of vanadium-substituted lithium cobalt titanium ferrite, $Li_{0.5+x}Co_{0.2}Ti_{0.2}V_xFe_{2.1-2x}O_4$. Ferrite was replaced with vanadium in the range 0.00-0.20 by 0.05 conventional ceramic method. The lattice parameters were nearly constant as the substituted content increased. The average grain size was increased with x. An increase in the vanadium content led to an increase in the saturation magnetization and then to some decrease whereas the coercivity decreased. The maximum saturation magnetization was 44.81 emu/g at x = 0.05, and the maximum coercivity was 120.4 Oe at x = 0.

Widatallah et al. [68] reported the cation distribution of aluminium substituted Li-ferrites. The cation distribution was investigated by using Rietveld refinement of the XRD data. It was found that the Al^{3+} ions replaced both Fe^{3+} and Li^{+} ions on octahedral sites and the substituted Li^{+} ions replaced Fe^{3+} ions at tetrahedral sites. Al-Darub et al. [69] prepared Ferrites type β-$LiFe_5O_8$ by Freeze drying. Starting from Li_2CO_3 and $FeC_6H_5O_7$ mixing and then dissolves in distilled water and sprayed in liquid nitrogen, the droplets were dried by using freeze drying system with (10^{-1}-10^{-2}) mbar and -40 ºC to produce a fine homogeneous powder. Two calcination stages were done. The powder was pressed as disk and ring, sintered at 900, 950, 980, 1000, and 1050 °C for 48h for each degree. The sample was that sintered at 1000 °C satisfy the most properties of β-$LiFe_5O_8$ phase according to XRD & FTIR and magnetization measurements. He got β-$LiFe_5O_8$ at Ts=1050ºC with many its properties without volatile Li ions because using FDM.

Gama et al [70] studied magnetic and structural properties of nanosize Ni-Zn-Cr ferrite particles. A secondary phase of hematite was observed in all the samples without chromium. The sample with 0.1 mol chromium exhibit only Ni-Zn cubic phase. The grain size slightly reduced with the increase in chromium concentration. The magnetic saturation was reduced by 34 % and coercivity by 77 % with the inclusion of chromium. This material has a high frequency transformer application.

3- Nanoferrites absorption for microwave and FMR

Torres et al. [71] carried out ferromagnetic resonance (FMR) measurements of polycrystalline Ni ferrites at 11 GHz from (77 to 400 °K). The different contributions to the FMR linewidth have been studied by a computational technique based on the parameters previously obtained for single-crystal Ni ferrite. A new qualitative comparison between the FMR

and disaccommodation measurements by means of the induced anisotropy formalism was presented. Bayrakdar [72] synthesized ferrite-polymer nanocomposite structures. He theoretically and experimentally investigated electromagnetic propagation, absorption properties of these nanocomposite materials at 8–20GHz in microwave guides. The microwave properties of the samples were investigated by transmission line method, and reflection loss of −59.60dB was found at 12GHz for an absorber thickness of 2mm. they suggested these nanocomposites may be attractive candidates for microwave absorption materials.

Hsiang [73] investigated the ferrite load effect on the thermo-mechanical and electromagnetic properties of NiZn ferrite powder- epoxy resin coatings. It was observed that the Young's modulus and glass transition temperature of the composites decreased as the ferrite load increased from 30 to 50wt% and increased as the ferrite load was further increased above 70wt%. The dielectric constants and initial permeability both increased with increasing ferrite load.

Shimba et al. [74] suggested obtaining thinner microwave absorbers for device design through increasing the volume fraction of magnetic nanoparticles by enhancing the permeability of composites. Composites were prepared using Ni-Zn ferrite nanoparticles surface-modified with (4-methacryloxyethyl trimellitate anhydride) and cross-linked with PEG-4SH (pentaerythritol tetra-polyethylene glycol ether with four thiol-modified terminals). These composites have a high volume fraction of nanoparticles (up to 72 vol%) and permeability ($\mu_r''_{max}$=5.9). In addition, the prepared composites showed good microwave absorption properties (R.L< -20 dB) with a smaller matching thickness than conventional microwave absorber using spinel-type ferrite.

Šutka [75] synthesed $Ni_{1-x}Zn_xFe_{2+z}O_4$ at (x=0, 0,3, 0,5, 0,7, 1 and z=-0,025, -0,01, 0, 0,05, 0,1, 0,15, 0,2) by sol-gel auto combustion. The samples were sintered from 800 to 1300°C. Nanostructured $Ni_{1-x}Zn_xFe_2O_4$, at (x=0; 0,3; 0,5; 0,7; 1) thin films on glass substrate were obtained by using spray pyrolysis. The DC resistivity increased with increasing zinc ion content due to the decrease in charge carrier (hole) concentration, which is attributed to Ni^{3+} reduction to Ni^{2+}. Electrical resistivity of nanostructured Ni-Zn ferrites, contrary to micro structured Ni-Zn ferrites, increases with increasing zinc ion content, due to its relatively low processing temperatures and an electron hole recombination. For

$Ni_{1-x}Zn_xFe_2O_4$ electrical resistivity increases if x<0.5 due to the charge carrier concentration, but it decreases if x>0.5 attributed to the addition of extra Fe^{2+}. Complex impedance spectroscopy spectra showed The resistance of the grain boundary was found to be higher than the resistance of the grain, as well as both of them decreased with increasing annealing temperature.

Tada [76] successfully prepared $Fe_3O_4/\gamma–Fe_2O_3$ polycrystalline films having a wide range of crystallite sizes by changing the plating conditions at 90 °C. The lattice constants and the crystallite size were determined by XRD. Natural resonance frequency f_r for the film increased from 0.8 to 1.9 GHz as the crystallite size D decreased from 63 to 30nm. In polycrystalline films, magnetic anisotropy field H_k is induced mainly by crystallite boundary/surface effect so that a larger crystallite will cause a weaker H_k.

Dias et al. [77] prepared hydrothermally NiZn ferrites which were sintered at different experimental conditions, leading to materials of composition $Ni_{0.34}Zn_{0.60}Fe_{2.06}O_4$. An investigation of the dielectric properties over a wide frequency range showed the semiconductor character of the ferrites. The relaxation was modeled using a Cole-Cole model and the parameters correlated with the microstructural evolution of the ferrites during the sintering. The contributions of hopping electrons and space charges to the total conductivity have been discussed. The static permittivity increase is related to the grain growth process rather than densification. The presence of ferrous ions in sintered samples and the observance of no peaks in dielectric constant in the low frequency region indicates that the conduction mechanism is the electron hopping.

Sun [78] prepared Ce-substituted lithium ferrite, $Li_{0.5}Ce_xFe_{2.5-x}O_4$ (x=0, 0.015 and 0.15), from metal nitrates by the citrate sol–gel method. The complex permittivity and complex permeability and microwave absorption properties of $Li_{0.5}Ce_xFe_{2.5-x}O_4$–paraffin wax composite were measured by the transmission/reflection coaxial line method in the range of (2–18 GHz). This investigation demonstrated that microwave absorbers for applications over 15 GHz, with reflection loss more than −20 dB for specific frequencies, could be obtained by controlling the substituted Ce element.

Schoenberg [79] found beyond 1300 °C, all Ni and NiZn ferrites samples exhibit low resistivities due to formation of Fe^{2+} ions. The losses of Zinc in NiZn materials at high temperature were expected to introduce

Fe^{2+} ions. Addition of small amount of iron in NiZn ferrite was reported to cause low resistivity and high conductivity.

Rowen et al. [80] reported the dependence of dielectric losses factor at 9.4 GHz on dc resistance for Ni ferrite. It was concluded that tanδ decreases sharply with the resistance increase. It was also concluded that the number of ferrous ions at octahedral sites plays dominant role in the conduction and polarization. The dielectric constant of $Li_{0.45}Mg_{0.1}Fe_{2.45}O_4$ decreased from 624 at 1 MHz to150 at 13 MHz because the electronic exchange between charge carriers cannot follow the frequency of the applied field. The frequency dependence of tanδ was found to be abnormal because some peaks were seen at certain frequency.

The dielectric response of $Li_{0.5-0.5x}Mg_xFe_{2.5-0.5x}O_4$ (x = 0.1-0.9, step: 0.2) in the range 1-13 MHz was reported by Ravinder et al. [81]. It was found that the real part (ε′) and loss tangent (tanδ) are reduced with reduction in Fe^{2+} content whose exchange with Fe^{3+} gives rise to maximum polarization. The composition of $Li_{0.45}Mg_{0.1}Fe_{2.45}O_4$ exhibited the highest value of ε′, ε″ and tanδ because it has maximum Fe^{2+} concentration.

Ravinder et al. [82] reported the frequency range (1-15 MHz) behavior of $Ni_{0.7}Zn_{0.3}Gd_xFe_{2-x}O_4$ (x=0.0-1.0, step:0.2). It was found that the composition of $Ni_{0.7}Zn_{0.3}Gd_xFe_{2-x}O_4$ has the highest value of dielectric constant (21.13) due to highest number of Fe^{2+} whose exchange with Fe^{3+} gives rise to maximum dielectric polarization. The composition of $Ni_{0.7}Zn_{0.3}Fe_2O_4$ has the lowest dielectric constant due to minimum Fe^{2+} concentration. The composition of $Ni_{0.7}Zn_{0.3}Gd_{0.6}Fe_{1.4}O_4$ exhibited the lowest value of the losses tangent (tanδ=0.061). It was found that the dielectric constant is inversely proportional to the square root of resistivity. The materials with low resistivity exhibit high dielectric losses and vice versa.

The effects of rare-earth oxides on physical properties of $Ni_{0.7}Zn_{0.3}Fe_{1.98}R_{0.02}O_4$, where R= Yb, Er, Dy, Tb, Gd, Sm, or Ce ferrite was synthesized by ceramic method were reported by Rezlescu et al.[83]. It was concluded that the permeability increases with the size of ionic radius. For Ce substitutions, initial permeability is enhanced continuously up to Curie temperature. Rare-earth ions having large size and stable valence of 3+ were found to be the best subsistent in order to improve electrical resistivity. In first series, large Sc^{3+} ions replace smaller ions Fe3+ions, so bond length increases and that limits the hopping probability. It was

concluded that, the two magnon theory developed for ferromagnetic relaxation is not valid for ferrites. The experimental set up should be devised to assess the porosity contribution to the linewidth. The anisotropy contribution to polycrystalline ferrites was neglected while porosity and eddy-current contribution to the line width also appeares.

Sattar et al. [84] reported the dielectric properties of $Cu_{0.5}Zn_{0.5}Fe_{2-x}R_xO_4$ (R=La, Nd, Sm, Gd at x=0, 0.1) in the frequency range 50-10^5 Hz. The real part of permititivity (ε′) and loss tangent (tanδ) showed decreasing with increasing frequency while ac conductivity (σ_{ac}) was generally increased. ε′, tanδ, and σ_{ac} were increased with temperature. The decrease in ε′ with increasing frequency is due to the fact that the electron exchange between ferrous and ferric ions cannot follow the applied field frequency. The decrease in ε′, tanδ and the increasing of σ_{ac} as a function of frequency are explained by Koop's model.

Kumar et al. [85] studied dielectric behaviour at (1-13 MHz) range for $Ni_{0.7}Zn_{0.3}Er_xFe_{2-x}O_4$ (x = 0.2-1.0, step: 0.2). The real part of dielectric constant (ε′), and loss tangent (tanδ) showed increasing with the increasing of Er contents. The composition $Ni_{0.7}Zn_{0.3}Er_{1.0}Fe_{1.0}O_4$ has a maximum value of dielectric constant of 882 at 1 MHz because it contains maximum number of Fe^{2+} ions. ε′ decreases continuously with frequency. A maximum of tanδ was observed at 7 MHz because hopping frequency was nearly equal to the applied electric field at this stage. ε′ was approximately inversely proportional to the square root of resistivity. It was found that the materials with low resistivity exhibit high dielectric losses and vice versa.

Berchmans et al. [86] reported the dielectric properties of $Ni_{1-x}Mg_xFe_2O_4$ as a function of frequency in the range 50 Hz to 10 KHz at room temperature. The dielectric constant decreases with rise in frequency which is explained on the basis of Maxwell-Wagner model. The lower dielectric constant was observed for the $Ni_{0.1}Mg_{0.9}Fe_2O_4$ sample due to lowest concentration of Fe^{2+} ions in the octahedral sites .

Mangalaraja et al. [87] reported dielectric properties of $Ni_{0.6}Zn_{0.4}Fe_2O_4$ synthesized by microwave-assisted flash combustion technique. It was found that the dielectric constant and dielectric loss factor are slightly higher than ferrites synthesized by flash combustion technique in normal heating. High density was obtained in case of microwave heating.

Rao et al. [88] studied the influence of V_2O_5 additions on the resistivity and dielectric properties of Ni-Zn ferrites. It was found that the dielectric

loss tangent increases with the increasing concentration of vanadium. The dielectric constant and the dielectric loss tangent were found to exhibit normal dielectric behavior up to lower megahertz region while showing peaks around 4 MHz. They [89] reported the dielectric properties of $Ni_{0.65}Zn_{0.35+x}Fe_{1.99-2x}In_{0.01}Ti_xO_4$ at (x=0.0-0.125) by step of 0.025. It was concluded that the dc resistivity increases with Ti content. It was found that the dielectric constant of these ferrites is in the order of 10^3 and the samples containing Ti exhibited lower dielectric losses compared to that without Ti because titanium ions on B-sites impede the hopping process. They [90] reported the FMR of $Ni_{0.65}Zn_{0.375}In_xTi_{0.025}Fe_{1.95-x}O_4$ ferrites nanoparticles prepared by using ball milled. Each samples exhibited asymmetric one peak. The linewidth was attributed to the decreasing of Fe^{3+} ions and showed large values ranges from 1400-1800 Oe.

Ataa et al. [91] measured the initial magnetic permeability and ac conductivity of $Li_{0.5-0.5x}Co_xFe_{2.4-0.5x}R_{0.1}O_4$, at x=0.0, 0.5 where (R=Y, Yb, Eu, Ho and Gd prepared by ceramic techniques method. The ac conductivity exhibited dispersion with frequency where the hopping process was the predominant. The initial permeability with temperature measuerment showed multidomain structure at x=0 and single domain structure for all other compositios.

Ajmal et al. [92] reported the effect of zinc addition on Ni ferrite properties. Particle size was 6.16 nm. The lattice parameters increased from 8.337 to 8.490 Å. The resistivity decreased from 1.629×10^6 to 3.0×10^3 Ω.cm at 360 K and activation energy decreased from 0.388 to 0.217 eV. The dielectric constant approached 31580 as zinc content increased at 100 kHz. Loss factor decreased from 9.057 to 0.456 as the frequency increased from 80Hz to 1MHz.

Sivakumar et al. [93] prepared $Ni_{0.5}Zn_{0.5}Fe_2O_4$ nanoferrite. The sample which grain size of 14nm showed lower dielectric losses than bulk Ni Zn ferrite. The increasing of tanδ with milling time was because of the resistivity reduction due to oxygen vacancies produced by milling. The electrical conduction as well as polarization was found to have similar mechnism.

Hua et al. [94] reported the influence of texture and sintering temperature on NiZn and NiCuZn ferrites properties. The initial permeability increased with the slight increase in Fe_2O_3 for both NiZn and NiCuZn ferrites while slight addition of Fe_2O_3 had no remarkable effect on

magnetic flux density. Power losses of NiCuZn ferrite were found to be less than that of NiZn ferrite samples at all sintering temperature. The higher resistivity values belong to smaller grain size. the samples had different microstructures but same initial permeability values, this was due to the big grain size. The sample with large grain size and closed pores could have minimum power loss. However, the sample having small grain size had better performance in the testing frequency range for the low induction condition. These results were described in terms of the effects of grain boundaries and closed pores to the domain wall movement.

Singh et al. [95] prepared $Zn_{0.5}Li_{1\ 2x}Mg_xFe_2O_4$ ($0 \leq x \leq 0.5$) ferrites by sol-gel auto combustion method. The impedance measurements measured dielectric properties in the frequency range 10 Hz-10 MHz and in the temperature range (310-473 K). The effect of temperature, frequency and composition on dielectric constant, dielectric losses and conductivity have been discussed in terms of hopping of charge carriers ($Fe^{2+} \leftrightarrow Fe^{3+}$). The occurrence of peak in the dielectric loss ($\tan\delta$) spectra was found to be temperature and composition dependent. Identical values of activation energy for dc conduction (E_{dc}) and for conductivity relaxation (EMN) reveal that the charge carriers have to overcome the same energy barrier while conducting and relaxing. The absence of hysteresis and non-attainment of saturation magnetization (even at 8 kOe) suggests the super paramagnetic behavior of these ferrites.

the magnetic spectral studied on Li Zn ferrites had been carried out by Raman [96] using two independent measurements. The results of RF frequency studies indicated the existence of the domain wall resonance. The microwave absorption studies at various static magnetic fields indicate the rotational resonance. These phenomena strongly depend on zinc content.

Tripathi et al. [97] prepared nano Ni-Zn ferrite samples with 30% (by wt.) filled polyurethane matrix. Simulation for metal backed monolayered absorber was done to study the microwave absorbing properties of different thicknesses of the samples. The VNA attached to coaxial set up was used to investigate the complex permittivity and permeability in a frequency range of 110 MHz to 18 GHz. SEM and TGA were performed to analyse the morphological and thermal behaviour of the composite. The complex permittivity and permeability were found to be frequency dependent. The

reflection loss increased from -7.95 dB to -12.93 dB at 12.27 GHz against the sample thicknesses of 1.0 mm, 2.0 mm and 3.0 mm.

Giannakopoulou [98] prepared Ni-ferrites at different temperatures via sol–gel method. The electromagnetic properties of these materials, namely permittivity and permeability were measured in the range (0.1–13 GHz) frequency range. Following a mathematical procedure, microwave absorption diagrams were constructed including the dependence of the microwave absorption of ferrite layer on microwave frequency and layer thickness. The permeability spectra broaden and the microwave absorption improves at (9–10) GHz with increasing of annealing temperature.

1.7. Outlines of the Dissertation

The Dissertation consists of five chapters. Chapter one (the first) which was given by previous sections, it is an introduction to the dissertation. It reviews the spinel structure and how cations occupy their sites in the structure. Magnetic properties represented by hysteresis loop especially of ferrites and its parameters meaning are given followed by briefly explanation of nanomagnetism. After that an introduction to microwave shielding is abstracted. The main aims of project is reviewed with the ways of their implementations and end with literature reviews of the most important previous works.

Chapter two presents a theoretical background of microwaves losses mechanisms in different materials which mainly related to dielectric and magnetic losses. The process of losses such as reflection and absorption and how they measured are displayed in this chapter. The chapter is end of some consideration and thoughts about designing for shielding materials.

The experimental part of the project is explained in chapter three. The preparation of samples of group one (without Fe^{2+}) and group two (with Fe^{2+}) are given. The preparation of ferrite-epoxy also is given. Then the characterizations and measuring of the produced ferrite and composite properties are exhibited.

The results of the performed structural, magnetic and microwave measurements is presented in chapter four. This chapter also contains the discussion of the causes of parameters behaviors. The results comparing with literatures is also found.

The last chapter is included the conclusions extracted from results, observations and literatures. The suggested future work and references is given in this chapter.

Chapter 2: Theoretical Part

2.1. Introduction

Microwaves can be transmitted, absorbed, reflected or more than one of them depending on the kind of material and frequency of wave. Some situations of interest demand absorbing microwave energy. There are several mechanisms by which materials absorb microwave radiation and transform electric or magnetic field (or both) to heat.

The electric and magnetic loss mechanisms are conduction, dielectric, hysteresis, eddy currents, domain wall and others. These different mechanisms depend on certain properties such as sample type and microstructure, frequency and temperature. The two main losses mechanisms for non- magnetic materials are dielectric (dipolar) losses and conduction losses. Conduction losses dominate in metallic, high conductivity materials and dipolar losses dominate in dielectric insulators. Magnetic materials also exhibit conduction losses with additional magnetic losses such as hysteresis, domain wall resonance and ferromagnetic resonance (FMR) [99,100].

The electric and magnetic behavior of a low-conductivity material is determined by three parameters, complex permittivity (ε*) which is describes the interaction of wave electric field with the material and Complex permeability (μ*) which is describes the interaction of the magnetic field with the material. The electrical conductivity (σ) expresses a material's ability to conduct an electric current as in eq.2.1 [101].

$$\boldsymbol{\varepsilon^* = \varepsilon' - j\varepsilon''}$$
$$\boldsymbol{\mu^* = \mu' - j\mu''}$$
$$\boldsymbol{\varepsilon'' = \frac{\sigma}{\omega}}$$
$$\boldsymbol{\varepsilon_r = \varepsilon_r' - j\frac{\sigma}{\varepsilon_0 \omega}} \qquad \text{..... (2.1)}$$

The electric and magnetic fields interact with materials in two ways, energy storage or lossless portion of the exchange of energy between the field and the material (real parts as ε′ and μ′) and energy dissipation (imaginary parts as ε″ and μ″) occurs when electromagnetic energy is absorbed by the material.

2.2. Dielectric Losses

The main mechanisms that contribute to the permittivity of a dielectric material are conduction, dipolar relaxation, atomic polarization and electronic polarization. In low frequencies, the parameter ε″ is dominated

by the influence of ion conductivity. At microwave frequencies, the variation of permittivity is mainly caused by dipolar relaxation as shown in Fig.2.1. When a material is subjected to an electric field, it will create an electric polarization $P_z(C/m^2)$ equal to the dipole moment (C-m) per unit volume (m^{-3}). There are three important polarization mechanisms in solids which lead to losses in the microwave region: (I) space charges arising from localized electrical conduction, (2) rotating electric dipoles, (3) ionic polarization associated with far-infrared vibrations [102], and(4) Electronic polarization process occurs in a neutral atom when the electric field displaces the electron density relative to the nucleus. Dipole relaxation and ionic relaxation contribute to dielectric relaxation because of applying electromagnetic field. They can be observed in the range from hundred Hz to hundreds of GHz [103].

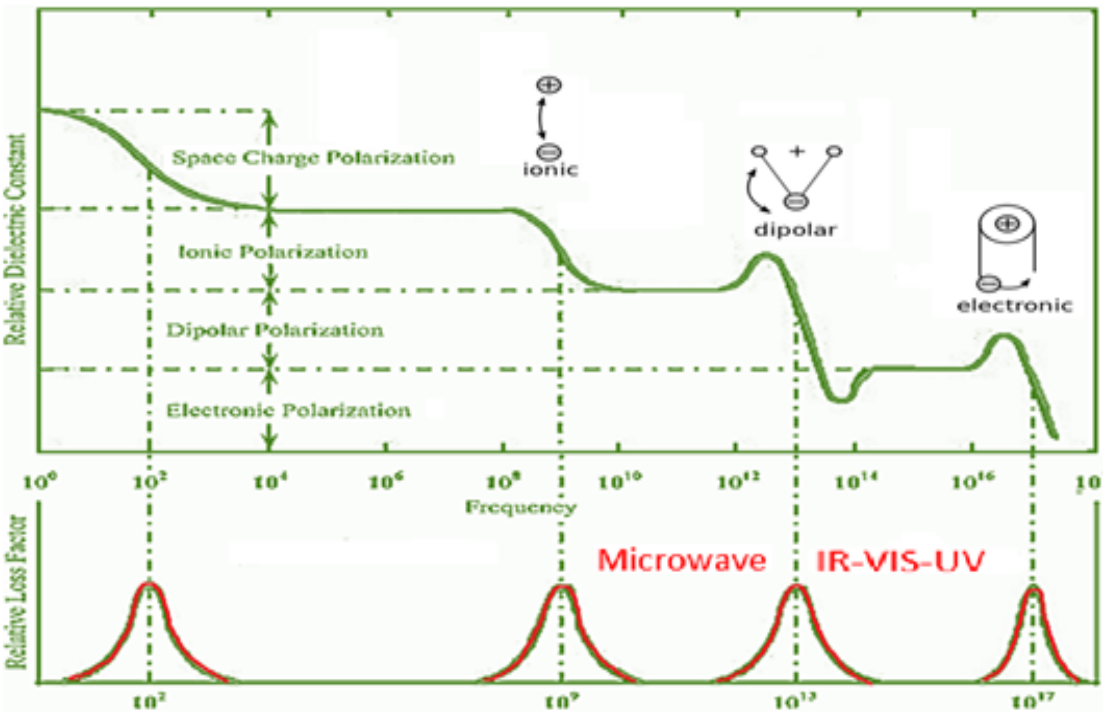

Fig.2.1. Relative dielectric loss factor with different dielectric absorption processes [101].

1-Dipole relaxation

It is measured by the time required for permanent or induced dipole to reach equilibrium orientation after apply electric field is reoriented. The dipole direction is interfered by thermal energy which changes the dipole

2-Ionic relaxation

Ionic relaxation comprises ionic conductivity and interfacial and space charge relaxation. Ionic conductivity predominates at low frequencies and introduces only losses to the system. Interfacial relaxation occurs when charge carriers are trapped at interfaces of heterogeneous systems. The charges may be separated by a considerable distance and therefore make contributions to the dielectric losses.

The dipole moment magnitude depends on the size and symmetry of the molecule. A molecule with a zero total charge may still have a dipole moment because molecules without a center of symmetry are polar. The potential arising from the total charge falls off as 1/r, that is because of the dipole moment as $1/r^2$, and that is because of the quadrupole moment as $1/r^3$, where r is the charges displacement [105].

2.2.1. Macroscopic Theory and Dielectric Losses Mechanism

When a steady electric field is applied to a dielectric, the distortion polarization (electronic) will be established very quickly compared with characteristic field time. The remaining dipolar part or orientation polarization takes time to reach equilibrium state. Relaxation processes are probably the most important of the interactions between electric fields and matter.

When microwaves propagate in a dielectric material, internal field is produced in the effected volume, thus inducing motions of free or bound charges like electrons or ions, and/or rotating charge complexes such as dipoles. They unite to give complex permittivity parameter. Dielectric losses occur in materials due to the damping of the vibrations of electrical dipoles, causing a great decrease in permittivity in most materials at MW frequencies. This damping results from inertial, elastic and frictional forces. Subsequently such resistance produces volumetric heating [25,106]. The variation of ε' and ε" for a dielectric is explained by 'Debye' relaxation as shown in Fig.2.2.

A macroscopic description uses an exponential law with a macroscopic relaxation time (t). The relation of orientation polarization P_z with electric field E_0 becomes a complex quantity or out of phase, as depicted by [108]:

where ε_∞, ε_0 and ε_s are the permittivity at infinite frequency, vacuum and static frequency, and ω is microwave frequency.

2.2.2. Debye's Model

The refractive index n corresponding to optical frequencies or very high frequencies is given by:

$$\boldsymbol{\varepsilon_\infty = n^2} \qquad \text{..... (2.3)}$$

where n is the refractive index for dielectric material. All polar substances have a relaxation time related to the real and imaginary parts of the dielectric permittivity according to Debye's model by the equation [147]:

$$\boldsymbol{\varepsilon = \varepsilon' - j\varepsilon'' = (n^2 + \frac{\varepsilon_s - n^2}{1+\omega^2\tau^2}) + j(\frac{\varepsilon_s - n^2}{1+\omega^2\tau^2}\omega\tau)} \qquad \text{..... (2.4)}$$

where ω is angular frequency, τ the relaxation time, ε_S is the static fields' permittivity. The real and imaginary parts of permittivity as function of frequency shown in Fig.2.2. The maximum dielectric losses and its associated frequency are given by [21]:

$$\boldsymbol{\varepsilon''_{max} = \frac{\varepsilon_s - n^2}{2}} \qquad \text{..... (2.5)}$$

$$\boldsymbol{\omega_{max} = \frac{1}{\tau}} \qquad \text{..... (2.6)}$$

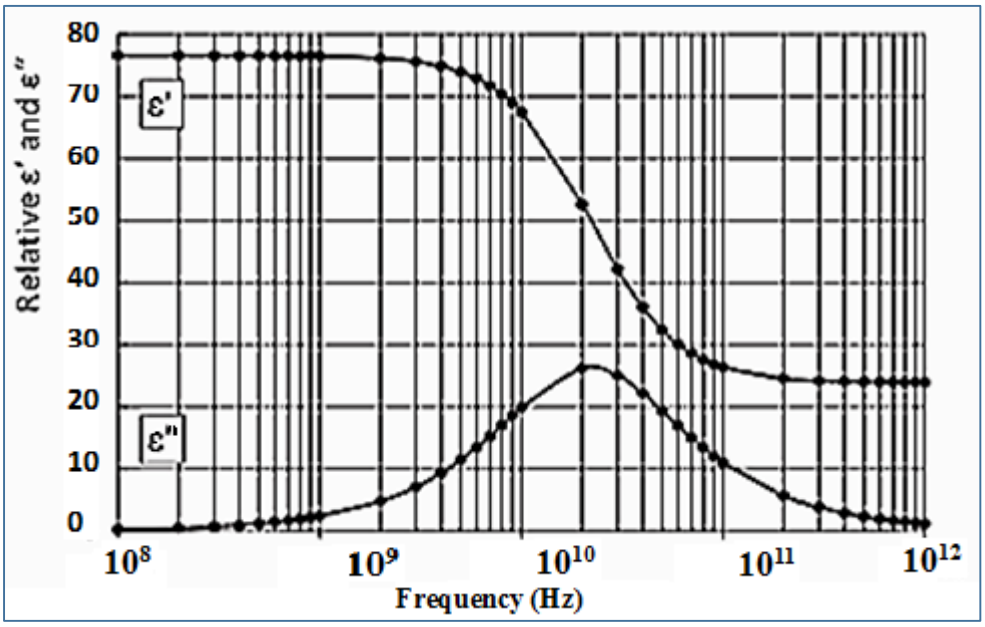

Fig.2.2. Real and imaginary permittivity of dielectric media as a function of frequency [21].

Dipole relaxation time at room temperature is ranges from $\mathbf{10}^{-10}$ to 10^{-4} s depending on solvent viscosity such as polymers or crystals. It is inversely proportional to temperature because movements become faster at higher temperature. The real part of the permittivity expresses the polarization component which follows the electric field. The imaginary part undergoes chaotic motion leading to thermal dissipation of the EM energy [21,105].

At sufficiently low frequencies there is no phase difference between the polarization and electric field and thus ε is a real number. But the static permittivity ε_s decreases as temperature increases because of the disorder increasing. At sufficiently high frequencies, the period (1/f) is much smaller than the τ, so the dipoles orientations remain random and thus at infinite frequency, $\varepsilon_{r\infty}$ is a real number. In some cases the relaxation phenomenon may be caused by different sources and the dielectric material has a relaxation-time spectrum [6,107].

The solid dielectric properties at MW frequencies are influenced by the ionic positions and changes caused by the lattice vibrations. The dielectric dispersion in solids depends on factors such as ionic masses, electric charge (valence state of the ions), force constant of the bond and lattice imperfections [105]. The dielectric losses can be classified into [6,107]:

1- *Intrinsic*. Occurs when the microwave interacts with: 1-magnetic dipoles, 2-electric dipoles, 3-charge carriers, 4-lattice vibrations, and 5-strongly relaxing ions. The low frequency phonons are responsible for the intrinsic dielectric losses in solid dielectrics.

2- *Extrinsic*. The extrinsic losses occur due to the interaction between the charged defects and the microwave fields.

2.2.3. Permittivity Against Frequency and Loss Factor

Regarding to Fig.2.1, when the frequency goes up to 1GHz, the real permittivity of a dielectric material can be considered as constant, then it decreases and there are some peaks and variance. Electronic polarization occurs in atoms when an electric field displaces the electrons with respect to the nucleus. If electronic (or atomic) polarization is the only present polarizations, the material is almost lossless at microwave range [110,111].

To find out the mathematical origin of the complex ε, it can be started with the electric field E of the microwave which is given by [105]:

$$\mathbf{E = E_o\, e^{i\omega t}} \qquad \textbf{…… (2.7)}$$

where E_o is maximum field value, i is $\sqrt{-1}$ and t is the time. The resulting electric flux density is:

where δ is the phase angle associated with the time lag in polarized material. The electric flux density (electric displacement) comes from the applied electric field and the electric polarization:

$$\mathbf{D = \varepsilon_o E + P_z = \varepsilon E} \quad \text{..... (2.9)}$$

The dielectric constant is the relative permittivity of the material

$$\mathbf{\varepsilon_r = \varepsilon/\varepsilon_o = D/\varepsilon_o E = D_o e^{-i\delta} / \varepsilon_o E = \varepsilon' - i\varepsilon''} \quad \text{... (2.10)}$$

The real part is in phase with the field $\varepsilon' = Do \cos\delta/\varepsilon_o E$, and the imaginary part is out of phase $\varepsilon'' = Do \sin\delta /\varepsilon_o E$ and the loss factor is measured by tanδ. The absorbed power per unit volume (W/m^3) is [112]:

$$\mathbf{W = (1/2)\, Eo^2\, \omega\, \varepsilon'\, \tan\delta} \quad \text{..... (2.11)}$$

So microwave absorption increases with field intensity, frequency and imaginary dielectric constant.

In microwave interaction we are dealing with inhomogeneous materials. Generally there are ceramic materials, organic compounds, and porosity present in the green ceramic body [102]. Transition metal oxides and sulfides such as magnetite and pyrite are easily heated, but insulators like alumina and silica are not. The absorption is due to heavy ion vibration with respect to oxygen anion for high dielectric permittivity material at high microwave frequencies [112].

2.3. Conduction Losses and Penetration Depth

The conduction losses mechanism is linked with dielectric losses mechanism. The conduction mechanism are located in two ranges [105]:

$$\boldsymbol{range\ I} \quad \boldsymbol{\omega\tau \ll 1} \quad \boldsymbol{\varepsilon'' = \frac{\sigma}{\omega}}$$

$$\boldsymbol{range\ II} \quad \boldsymbol{\omega\tau \gg 1} \quad \boldsymbol{\varepsilon'' = \frac{\varepsilon_s - \varepsilon_\infty}{\omega t}} \quad \text{..... (2.12)}$$

In solids, conduction losses are usually enhanced by material defects that reduce the energy gap between the valence and conduction bands. Since the conduction losses are high for carbon black powder, the material can be used as lossy impurities or additives to induce losses within solids. Metal particles are not heated despite their high electrical conductivity. Metals, semimetals and narrow-band semiconductors cannot be heated because electric fields are unable to penetrate much below the surface. Skin depth δ is defined as the depth at which the electric or magnetic field drops to 1/e of the surface value. It is related to frequency f, permeability μ and conductivity σ by the relation [113,102]:

$$\mathbf{\delta = 1/\sqrt{\pi \mu \sigma f}} \quad \text{..... (2.13)}$$

The skin depth is about 1cm at 60Hz and less than 1μm at microwave frequencies, since field penetration is proportional to $\sigma^{-1/2}$. The metals conductivity decreases with temperature, in contrast to semiconductors.

The energy dissipation W can be evaluated using the equation [102]:

$$W = \sigma \int E^2 \, dv \quad \ldots\ldots\ldots\ldots\ldots\ldots (2.14)$$

where dv is volume element, E is electric field intensity. For a two-layer system consisting of equal amounts of conducting high-permittivity material (e.g. ferrite) and an insulating low-permittivity material such as polymer, the relaxation frequency at which absorption occurs is [102]:

$$\omega = \sigma/\varepsilon \quad \ldots\ldots\ldots\ldots\ldots\ldots (2.15)$$

The frequency lies in the microwave region for semiconductors which has the optimum conductivity for microwave absorption. Magnetite with mixed cation valences are among the best microwave absorbers. It is an n-type semiconductor in which electrons are transferred by hopping or valence exchange conduction which proposed by Verwey [17]. He suggest that the unit cell remains cubic in spinel structure at low temperature, with Fe^{2+} and Fe^{3+} ordered in alternate <110> directions. When the temperature increases over critical one, thermal energy allows the electrons to transfer from Fe^{2+} to neighboring Fe^{3+} of the same type on equivalent lattice sites, for example in magnetite $Fe^{2+} \leftrightarrow Fe^{3+} + e^{-1}$. Fe^{2+} and Fe^{3+} become therefore indistinguishable. The conduction process in p-type involves holes transfer between trivalent and divalent nickel ions as in lithium doped nickel oxide.

If the irradiated sample is an electrical conductor, the charge carriers (electrons, ions, etc.) move via the material under the effect of the electric field resulting in a polarization. The induced currents will cause heating the sample due to electrical resistance. For a very good conductor, complete polarization may be achieved during about 10^{-18} seconds. The conducting electrons move precisely in phase with the field. Metal reflect most of the microwave energy. The losses in a semiconductor is composed of the dielectric losses (polarization) and the conductive loss, as [102,114]:

$$\varepsilon_r'' = \varepsilon'' + \frac{\sigma}{\omega \varepsilon_0} \quad \ldots\ldots\ldots\ldots (2.16)$$

The Phase angle is defined as the angular difference in phase between the applied AC-potential difference and the component of AC-current. The tangent of phase angle is the loss factor [114].

2.4. Magnetic Losses

Although the most microwaves-matter interactions take place through the electric field, the magnetic field can induce losses in magnetic materials by interaction with spins. In case of decreasing the reflection from a high conductor surface by a thin isotropic single layer absorber, magnetic absorber is placed directly onto the surface, while the dielectric absorber should be located at λ/4 from the conductor surface, that needs an additional dielectric layer because the peaks of magnetic and electric fields are at these position respectively from the surface of conductor. Construction like these are called Salisbury screens [115,116].

The disadvantages of magnetic media, with respect to dielectric one, are usually heavy, good conductor and anisotropic. A high conductivity means a very small penetration depth, resulting in a nearly total reflection of the wave. The way to overcome this limitation is by utilizing composite materials with ferromagnetic particles. Then one can obtain a lower weight and conductivity. Anisotropy leads to a rather analyzing difficulty due to the complex nature of ferromagnetic materials.

Loss mechanisms in magnetic materials are listed below [102, 110]:

1) Spin moments lagging magnetic field.
2) Hysteresis losses arising from irreversible domain wall displacements.
3) Eddy current losses from field-induced electric currents.
4) Domain wall oscillations.
5) Magnetic resonance from processional motion of magnetic dipole moments, i.e. ferromagnetic resonance (FMR).

The loss mechanisms above contribute to relative complex permeability through imaginary party which can be expressed by [118]:

$$\mu_r = \mu' - i\mu'' \qquad \ldots\ldots\ldots\ldots (2.17)$$

where μ' and μ" are the real and imaginary permeability (magnetic losses) respectively. A loss tangent $\tan\delta_m$ can also be defined as:

$$\tan\delta_m = \mu''/\mu' \qquad \ldots\ldots\ldots\ldots (2.18)$$

The power P that is absorbed per unit volume (W/m3) is:

$$P = (1/2)\,\omega\mu''\,|H|^2 = (1/2)\,\omega\mu'\,\tan\delta_m\,|H|^2 \quad \ldots (2.19)$$

It can be seen that the power absorbed varies linearly with frequency, permeability, the loss tangent and the square of the magnetic field (or complex permeability). For a ferrite the magnetic loss tangent or loss factor can be expressed in terms of three main contributors:

$$\tan\delta_m = \tan\delta_h + \tan\delta_e + \tan\delta_r \qquad \ldots\ldots (2.20)$$

in which $\tan\delta_h$, is included the hysteresis besides domain wall oscillation, $\tan\delta_e$, is eddy current and $\tan\delta_r$ is the 'residual' loss tangents included the resonance losses and these will often dominate at high frequencies [107].

The resonance behavior due to magnetic losses and complex permeability behavior with frequency is shown in Fig.2.3. One can observe at static field μ″ is lower than μ′, and the two values remain more or less constant at low and medium frequencies, rising slowly to a peak. As the magnetic losses increase at higher frequencies μ′ suffers a sudden decrease, but μ″ remains constant at this point until it drops slightly toward higher frequency. Just before μ″ drops it experiences a slight increase from resonance frequency, giving its maximum value which occurs at the same frequency at which μ′ has dropped to half its original value, and this is the natural FMR frequency depending on crystalline anisotropy [25,117].

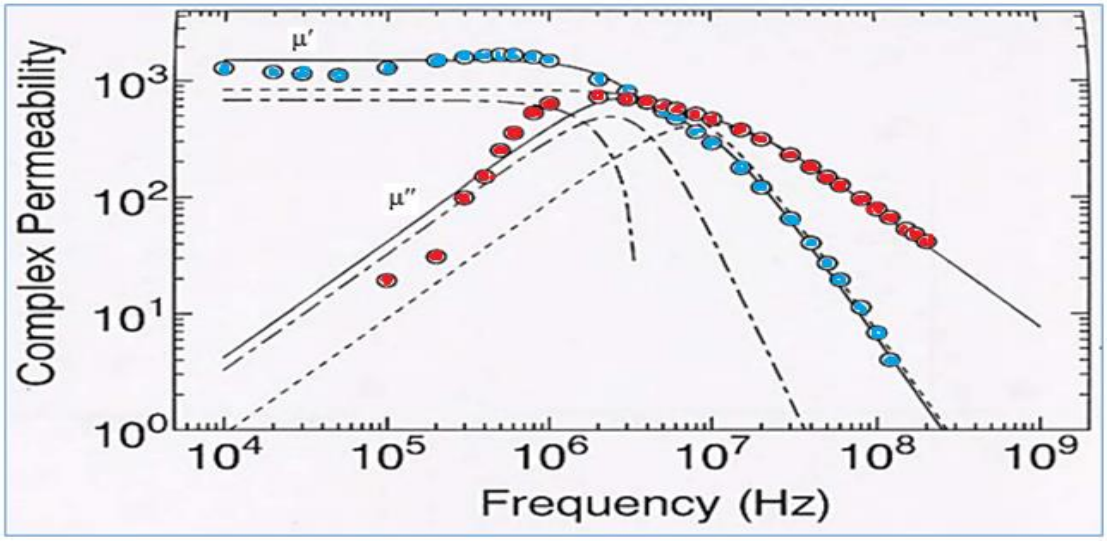

Fig.2.3. Complex permeability of Ni-Zn ferrite, circles for experimental values, sold line for total calculated values, broken line for spin rotation contribution and dash-dotted line for domain wall contribution [117].

Magnetic absorber usually is based on carbonyl iron and ferrites giving absorption band is in the MHz and GHz ranges. The absorber function is dissipating energy, i.e. efficient absorber is high losses material. Besides that absorbers should satisfy some condition: good absorption, as thin as possible, light, durable, work over a broad frequency range. The resonance frequency is related to particle size and can be tuned to absorb at higher frequencies (5-20GHz) [23]. Absorbers can be divide into two types according reflected surface waves:

1. *Specular absorbers*: absorb incoming electromagnetic waves and preventing them from being reflected. If magnetic absorber has known frequency behavior and high losses then it can be thinner with broad

bandwidth. On the other hand the thickness and bandwidth of the electric absorber is limited by the quarter of a wave length requirement.

Rozanov [99] presented a relation for the finite bandwidth with certain thickness and reflection coefficient r, for a magnetic absorber, That is:

$$\frac{f_1 - f_2}{f_1 f_2} < \frac{2\pi^2 \mu_s d_L}{c \ln \frac{1}{r}} \qquad \text{..... (2.21)}$$

where μ_s is the static permeability of the layer, f_1 and f_2 are band edges frequencies, c is speed of light and d_L the thickness of the layer. This relation shows that the low reflection is obtained only in a limited band and tells that magnetic absorbers have broader band than electric absorbers.

2. *Nonspecular absorbers:* typically absorb electromagnetic waves propagating along structures. The propagation of waves along conductor surface sometimes leads to undesirable results. It may produce scattering in undesirable directions in radar cross section reduction applications. The best way to lowering surface waves is by using a magnetic thin nonspecular lossy absorber sheet attached to the surface, where the magnetic field has its max value [99, 118].

The transition metal oxides like iron, nickel, or cobalt oxide, have high magnetic losses. These powders can thus be used as lossy impurities or additives to induce losses within solids for which dielectric losses are too small [21].

2.4.1. Spin Moments Lagging

Spin moment lagging is understood by movement of atom magnetic moment in frictional media producing lagging of moment behind magnetic field and generating heat in the media. The heat comes from the magnetic field energy. The magnetic field interacts with a magnetic material in such a fashion that the moments try to align in field direction to produce a magnetization. During that interaction, energy is dissipated in the material. The magnetic field H of the microwave radiation can be represented by:

$$\mathbf{H = H_o\, e^{i\omega t}} \qquad \text{..... (2.22)}$$

where H_o is maximum field value, ω angular frequency and t is the time. The resulting flux density is:

$$\mathbf{B = B_o\, e^{i(\omega t - \delta)}} \qquad \text{..... (2.23)}$$

$$\mu = \frac{B}{H} = \frac{B_o\, e^{j(\omega t - \delta)}}{H_o\, e^{j\omega t}} = \mu_o\, e^{-j\delta} \qquad \text{..... (2.24)}$$

Equations 2.17 and 2.18 can be derived from eq.2.24. This mechanism is dominant at microwave and implemented in the $\tan\delta_r$ term in eq.2.20.

2.4.2. Hysteresis Losses

As a result of hysteresis, energy is dissipated as heat in a magnetic material as it travels around a B - H hysteresis loop. The hysteresis energy loss per unit volume W_h of material is:

$$W_h = \oint B.dH \quad \ldots\ldots\ldots\ldots\ldots\ldots (2.25)$$

This loss is dominant at low frequency and controlled by factors that control low frequency permeability and coercivity such as porosity, grain size and impurities as well as the crystal structure (intrinsic) properties [119]. Since extrinsic losses arise from the inhomogeneity due to porosity, impurities, crystal imperfections, roughness and grain boundaries, besides fast and slow relaxing impurities dominate at higher frequencies. Such imperfections will induce magnetic poles (DC field) at the surfaces of them, contributing to FMR line width [6,25].

2.4.3. Eddy Current Losses

It is the main mechanism of losses in conductor material which is determined by electric conductivity. Conduction mechanism in ferrites is due to electron hopping conduction. Magnetite is one of the most conductive oxides with conductivity approximately 10^4 S/m at room temperature.

Effect of eddy currents on the magnetic field is totally ignored if the skin depth is larger than the sample size. This happen when materials have very low conductivity. Table2.1 shows some minerals and their penetration depth.

Table 2.1 Penetration depth of selected mineral at 2.45 GHz [23].

Mineral		Penetration Depth (m)
Quartz	(SiO_2)	5.86
Hematite	(Fe_2O_3)	0.21
Magnetite	(Fe_3O_4)	0.06
Pyrite	(FeS_2)	0.11

For high conductivity materials such as metals and for very large samples, where the skin depth is less than the dimensions of the sample, the influence of eddy currents on the magnetic field can be negligible. In this situation a broad range of spin waves are excited. The conductivity of a ferrite due to hopping increases with temperature T, exponentially as shown by the following equation [120]:

$$\sigma = \sigma_o \, e^{-(E_p / K_B T)} \quad \ldots\ldots\ldots\ldots\ldots\ldots (2.26)$$

where E_p is the activation energy and k is Boltzmann's constant (1.38 x 10^{-23} J/K). There is a log relation between eddy current losses and temperature and that eddy current losses are more likely to become important at high temperatures. The disadvantages of higher conductivity is preventing usage in contact with electronic components [23]. The conduction losses are usually enhanced by material defects which sharply reduce the energy gap between the valence and conduction bands.

There is a critical frequency, f_c, above which effective permeability μ falls rapidly as a function of 1/frequency due to eddy current losses. It is also related to the resistivity and thickness of the material d_s and is given by the equation:

$$f_c = \frac{4\rho}{\pi \mu d_s^2} \qquad \text{..... (2.27)}$$

where ρ is the specific electrical resistance of the piece of material [25].

2.4.4. Domain Wall Resonance Losses

The resonance phenomena can be divided into two distinct mechanisms; domain wall resonance and those due to FMR. The small displacements of a domain wall with an applied field introduces restoring forces. The wall has inertia and its movement is accompanied by microwave energy dissipation like what happen in damping harmonic motion [187]. The resonance frequency will occur if damping is small, at angular $\omega_0 = (4M^2/m \chi \xi)^{1/2}$ where χ is the initial susceptibility and ξ is the wall thickness, m is the inertia (typical value 10^{-9} kg.m^{-2}) and M is the magnetization. Domain wall resonance occurs at approximately one tenth of the frequency of FMR, typically at 50 MHz for Mn ferrite. This resonance is negligible for smaller grain and there is no domain wall resonance when grains are single domain. Single domain will remove the domain wall resonance effects, otherwise a diffuse FMR peak or multiple peaks can occur [3,10,25].

2.4.5. Ferromagnetic Resonance (FMR)

FMR is one of the most employed techniques to characterize magnetic materials, since it is very sensible to local fields and inhomogeneities [3].

The unpaired electrons posses spin and negligible orbital moments. If they are exerted to apply magnetic field their levels are splitted according to Zeeman Effect as shown in Fig.2.4. When a static magnetic field is applied the magnetic moment rotates (precess) around (aligns with) the field to minimize its potential energy. The magnetic field exerts a torque

on the sample magnetization which causes the magnetic moments in the sample to precess.

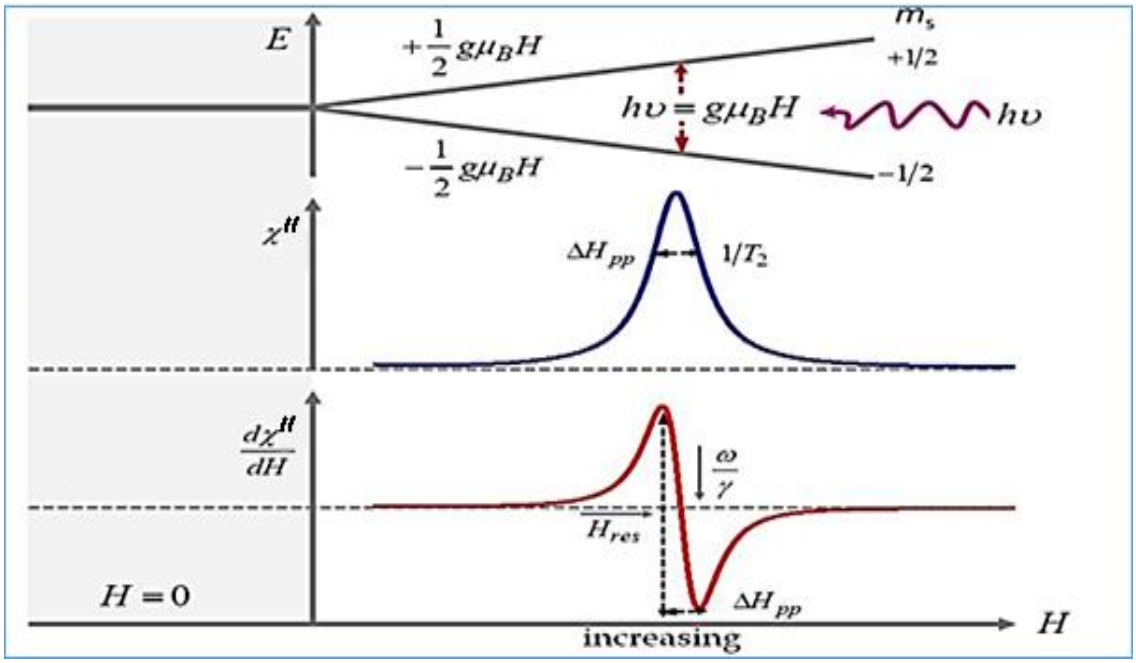

Fig.2.4.The energy levels and free electron resonance at zero field and with applied field H. As the value of H increases, the separating between levels increases. Arbitrary units are used for χ″ and dχ″/dH [3].

The precession frequency of the magnetization depends on the orientation of the material, the strength of the magnetic field, as well as the macroscopic magnetization. The moment M will rotate around static field due to the torque H x M with angular frequency ω given by [19]:

$$\omega = \gamma H \qquad \text{..... (2.28)}$$

where γ is the gyroscopic ratio ($\gamma = g\mu_\beta/\hbar = 1.76\times10^{11}$ rad/$T^{-1}.s^{-1}$ =28 GHz/T), H is the magnetic field in Tesla and the frequency f is given in GHz $f=35.2 .10^6$. H [19,28].

If a microwave field is applied normal to the static field as in Fig.2.5 at the same frequency of the resonance precession, then the torque T will be in the direction such that it opens up the precession angle. Thus microwave field energy will be absorbed and the moment will rotate with a larger angle [121,19]. There is a damping torque, proportional to $M \times (H \times M)$, that pushes the magnetic moment to eventually relax along field direction.

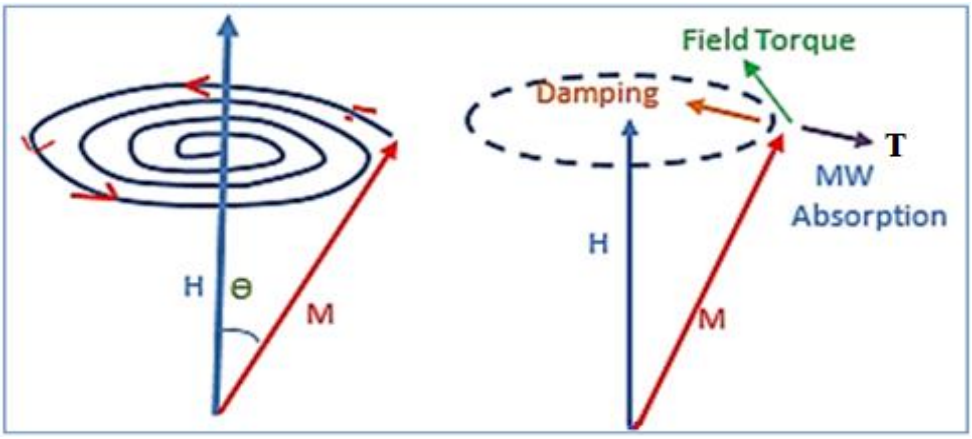

Fig.2.5. A dipole moment (or magnetization) M precessing about a static magnetic field H_0.

If there is no external field, the crystalline anisotropy field H_k (section 1.4.2) will be the alternative for H. A larger Ms or smaller k_1 will redshift the resonance frequency. The absorbed power increases when its frequency comes near to separation and gets maximum at point when they are equal as shown in Fig.2.4. When the microwave field is cut off, the magnetization will be decayed spirally to the minimum energy state. During that it lost the absorbed microwave energy with other degrees of freedoms of the system, such as lattice vibrations by spin-lattice interaction and other modes of the spin system by spin-spin interaction [102,121].

The important modes that are excited by microwave are the spin wave modes. A spin wave is a propagating disturbance in the moments ordering, often called magnons [107]. They are quantized and have their phase and group velocity as shown in Fig.2.6.

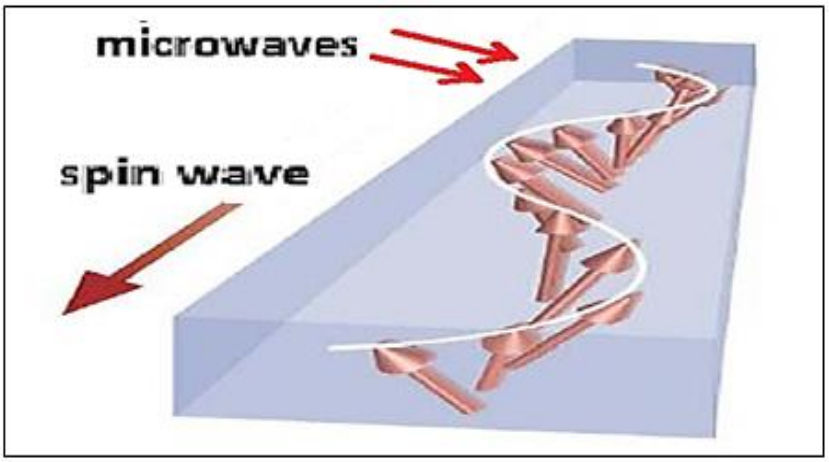

Fig.2.6. Spin wave excitation by microwave [3].

The field sweep of FMR system measures the derivative of absorbed power versus the applied field at fixed frequency, but frequency sweep

FMR system will measure this derivative versus frequency at a fixed H. The curve can be integrated to get average power which is linearly proportional to the imaginary susceptibility χ'' as follows [122,123]:

$$\langle P \rangle = (1/2)\, h^2\, \chi''\, \omega_0 = (1/2)\, \gamma\, h^2\, \chi'\, \tan\delta_m\, H_0 \qquad \ldots\ldots\ldots\ldots (2.29)$$

where h is the magnetic field of microwave. Supposing that the two spinel sublattices are still coupled (two sets of spins rotation in phase in the same rotational direction) during experiment. The precession belongs to the resultant magnetization and ω_0 is in the microwave range. There is another FMR resonance mode in which the sublattices moments rotate in the same rotational direction but out of phase. This results in resonances in the infrared regions, where the applied magnetic field is very large [107, 25].

2.4.6. FMR Linewidth and Relaxation Processes

The losses in ferrites materials quench the resonance and precessional motion by relaxing forces to relax the magnetization back to the equilibrium state. The range of static magnetic field at certain frequency over which the absorption is significant, is denoted by the linewidth ΔH (FWHM) of the χ'' curve versus static field, or by peak to peak $\Delta H_{p.p}$ of the $d\chi''/dH$ curve versus field as shown in Fig.2.4. As FMR line width is related to magnetic losses, the smaller the line width, the less loss the specimen. A more loss material has a broader FMR [124,149,164].

The relation between the frequency linewidth $\Delta\omega$ and field linewidth ΔH depends on the following relation:

$$\Delta\omega = (d\omega/dH_{int})\, \Delta H \qquad \ldots\ldots\ldots\ldots\ldots\ldots (2.30)$$

The Quality factor is connected to the resonance frequency ω_0 and the FWHM line width $\Delta\omega$ of the transmission peak by [126]:

$$Q = \omega_o/\Delta\omega = f_r / \Delta f \qquad \ldots\ldots\ldots\ldots\ldots\ldots (2.31)$$

The complex susceptibility χ_e in terms of the real part χ'_e and the negative imaginary part χ_e'' is $\chi_e^* = \chi'_e - i\chi''_e$. For uniformly magnetized nonconducting spherical samples with a uniform linearly polarized microwave, the theoretical susceptibility is described by [47,128]:

$$\chi_e^* = \frac{\omega_o\, \omega_m(\omega_o^2+\alpha^2\omega^2-\omega^2)}{(\omega_o^2-\omega^2(\alpha^2+1))^2+4\omega_o^2\alpha^2\omega^2} - j\frac{\alpha\omega\omega_m(\omega_o^2+\alpha^2\omega^2-\omega^2)}{((\omega_o^2-\omega^2(\alpha^2+1))^2+4\omega_o^2\alpha^2\omega^2} \ldots\ldots (2.32)$$

where $\omega_o=\gamma H_o$, $\omega_m=\mu_o\gamma M_s$, α damping factor, M_s the saturation magnetization, and ω is the microwave frequency. Here the FMR

frequency (f_r) is defined as the frequency at which χ_e'' is at a maximum and coincides with the half peak value of χ_e' [153]. The real part describes the dispersion and imaginary part describes the absorption by FMR. The imaginary susceptibility χ'' is directly proportional to damping factor α in eq.2.32 which is in turn proportional to ΔH as given by [129]:

$$\alpha = \frac{\gamma \Delta H}{4 \pi f} \qquad \ldots\ldots (2.33)$$

Two factors determine linewidth ΔH. The first one is the *intrinsic (homogeneities)* relaxation of system magnetization. The second parameter corresponds to the magnetic *inhomogeneities* of the ferromagnetic sample. The FMR linewidth inhomogeneous broadening happens mostly because of the sample's mosaicity and defects. Then the ΔH is given by [123]:

$$\Delta H = \Delta H_{inhom.} + \Delta H_{hom.} \qquad \ldots\ldots\ldots\ldots (2.34)$$

where the first term represents the inhomogeneous due to extrinsic ΔH_{ex} line broadening and the second term represents the homogeneous one due to the intrinsic contribution ΔH_i to the line broadening. In the entire intrinsic damping, the FMR linewidth should depend linearly on the microwave frequency as in eq.2.33, so α can be determined. To illustrate linewidth in terms of their contribution polycrystalline magnetic insulator is given by [131-133]:

$$\Delta H_{inhom} = \Delta H_i + \Delta H_a + \Delta H_p + \Delta H_e + \Delta H_{id} \quad \ldots (2.35)$$

where the subscripts stand for the following: (i) intrinsic; (a) anisotropy; (p) porosity; (e) eddy current within the cavity wall; (id) inhomogeneous demagnetization. The resonance frequency related to fields is now given by [13, 134]:

$$\omega_r = \gamma(H_{exp} + H_a + H_p + H_e + H_{id}) \qquad \ldots\ldots (2.36)$$

where H_a is the anisotropy field, exp: experimental. The limitations by losses make the low loss microwave ferrite devices operate in a certain frequency range. It is preferably above the natural or limiting resonance frequency ($\omega_{lim} = \gamma 4\pi Ms$). The biasing field in applications saturates the ferrite and so shift the FMR to higher frequencies, then interaction with the microwave field becomes negligible as $\omega > \omega_o$. At frequencies above X-band the bias magnet is so expensive, therefore spinels are applied at frequencies up to 30 GHz, while garnets at 10 GHz and hexaferrites can attain 100 GHz for [13,135].

The spinel structure is cubic and the resultant anisotropy fields (H_a) has low value and typically it is tens of Oe. So when no field is applied, FMR frequency of spinel ferrites is typically lower than 1 GHz [135].

In most polycrystalline ferrites extrinsic contribution to ΔH_{ex} are associated with structural imperfections. The most common of them are the dislocations, vacancies, porosity, impurities (that induce dispersions in the local fields), magnetic impurities, local strain, porosity, grain boundaries, fast and slow relaxing impurities(rare earth slow relaxers) etc. The thickness variation, surface roughness, randomly oriented crystallites, hopping conduction process, the sample shape, measurement geometry, presence of surfaces, and interfaces are other types of extrinsic contribution to ΔH_{ex}. These factors produce local anisotropy, random demagnetizing effects and subsequently broadening FMR. They increase the losses through modifying permeability and coercivity [6-10].

Intrinsic effects of polycrystalline are negligible compared to extrinsic one. The FMR line shape resulting from extrinsic processes is usually non-Lorentzian. The typical linewidth of single crystal ferrite is about 1Oe, while of polycrystalline ranges from tens to hundreds of Oe. The identification and quantization of each process demand extensive measurements and numerical analyses. So that ΔH is used typically as a measure of the overall loss of the material [47,136].

The size dependent contributions are eddy current and inhomogeneous demagnetization. The linewidth is mainly due to conduction mechanisms, porosity with low anisotropy and intrinsic relaxation in bulk materials and coarse-grain sintered polycrystalline. Part of inhomogeneities is a frequency-independent related to the thermal history of the sample and the growth process [133,137].

Relaxation channels after microwave absorption are: magnon phonon relaxation, two magnon relaxation which is the important one, charge transfer relaxation, three magnon relaxation (induced by dipolar interaction). The first three processes associated with slowly relaxing impurity and rapidly relaxing impurity are dominant in ferrites. The two magnons can be relaxed to a phonon or three magnons which in turn relax to phonon. Each relaxation process has its relaxation time [126,127]. The different mechanisms have different dependencies on certain properties such as sample type and microstructure, frequency and temperature. However, in polycrystalline powders the grain boundaries provide

sufficient discontinuity to break up spin waves. Two-magnon relaxation is important in polycrystalline, porous and random anisotropy ferrite. In single-crystals surface roughness is a source of losses [122,130].

Ferrites usually contains ions with an orbitally degenerate cubic ground state such as the rare-earth ions or L-state transition metal ions. Rare earths and Fe^{2+}, Co^{2+}, Mn^{3+}, Cu^{2+} ions have large orbital momentum comparing to S state ions like Fe^{3+}. Since to increase damping it should increase rare-earth ions and L-state transition metal ions whereas reducing the others to increase the spin-lattice relaxation. In this case linewidth might increase by several orders of magnitude due spin-orbit relaxation processes which pass part of energy to lattice as heat. In practice presence of very high relaxation ions that have not half-full outer shell 3d (<5 electron spins) besides orbital moment with spin-orbit coupling such as Fe^{2+} is the main factor which contributes to linewidth [20].

2.5. Quality Factor and Loss Factor

Quality factor is defined as [105]:

$$\mathbf{Q = \frac{(\omega).Maximun\ energy\ stored\ per\ unit\ volume}{Time\ average\ power\ lost\ per\ unit\ volume}} \quad \textbf{..... (2.37)}$$

where ω is the angular frequency. For dielectric lossy material:

$$\mathbf{Q = \omega\ \varepsilon'/\sigma_e = 1/\ tan\delta_d} \quad \textbf{..... (2.38)}$$

Parameters ε' and σ_e are permittivity and conductivity respectively. The real part represents charge storage whereas imaginary permittivity is a measure of losses. Similarly, real and complex permeabilities represents magnetic storage and losses respectively. The losses extent which can be assessed by calculating dielectric or magnetic loss factor (tanδ).

If $\sigma_e = 0$ (i.e. $\tan\delta_d = 0$) the medium is termed an ideal dielectric and the dielectric permittivity is just a real part. If the medium is strongly lossy we have $\omega\ \varepsilon' << \sigma_e$, so that $\tan\delta_d = \sigma_e/\omega\ \varepsilon' >> 1$ which for good conductors where $\varepsilon'' \approx 0$. If $\sigma = \infty$ ($\tan\delta_d = \infty$) the medium is a perfect conductor [105,138]. Materials can be classified according to response to microwave into:

i. Reflector.
ii. Low loss or transperant (tanδ<0.1).

Low dielectric constant, ($\varepsilon_r \geq 4$, tanδ<0.001), high dielectric constant, ($\varepsilon_r \geq 10$, tanδ<0.001), Very high dielectric constant, ($\varepsilon_r \geq 100$, tanδ<0.0002).

iii. Lossy dielectric (tanδ>0. 1).

Materials with high loss factor at the incident radiation frequency will be heated at faster rate from core to surface. At 2.45 GHz, fused quartz,

zircon, several glasses, ceramics, SiO_2 and Teflon are good transmitter, hence no heating occurs. Loss tangent is frequency dependent property and increases with the rise of frequency. It determines the ability of a ferrite to suppress the electromagnetic frequency. It should be noted from eq.2.31 and eq.2.38 the linear proportion of loss factor and line width [14,15,119].

2.6. Interfacial Relaxation and the Maxwell – Wagner Effect

Microwave radiation can be dissipated by scattering at interfacial boundaries in inhomogeneous materials. In the visible region, distribution of small particles in a transparent medium can make it opaque. The same feature arises in dielectric media when particles are dispersed within a matrix. This is known as the Maxwell–Wagner process. If the dielectric material is not homogeneous and related to several phases with different dielectric characteristic, the relaxation processes will relate to Maxwell–Wagner processes occurrence within that heterogeneous materials [105].

2.7. Shield Effectiveness (SE)

SE is defined as the ratio of the residual or transmitted power (P_{out}) to incident power (P_{in}). The EMI attenuation related to three processes as shown in Fig.2.7. The first is the reflection of the wave from the shield (R); the second is the absorption of wave passing via the shield (A); and the third is the multiple reflections of the wave at various interfaces within the shield (Mu). The total SE can be given in the form [28]:

$$\mathbf{SE = -10log\frac{P_{out}}{P_{in}} = SE_R + SE_A + SE_{Mu}} \quad \text{..... (2.39)}$$

The reflection shielding effectiveness, SE_R, can be approximated as SE_R=-10log(1-R). Also the multiple reflection shielding effectiveness, SE_M can be expressed as SE_M=-/10log (1-Mu). Thus, the absorption shielding effectiveness, SE_A, is approximated as SE_A=-10log[T/(1-R-Mu)], where T represents transmission.

The intensity of the EM wave inside the shield after primary reflection is based on quantity (1-R), which can be subsequently used for normalization of absorbance (A) to yield effective absorbance A_{eff}=[(1-R-T)/(1-R)] so that experimental reflection and absorption losses can be expressed as [6, 139]:

$$\mathbf{SE_R = 10log(1 - R)} \quad \text{..... (2.40)}$$

$$SE_A = 10log(1 - A_{eff}) = 10log\left|\frac{T}{(1-R)}\right| \quad \ldots\ldots (2.41)$$

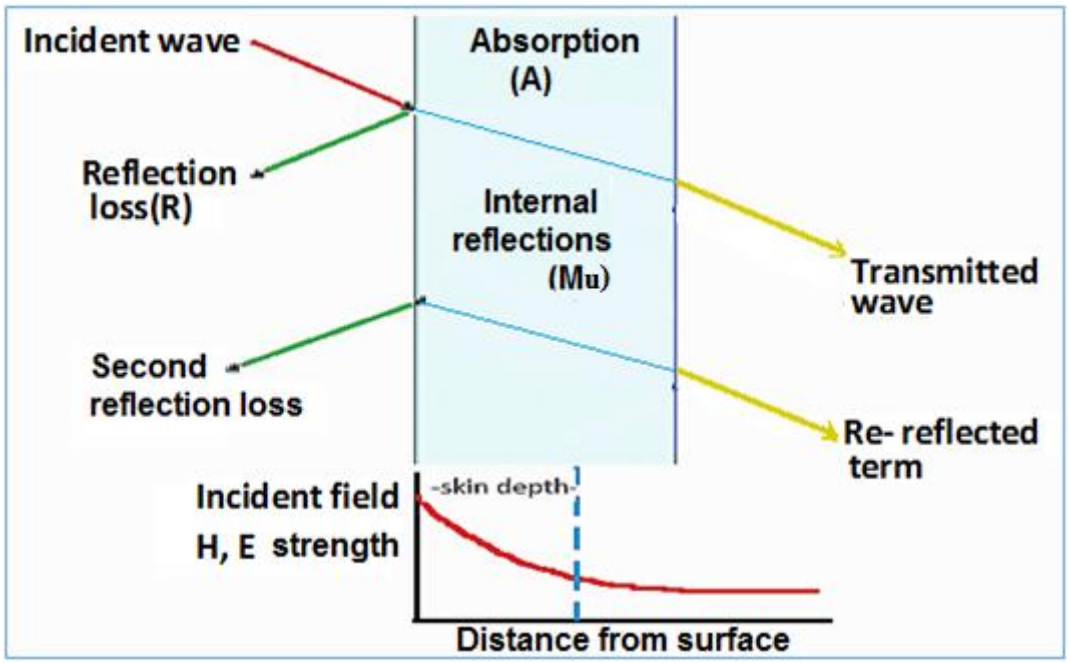

Fig.2.7. Microwave interactions with the shield [139].

The shielding effectiveness is generally measured in terms of reduction in magnitude of incident power or field upon transition across the shield. Mathematically shielding effectiveness (SE_T) can be expressed as [28]:

$$\mathbf{SE_T(dB) = SE_R + SE_A + SE_{Mu} = 10\log\left(\frac{P_T}{P_I}\right) = 20\log\left(\frac{E_T}{E_I}\right) = 20\log\left(\frac{H_T}{H_I}\right)} \quad \ldots\ldots\ldots\ldots\ldots (2.42)$$

where P_I, E_I and H_I are the incident of power, electric and magnetic fields respectively and P_T, E_T and H_T are the transmitted ones. As shown in Fig.2.7, three different mechanisms namely reflection (R), absorption (A) and multiple internal reflections (MIRs) contribute to overall attenuation with SE_R, SE_A and SE_M as corresponding shielding effectiveness components due to reflection, absorption and multiple reflections respectively.

Shielding effectiveness in terms of thickness and impedance can be defined as [6,113,140]:

$$\mathbf{SE_T(dB) = 20\log\left[\frac{4k}{(k+1)^2}\right] + 20\log\left(e^{-\gamma_p d}\right) + 20\log\left|1 - \frac{(k-1)^2}{(k+1)^2}e^{-\gamma_p d}\right|}$$

$$\mathbf{k = Z_\omega/\eta \quad , \quad \eta = [j\omega\mu / (\sigma + j\omega\varepsilon)]^{1/2}} \quad \ldots\ldots\ldots (2.43)$$

where d is shield thickness, Z_ω is the incident wave impedance, for free space Z_o=377 Ω, η is material impedance and γ_p is the propagation

constant. If δ is the skin depth, two situations can be visualized: the first is (d << δ), it occurs at low ω or low σ. The absorption can be neglected and attenuation is due to reflection. The material seemes to be transparent. The second is (d >> δ), it occurs at higher frequencies or high conductivity. The attenuations is due reflection, absorption and multiple internal and depends on ε, σ and μ vlues or matching between Zω and η [6].

2.7.1. Shield Effectiveness by Reflection Loss (SE_R)

The reflection loss is related to Z_ω and η. The magnitude of reflection loss under a plane wave (far field condition) can be expressed as:

$$SE_R(dB) = -10 \log\left(\frac{\sigma}{16\omega\varepsilon_0\mu_r}\right) \quad \text{..... (2.44)}$$

The above expression shows that SE_R is a function of the ratio (σ/μ_r) of the shield material. For a given material (σ/μ_r is cons.) SE_R is reduced as frequency is increased. Therefore, the larger the permeability the lower the reflectance. In terms of impedance the reflectivity r_f at normal incidence is given by [141]:

$$r_f = | (\eta - Z_o) / (\eta + Z_o) | \quad \text{..... (2.45)}$$

The reflection loss is given in terms of impedance by [142-145]:

$$RL\ (dB) = 20 \log \left| (\eta - Z_0) / (\eta + Z_o) \right| \quad \text{..... (2.46)}$$

The magnetic permeability and dielectric constant are frequency dependent, but their variation with frequency is different. A good impedance matching can be done by suitable dielectric, magnetic, conductive matrix filler [47].

2.7.2. Shield Effectiveness by Absorption Loss (SE_A)

When an electromagnetic wave passes through a medium as shown in Fig.2.7, its amplitude decreases exponentially. The absorption loss due to induced currents producing ohmic losses is expressed by [142]:

$$SE_A = -20 log e^{\frac{d}{\delta}} = -8.68 d \left[\frac{t}{\delta}\right] = -8.68 d \left[\frac{\sigma\omega\mu_r}{2}\right]^{1/2} \quad \text{..... (2.47)}$$

where (d) in inches and (f) in Hertz. The SE_A is proportional to the quantity $(\sigma.\omega.\mu_r)^{1/2}$. For a given material, SE_A increases with frequency increasing, so a good absorber should possess high (σ) and (μ_r) at enough (d) to reach the suitable value of skin depths even at the lowest (f).

2.7.3 Shield Effectiveness by Multiple Internal Reflections (MIRs)

If the shield is thin, the wave suffers multi reflections between shield boundaries as in Fig.2.7. The produced attenuation SE_{Mu} is expressed by:

$$\mathbf{SE_{Mu} = 20\log_{10}(1 - e^{-2d/\delta}) = 20\log_{10}\left|\left(1 - 10^{-SE_A/10}\right)\right|} \quad \mathbf{...(2.48)}$$

It can be seen SE_{Mu} is closely related to SE_A. SE_{Mu} is also important for porous structures and for certain types of filled composites and for any design geometries enhancing Maxwell-Wagner's effect. It is neglected for thick absorber because the wave vanishes in single pass. For highly absorbing materials or at very high frequencies (~GHz), if $SE_A \geq 10$ dB the SE_{Mu} can be ignored [6,152].

2.8. Near Field and Far Field Absorption

EMI shielding is classified into the near field (NF) region (source-shielded distance $\leq \lambda/2\pi$) and the far field (FF) region (source-shielded distance $\geq\lambda/2\pi$). The tangential electric field is zero on a conducting wall while the magnetic field is maximum. [10,28]

The near field is defined as the region very close to a radiating element where the relationship between the electric and magnetic fields is complex. NF absorbers are placed near or directly on a radiating element, since the energy in the near field is predominantly magnetic. It should have high (μ) and high magnetic losses. It must have very low (σ) because it usually be in touch with circuit elements. All circuits contain elements like inductors or capacitors or connecting wires radiate at particular frequencies. Load materials are generally magnetic absorbers which are easily machined or molded [6, 10].

2.9. Design Considerations for Shielding Material

A fine comparison among shielding materials properties, leads to the fact that no single phase material can take care of all the shield aspects, like absorption coefficient, thickness, volume and broadband response. The shield must have a balanced combination of (σ), (ε), (μ) and physical geometry. Initially the reflection from the front face depends on impedance matching. The shield should have free charge carriers causing heating in the shield, conductivity in the range 10^{-3}-1.0 S/cm is suitable. Secondly the absorption within the shield that requires electric and/or magnetic dipoles interacts with the EM fields of the radiation [6, 19].

Metals are the most common materials for high reflection depending on only (σ/μ) ratio. The absorption loss (SE_A) is a function of the product ($\sigma.\mu$). In conducting medium, still ε plays an important role in determining SE_R and SE_A. On other hand metal based compositions suffer from reflection, corrosion and weight penalty. Carbon based materials (graphite, carbon black, CNTs and graphene) have been studied as EMI shields, but they are expensive. Intrinsic conducting polymers (ICPs) with variable conductivity and compatibility with polymeric matrices are good alternative. ICPs is used either as conducting filler for insulating matrices or as a conducting matrix with conducting, dielectric, magnetic fillers.

Recently, nanomaterials with controlled electrical and EM properties have produced good shielding materials. Composite of dielectric or magnetic nanoparticles like ferrites and conducting polymer like PANI form material possessing certain dielectric and magnetic properties valuable for EM noises suppression and radar signals attenuation. PANI has weak ferromagnetic behavior, but adding ferrite enhances M_s with reduction in H_c. Higher M_s and lower H_c values are desired to enhance μ_i value and subsequent increase the microwave absorption capability [142].

At low GHz frequencies or below, dielectric losses are smaller than conduction losses and it increases in proportion to ω. whereas conductor losses increase as $\omega^{1/2}$. So, at 10-30 GHz, the dielectric losses can exceed conduction losses.

The broad bandwidth materials are thick, heavy and expensive. For broadband operation, magnetic nanocomposites can be used. The reduction in microwave losses requires that the magnetic materials should have low conductivity for full penetration of the RF field. At low frequencies this interaction is small and the eddy current losses are negligible. If the resonances occur in the medium, then the real parts of the permittivity and permeability may obtain negative values [19,21].

2.10. Scattering Parameters

When microwave falls on absorber surface, the reflection and transmission coefficients are determined by scattering parameters. They are: S_{11} is the Input port voltage reflection coefficient , S_{12} is the reverse voltage gain, S_{21} is the forward voltage gain, S_{22} is the output port voltage reflection coefficient, as shown in Fig.2.8. They can be given by:

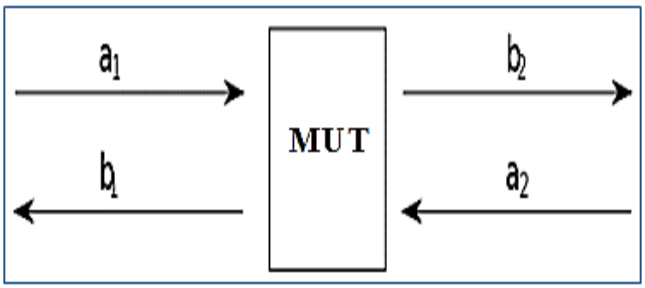

Fig.2.8 Reflection and transmission wave components for material under test MUT.

$$S_{11}=b_1/a_1,\ S_{12}=b_1/a_2,\ S_{21}=b_2/a_1,\ S_{22}=b_2/a_2 \quad \text{.....(2.49)}$$

where a_1, a_2, b_1 and b_2 are measured by voltage signal. In terms of decible (dB) s-parameters is given by:

$$S_{11} = 20 \log S_{11}\ dB \qquad S_{21} = 20 \log S_{21}\ dB$$
$$S_{12} = 20 \log S_{12}\ dB \qquad S_{22} = 20 \log S_{22}\ dB \quad \text{....(2.50)}$$

Reflection coefficient is the ratio of reflected to incident energy, which is usually expressed in dB by [147]:

$$\text{Reflection (dB)} = 10 \log(1/|r|^2) = -20 \log|r| \quad \text{....(2.51)}$$

The voltage reflection coefficient r is equivalent to the S_{11} (or S_{22})-parameter in dB. In most cases with absorbers the material is backed by metal. The total reflection coefficient or reflectivity r_{MB} in dB is given by:

$$\text{Reflectivity (dB)} = 10 \log(1/r_{MB}^2) \quad \text{.....(2.52)}$$

Transmission coefficient in dB is given by:

$$\text{Transmission (dB)} = 10 \log(1/|T|^2) = -20\log|T| \quad \text{...(2.53)}$$

which is equavalent to S_{12}(or S_{21})-parameter in dB.

A metal plate has a reflectivity about 0 dB. A material which reflects half of the incident energy is 3 dB down or has a reflectivity of -3 dB. A material which reflects one tenth of the incident energy has a reflectivity of -10 dB. When the source and load impedances are known values, the reflection coefficient is given by eq.2.46 [146,147].

2.10.1. Insertion Loss (IL)

It is the reduction in energy emitted from point A to reach point B caused by the insertion of an absorber material between the two points. A signal is transmitted through one antenna and the response is measured at the second antenna. The material under test is then placed between the

antennas and a measurement is performed. The insertion loss is expressed in dB as a function of frequency.

In case of two measurement ports that use the same reference impedance, IL is the magnitude of the transmission coefficient $|S_{21}|$ expressed in decibels. It is thus given by [149, 150]:

$$\mathbf{IL = -20log|S_{12}|\ \ (dB)} \quad \text{..... (2.54)}$$

2.10.2. Return Loss (RL)

It is the loss of power for reflected signal by a discontinuity in a transmission line. It is considered as a measure of how the sample impedance matches incident space impedance. Return loss in terms of incident power Pi and the reflected power P_r is expressed in decibels by:

$$\mathbf{RL\ (dB) = 10\ log\ P_i/P_r} \quad \text{..... (2.55)}$$

Return loss relate to S_{11}- parameter by:

$$\mathbf{RL(dB) = 10log\left|\frac{1}{(S_{11})^2}\right| = -20log|S_{11}|} \quad \text{.... (2.56)}$$

Return loss is sometimes used as the negative of the quantity defined above, but this usage is, strictly speaking, incorrect based on the loss definition [28, 149]. Return loss is the negative of the magnitude of the reflection coefficient in dB, since power is proportional to the square of the voltage, as given by eq.2.49. Return loss has a positive sign in eq.2.55, but in fact it produces negative sign due to the ratio of reflected to incident and log action. Reflection loss is equal to return loss if MUT is backed metal and measured by single port.

2.11. Hydrothermal Process

Hydrothermal process is generally defined as a method to synthesize nanosized crystals of complex compounds (Peroviskite, spinel etc.) under high temperature and water pressure conditions from different substances. Hydrothermal synthesis is usually carried out below 300°C [151,152].

Synthesizing particular composition by this method is included by preparing water solution of soluble salts (hydroxide, chloride, nitrate etc.). After adjusting the pH-value, it is placed in autoclave. A suitable pressure is built by raising the temperature of vessel. At certain temperature, reaction time is adjusted to get nanocrystallites. The stable crystals at the bottom of vessel are filtered out and washed with deminearlized water/organic solvent many times. Then they are dried in air and finally calcined to obtain purified nanocrystalline powder. Low synthesis

temperature, environment friendly, a single crystal growth and a wide range of nanosize powder production are the main advantages of this process [15]. The important benefits of using hydrothermal process for production nanostructuers are narrow sized distribution, controlled shape and simplicity [152]. The desired products can be obtained from:

1- homogeneous phase.

2- heterogeneous reactions between aqueous species and solid reactants.

This procedures can produce microporous, mesoporous and low-dimensional solids for a variety of applications. Hydrothermal process always contains a reaction, crystallizing substances, and particles growth. This procedure is based upon a phase transfer and separation between liquid and solid [153].

2.11.1. Formation of Magnetic Nanoparticles

Many chemical techniques have been developed to prepare nanoparticles, but overall understanding of the nucleation and growth is still challenging. A short sudden nucleation, followed by slow controlled growth and separation between them is important factors for preparing monodisperse nanoparticles. The three steps in the crystal formation mechanism are:

a. Nucleation

This stage implements formation of many nuclei at the same time, then they grow. The "sudden nucleation" enables a control of size distribution and highly uniform nanocrystals. In the beginning of nanoparticles crystallization, the homogeneous or heterogeneous nucleation occurs as an initial step. The homogeneous nucleation includes all nuclei emerging in a homogeneous solution simultaneously and then the growth step begins without more nucleation. The separation between nucleation and growth processes leads to a homogeneous nucleation and then monodisperse nano-sized particles. The role of high temperature, a strong reduction agent and supersaturated solution supply an energy to overcome energy barrier for nucleation, which is high because of change phase from homogeneous to heterogeneous[153, 154].

The growth by seed is the common method for crystal formation process, where the nucleation is separated from the growth by using nanocrystal seed nuclei. In the heterogeneous nucleation, the nuclei start to form at different times and in different ways. That produces different shapes and size, but correct conditions can control this procedure to produce the required structure [152].

b. Growth

The crystal growth occurs subsequent to the nucleation. In the absence of more nucleation, a narrow sized distribution of nanoparticles can be formed. The growth is continuing as long as the monomer solution is supersaturated.

The important factors which influence the growth process, nanocrystals size and morphology are surface energy, growth rate, capping molecules and temperature. These factors affect the nanocrystal growth which contains three main stages: (1) fast increasing of monomer concentration which generates nuclei formation, (2) assembling of monomer on the nuclei which starts crystal growth and causes the reduction of monomer concentration (3) surface stabilization with suitable capping agents which controls the physical properties in nanocrystals.[151,152]

c. Aging

The aging process is the step following growth step to control the formation of particles in certain size, shape and morphology. It can change the size distribution of nanocrystals or keep it the same.

Two main processes may happen in the aging stage, Ostwald ripening and aggregation. Ostwald ripening occurs during of the crystallization process and can affect the size, shape and even monodispersity of the samples. In this process larger crystals are grown from smaller ones that have a higher solubility than the larger ones. Aggregation is a process that sticks the nanoparticles together which is usually undesirable. If this process can be oriented in the same direction it will produce the anisotropic nanoparticles like elongated particles. This may set material properties by controlling defect density, morphology, and size as well as size distribution [152, 155].

Chapter 3: Experimental Part

3.1 Introduction

This chapter includes the preparing of Li-Ni ferrite nanoparticles by hydrothermal method, the preparing of paints and the used methods in the diagnosis for their structural, magnetic, and microwave properties. Due to the need of autoclave to be used for hydrothermal process, it is appropriate to begin with the autoclave fabrication.

3.2. Autoclave Fabrication

Usually autoclaves are made from stainless steel with Teflon or Pyrex vessel inside [156]. The autoclave has stainless steel pipe of a diameter equal to 10cm and length of 20cm. The lower base is 5mm thick stainless steel with diameter 14cm. The upper base is also stainless steel with 3mm thick disc with 6 holes of 8 mm diameter. These holes match screws in welded ring at upper edge of the pipe as shown in Fig.3.1. (A) and (B).

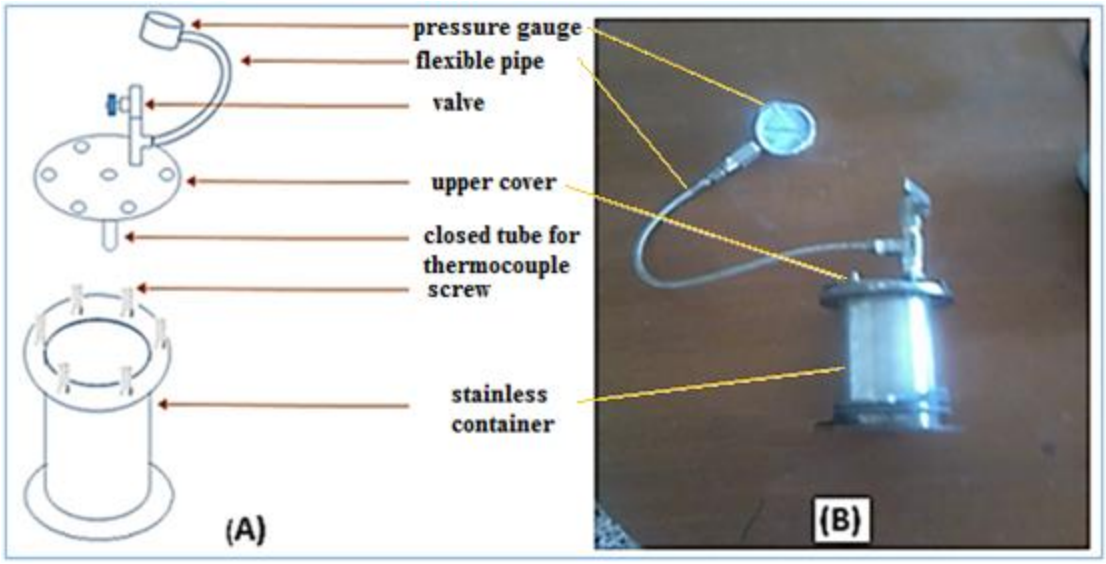

Fig.3.1 The homemade autoclave. (A) Sketch. (B) Photo.

The above homemade autoclave is supplied by pressure gauge of 20bar and closed end tube to feed thermocouple or thermometer. A Pyrex volumetric flask of 500ml is used as solution container inside stainless steel autoclave. A cork sheet of 2mm is used as gasket washer between screws base and upper disc cover.

The experimental set up is shown in Fig.3.2 where the stirrer hotplate is used as mixing and heating source during hydrothermal process. The autoclave as whole is covered with glass wool coat to get required rising temperature rate at stable fixed temperature.

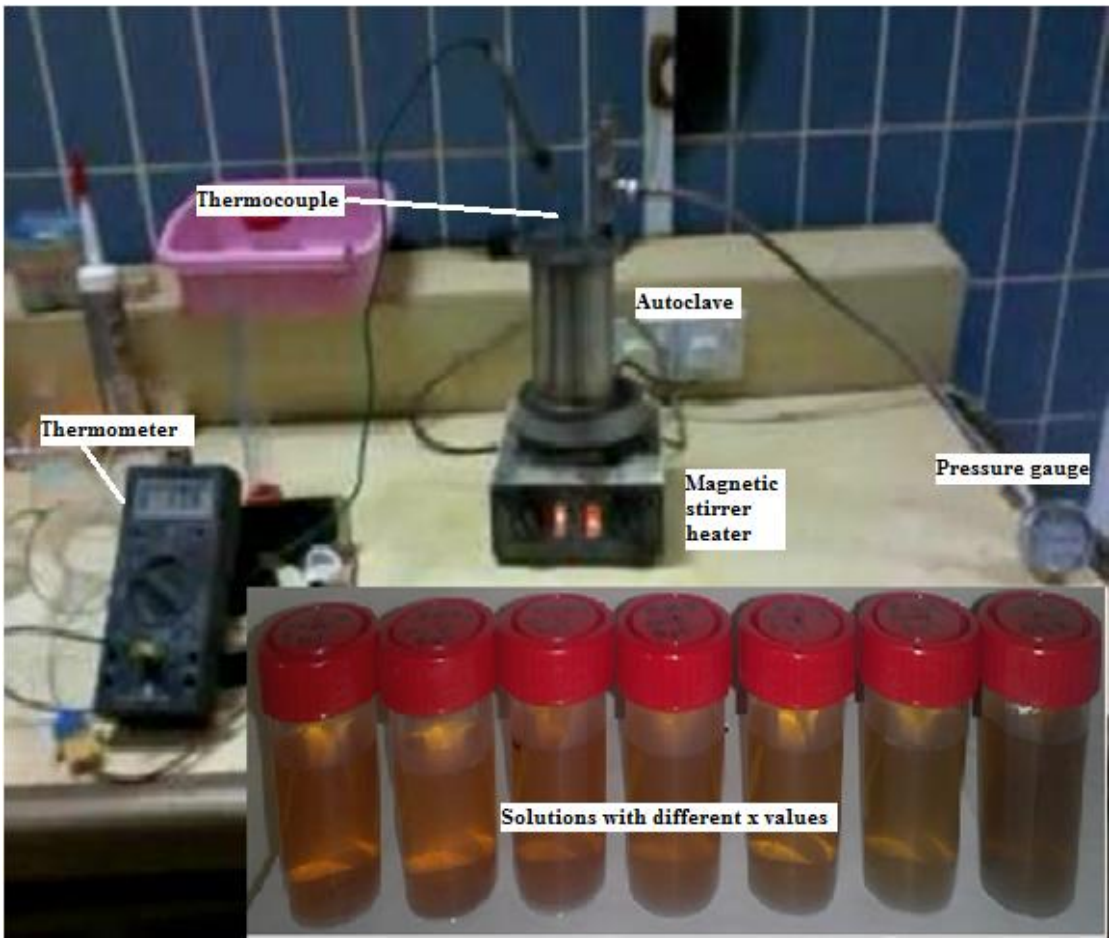

Fig.3.2. Hydrothermal process set up and the used mixed solutions.

3.3. The Preparation of Li-Ni Ferrites Powder.

Two sets of solutions were used as starting material. The first used the following metal chlorides as starting materials $LiCl.H_2O$, $NiCl_2.6H_2O$, $FeCl_3$, besides NaOH and distilled deionized water. They were used in different accurate measured weights to produce Li-Ni ferrite without Fe^{2+} of molar ratios (x=0, 0.1, 0.3, 0.5, 0.7, 0.9, 1). The second set was the same as previous one but with use of an additional solution which was $FeSO_4.7H_2O$ as a source of Fe^{2+} and keeping the ratio of Fe^{+3}(from $FeCl_3$)/Fe^{+2}(from $FeSO_4.7H_2O$) is constant at 1.7. All material with analytical degree were obtained from BDH chemicals.

3.3.1. The Preparation Process of Li-Ni Ferrite without Fe^{2+}.

The preparation of $Li_{0.5-0.5x}Ni_xFe_{2.5-0.5x}O_4$ ferrite without Fe^{2+} at different x values utilized the following chemical equations:

1- At x=0

$$2.5FeCl_3 + 0.5LiCl.H_2O + 8NaOH \longrightarrow Li_{0.5}Fe_{2.5}O_4\downarrow + 4.5H_2O + 8NaCl$$

2- At x=0.1

$2.45FeCl_3+0.45LiCl.H_2O+0.1NiCl_2.6H_2O+8NaOH \longrightarrow Li_{0.45}Ni_{0.1}Fe_{2.45}O_4+ 5.05H_2O + 8NaCl$

3- At x=0.3

$2.35FeCl_3 +0.35LiCl.H_2O+0.3NiCl_2.6H_2O+8NaOH \longrightarrow Li_{0.35}Ni_{0.3}Fe_{2.35}O_4 + 6.15H_2O + 8NaCl$

4- At x=0.5

$2.25FeCl_3+0.25LiCl.H_2O+0.5NiCl_2.6H_2O+8NaOH \longrightarrow Li_{0.25}Ni_{0.5}Fe_{2.25}O_4 + 7.25H_2O + 8NaCl$

5- At x=0.7

$2.15FeCl_3+0.15LiCl.H_2O+0.7NiCl_2.6H_2O+8NaOH \longrightarrow Li_{0.15}Ni_{0.7}Fe_{2.15}O_4 + 8.35H_2O + 8NaCl$

6- At x=0.9

$2.05FeCl_3+0.05LiCl.H_2O+0.9NiCl_2.6H_2O+8NaOH \longrightarrow Li_{0.05}Ni_{0.9}Fe_{2.05}O_4 + 9.45H_2O + 8NaCl$

7- At x=1.0

$2FeCl_3 + NiCl_2.6H_2O + 8NaOH \longrightarrow Ni_1Fe_2O_4 + 10H_2O + 8NaCl$

Depending on the number of moles in the chemical equations, the weights of starting materials were calculated for 0.01mole for final ferrite product as shown in the Table3.1. The weights were divided by 100 to get 0.01mole of ferrite and produce around 2.5 g of each run. The weights of NaOH in the table which relate to chemical equations are lower than that used experimentally, due to the need to reach a specified pH value.

Table 3.1 Starting material weights for 1 mole Li-Ni ferrites for different x values.

		x=0.0		x=0.1		x=0.3		x=0.5	
Starting materials	**Mw gm/mol**	**N Mol.**	**W gm**	**N Mol.**	**W gm**	**N Mol.**	**W gm**	**N Mol.**	**W gm**
$FeCl_3$	**162.21**	**2.5**	**405.5**	**2.45**	**397.42**	**2.35**	**381.2**	**2.25**	**364.97**
$LiCl.H_2O$	**60.40**	**0.5**	**30.2**	**0.45**	**27.185**	**0.35**	**21.14**	**0.25**	**15.1**
$NiCl_2.6H_2$	**237.7**	**0**	**0**	**0.1**	**23.77**	**0.3**	**71.31**	**0.5**	**118.85**
NaOH	**39.1**	**8**	**312.8**	**8**	**312.8**	**8**	**312.8**	**8**	**312.8**

		x=0.7		x=0.9		x=1.0 Ni ferrite	
Starting materials	**Mw gm/mol.**	**N mol.**	**W gm**	**N** mol.	**W gm**	**N mol.**	**W gm**
$FeCl_3$	**162.21**	**2.15**	**348.75**	**2.05**	**332.53**	**2**	**324.42**
$LiCl.H_2O$	**60.40**	**0.15**	**9.0615**	**0.05**	**3.0205**	**0**	**0**
$NiCl_2.6H_2$	**237.7**	**0.7**	**166.39**	**0.9**	**213.93**	**1**	**237.7**
NaOH	**39.1**	**8**	**312.8**	**8**	**312.8**	**8**	**312.8**

Each salt dissolved in 100ml deionized distilled water under stirring for about 5 min. Then the two or three solutions were mixed with each other. After that NaOH solution of 2.5M was adding drop by drop under continuous high stirring speed until required pH was reached which is 11. The stirring continued for 30 min after adding NaOH. Then the suspension in the flask was transferred to an autoclave. These steps are shown in Fig.3.3. It will be shown that the Li ferrite phase (x=0) is not formed under this method conditions.

Some distilled water was placed in the autoclave outer the flask to distribute heat uniformly and to prevent vaporized water in flask from condense in this field. The subsequent step was closing the autoclave and setting the calibrated hotplate to the required temperature.

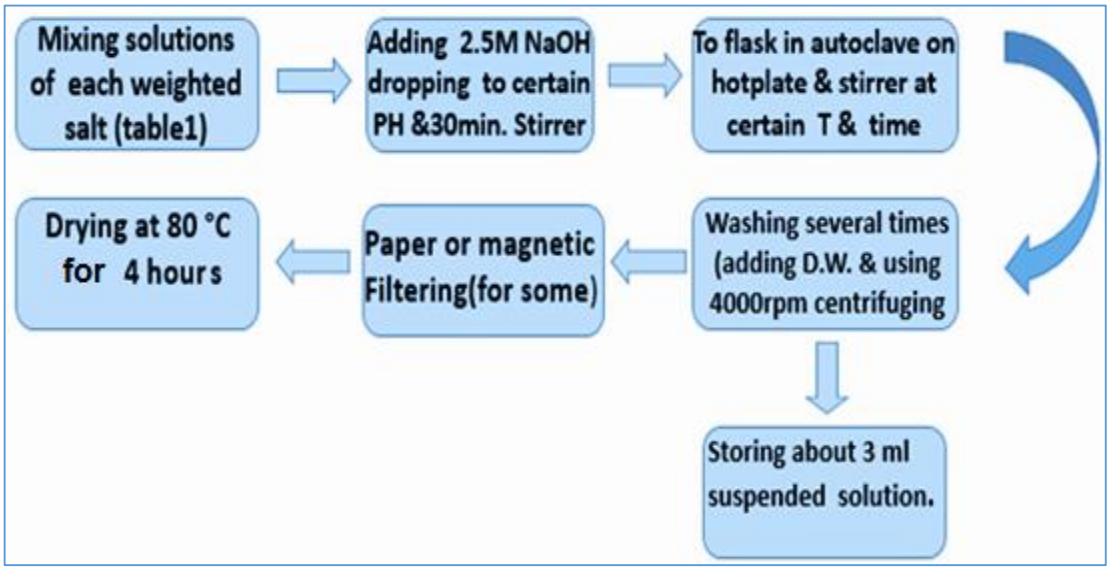

Fig.3.3 Block diagram of hydrothermal process.

Stirring was still working during hydrothermal process. When the preparing temperature was reached, which is 155 ˚C in this case, the autoclave was sustained for a certain time (3hr) under these conditions. The pressure was rising autogenously. After the required time was finished the heater was turned off. When room temperature was attained the suspension was got out. After that the precipitate washed 4-5 times by distilled water followed by drawing about 3ml of suspension for additional test. Then filtered by centrifuge machine and by magnetic filtering. The rest suspension was dried at 80 ˚C for about 4 hours. The balance KERN ASC 120 with accuracy 0.1mg with four digit was used for weighting the salts.

3.3.2. The Preparation Process of Li-Ni Ferrite with Fe^{2+}.

The procedure was similar to that of section (3.3.1), except that $FeSO_4.7H_2O$ was used as source of Fe^{+2} besides $FeCl_3$ as source of Fe^{+3}. The ratio of (Fe^{+3}/Fe^{+2}) was kept at 1.7 and the total Fe ions still satisfied the stoichiometric with Li and Ni ions. the suggested reaction equation at x=0.1 is:

$$(2.45*1.7/2.7)FeCl_3 + (0.45)\ LiCl.H_2O + (0.1)\ NiCl_2.6H_2O + (2.45*1/2.7)\ FeSO_4.7H_2O + (1+ (2.45*1/2.7))\ NaOH + \{4-(1+ (2.45*1/2.7))+ ½(1+ (2.45*1/2.7))\}O \rightarrow Li_{0.45}Ni_{0.1}Fe_{2.45}O_4 + 14H_2O + 8\ NaCl + 2.45*1/2.7\ NaSO_4 + 1H_2O$$

Some notes should be mentioned on this equation. First the numbers in red color belong to x=0.1 and can be changed to their corresponding values in other compositions as given in Table3.2. The second note is that the final term of starting material is related to oxygen which is not added experimentally but it is extracted from reaction surroundings. The $14H_2O$ results from water molecules linked with metal salts, but the term $1H_2O$ results from OH and surroundings O.

Table 3.2. Selected molar ratio with the corresponding compound.

x	Chemical formula
0	$Li_{0.5}Fe_{2.5}O_4$
0.1	$Li_{0.45}Ni_{0.1}Fe_{2.45}O_4$
0.3	$Li_{0.35}Ni_{0.3}Fe_{2.35}O_4$
0.5	$Li_{0.25}Ni_{0.5}Fe_{2.25}O_4$
0.7	$Li_{0.15}Ni_{0.7}Fe_{2.15}O_4$
0.9	$Li_{0.05}Ni_{0.9}Fe_{2.05}O_4$
1	$NiFe_2O_4$

3.4. Preparation of Li-Ni Ferrite-Epoxy Composite

After ferrites preparation, manual milling for short time of powders was done. Then powder was mixed with epoxy and resin by using mixer for 5 min. Then the mixture was casted into two homemade sample holders which act as mold simultaneously. The first one was made from brass with interior dimension 22.9 mm x 10.2 mm and the second was made from aluminum with dimensions 15.8mm x 7.9 mm and Teflon base inside them to test sample in X-band and Ku-band in rages 8.2-12.4 GHz and 12.4-18 GHz respectively as shown in Fig.3.4

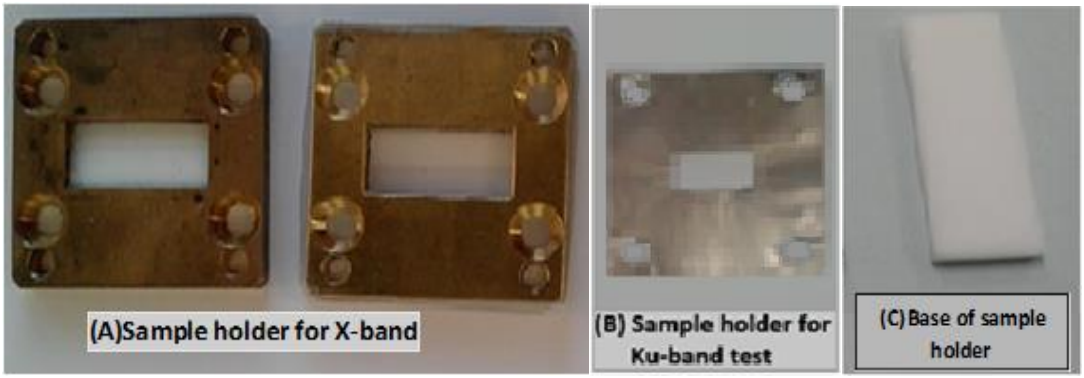

Fig3.4. Samples holder. Interior dimensions of (A) are 22.9mmx10.2mm for X-band. Internal dimension of (B) are 15.8mmx7.9mm for Ku-band. (c) Base of sample holder.

After casting the composite, the assembly was left 24 hour to be still in green state, then it was removed from holder and base. The weight of ferrite in x-band tests was 0.125 gm to each 0.158 ml of epoxy. The type of epoxy was phenol Novolacs (EPN) from BAUMERK /Turkey with liquid density 1.2 gm/cm^3. So the mixing ratio of ferrite weight/total weight was about 39.7% and ferrite volume/total volume was about 19.8%, using ferrite pellet of density is 3.2 gm/cm^3 in about 1.9 Ton/cm^2 compression.

3.5. Structural Tests

3.5.1. XRD Test

This test was performed with Panalytical Expert XRD diffractometer at the Physics Department -College of Science at Al-Nahrain University. All produced powder samples were checked and analyzed by this diffractometer. The scanning range of 2Θ was from 20^0 to 80^0. The source and detector slits were 0.2 mm. Glass substrate with dimensions of about 2cm x 3cm was used as sample holder for all samples. The powder was spread onto glass then gently press by stainless steel spatula to have smooth surface. Lattice constant and XRD density were extracted from this text. The working voltage was 45 kV and the current was 40 mA. Step size was 0.1 and time per step was 5 sec. giving overall scanning time of about 50 min. The source was working at Cu Kα line with λ=0.15405 nm.

3.5.2. FTIR Tests

Testscan Shimadzu FTIR 8000 spectrophotometer was used to accomplish this test. The sample here is a pellet of mixing ferrite powder and KBr powder. The scanning was from 200cm^{-1} to 1000cm^{-1}. The device is shown in Fig.3.5. FTIR test provides information about tetrahedral and

octahedral sublattice sites vibratis and can give help to analyses about cation distribution. It was performed at Chemistry Department-College of Science at Al-Nahrain University.

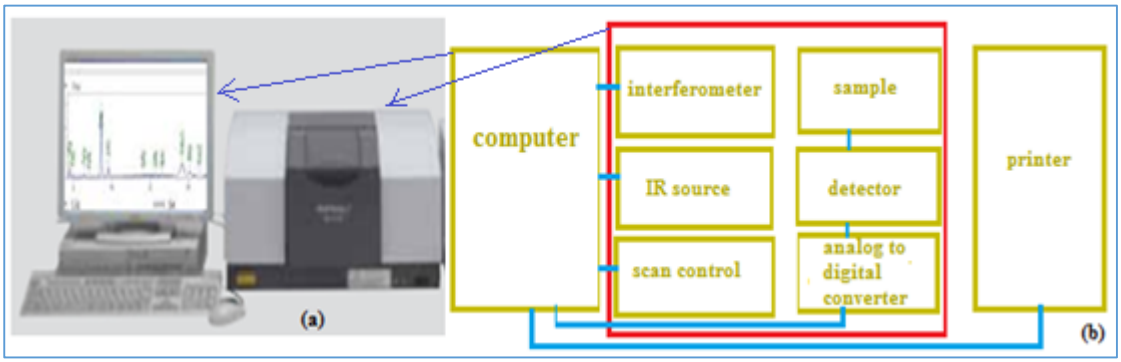

Fig.3.5. Shimadzu 8000 FTIR spectrophotometer device.(a) front view image, (b) Block Diagram.

3.5.3. SEM and TEM Tests

The devices FEI LEO 1550 SEM and Philips CM 12 TEM were used to analyze the powder, by performing EDX and imaging for nano size particles, where some of the suspensions and powders samples were subjected to this tests. These devices are shown in Fig.3.6. The working potential of SEM is up to 30kV, whereas for TEM it is up to 200kV. These tests is considered as effective common tools to analyze morphology, size distribution, shape some time crystalline structure of particles. These tests were accomplished at AG-Farle of Duisburg-Essen University/Germany.

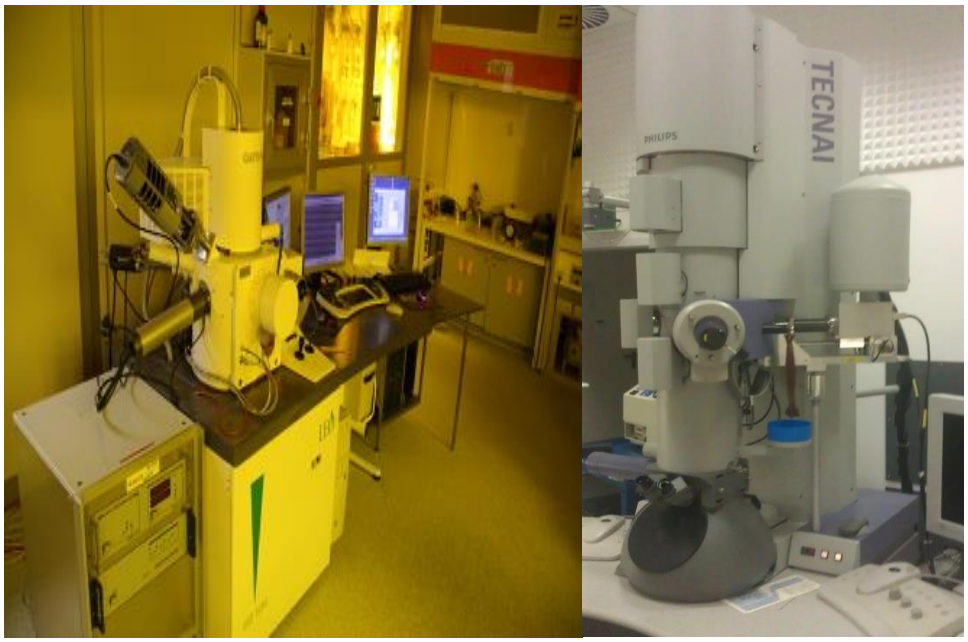

Fig.3.6. SEM and TEM devices.

3.6. Magnetic Properties Measurements

Hysteresis loop curve represents the basic characteristic of magnetic material and provides the information about the magnetic parameters like permeability, coercivity and magnetization. Measuring these parameters is essential for analysis of magnetic losses. The hysteresis loop was performed by Quantum Design MPMS XL SQUID, with specification: field range ± 5 Tesla, Temperature range: 1.9 – 400 K and DC Magnetization absolute sensitivity: 1 x 10^{-8} emu at 2,500 Oe. The used instrument is illustrated in Fig.3.7. Hysteresis loop curve test was performed at AG-Farle of Duisburg-Essen University/Germany.

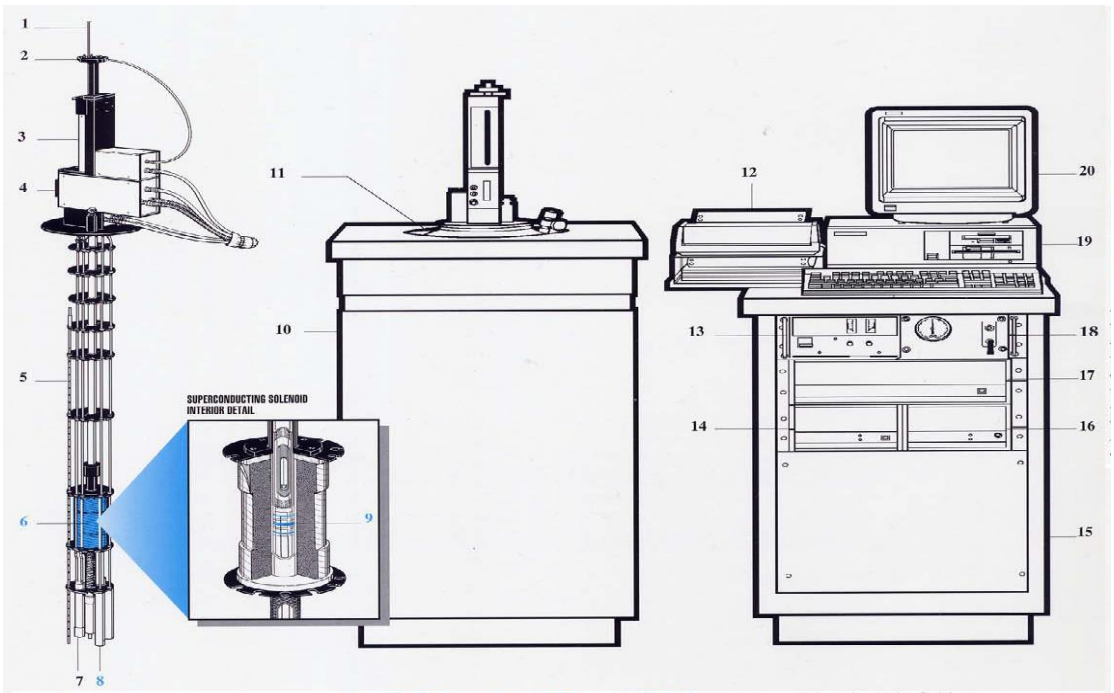

1. Sample Rod
2. Sample Rotator
3. Sample Transport
4. Probe Assembly
5. Helium Level Sensor
6. Superconducting Solenoid
7. Flow Impedance
8. SQUID Capsule with Magnetic Shield
9. Superconducting Pick-up Coil
10. Dewar Isolation Cabinet
11. Dewar
12. HP Thinkjet Printer
13. Magnet Power Supply
14. Model 1802 Temperature Controller
15. Console Cabinet
16. Power Distribution Unit
17. Model 1822 MPMS Controller
18. Gas/Magnet Control Unit
19. HP Vectra Computer
20. Monitor

Fig. 3.7. The SQUID device components.

3.7. Microwave Losses Measurements by VNA

Two tests were used to perform these measurements. They were *reflection loss* and *insertion loss* conducted on Vector Network Analyzer (VNA). The main VNA function is measuring the s-parameters of material or device under test (DUT). It can measure impedance and Smith chart of DUT. The VNA block diagram of main parts is shown in Fig.3.8. In part (A), the signal processing of single port and in part (B) The signal processing of two port.

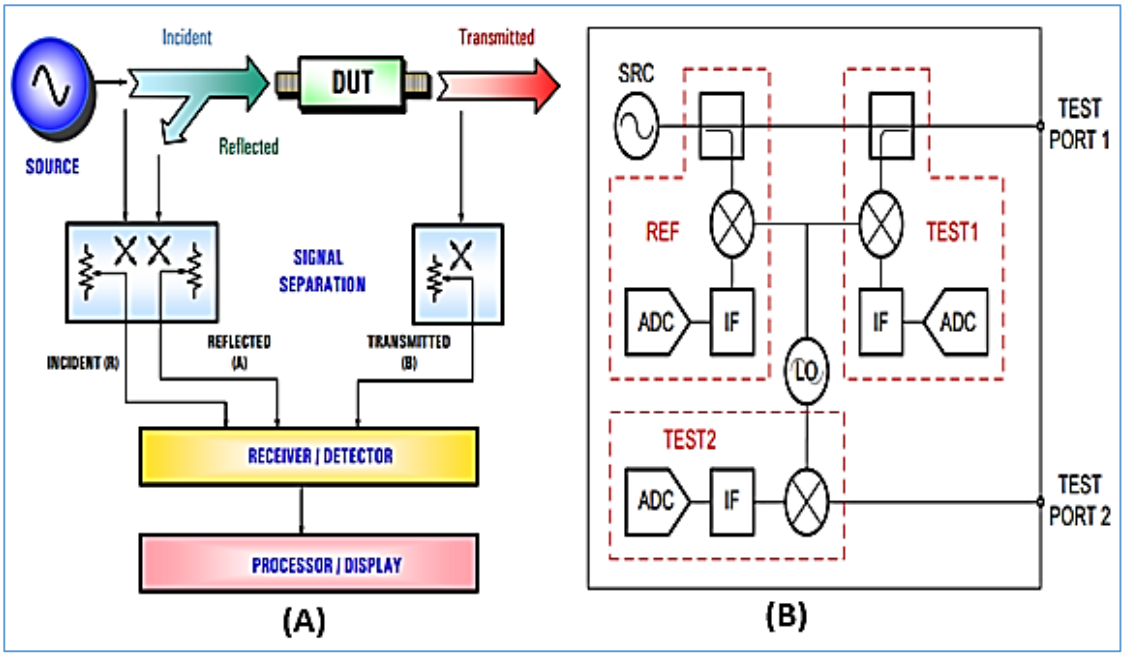

Fig.3.8. VNA block diagram (A) single port (B) Two port.

In this block diagram there are four parts to measure reflected and transmitted waves:

- MW source usually voltage controlled oscillators (VCO).
- Wave splitter or coupler to divide incident signal to measure it. It is also used to separate the incident and reflected wave.
- Detectors: diodes accompanied by analyzer to measure the phase.
- Processor and display: processors accompanied by spectrum analyzer which works under operating system such as Dos or Windows [157,158].

The two port VNA has two single port VNA connected via same source, processor and display.

According to previous features, VNA can measure S_{11}, S_{12}, S_{21} and S_{22} parameters by measuring the detectors voltages for incident, reflected and transmitted signals.

Analyzing composite sample was done by two techniques. Transmission reflection line technique (T/R L) by wave guide was used in x-band range for measuring MW losses, as shown in Fig.3.9 and Fig.4.10. The other technique is coaxial short cut technique (CO-SCT) which is connected to FMR device.

Two VNA instruments were used to measure the s-parameters. They are HP 8510C from Agilent Technologies and Anritsu MS4642B Vector Star Vector Network Analyzer 10 MHz to 20 GHz 2Port as shown in Fig.3.11.

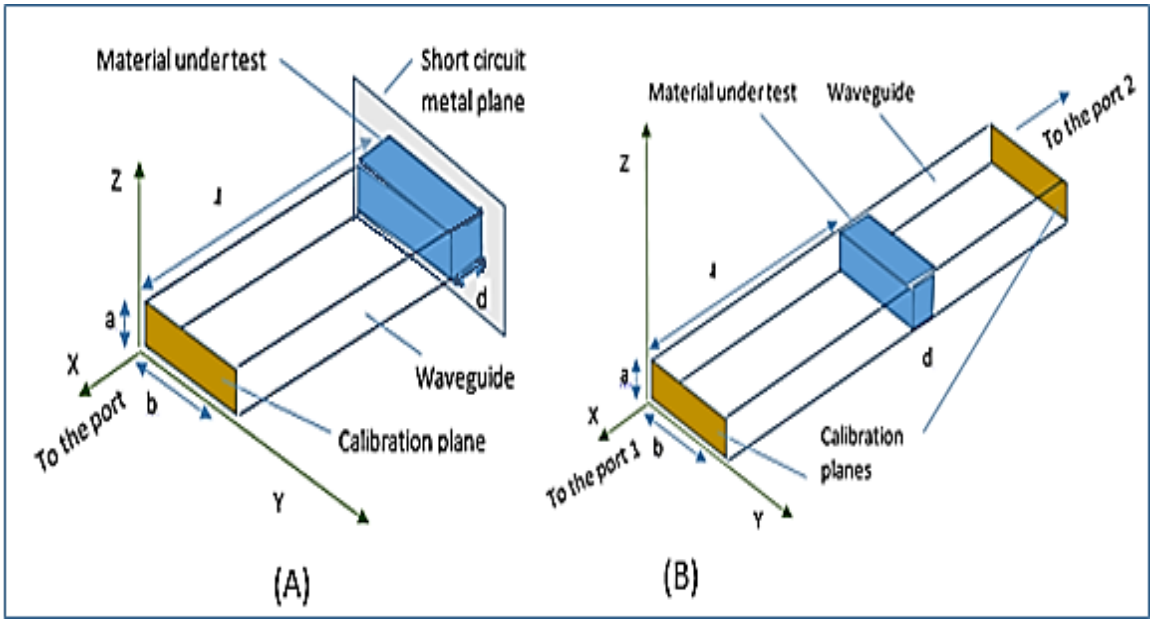

Fig.3.9. (A) Waveguide SCT technique (B) Waveguide T/R line technique.

This test was performed on all prepared samples as well as additional two samples at x= 0.5 with using Fe^{2+} at different thicknesses of 1.5 mm and 2 mm. VNA test was accomplished at Industrial Research and Development Department-Ministry of Research and Technology/Baghdad and at Department of General and Theoretical Electrical Engineering-Duisburg-Essen University/Germany.

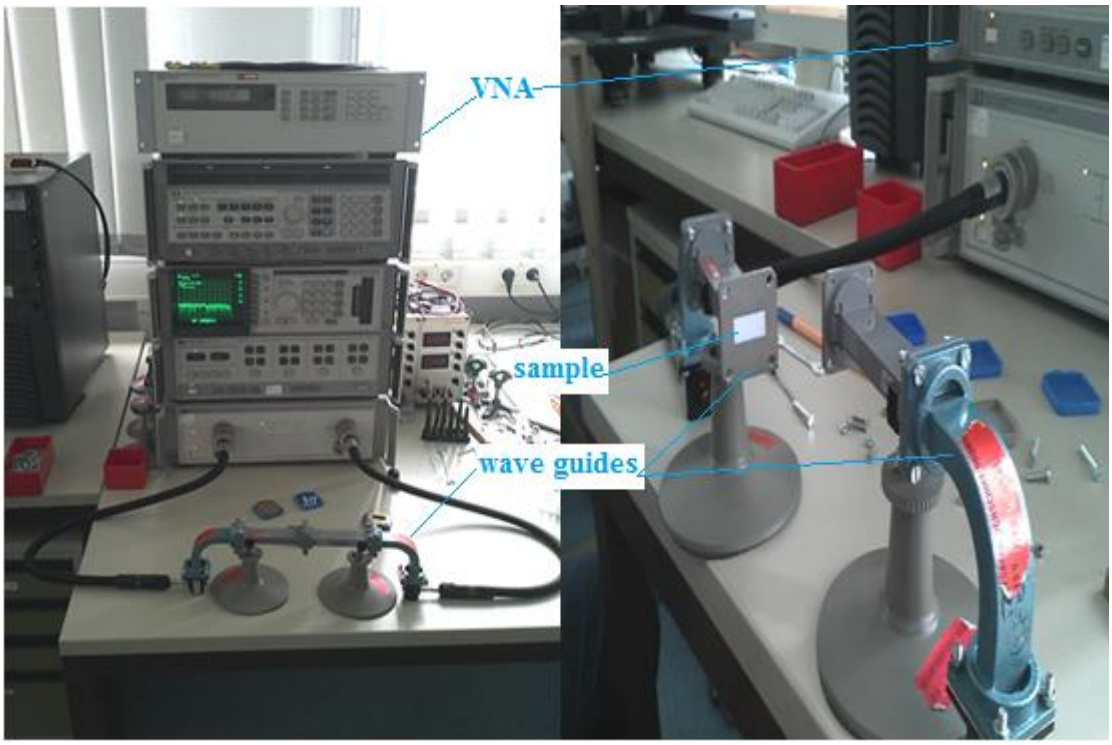

Fig.3.10. VNA set up for T/R line and SCT techniques with HP 8510C VNA.

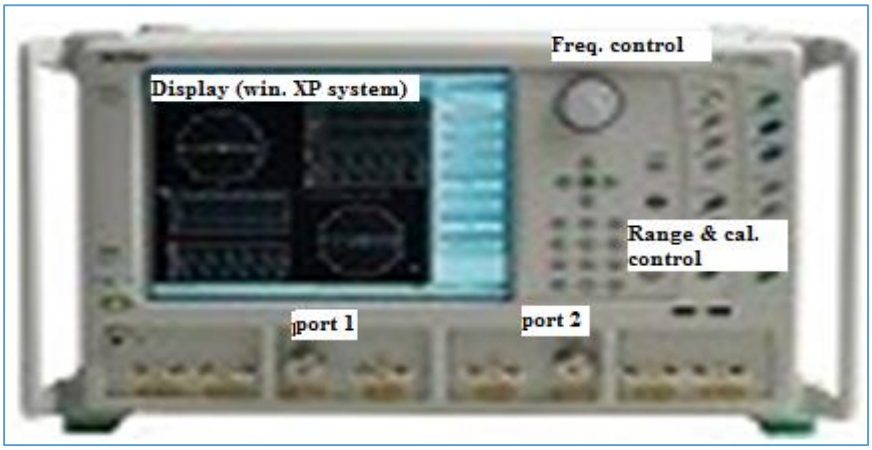

Fig .3.11. Anritsu MS4642B Vector Star Vector Network Analyzer

3.8. Ferromagnetic Resonance (FMR) Tests

FMR instrument construction is shown in Fig.3.12. It can be used to define complex susceptibility of sample at such microwave frequency when static magnetic field is applied. The complex susceptibility means absorbed energy. There are two sets up, the first uses a fixed frequency and sweeping static field usually accompanied by the cavity resonator and the second uses a fixed field and sweeping frequency.

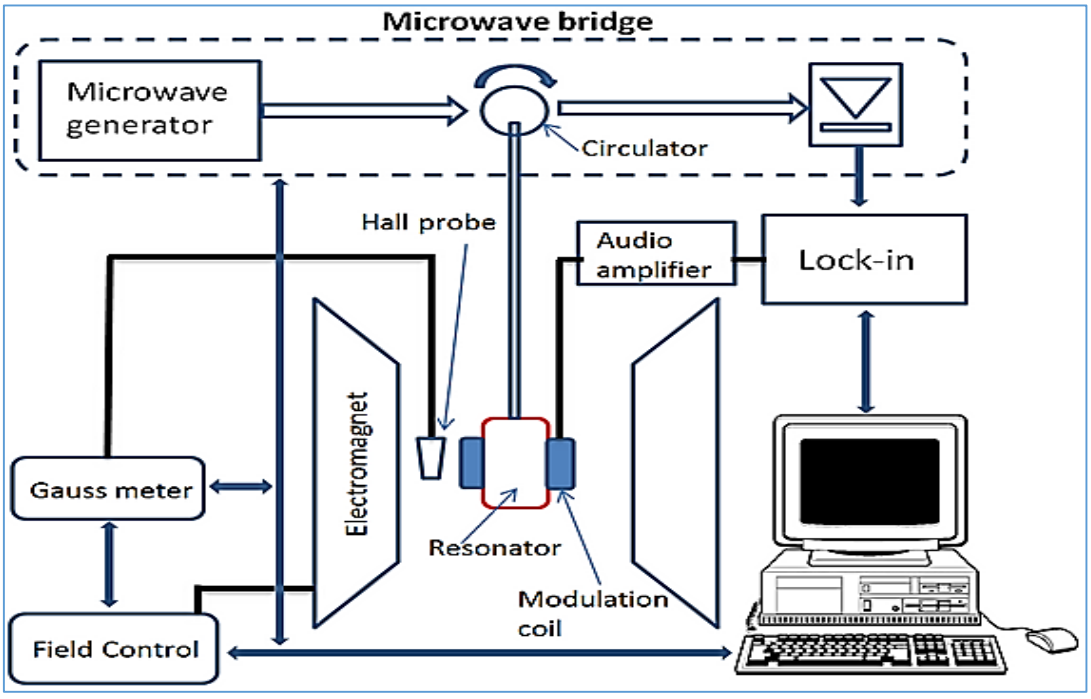

Fig.3.12. Block diagram of FMR spectrometer.

The first set up consists of electric magnet which provides magnetic field up to 5 Tesla supported by suitable power supply and cooling unit. The instrument uses a diode as detector for radiation to measure the change in reflected power from the cavity. The source of microwave is klystron

transferred to cavity resonator by waveguide. The circulator organizes the passage of incident and reflected waves through the same waveguide. The Bridge is a term used for the collection which includes the source, detector, circulator and related electronics. Lock in amplifier is used to enhance the signal to noise ratio. The source frequency, cavity and detector can be modified slightly to match the resonance condition by enhancing the quality factor. Gauss meter with Hall probe is used to measure the applied field. Data acquisition is utilized to connect all previous parts with computer. The cavity is a metallic box or cylinder. In this case the waveguide is shortened by cavity resonator. The used system has automatic measurements, magnetic field up to 2.6 T, sliding fields, microwave cavities with quality factors of up to 8000, Frequency-tunable cavities (8-14 GHz), and field modulation up to 100 kHz. Sample weight is 0.3 mg inserted in the cavity by plastic tube from certain window.

The second set up is similar to the first one except there no cavity but there is a coaxial short cut, also there is a collection of circulators each one works with certain band.

The first set up is used to test all samples at frequency around 9.7 GHz, and the second is used for all samples at frequency range 2-26 GHz. The second set up is used to record diode signal in case of no sample / case of presence of the sample, i.e. $(\text{Reflected power})_{\text{no sample}}/(\text{Reflected power})_{\text{with sample}}$. This ratio equivalent to the ratio $(\text{Absorbed power})_{\text{with sample}}/(\text{Absorbed power})_{\text{no sample}}$. The test were done on all samples to show the magnetic response of samples for frequency range 1.5-26 GHz. The two sets up are shown in Fig.3.13 and Fig.3.14. This test was performed at AG-Farle of Duisburg-Essen University/Germany.

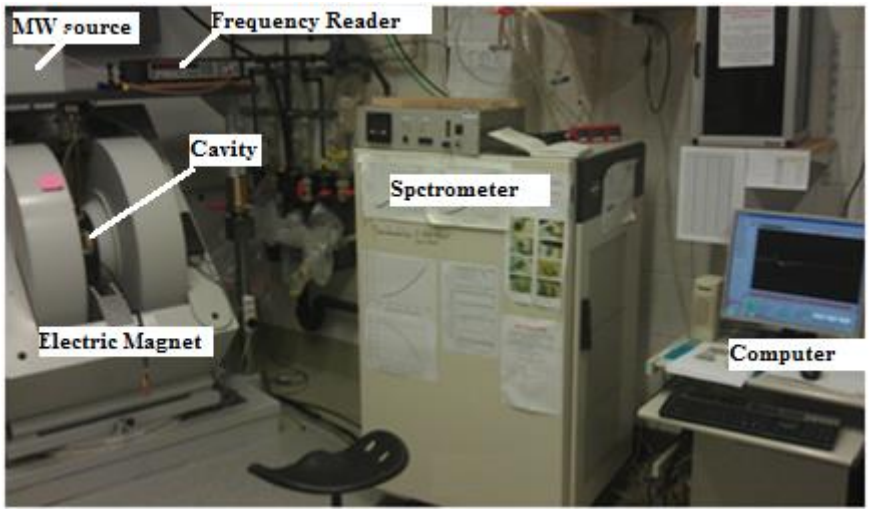

Fig.3.13. BRUKER instrument sweeping field (field dependent) set up.

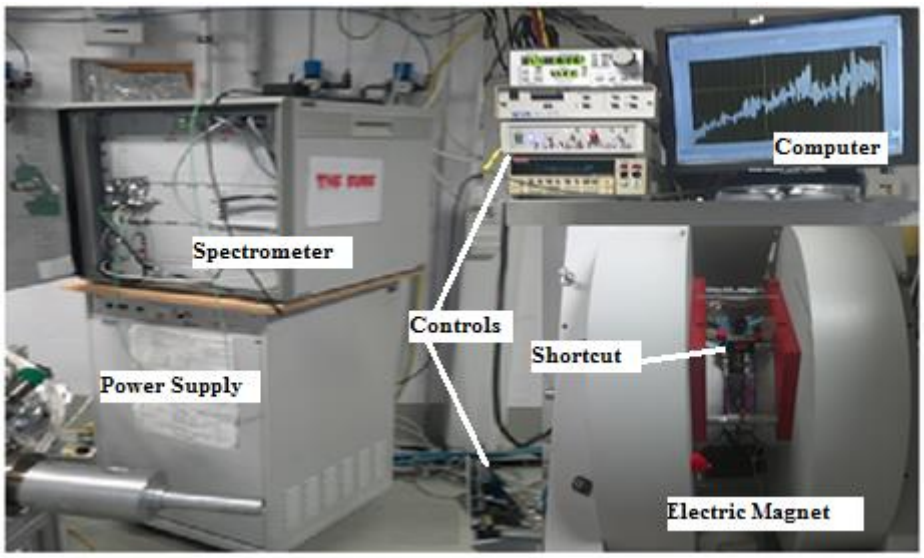

Fig.3.14. BRUKER device, possibility of sweeping the frequency (frequency dependent test).

2.9. Composition Tests

Composition test was performed on all samples by two techniques. The first check was done by Energy Dispersive X-ray Spectroscopy (EDX) that is accompanied by SEM and TEM systems mentioned previously. Unfortunately EDX spectroscopy has no ability to detect light element of atomic number lower than 8, because the sensitivity to characteristic x-ray of these elements is lower than that of Bremsstrahlung one, absorption by sample and detector window and these electrons are valence electrons so their position is affected by compound type. That leads to use the second technique which is Atomic Absorption. The EDX test achieved by LEO and FEI and by Philips CM 12 TEM. The atomic absorption instrument was Varian SpectrAA shown in Fig.3.15.

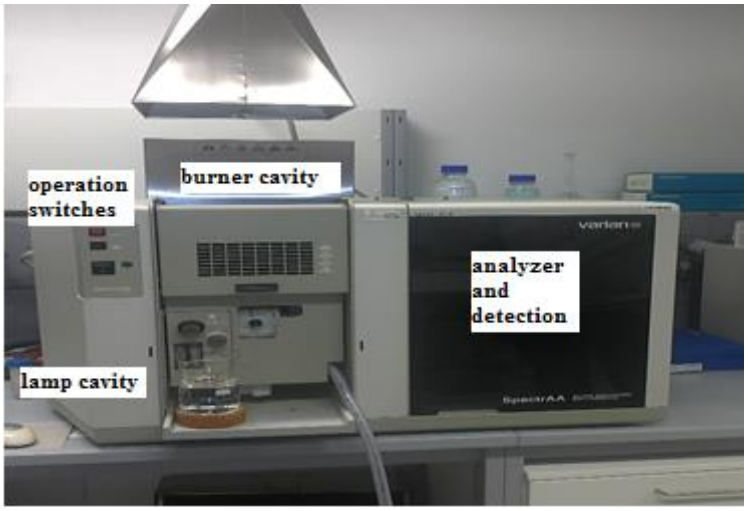

Fig.3.15. VARIAN spectrAA Atomic Absorption instrument

Chapter 4: Results and Discussions

4.1. Introduction

The preparation of ferrite powder samples and paints of epoxy composite samples was the plan to complete the measurements and analysis of those were proposed before. The structural, magnetic and microwave properties result will be displayed and discussed in this chapter. The discussions of the results is the main tool to conclude the best procedure for the application.

4.2. Structural Properties Results

The structural properties are involving the XRD, FTIR, SEM, and TEM results as mentioned in section 3.5. The tests results will be exhibited and associated with trying to give the reasons explaining results and behaviors.

4.2.1. XRD Results of Li-Ni Ferrite without Fe^{+2}

The result of the prepared Li-Ni ferrites by XRD charts at different molar ratios (Nickel content) from x=0-1 is shown in Fig.4.1. The sample was scanned in range 2Θ from 20°- 80°, this range contains nine peaks of the most intensive peaks of spinel ferrite. The other peaks are located beyond 80°, they are weaker than that appeared in the chosen range. The analysis of phases was done by High Score Analysis and Match Crystal Impact 2.

It was found that the formed phase is hematite at x=0, which is antiferromagnetic phase, with very small other iron oxide phases quantities. The increasing of (x), spinel ferrite was more dominant. Samples with x > 0.5 have reasonable match with Li-Ni ferrite JCPDS reference code (00-013-0207) especially at high x values which are belonged to space group Fd3m. The non-exact matching of some peaks is related to residuals of NaCl and Hematite, these were appeared around 32°, 33.1°, 41.5° and 49.5° as shown in Fig.4.2.

It was thought that low molar ratio of non-forming of spinel ferrite was related to isovalent substitution with the same oxidation. In this case, there were three lithium ions Li^{+1} substitute one ferric ion Fe^{+3} and there was no divalent ions (or any equivalent) formed under preparation condition. It is worth mentioning that, in section 1.3.1, the chemical formula of ferrite is $M[Fe_2]O_4$ (M is any divalent cation or what equivalent) which is very important to form spinel structure. Unfortunately M cation is not present and the activation energy to form its equivalent is not reached. It was believed as (x) is increased the activation energy to make its equivalent is reduced.

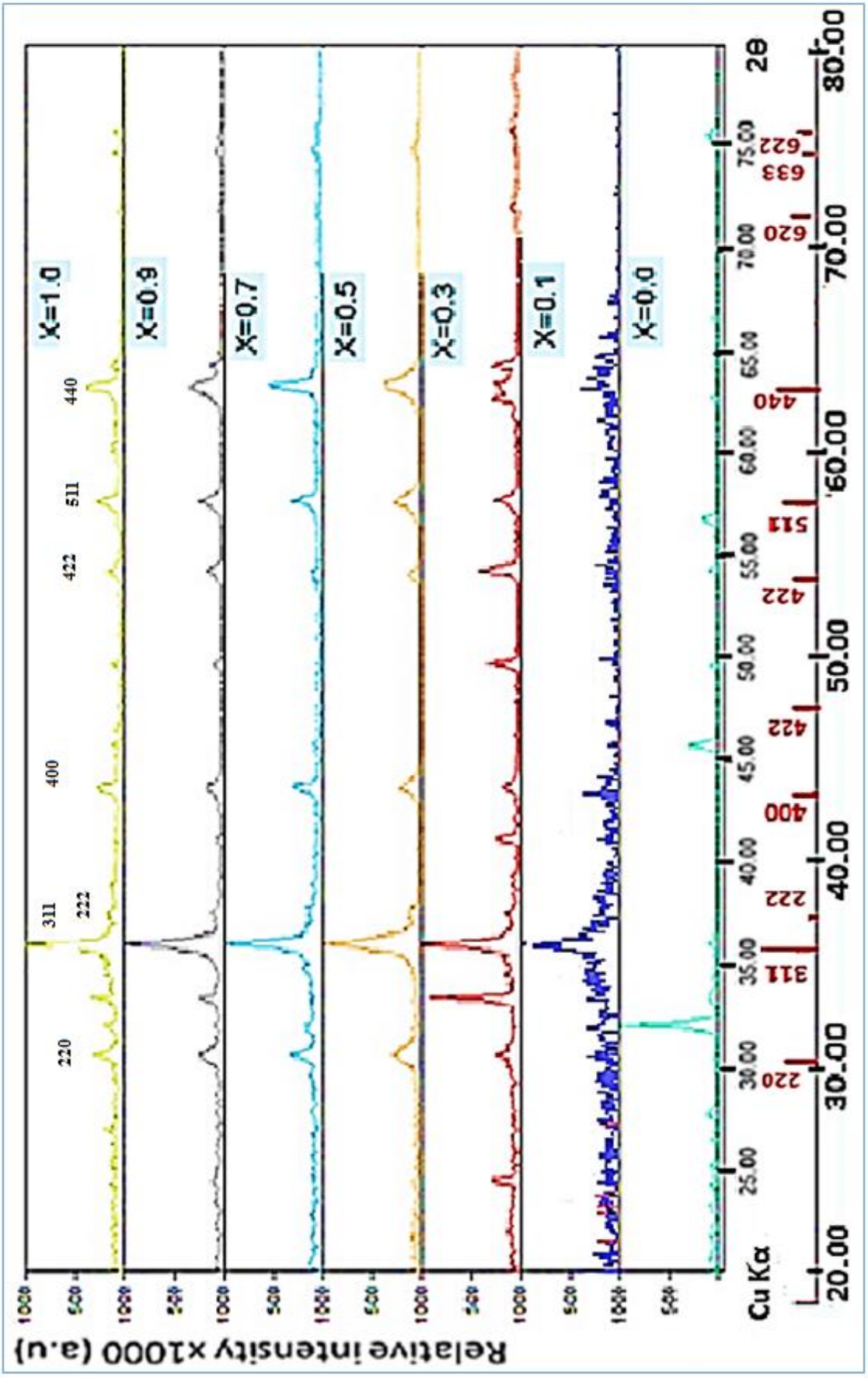

Fig.4.1 XRD patterns of the prepared Li-Ni ferrites without

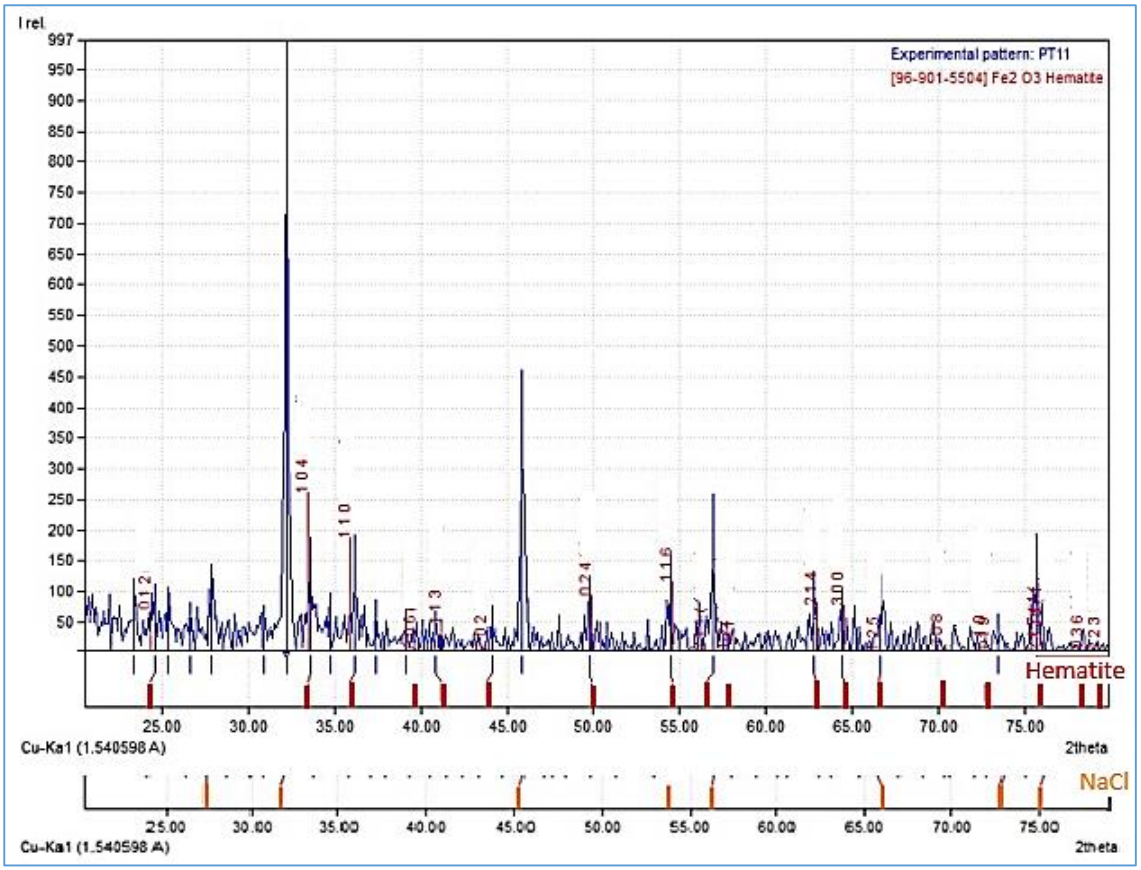

Fig 4.2 The experimental patrren of NaCl (Halite) and hematite XRD pattern formed at x=0. The spectrums of NaCl and hematite are denoted by orange and red lines within x-axis respectively.

The output results of XRD represented by the calculated lattice constant for different molar ratio x are illustrated in Fig.4.3.

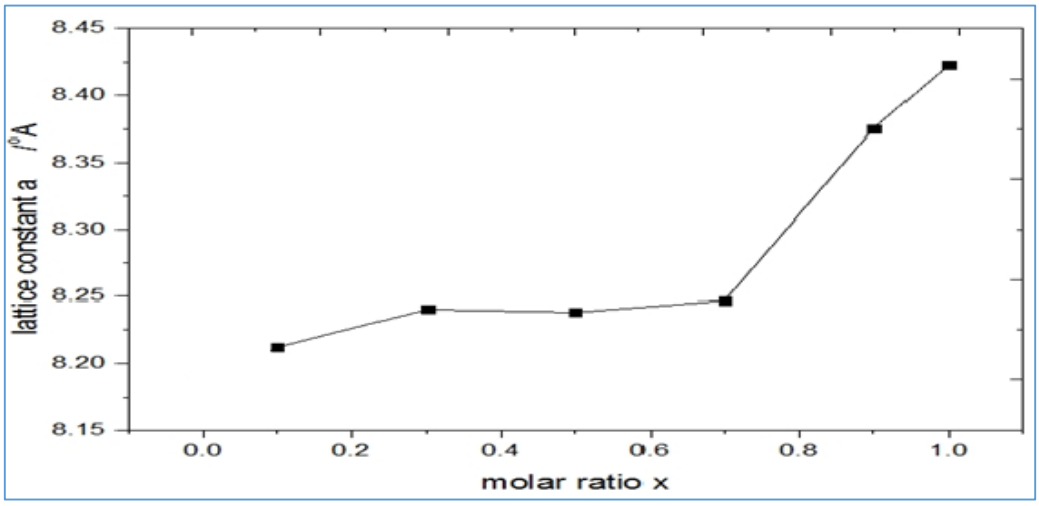

Fig.4.3. Lattice constant of prepared Li-Ni ferrites without Fe^{+2}.

These calculations were done at the most intensive peak around 36.2^0 by the following relation [29,30]:

$$a_{exp} = d_{hkl}\,(h^2+k^2+l^2)^{1/2} \quad \ldots\ldots\ldots\ldots\ldots\ldots 4.1$$

where d_{hkl} is the planes spacing and h,k, and l are miller indices. These values are in agreement with the theoretical and experimental values given by S.S. Bhatu [40] at some x values for Li Ni ferrite prepared by double sintering as given in Table 4.1, but lower than that prepared by citrate gel method [162].

Table 4.1. The theoretical a_{th} and experimental a_{exp} lattice constants [40].

Content (x)	a_{th} (nm)	a_{exp} (nm)
0.0	0.8313	-
0.2	0.8321	0.8321
0.4	0.8330	0.8303
0.6	0.8338	0.8283
0.8	0.8346	0.8258
1.0	0.8353	-

One can conclude there are two regions of lattice constant as in Fig.4.3, the first one extends from 8.21 to 8.245 Å when x increases from 0.1 to 0.7. The second region exhibits sharp increasing in range (a=8.245 -8.42 Å) at (x= 0.7-1.0). It was mentioned that the triplet ions prefer tetrahedral and divalent prefer octahedral, and the larger ion takes octahedral sites while smaller ones occupy tetrahedral sites. It is believed that the two different rates of increasing lattice constant are related to substitution of Fe^{3+} ions (0.64 Å) by Ni^{2+} ions (0.69 Å) in octahedral sites, i.e. smaller ions by larger one. Li ions (0.73 Å) stay in their sites unaffected although their concentration is lowered. On the other hand, the increasing in lattice constant can be explained according to the chemical formula of Li-Ni ferrite $Li_{0.5-0.5x}Ni_xFe_{2.5-0.5x}O_4$ so increasing Ni content means decreasing of both lithium and ferric ions concentrations and according to the ions radii it will be: $\mathbf{2Ni^{2+} \rightarrow Li^{1+} + Fe^{3+}}$

Giving that in size:

$$2x\ 0.69\ Å > 0.73\ Å + 0.64\ Å \quad \text{or } 1.38\ Å > 1.37\ Å$$

The third suggested explanation of increasing lattice constant is based on Vegard's Law that states lattice constants have a direct effect on solid solution of A and B given by [159]:

$$\mathbf{a_{A_{(1-x)}} = (1-x)a_A + xa_B} \quad \ldots\ldots\ldots\mathbf{4.2}$$

where A and B solids have the same crystalline structure. So increasing of one sublattice (like octahedron containing Ni^{2+}) will increase the lattice constant of the whole sublattice.

XRD density was calculated for samples without Fe^{2+} to understand the effect of molar ratio x on the calculated density of material as shown in Fig.4.4. The XRD density dx is given by:

$$dx = 8\ M/N_A\ a^3 \qquad \text{.....4.3}$$

where 8 is the number of ferrite molecules per unit cell, M molecular weight of structure, N Avogadro number, a lattice constant. The linear increasing of the XRD density with clear molar ratio, except the drop of density at x= 0.9 which is unknown behavior. It was obvious that as (M) increases (dx) increases, but it decreased with increasing lattice constant increasing. Here the effect of molecular weight is larger than the effect of lattice constant.

The values of (dx) are very near (slightly lower) to the values given in other references [162,163], the difference may be related to preparation conditions that encourage preferred sites which affect lattice constant.

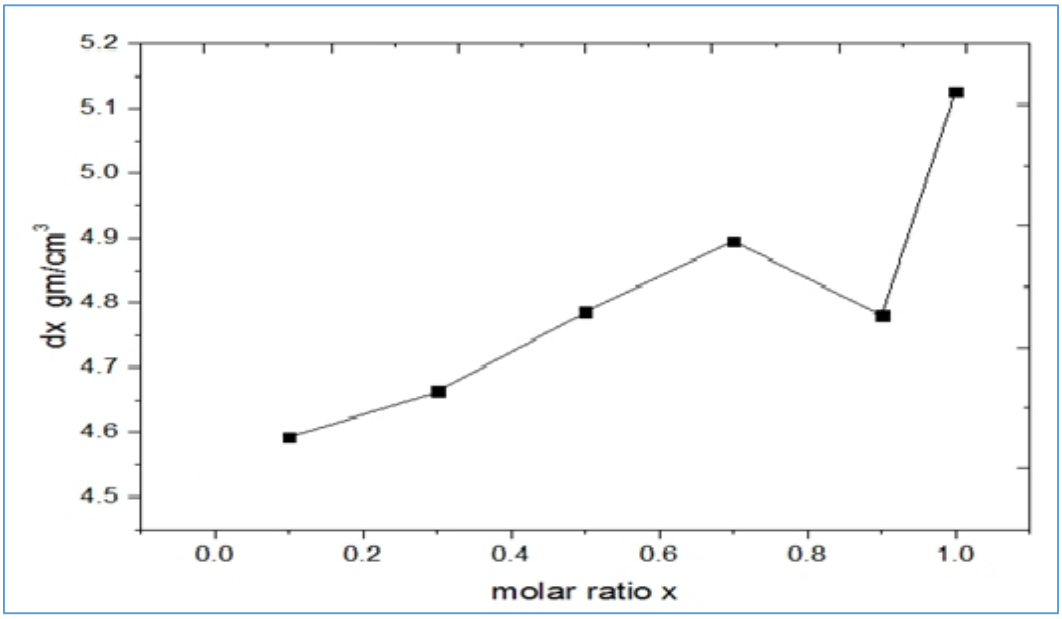

Fig. 4.4. The XRD density dx versus molar ratio x without Fe^{2+}.

4.2.2. XRD Result of Li-Ni Ferrite with Fe^{+2}.

The problem of the absent spinel ferrite phase at low molar ratio values was solved by introducing Fe^{2+} to complete the requirements of forming the ferrite structure using $FeSO_4.7H_2O$. The ratio of Fe^{3+}/Fe^{2+} was kept constant at 1.7. The result of this experimental part is demonstrated in Fig.4.5. The patterns are perfect match JCPDS reference code (00-013-0207) of Li-Ni ferrite (x=0.8) which appeared in red color within x-axis. The pattern of hematite in green color also appears within x-axis.

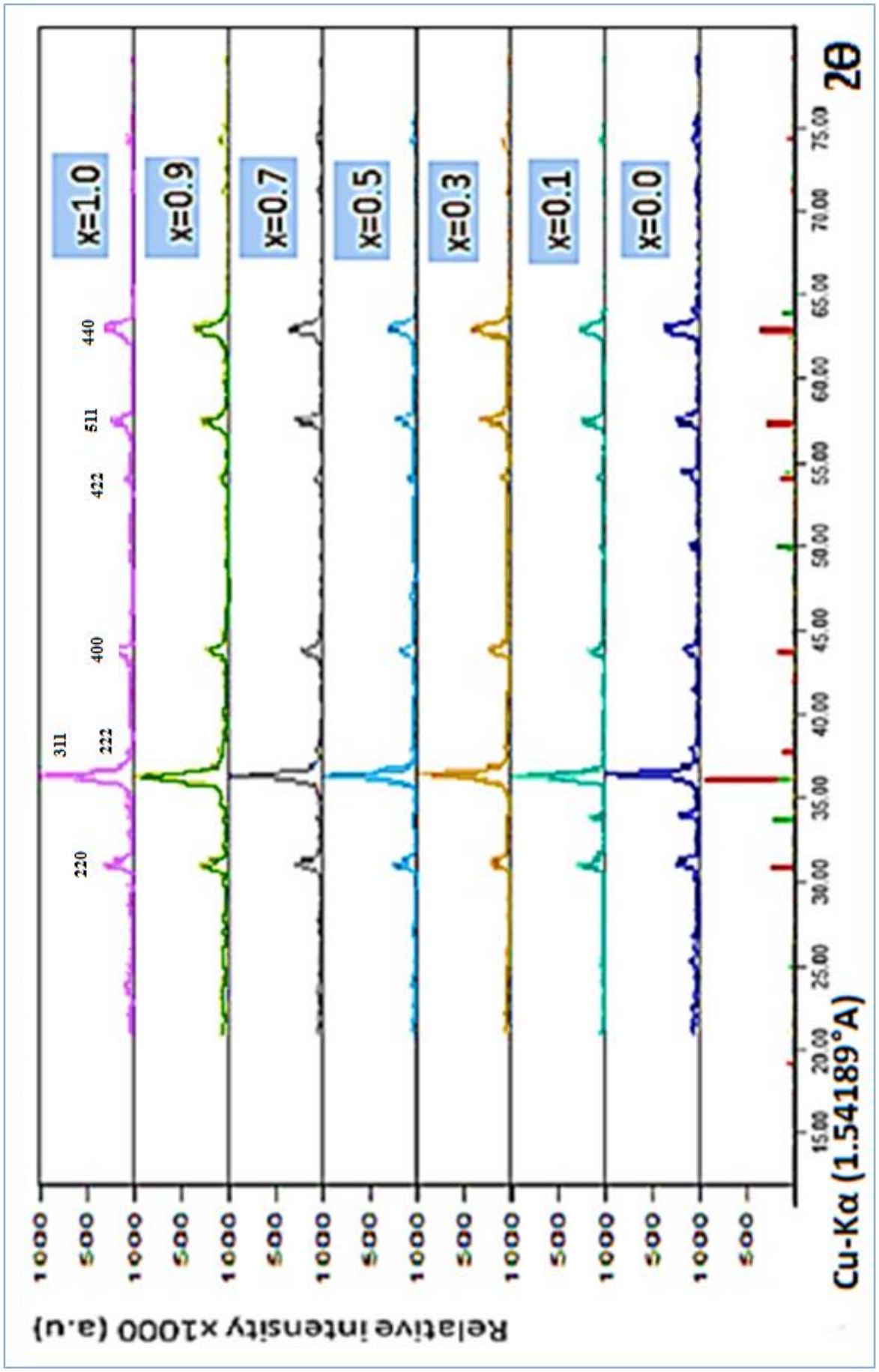

Fig.4.5. XRD patterns of the prepared Li-Ni ferrites with Fe^{+2}.

The second note is that the peak around 33.3° which is related to hematite existed at low x values (x=0 and x=0.1) and vanished at higher values. The third note is that one may recognize some slight shift of the main peak around 36.3° due to slight difference in ionic radii.

Here it was mentioned that samples without Fe^{2+} had no response to magnet before hydrothermal process. While the samples with Fe^{2+} showed high response to magnet before hydrothermal process. Also samples with Fe^{2+} had darker color than without Fe^{2+} ones. That is shown in Fig.4.6.

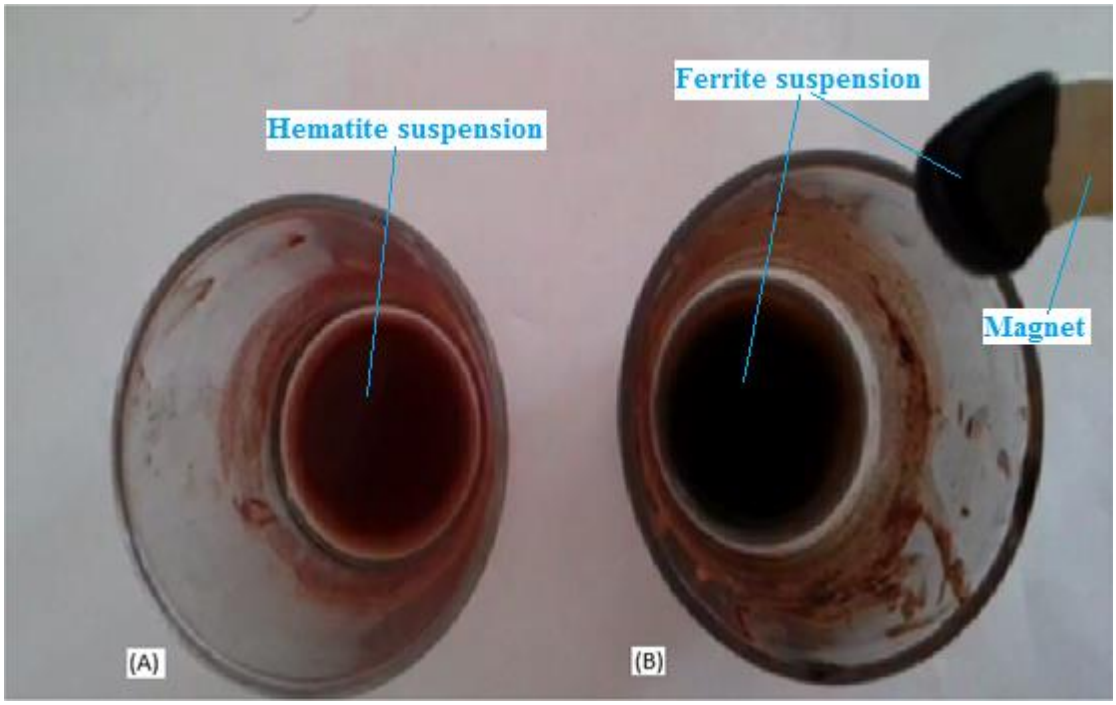

Fig. 4.6. The difference between samples in color and attraction to magnet before hydrothermal process (A) without Fe^{2+} (B) with Fe^{2+}.

Also one can note all pattern in Fig.4.1 and Fig.4.5 are broad, giving an indication that crystals are in nano size.

The lattice constant a function of molar ratio x for the samples with Fe^{2+} is shown in Fig.4.7. These results can be explained as that the lattice constant has an average value of 8.26 Å with a maximum tolerance of ±0.06 Å. In other words, the lattice constant did not change by increasing (x) and that observed variation of (a) in the figure is just a fluctuation around constant value which is 8.26 Å. This may be related to high presence value of Fe^{2+}. On the other hand, one can say there is a general behavior of a slight increasing in lattice constant with increasing x, this what is denoted by dashed red line in the figure. The presence of relatively large amount of Fe^{2+} with respect to Li^{1+} as well as may limit lattice

constant from being larger. The presence of Fe^{2+} usually has a complex effect on cations distribution [17]. The Fe^{3+} (smallest ion) and Fe^{2+} (large ion) are both decreased with x (Ni^{2+}) increasing.

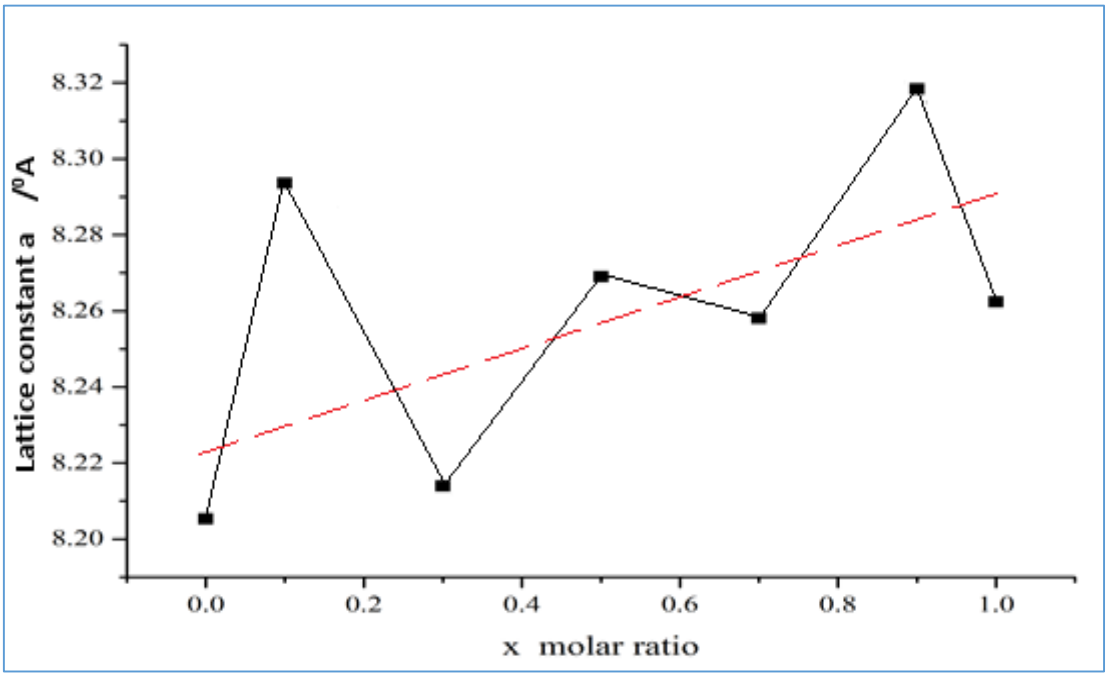

Fig.4.7. Lattice constant of Li-Ni ferrite with Fe^{2+} as a function of molar ratio. The dashed line represents the suggested fitting values.

The XRD density of samples with Fe^{2+} is shown in Fig.4.8. These results exhibit that the rate of density increasing is lower than that for samples with Fe^{2+}. This rate is enhanced at higher (x) values, this is related to increasing of the Ni^{2+} role, being more apparent compared with Fe^{2+}.

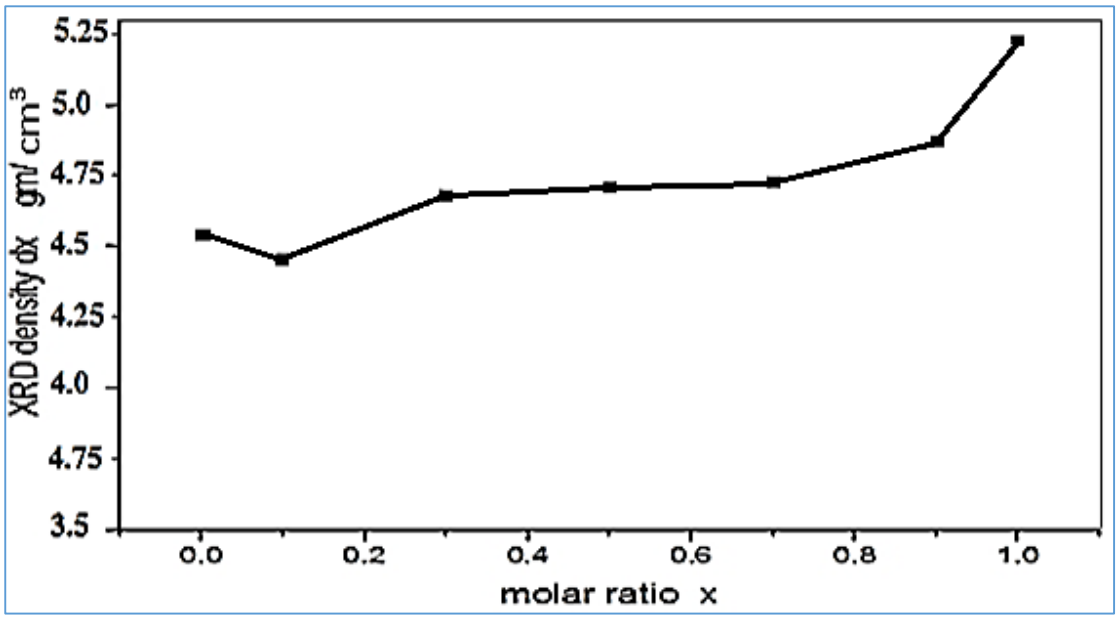

Fig .4.8. The XRD density of prepared Li-Ni ferrite with Fe^{2+}.

The ferrous ion size is 0.08 nm, it is largest of all used cations. This may explain the small varying of lattice constant around 8.26 Å and the semi stability of XRD density unless for high content of Ni^{2+}. These values are lower compared with values given in other references [162.163] that may be due to preparing method which enhances lower or bigger lattice constant.

4.2.3. Crystallite Size Calculations

The Debye-Scherrer formula gives average crystallite size L by [161]:

$$L = \frac{0.9\,\lambda}{\beta cos\theta} \qquad \text{.....4.4}$$

where 0.9 is a constant related to shape of crystallite (typically is 0.9), β is FWHM of the XRD peak in radian, cosθ calculated from 2θ axis at maximum of the XRD peak, 2θ can be in degree or radian, λ=0.150456 nm [161]. The calculations were done for samples which have Fe^{2+} ions and others without Fe^{2+} ions for plane (311) around 2θ=36.2° which is the most intensive peak in spinel ferrite.

The average crystallite size results from the samples without using Fe^{2+} are shown in Fig.4.9. The behavior is very clear and smooth via reaching a minimum size 17.9 nm at (x=0.5) and maximum at (x=0.1) and (1.0).

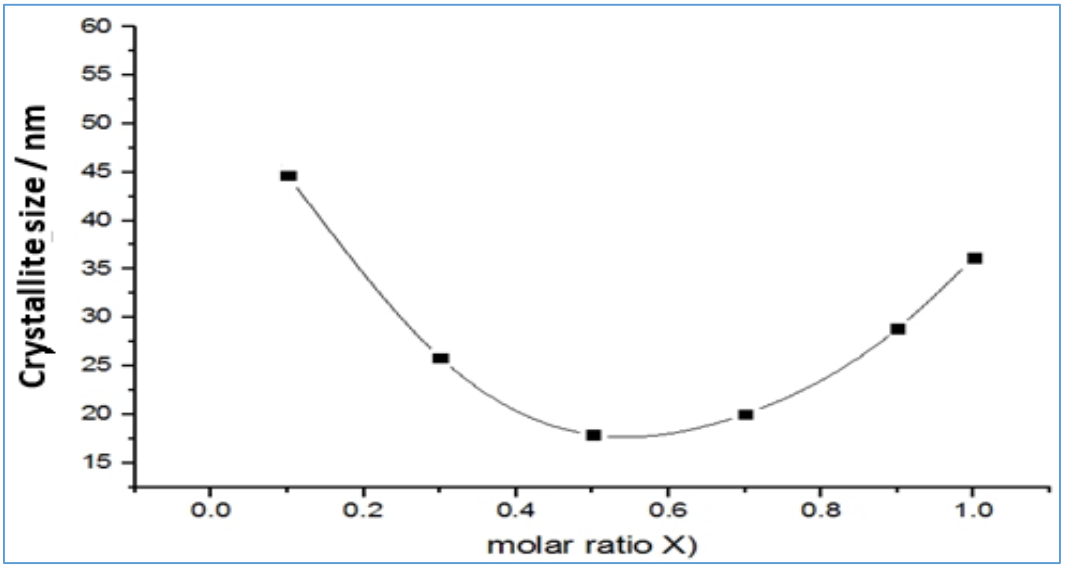

Fig.4.9. Average crystallite size versus molar ratio of samples without Fe^{2+}.

It was believed that the increasing of (x) or Ni content leads to increasing in the nucleation centers. In other word, more crystals and so smaller size are due to consumption of solution by larger number of

crystals. This continue until reaching (x=0.7), but when x increased more than 0.7 the excess Ni ion content leads to enhance the growth rate after the nucleation rate being saturated. This mechanism depending on observation of XRD pattern, when the spinel ferrite formation phase is improved with x value increasing.

The behavior of samples with Fe^{2+} is quite different as shown in Fig.4.10 and remains nearly constant to (x=0.7). The crystal size was got maximum at (x=0.3). Here we believed that the nucleation rate is nearly constant due to the constant presence of Fe^{2+} with respect to Fe^{3+}.using Fe^{2+}.

Increasing of (x) from 0 to 0.1 values leads to increase crystallite size from 15 nm to 32.7 nm. The growth rate is higher due to increasing of Ni ion content that enhances growth of Li-Ni ferrite. The nucleation has negligible effect due to presence of Fe^{2+} ions. There is nearly a constant crystallite size at ($x \geq 0.3$) which might be due again to more nucleation producing or the existence of $NiCl_2.H_2O$ which might enhance the crystalline growth.

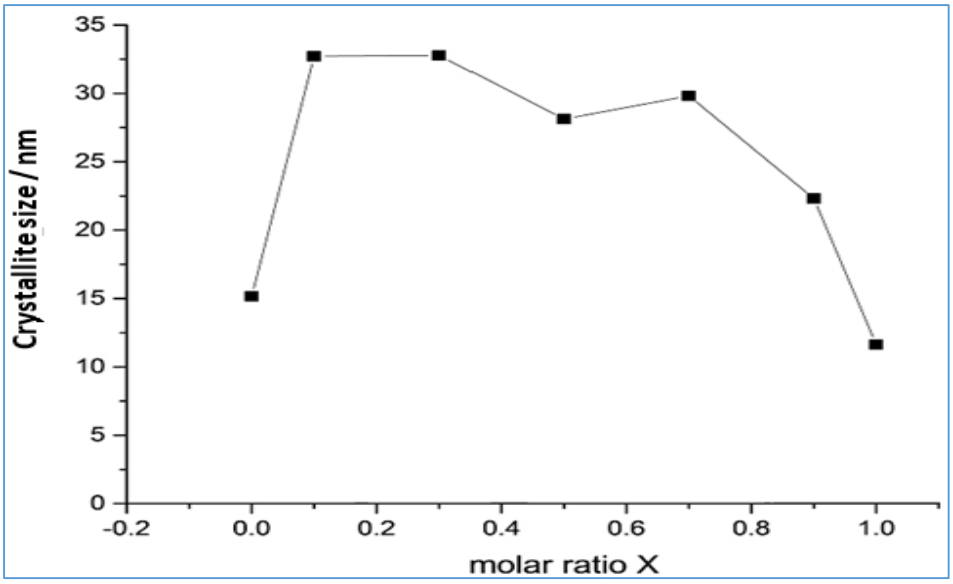

Fig.4.10. Average crystallite size versus molar ratio of samples with Fe^{2+}.

The crystallite size of the prepared samples in general is lower than other ferrite prepared by hydrothermal method of Ni ferrite [164], nearly equal to magnetite [165] and lower than that of Zn Mn ferrite [166], but larger than that of Ni ferrite (microwave hydrothermal) [167] and is smaller than that of Li ferrite [166-170]. Of course these differences are related to the differences in chemical composition and starting material as well as preparation conditions and presence of Fe^{2+}.

4.2.4. Results of FTIR Test

FTIR spectroscopy can sense the existence of octahedral and tetrahedral sites in the structure via absorption or transmission bands. The absorption of vibrational bands in ferrites is known as υ_1, υ_2, υ_3 and υ_4. The major bands υ_1 and υ_2 are confined in the range 350-600 cm^{-1}. The lower band is related to vibration of ions in octahedral sites whereas the higher band related to vibrations of ions in tetrahedral sites [29,30]. The samples with Fe^{2+} ions have no bands at wave number larger than 600 cm^{-1}as shown in Fig.4.12, in contrast to some samples without Fe^{2+} as shown in Fig.4.11.

There are two bands υ_1 and υ_2 around 590 cm^{-1} and 390 cm^{-1} respectively due to the bond length as shown in Fig.4.11. There is a shift in the peak at 590 cm^{-1} beginning from 563 cm^{-1} to 605 cm^{-1} with increasing molar ratio x. Although the shift is not regular generally, one conclude there is a shifts toward high wavenumber in tetrahedral band and toward lower wavenumber in octahedral band. These may be as a result of substitution B-site ions (Li^{1+}) by Ni^{2+} which makes O^{2-} tend toward new ion because low force constant (weak bond). The opposite happens at tetrahedral site.

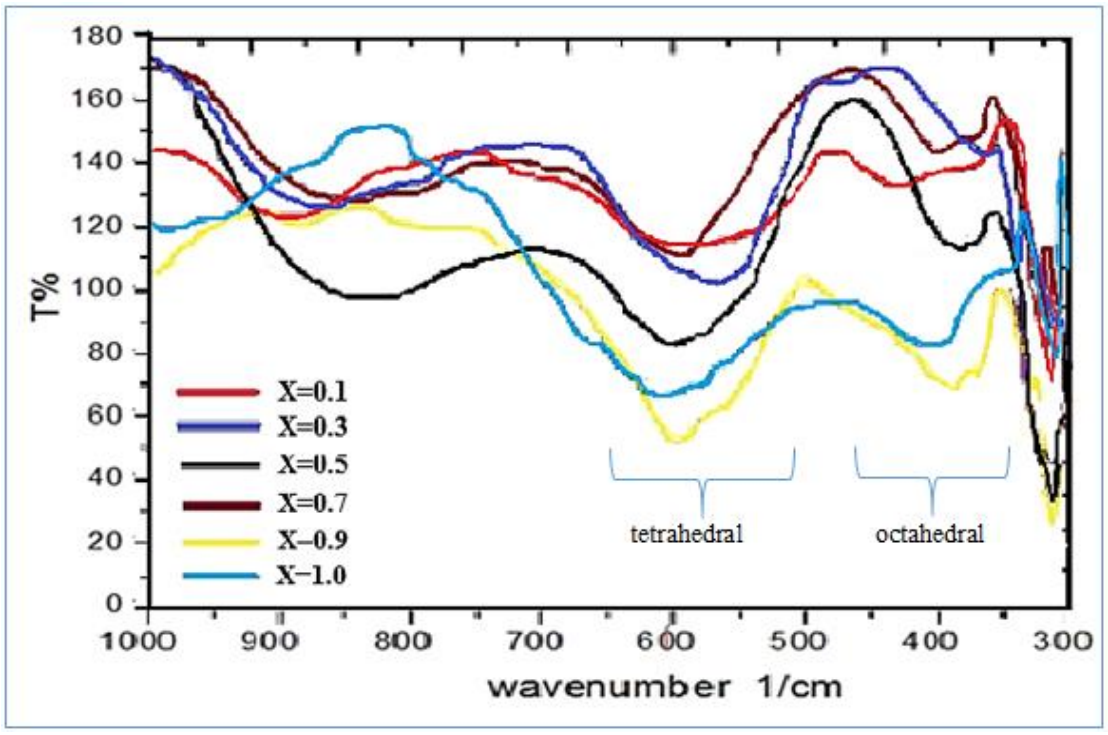

Fig.4.11. FTIR spectrums of prepared Li-Ni ferrite without Fe^{2+} for different molar ratios (x).

This gives an indication to cations distribution according to following expression suggesting inverse spinel structure:

$$(Fe^{3+}{}_{(2.5-0.5x)/2})[Li^{1+}{}_{0.5-0.5x}\,Ni^{2+}{}_{x}\,Fe^{3+}{}_{(2.5-0.5x)/2}]O_4$$

The multiplying by 1/2 is based on the fact that the number at octahedral cations is equal to that of tetrahedral cations.

There is a second weaker band at about 850 cm^{-1} that is believed to indicate the presence of intrinsic A-site vibration [160]. The results of FTIR analysis of Li-Ni ferrites in presence of Fe^{2+} are illustrated in Fig.4.12. The two bands are located nearly at the same band positions of samples without Fe^{2+}. The shift also is maximum for middle x values to lower wave numbers. While the bands are shifted to high wavenumbers for other low and high x value, that means a minimum A site – O bond length was at x around 0.5.

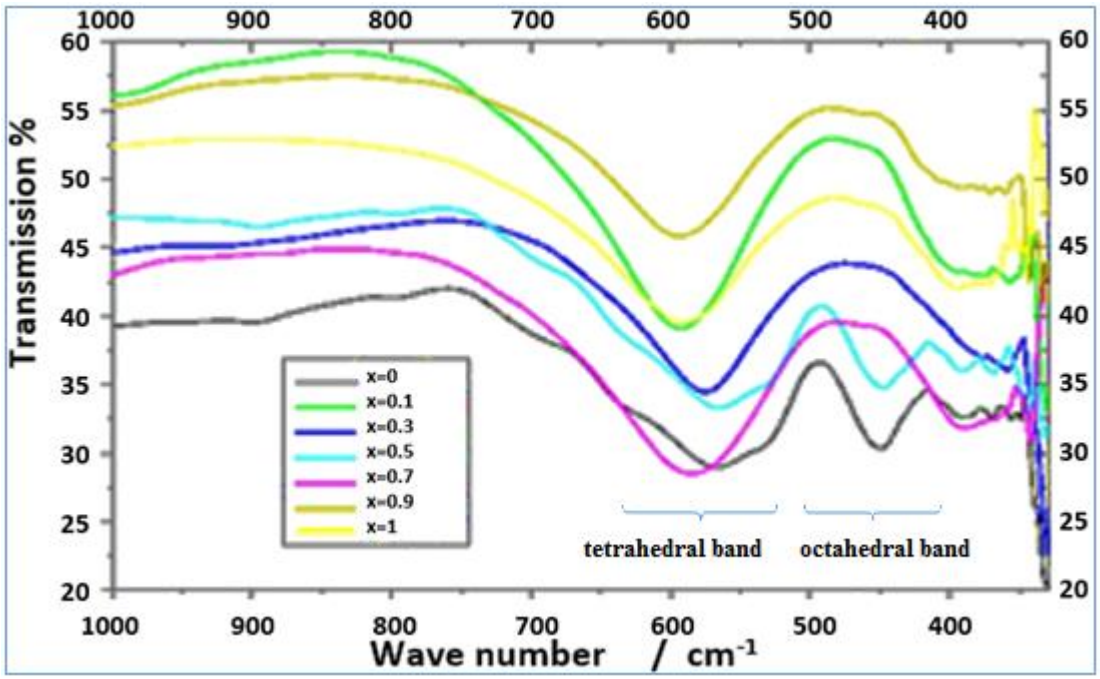

Fig.4.12. FTIR spectrums of prepared Li-Ni ferrite with Fe^{2+} at different molar ratios of x.

4.2.5. SEM and TEM Microscopy Tests

a. The Morphology of Nanoparticles

The analysis of SEM and TEM microscopy was done to investigate the particles size distribution and particle shape. The EDX analysis was used to confirm the ionic ratio in the mixture. The images of SEM for the sample powder prepared with Fe^{2+} ions at (x=0) without Fe^{2+} at x=0.1 are shown in Fig.4.13 (a) and (b) respectively. Three different particles shapes were recognized by using SEM and TEM microscopies: nanorods, nanocube, nanosemisphere, and micro flakes as shown in Fig.4.13 and Fig. 4.14.

It is clear that the predominant particles have spherical shape for samples with Fe^{2+} ions as in Fig.4.13 (a). Whereas the predominant particles were the nanorod for the sample prepared without Fe^{2+} ions at (x=0.1) as in Fig.4.13 (b).

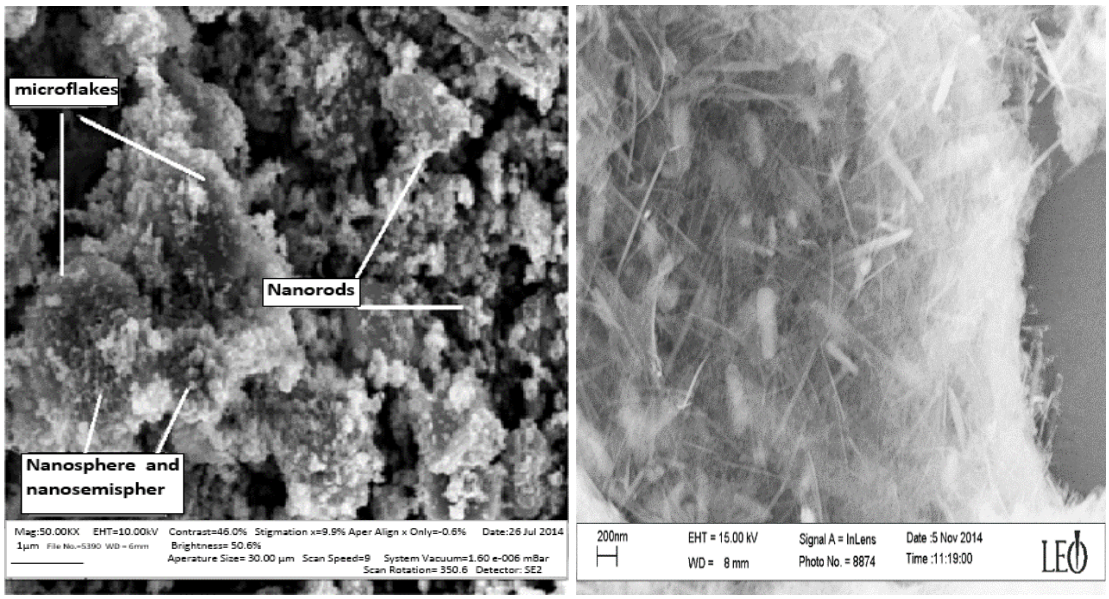

(a) (b)

Fig.4.13. Particles shapes. (a) SEM image at x=0 with Fe^{2+}, the bar length=1µm. (b) SEM image without Fe2+ at x=0.1.

The images of TEM in Fig.4.14 (a) and (b) for the samples with and without Fe^{2+} ions show these different nanostructures.

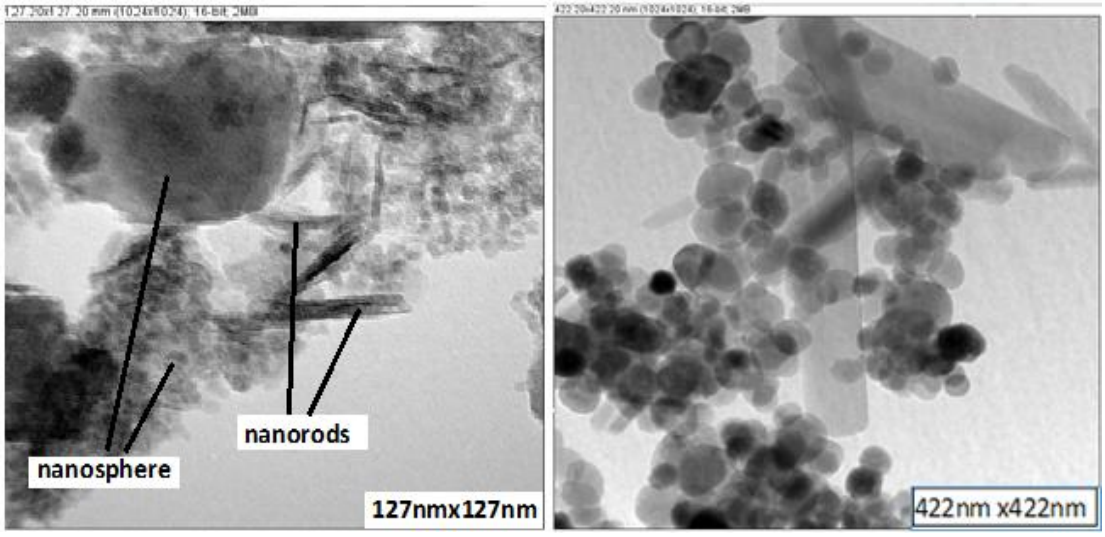

(a) (b)

Fig.4.14. Particles shapes. (a) TEM image at x=0 with Fe^{2+}. (b)TEM image at x=0.9 without Fe^{2+}.

It was considered that the rods dominated at high x values are smaller in size and have low concentration as seen in Fig.4.14 (b). One can note from 4.13(b) and 4.14(a) the rods may be bended especially at low diameter at high aspect ratio. The low concentration of nanorods existence at high x values is believed due to ferrites, this is proved by electron diffraction as shown in Fig.4.15 (a) and (b).

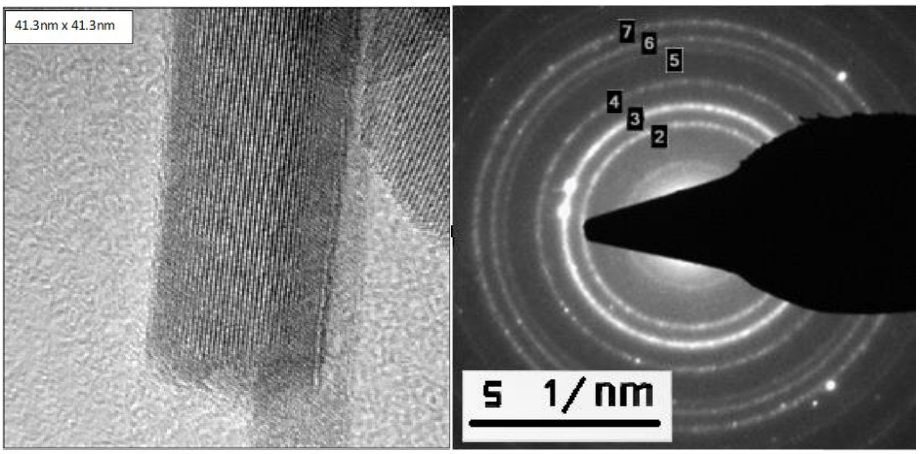

Fig.4.15. (a) HRTEM image of ferrite nanorod. (b) Electron diffraction of Li Ni ferrite nanorod.

The diameter of these nanorods ranging from 10 nm to 65 nm and the length is from few hundred nanometers to few microns. It must be mentioned that, all samples without Fe^{2+} except those at low x, have the predominant particles as spherical or semispherical shape. The microflakes had low concentration but large size (in micrometer range), they contain aggregation of few microns particles.

Nanocube also observed in all investigated samples, which they were related to spinel structure as shown in the HRTEM image in Fig.4.16 (a).

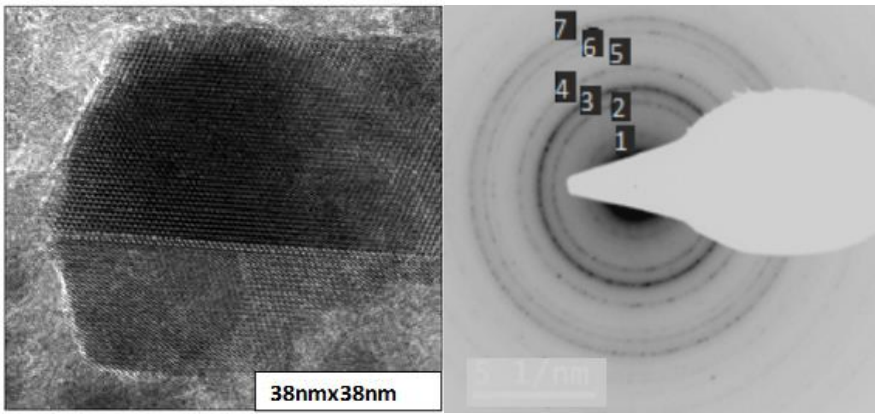

(a) (b)

Fig.4.16 (a) TEM image at x=0.7 without Fe^{2+}. (b) Electron diffraction of ferrite nanocube at x=0.7.

This cube is related to spinel structure of Li-Ni ferrite. The electron diffraction of that cub is illustrated in Fig.4.16 (b). The diffraction rings is denoted by 1, 2, 3, 4, 5, 6 and 7. These ring numbers correspond to the planes (111), (220), (311), (222), (400), (422) and (511) respectivily. The contrast in rings intensity can be noticed easily, where miller indices for 311 are still the strongest one as was observed by XRD.

In general, the most particles aggregated in large clusters each one contains hundreds of particles. The tendency of particles for agglomeration is connected to high surface energy of nanoparticle, besides the magnetisms of nanomagnetic materials, as shown in 4.14b and 4.17b.

Different nanostructures also appeared in Zn ferrites and Ni ferrites prepared by co-precipitation [171]. Comparing the result of Fig.4.13 (B) with results of Ni ferrite prepared by hydrothermal method given by other researcher [50], shows that the same intensive plane at (311). Aggregation of particles also appears in Li-Ni ferrites prepared by citrate gel autocombustion method but with larger particle size [162].

b. The Particle Size Distribution

The particle size distribution analysis was done by SEM and TEM for some samples. Several images (5 to 10) were used for each sample to measure particles sizes, the sizes are divided in ranges, each range has width of 10nm. Then the sum of counts for each range for all image is summed to give a total number for each range of such sample, these calculation were done by using ITEM, Image-J and DM3 reader plugin software. Fig.4.17 (a) and (b) represent examples of TEM and SEM image of particles clusters used for particle size distribution calculation.

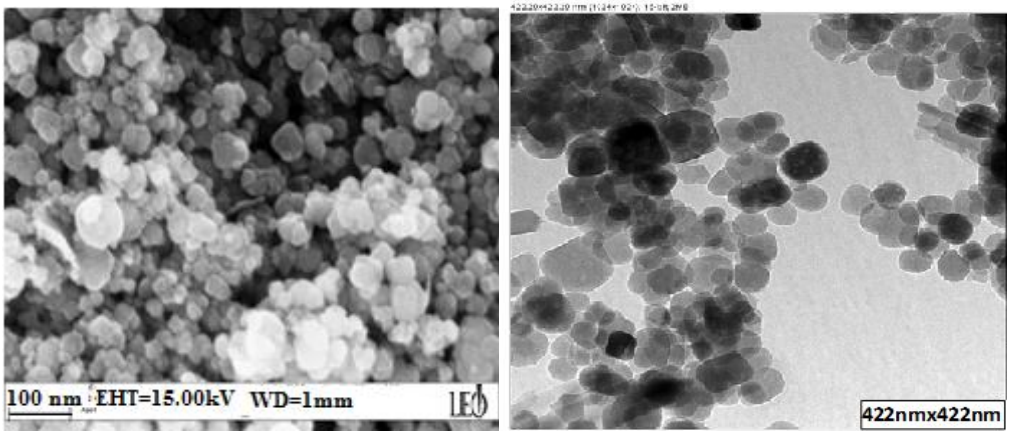

(a) (b)

Fig.4.17. (a) Cluster image by TEM at x=0 with Fe^{2+}. (b) Cluster image by SEM used for, bar length=100 nm, at x=0.5 with Fe^{2+}.

A histogram curve of particle size distribution of sample with Fe^{2+} is shown in Fig.4.18. All samples which have average size confined in range from (10 -30 nm) shown in Fig.4.17. There was a fair proportion of particles out of this range especially larger than 30 nm. One can notice that the distributions are non-symmetric around the peak value, and the distributions extend more to higher particles sizes.

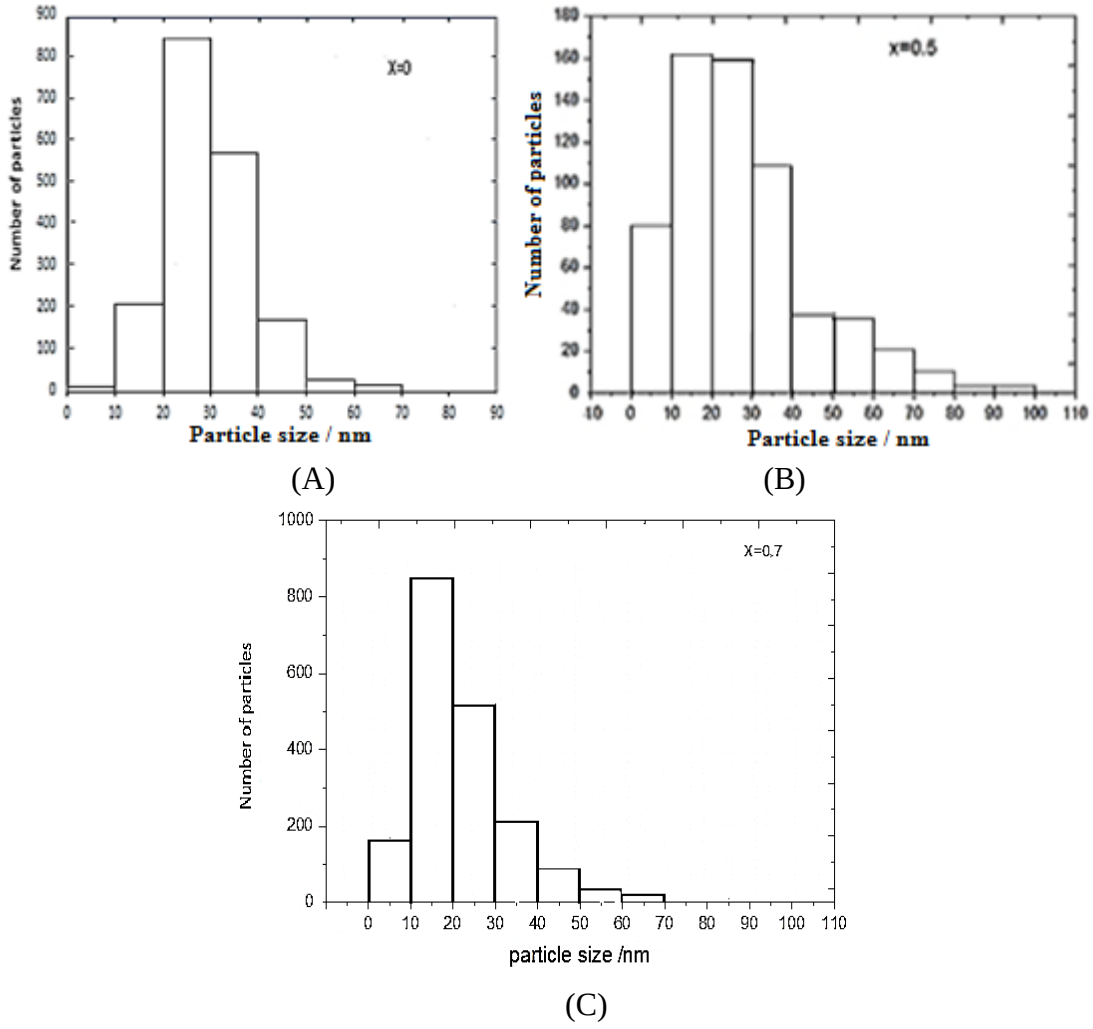

Fig.4.18. Particle size distribution of samples with Fe^{2+}, at (A) x=0, (B)x=0.5, (C)x=0.7.

The same features of average particle size and asymmetric of the distribution around maximum are repeated again in Fig.4.19. In general, the distribution of samples without Fe^{2+} ions is not as sharp as samples with Fe^{2+} besides it is somewhat boarder. That is believed due to Fe^{2+} which encourages nucleation and that in turn lower the competition in growth for different and large sizes. Comparing crystallite size with particle size gives that crystallite size is equal, or somewhat larger than average particle size. That result leads conclude that most of particles contain one crystal, but

also there is a good number of particles which contain more than one crystals.

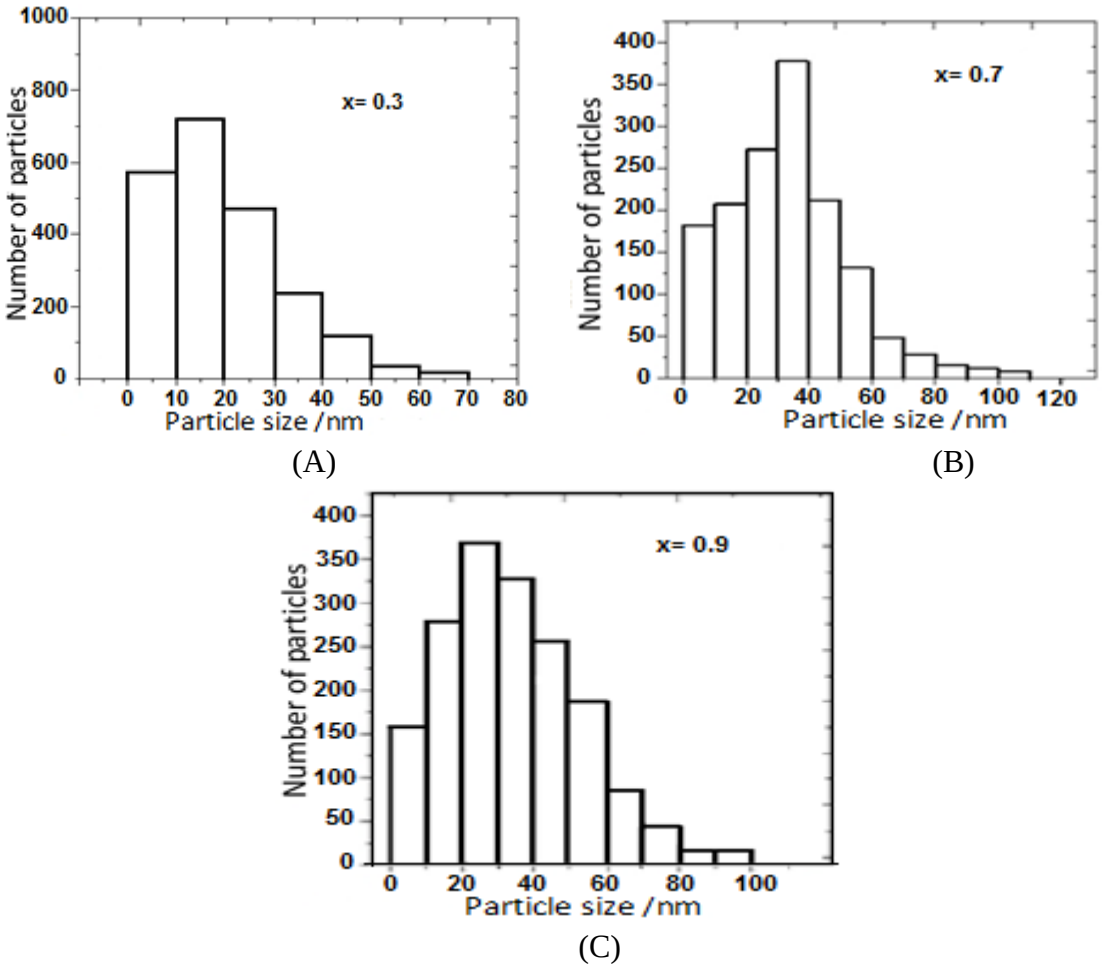

Fig.4.19. Particle size distribution of samples without Fe^{2+}, at (A) x=0.3, (B) x=0.7, (C) x=0.9.

The prepared particles have broader distribution than that of other researchers for Ni ferrite [172], and other ferrites [173-176].

4.3. Magnetic Properties Results

Hysteresis loop had been done to conclude the main magnetic parameters to determine the magnetic properties of samples with and without Fe^{2+}.

4.3.1. General M-H Loop

The magnetization-applied magnetic field loops of samples without Fe^{2+} are shown in Fig.4.20. The samples having medium values of x (0.3, 0.5 and 0.7) show normal soft loop with very small coercive field, while the others show unsaturated curve. This behavior might be related to

multiphases which are ferrites and hematite at lower x values, superparamagnetic state and redistribution of cations at high values.

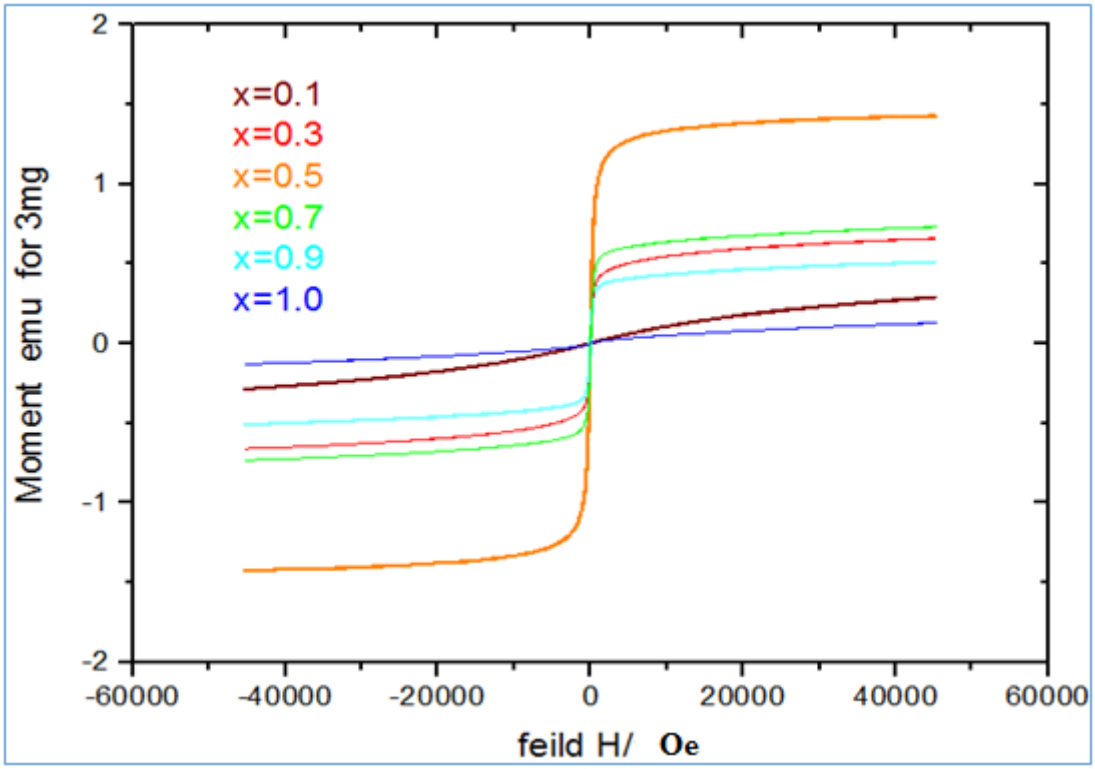

Fig.4.20. Hysteresis loops of Li-Ni ferrites samples without Fe^{2+}.

The XRD patterns at high x values eliminate the probability of existence a multiphases and support the supposition at low x values. So it was believed that cations redistribution or superparamagnetic state may responsible for this behavior. When x increases Ni^{2+} ions occupy octahedral sites as mentioned before depending on ionic radius, electronic configuration and electronic energy in spinel lattice, according to Hund's rule and forming inverse spinel structure. When Ni content (x) exceeds 0.5 it begins to push Fe^{3+} to occupy tetrahedral sites leading to opposite moments at octahedral sites. Subsequently the material going to be paramagnetic like. The FTIR results and lattice constant changing from decreasing to increasing may support this assumption.

The magnetic hysteresis loops of samples with Fe^{2+} are shown in Fig.4.21. The samples have generally similar soft magnetic loops. It is believed that all samples have superparamagnetic behavior depending on the s-shape of the loops. This should be nearly associated with coercivity (<10 Oe) and particle size (<30 nm) [177].

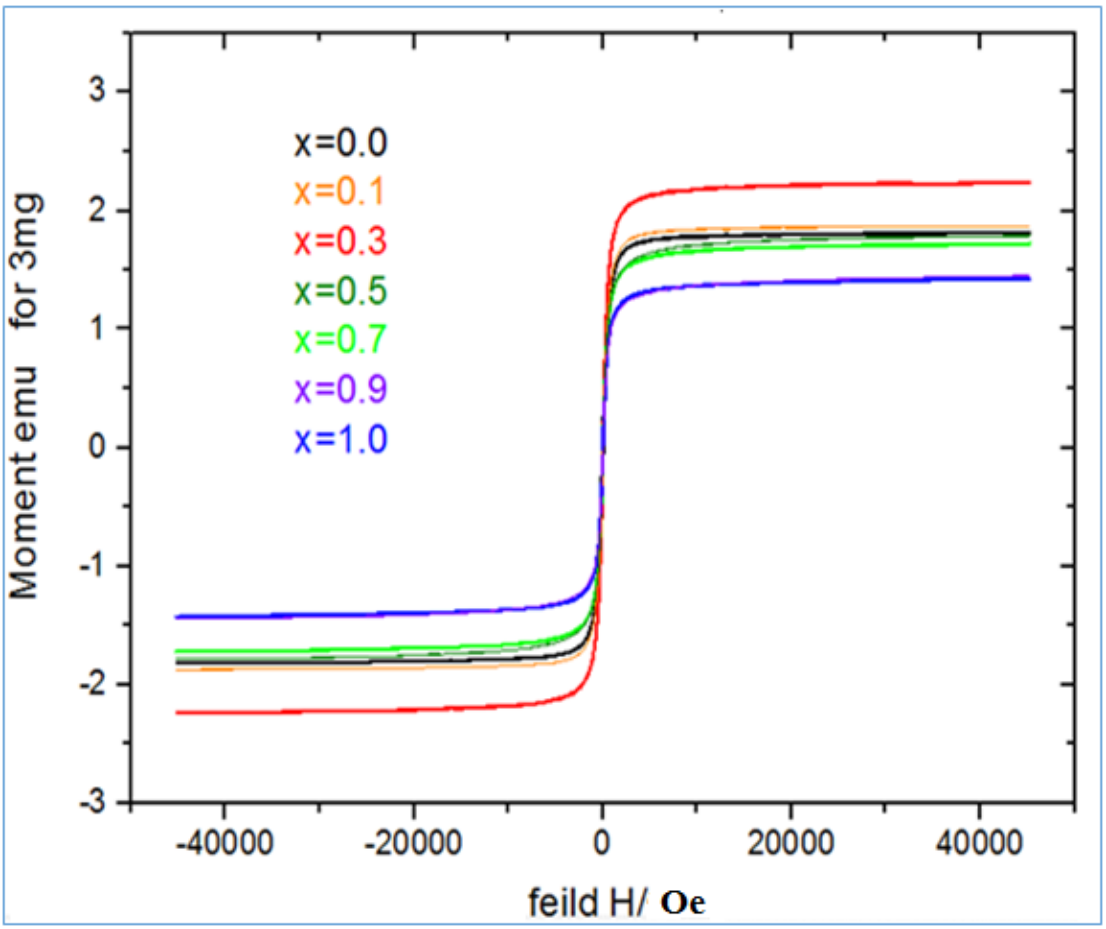

Fig.4.21. Hysteresis loops of Li-Ni ferrites samples with Fe^{2+}.

4.3.2. Coercivity

The precise investigation of the loops leads to determine the magnetic parameters. One of them is the corecivity which is shown in Fig.4.22. The figure indicates variation of coercivity with molar ratio x for samples without Fe^{2+}. The increasing of Ni content (x) at low x values produces decreasing in H_c, that is due to th decrease in crystallite size (more grain boundaries) as mentioned before in Fig.4.9 respectively. The second probable reason for dropping H_c within (x) range (0.1-0.3) depends on Table1.2. The Ni ferrite has lower crystalline anisotropy (K) than Li ferrite. The H_c parameter is related to K by the equation $H_c=2K/M_s$, so lower K means lower H_c [178]**.** The third reason that is believed behind that might be related to Yafet-Kittel effect or spins canting [179]. It means that spins are tilted by a small angle about their axis rather than being exactly co-parallel of Fe and Ni ions by Li ions. The fourth reason is related to existence of multiphases material (ferrite and hematite) and their direct and indirect influence to magnetic properties.

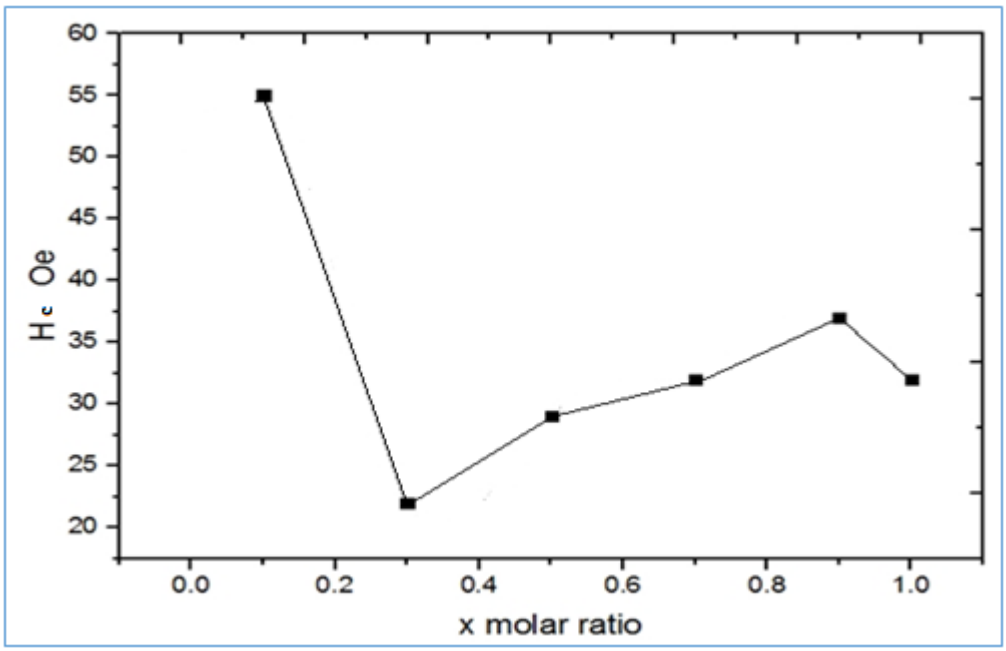

Fig. 4.22. Coercive force versus molar ratio x for samples without Fe^{2+}.

When (x) is increases more than 0.3, H_c increases by nearly a linear proportion. The increasing in H_c is due to cations distribution which tends to enhance B-B and A-B interactions which is stronger than A-A interaction, causing increase in of crystalline anisotropy constant. Another reason is thought associated with eliminating spin canting effect as result of reducing Li ion content. Remembering that Ni^{2+} has better orbital contribution to moment than Fe^{2+} that is responsible for the interactions.

A quick look at the results of samples with Fe^{2+} in Fig.4.23, shows that these results are similar to samples without Fe^{2+}.

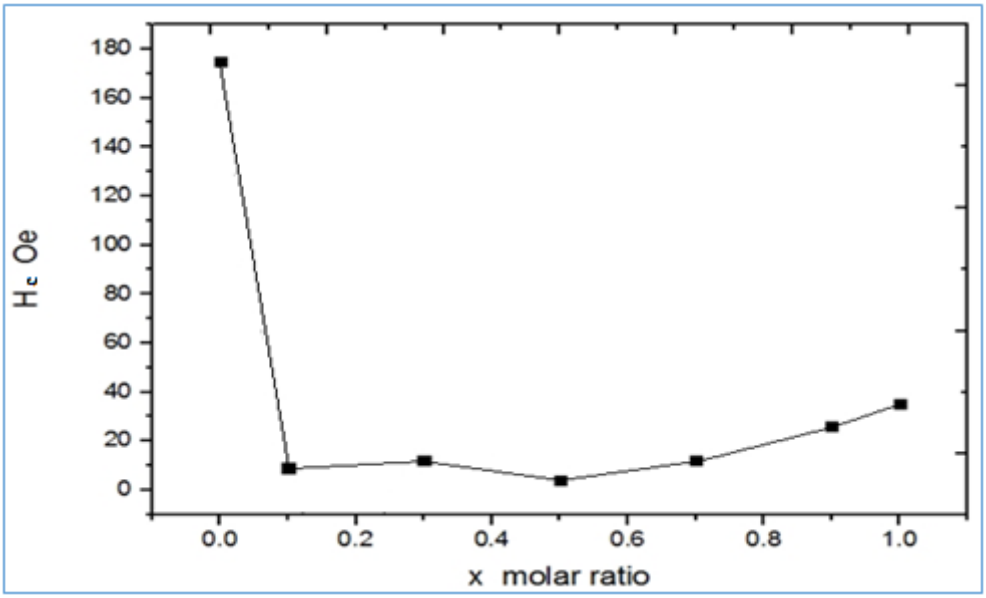

Fig.4.23. Coercive force versus molar ratio of samples with Fe^{2+}.

The difference is that samples with Fe^{2+} had high value of H_c at x=0. It was believed that high value is due to pure phase of Li ferrite due to presence of Fe^{2+}. There are other parameters which have direct effect on determination of H_c especially for nanomagnetic material at low x values, which is represented by particle size and crystallite size (grain boundaries). The effects of these two reasons or factors, in general, are believed to have no high impact on H_c in this case. The particle size is comparable to critical size of superparamagnetic that is mentioned previously so the effect of grain boundary is negligible. Besides the crystallite size behaves in a different manner for the two sets of samples corresponding to H_c which has same behavior for the two sets. The nano size still confine H_c in the low range of values.

All prepared samples have lower H_c values prepared compared with other samples prepared by sol-gel [180], but very near to that prepared by double sintering [32], lower than that of prepared by ceramic method at x=0.25[181], lower than the samples prepared by CVD as a single crystal Li ferrite and Ni ferrite [182], lower Li ferrite prepared by PLD [65], lower than Li-Ni ferrite prepared by rheological phase reaction [29], and higher than sol-gel Ni-ferrite [52]. The differences in results are related to difference in composition, particle size and other preparation conditions.

4.3.3. Magnetic Remanence, Saturation Magnetization and Initial Mass Susceptibility

The rest of magnetic parameters extracted from hysteric loop are magnetic remanence M_r, saturation magnetization Ms and initial mass susceptibility χ_i. The results of these parameters are illustrated in Fig. 4.24, Fig.4.25 and Fig.4.26 respectively for samples without Fe^{2+} ions. It can be recognized simply the manner of variation with x of these parameters is similar to each other. When x varies from 0.1 to 0.7, there is a maximum value of these parameters at (x= 0.3) for M_r and at (x=0.5) for M_s and χ_i.

The values of saturation magnetization for ferrite samples nanoparticles are lower than that of the bulk samples (55 emu/g)[183]. Smit and Wijn [177] reported that M_s is equal to 50 emu/g for bulk nickel ferrite particles. The magnitude of M_s is about 3 times larger than that of Li-Ni ferrite prepared by sol-gel [184], and lower than that of Ni substitute Li-Mg ferrite by ceramic method [181], and it is larger than that of Li-Ni ferrite by ceramic method [185].

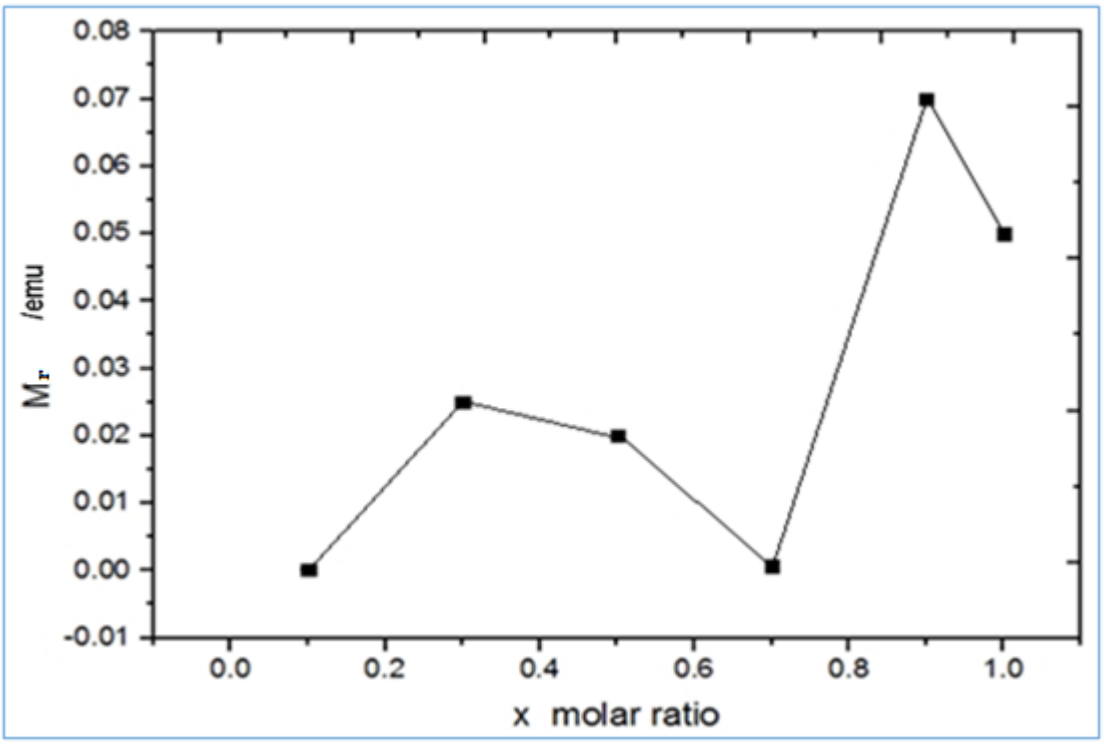

Fig.4.24. Remenance magnetization M_r versus molar ratio for samples without Fe^{2+}.

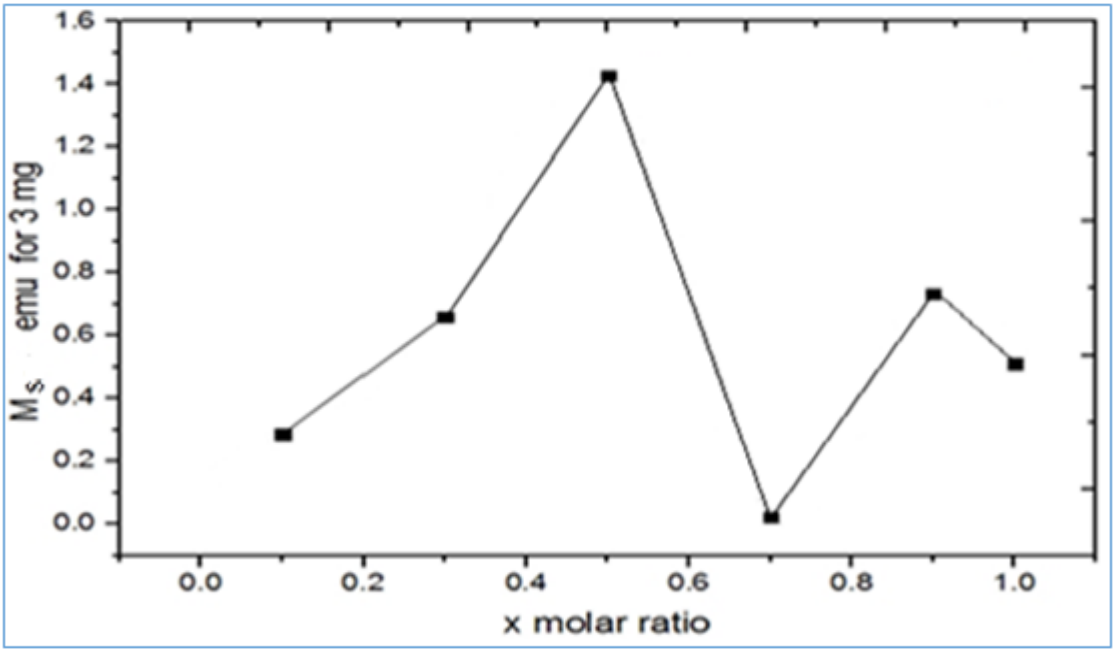

Fig.4.25. Magnetization saturation M_s as a function of molar ratio variation for samples without Fe^{2+}.

It is well known that Fe^{3+} and Ni^{2+} ions concentration and their distribution are responsible for magnetism of samples without Fe^{2+}. It was stated previously that the Ni^{2+} and Li^{1+} ions prefer octahedral sites and Fe^{3+} distributed over octahedral and tetrahedral sites. It was considered that

as Ni^{2+} ion concentration (or x) was increased it occupied octahedral sites (B-site) instead of Fe^{3+} and Li^{1+}. This consideration supports our previous supposition about lattice constant increasing.

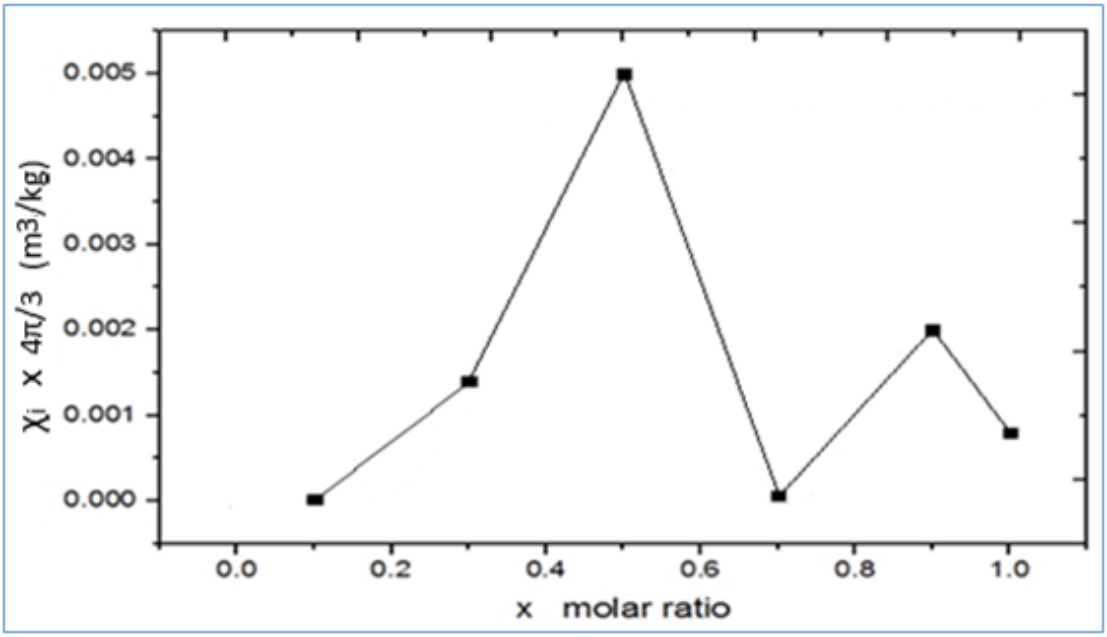

Fig.4.26. Initial mass susceptibility as function of molar ratio x for samples without Fe^{2+}.

The substitution will be accompanied by migration of Fe^{3+} from octahedral site to tetrahedral site. The samples without Fe^{2+} exhibited increasing in M_s when x was increased from 0.1 to 0.5 which is related to that of the substitution of nonmagnetic Li^{1+} cation by magnetic Ni^{2+} one according to Neel theory[20]. It can be concluded that the concentration of opposite moments of Fe^{3+} at tetrahedral sites of ferrite structure results from substitution and will not stabilize increasing of M_s, due to its low value. The theoretical effective magnetic moment is given in terms of number of unpaired electrons n and Bohr magniton as:

$$\mu_{eff} = \sqrt{n(n+2)}\ \mu_B \qquad \text{.....4.5}$$

Giving that for Fe^{3+} ions the value of μ_{eff} is $5.9\mu_B$ and for Ni^{2+} it is 2.8 μ_B, on the other hand, the observed moment values of Fe^{2+} , Ni^{2+} and Fe^{2+} are $5\mu_B$, $3.3\mu B$ and $5.7\mu B$ respectively. So one can write: *$6.65\mu B$ (of $2Ni^{2+}$) – {$5\mu B$ (of $1Fe^{3+}$) + $0\mu B$ (of $1Li^{1+}$)} = $1.6\mu_B$.* Also Neel's theory states that the A–B exchange interaction is stronger than that of A–A and B–B exchange interaction as long as A and B cations have high or comparable concentrations. The decreasing of M_s within the range (x= 0.5 - 0.7) is due

to the decreasing of Fe^{3+} at octahedral site (B) which will decrease A-B interaction and subsequent decrease M_s as in [187].

The saturation magnetization is given by the vector sum of the magnetic moments of the individual A and B sub-lattices. Some researchers supposed that the decreasing of M_s may relate to occupying tetrahedral (A) sites by Ni ion besides (B) sites [187]. Spin canting according to presence of nonmagnetic like Li^{1+} may also produce degradation in M_s.

It should be noted here there is a compatible variations of (M_s) and (M_r), which tends to accept the same reason for both. Susceptibility variation with (x) in Fig.4.25 can be explained in terms of μ_i and M_s by the following equation:

$$\mu_i = \frac{M_s^2\, dm}{K_1} \qquad \text{.....4.6}$$

where μ_i is the permeability and dm is the particle size. The proportion of μ_i with M_s is clear in the relation compared to anisotropy constant K_1 due to the power squared [186].

On the other hand, the same magnetic parameters include remnant magnetization M_r, magnetization saturation M_s and initial susceptibility χ_i for samples with Fe^{2+} ions as explained in Fig.4.27, Fig.4.28 and Fig.4.29 respectively.

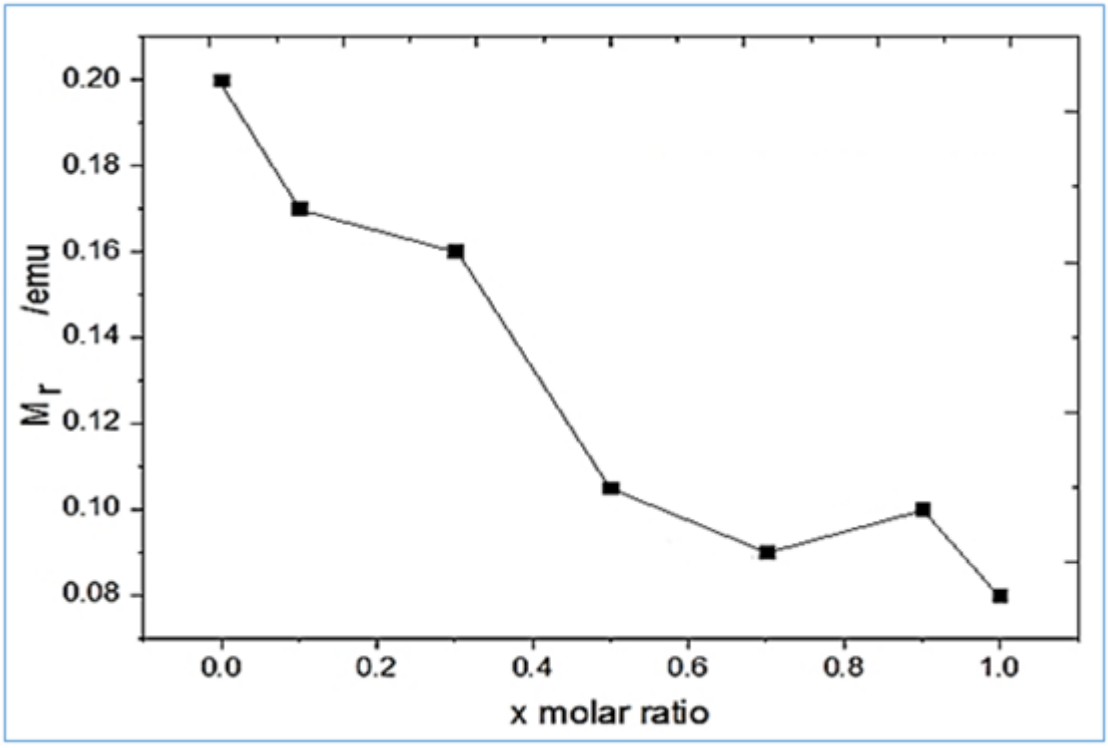

Fig.4.27. Remanence magnetization M_r versus molar ratio for samples with Fe^{2+}.

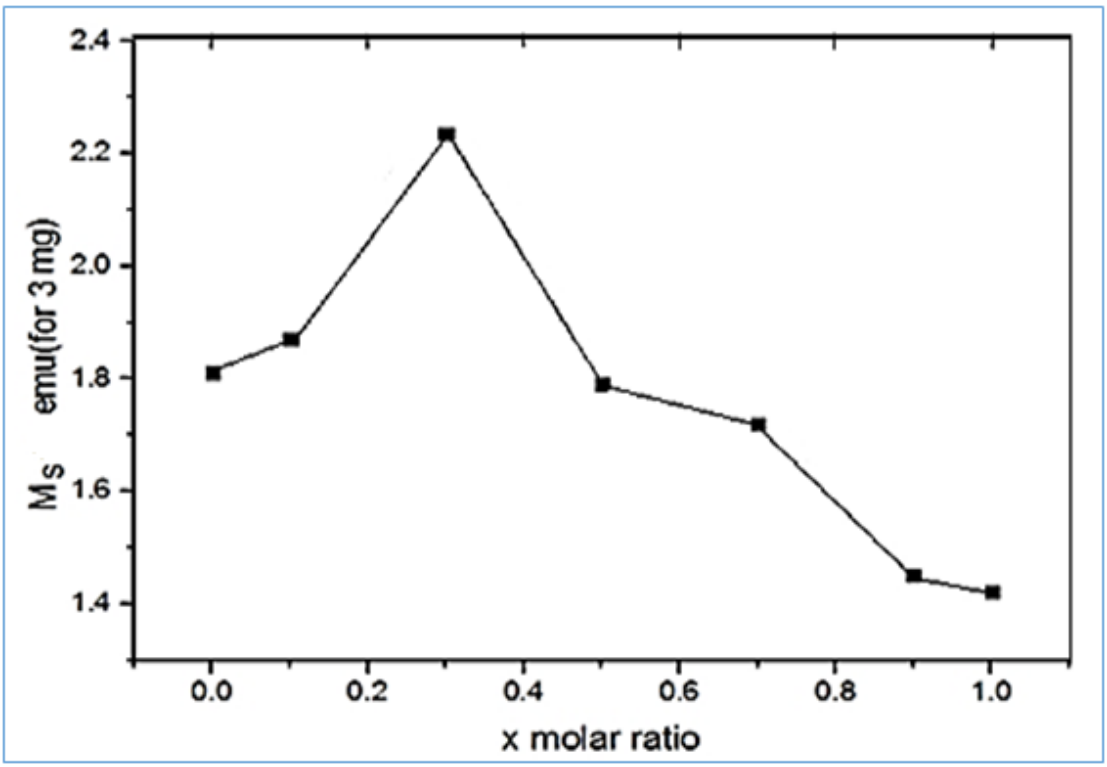

Fig.4.28. Magnetization saturation for samples with Fe^{2+}.

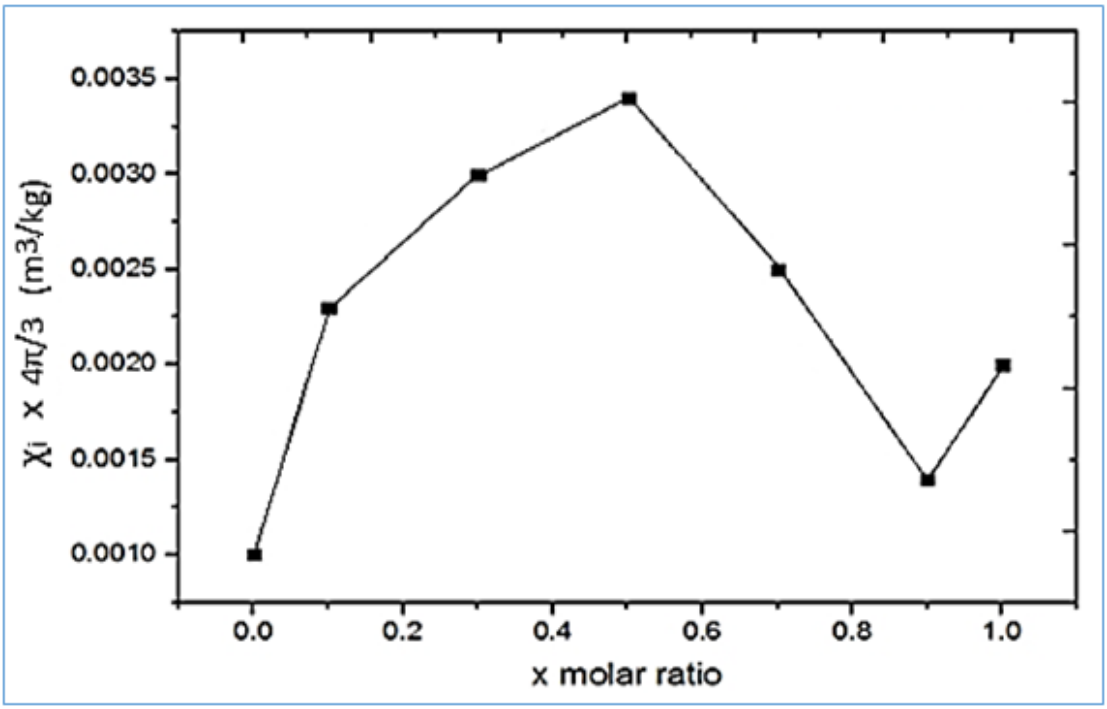

Fig.4.29. Initial permeability as a function of molar ratio x for samples with Fe^{2+}.

The magnetic remanence (M_r) values in Fig.4.27 are greater than (M_r) values for samples with Fe^{2+}. They decreased as x increases. The difference in the behavior of both samples with and without Fe^{2+} may be related to

the presence of Fe^{2+}. In other words the Fe^{2+} with a reasonable concentration occupied B-site as stated before [10]. So the substitution of Fe^{3+} cations by Ni^{2+} cations shifted them to A-site and that the reason for decreasing M_r.

The variation of (M_s) and (χ_i) with molar ratio (x) is roughly similar to results of samples without Fe^{2+}, they have a maximum at (x=0.3 and 0.5) respectively. The decreasing of (M_s) and (χ_i) is related to same reason mentioned above for (M_r), as well as spin canting due to presence of Li^{1+}. The increasing of (M_s) and (χ_i) at low x values is due to the substitution of Li^{1+} by Ni^{2+}.

4.4. Microwave Properties Results

The Microwave properties results contain ferromagnetic resonance (FMR) results, reflection loss results (RL) and insertion loss results (IL).

4.4.1. Ferromagnetic Resonance (FMR) Results

4.4.1.1. Cavity Ferromagnetic Resonance (FMR) Results

These results of FMR measurements were performed under incident microwave power of 0.12mW (35dB) and at frequency of 9.7 GHz. The FMR lines of samples without Fe^{2+} is shown in Fig.4.30. These results show nearly symmetric lines at different x values.

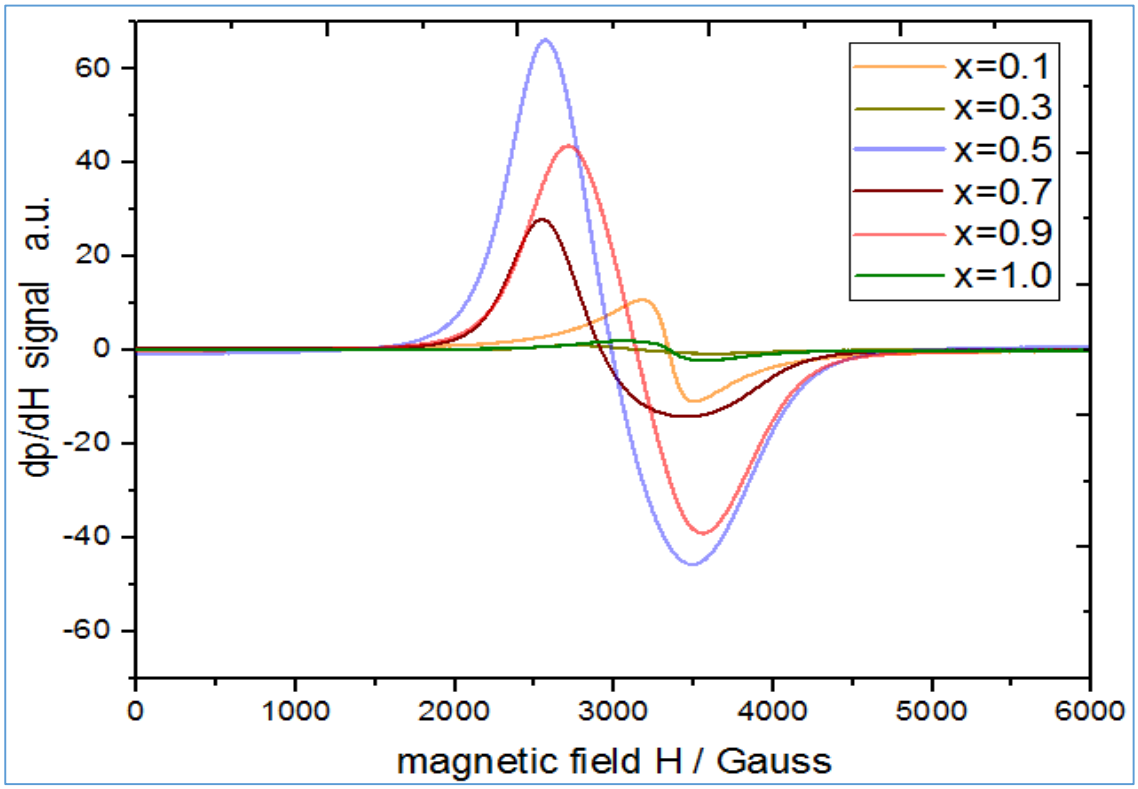

Fig.4.30. FMR line shape of samples without Fe^{2+} at 9.7 GHz.

The refinement of these results gives useful information illustrated in subsequent figures. The extracted quantities are the imaginary part of susceptibility χ″ (absorbed power) and linewidth ΔH.

The instrument signal dχ″/dH as a function of the field H is integrated to give imaginary susceptibility χ″ which represents the absorbed power as a function of field as mentioned in Fig.4.31. The integration was done by OriginPro 9.1 software.

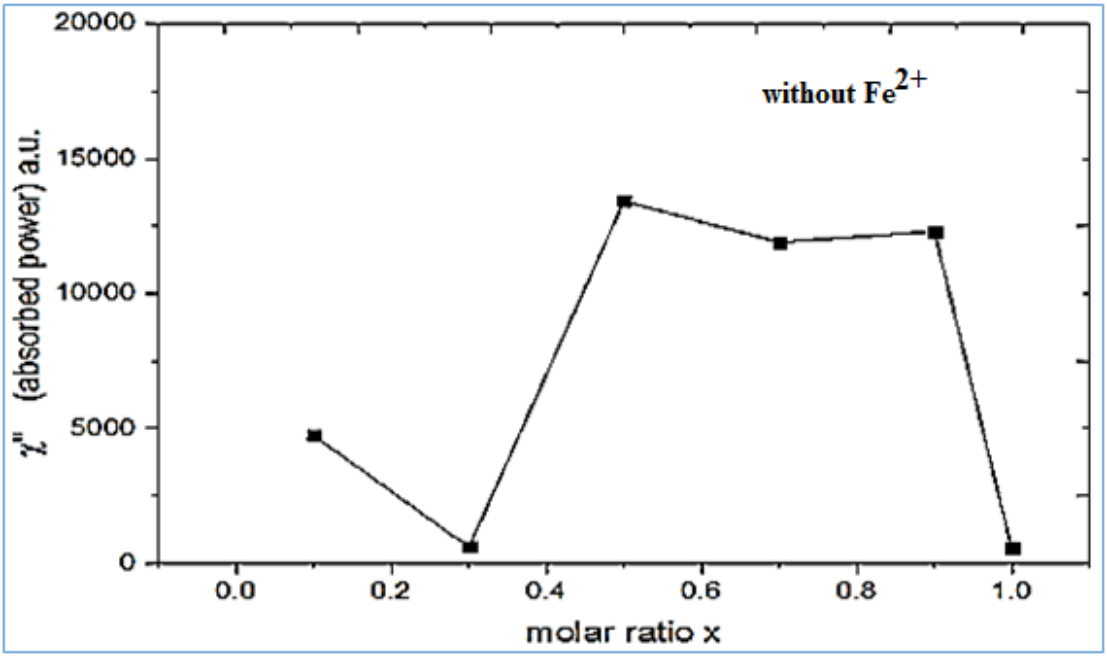

Fig.4.31. FMR Imaginary susceptibility of samples without Fe^{2+}.

It can be seen there is a maximum value in χ″ curve at (x=0.5) and high values of χ″ extend to (x=0.9) comparable to other values of χ″. This behavior can be explained in terms of magnetic parameters M_s and H_c according to relations for single wall anisotropic particles [142]:

$$\mu'' = M_s / 2\mu_0 H_A \alpha \qquad \text{.....4.7}$$

where H_A is the anisotropy field, given by $\boldsymbol{H_A = 2K_1/M_s}$, then one has:

$$\mu_r'' = M_s^2 / 4\mu_0 K_1 \alpha \propto \sigma_s^2 / H_c \propto M_s^2 / H_c \qquad \text{.....4.8}$$

By comparing the results of Fig.4.31 with that of Fig. 4.22 and Fig.4.25 there is a good agreement between these result and eq.4.8 where maximum value of (M_s) corresponds to maximum of χ″, there is also small degradation in χ″ at (x= 0.7) for same reasons. This of course is related to cations distribution which affects magnetic properties as mentioned before.

Linewidths at HWFM of FMR signals ΔH as a function of molar ratio for samples without Fe^{2+} are shown in Fig.4.32.

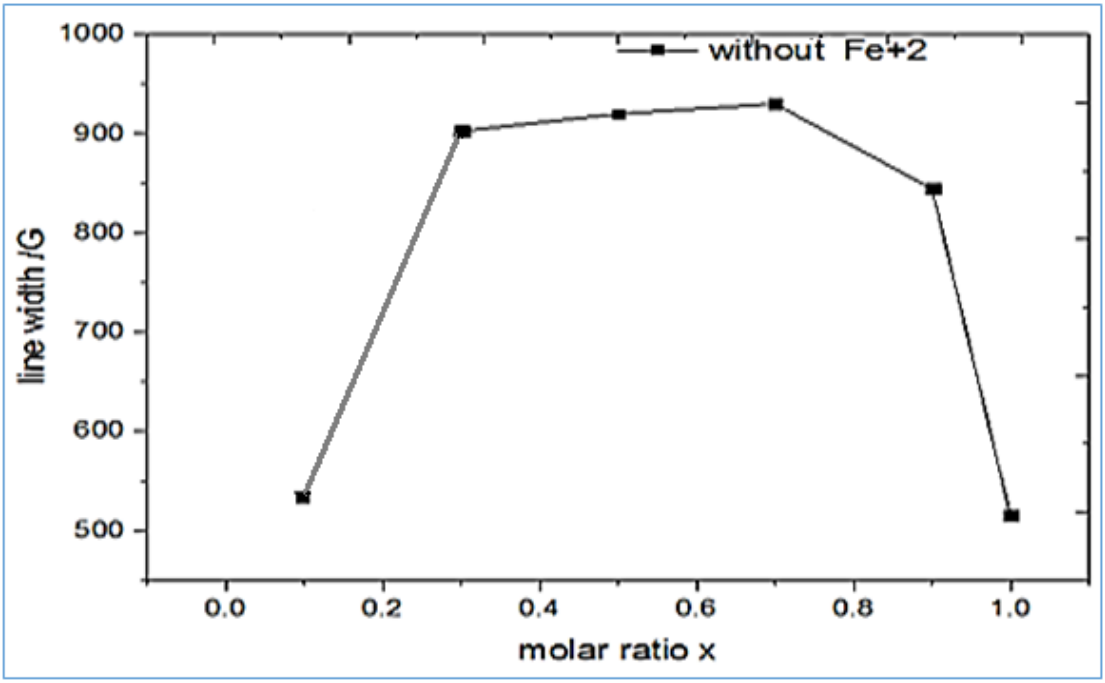

Fig.4.32 FMR linewidth of samples without Fe^{2+}at 9.7GHz.

There is an increase in ΔH with increasing in molar ratio (x) and maximum value is attended at (x=0.7). Line width has a strong correlation with χ'' (as discussed in chapter 2) and in turn by absorbed power. So broader linewidth is preferred for microwave absorbing material.

There are six factors which affect the linewidth. The multiphase presence at low (x) values is the reason behind linewidth increasing. It is believed at (x=0.3-0.7) values the contribution of inhomogeneous or extrinsic broadening which contains porosity, anisotropy, eddy, and inhomogeneity demagnetization has the main effect on linewidth. The nano size of particles means more surfaces, interfaces, grain boundaries, and surface imperfections are responsible for dominant broadening by enhancing anisotropy broadening. This increasing may be related to crystal imperfections due to increasing ferrite phase growth with increasing Ni content and getting maximum around (x=0.5). Imperfections lead to induce different local fields and in turn different local anisotropy. It is important to mention that Ni^{2+} is classified as heavy ion which leads it to act as fast relaxing ion producing a max ΔH at certain x depending on spin wave correlation to crystallite phase of ferrite.

Adding Fe^{2+} has a great significance on FMR results compared with results for samples without Fe^{2+}. The FMR line shape of the derivative signal of the samples of with Fe^{2+} is shown in Fig.4.33. It can be observed that lines are asymmetric compared to samples without Fe^{2+}. The negative part is more flat than positive one, this may be due to conduction by hopping which enhances relaxation.

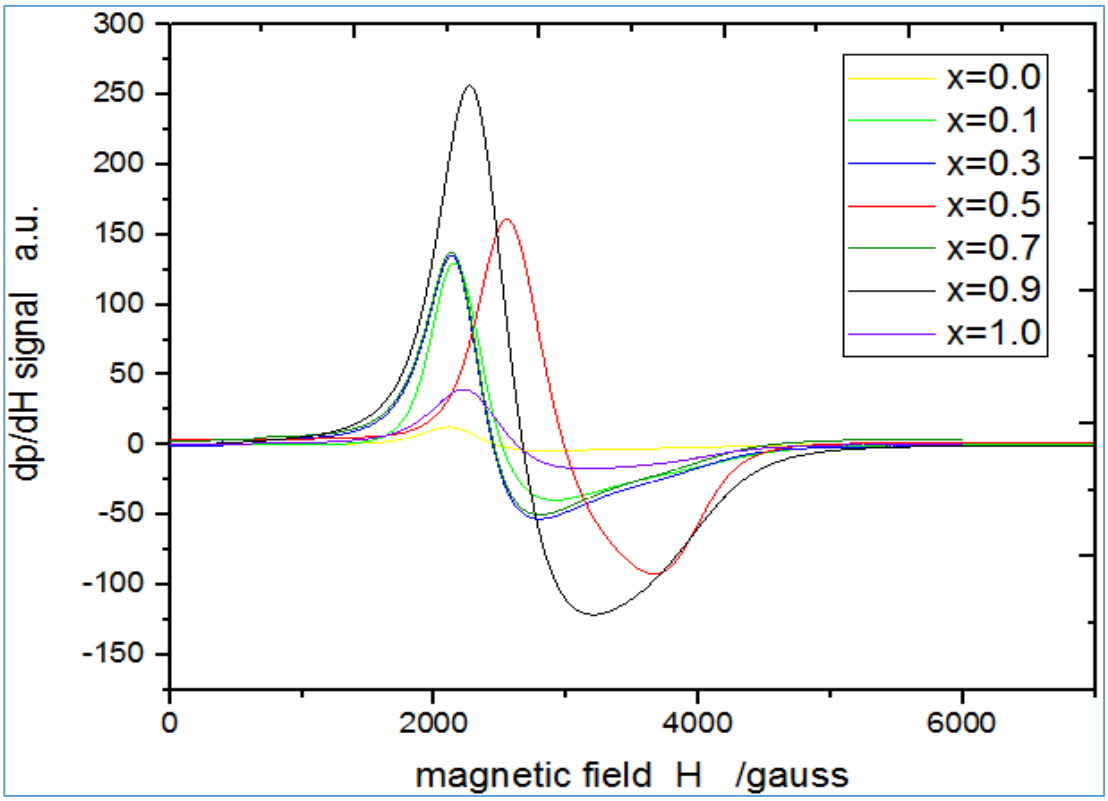

Fig.4.33. FMR line shape of samples with Fe^{2+}

The imaginary susceptibility (absorbed energy) results of samples with Fe^{2+} is shown in Fig.4.34. There is a minimum at x=0.5 and maximum value at (x=0.9). The values of absorbed power of samples with Fe^{2+} are higher than those of samples without Fe^{2+}. That is related to high loss produced from conduction by electron hopping through Fe^{3+} to Fe^{2+}.

The linewidth of FMR curve versus molar ratio (x) for samples with Fe^{2+} is illustrated in Fig.4.35. This may be related to proportion between linewidth and imaginary susceptibility through the damping factor. The large linewidth and high absorbed power at x=0.9 are believed because of large Ni content in presence of Fe^{2+} forming more deformation. This believing is based on that Ni^{2+} ions have a significance effect on χ'' and ΔH as relaxing ion. This behavior appears not agreed with equation 4.8. This may be due to existence of Fe^{2+}.

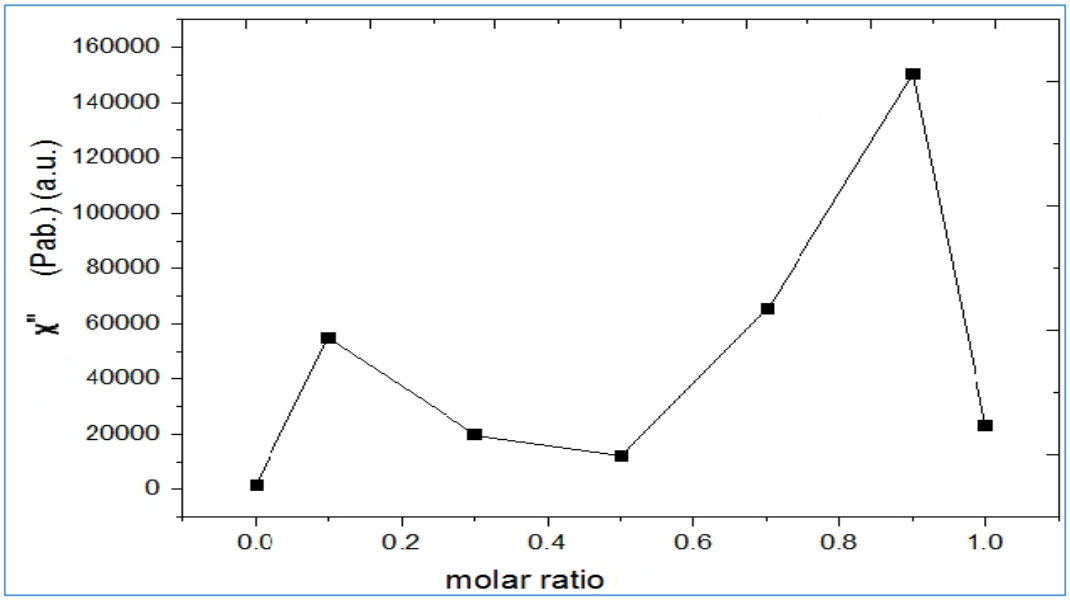

Fig.4.34. FMR Imaginary susceptibility of samples with Fe^{2+} versus molar ratio.

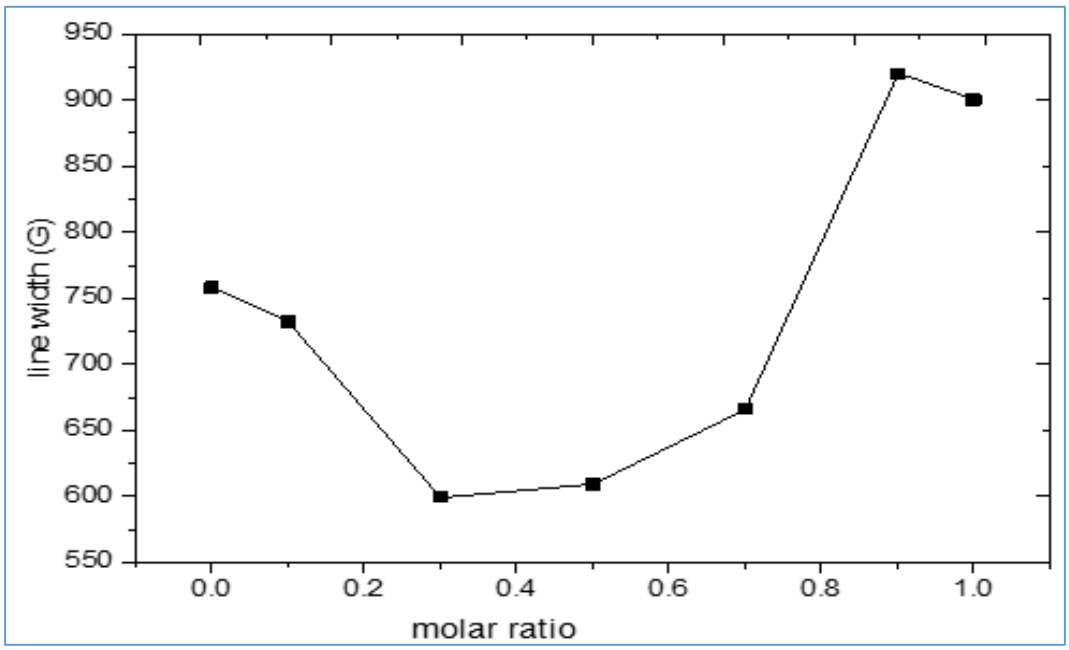

Fig.4.35. Linewidth of versus molar ratio for samples with Fe^{2+}.

Most ferrites having polycrystalline structure possess linewidth in range 10-100 Gauss and grow to several hundred for nanoferrite and spin-orbit interaction [19]. The values of linewidth in Fig.4.32 and Fig.4.35 are higher than values of orientated Li ferrites [65], but they are lower than that for $Ni_{0.65}Zn_{0.375}In_xTi_{0.025}Fe_{1.95-x}O4$ nanoparticles which reach up to 1800 Oe [90]. It is larger than polycrystalline Ni ferrites (500-1000 Oe) [46, 48]. These differences of course are mainly related to conductivity of sample,

grain size, containing relaxing ions and complexity of ferrite molecule. Hexaferrite has broader linewidth due to higher anisotropy constant [163].

4.4.1.2. Multi-frequency Shortcut Ferromagnetic Resonance (SC-FMR) Results

Ferrite-epoxy composite Samples 1mm thickness with Fe^{2+} and without Fe^{2+} are tested by shortcut in range 1.5-26.5 GHz. The signal in case of no sample to the case of sample presence $(\text{Reflected power})_{\text{no sample}}$ / $(\text{Reflected power})_{\text{with sample}}$ was calculated. The result of samples without Fe^{2+} is illustrated in Fig.4.36. The general appearance of the manner show two areas, the first extend from 1.5GHz to 13GHz associated with roughly no absorbance, the second area is extended from 13GHz to 26.5GHz that was characterized by clear absorbance having following absorption peaks 20.7, 22.05, 22.9, 23.65, 25.5 GHz. These peaks still takes the same positions of frequencies for all samples, which means the composition has no effect on peaks positions of magnetic losses.

The composition effect is seemed clearly on the peaks intensity, where the most intensive peak 22.05 GHz have high intensity for the molar ratio (x=1.0) then it drop with x and again get rise at (x=0.3). The peak intensity is higher at (x=1.0) than that of (x=0.3), this may be related to matching with decreasing of H_c values in Fig.4.22.

It is believed that on the bases of Snok's law ($\mu_i f_r = constant$) [22] and low value of crystalline anisotropy constant of spinel ferrite the natural FMR is at frequency lower than 1GHz. The minimum susceptibility (or permeability) value at x=0.3, 0.7 and 1.0 in Fig.4.26 could not push the resonance frequency to higher region of frequencies. The absorption beyond 16 GHz is thought be related to conduction and to spin moments lagging as well as eddy current. The contrast in relative absorption intensity from sample to other is related to difference in values of H_c and Ms.

The relative intensity of MW reflection for samples with Fe^{2+} is shown in Fig.4.37. The general behavior of the spectrum is similar to that of samples without Fe^{2+}. Here again the composition seems has no effect on peak position, but has important effect on the intensity. The value of relative intensity which represent absorption for samples with Fe^{2+} is higher than samples without Fe^{2+} especially at x=0.9. The higher values of samples with Fe^{2+} can be attributed to conduction mechanism through electron hopping from Fe^{3+} to Fe^{2+} and to higher losses by moments lagging due to different values of M_s and H_c.

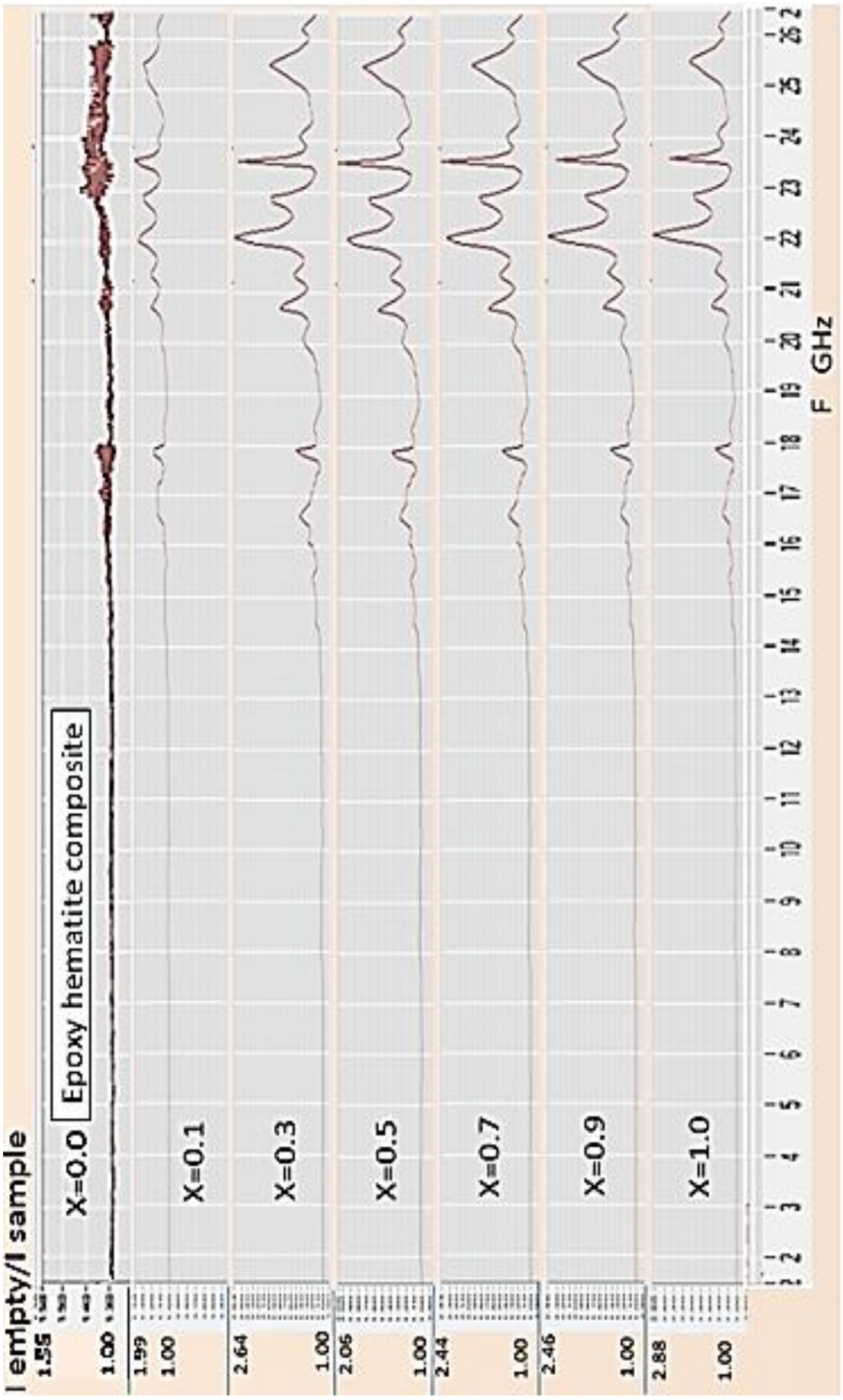

4.36. Relative response of shortcut versus molar ratio for samples without Fe^{2+}.

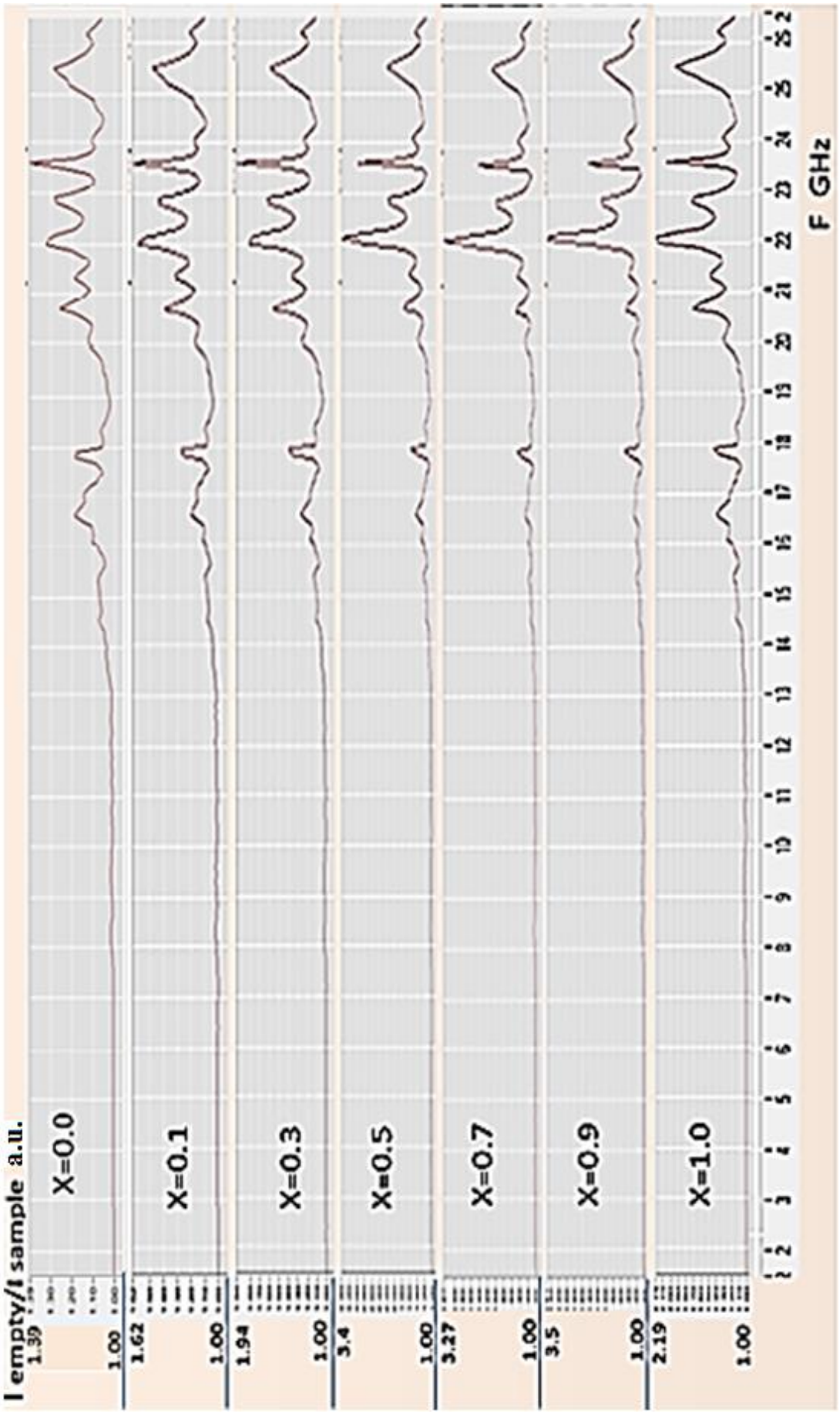

Fig4.37. Multi frequency SC-FMR versus molar ratio for samples with Fe^{2+}.

4.4.2. Return Loss and Insertion Loss in X-Band

The insertion loss and return (reflection) loss are measured by VNA for the two sets with and without Fe^{2+} at 1mm thickness. When the s-parameter value in dB increases in negative ward, this means that the reflection or transmission is decreased. That is based on neglecting the minus sign of the experimental s-parameter which represents loss (not gain). The minus sign gives infinite not understandable values of reflection coefficient. So caution should be taken in discussing increasing or decreasing due to sign defining [188,189]. The theoretical reason for the minus sign is shown in eq.2.56. The S_{21}-parameter in dB in two port is a measure of insertion loss IL, whereas S_{11}-parameter in dB represents return loss, reflection loss or reflection shielding effectiveness SE_R. The S_{11}-parameter is identical also to reflectivity in dB of eq.2.52. Return loss is given by 2.56, thus, a large positive return loss (i.e. eliminating experimental minus sign) indicates the reflected power is small relative to the incident power, which indicates good impedance match from source to load.

In Fig.4.38 the return loss of samples without Fe^{2+} is displayed versus frequency in x-band. It can be observed there is a minimum reflection or return loss at two main bands which are shifted to lower frequency as molar ratio x increases from 0.1 to 0.5 reaching 8.7GHz and 10.1GHz for sample with molar ratio x=0.5.

The molar ratio also has a considerable effect on reflection intensity, where the reflection gets lower value as x increases and the minimum reflection appeares at x=0.5. It is considered that low reflection is mainly because of magnetic absorption, that is connected with magnetization saturation Ms where it has maximum at x=0.5 as shown in Fig.4.25.

Continuous increasing of (x) does not minimize reflection, but gives irregular behavior, where at (x=1.0) the return loss value is approaching that at (x=0.5).

It should be noted here the absorption does not relate to magnetic loss alone but there is a contribution of dielectric losses. It is believed that the increasing of x up to 0.5 enhances ferrite phase formation that is in turn enhance magnetic losses besides dielectric losses. More increasing may affect the dielectric losses because Ni ferrites have lower dielectric losses (dipolar polarization) as well as decreasing in magnetization saturation as illustrated earlier in Fig.4.25.

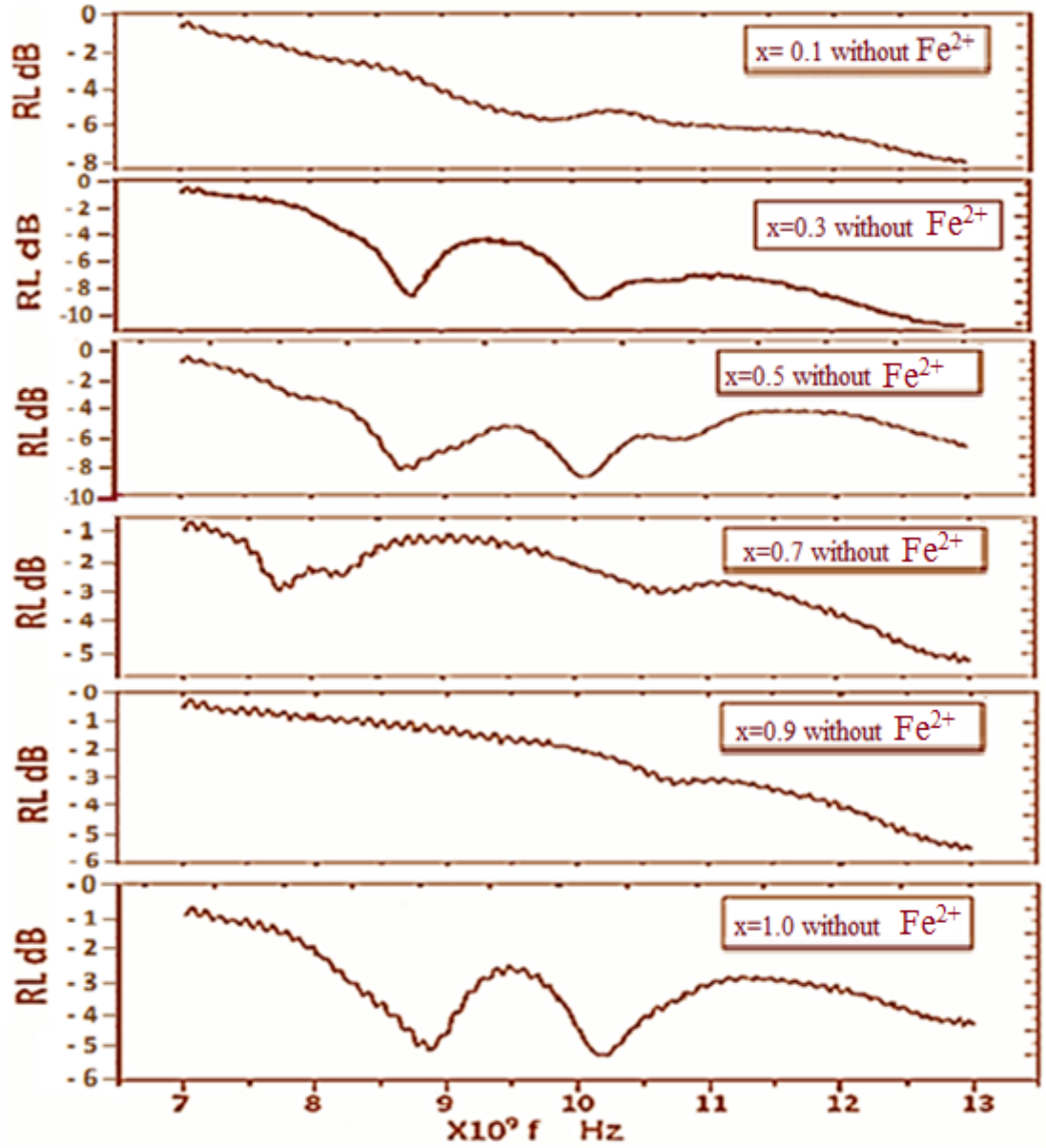

Fig.4.38. Return loss RL versus frequency in x-band for samples without Fe^{2+}.

The effect of Fe^{2+} ions on the return loss is illustrated in Fiq.4.39 for the composite samples having Li-Ni ferrite with Fe^{2+}. The minimum reflection again appears in sample of x=0.5 with two peaks diffused in range 10-11.5 GHz. The variation of the minimum location versus (x) may be explained on the basis of the peak shift. If the case of (x=0.9) is excluded, there is a blue shift followed by red shift. The maximum blue shift is at (x=0.3). The ferrite composition play the main role here where it has maximum crystallite size besides high Ms and χ_i. But how these parameters relate to frequency shift is not understood yet. The effect of dielectric losses and

conduction losses in this range is not negligible, so they may responsible for the peaks of blue or red shift.

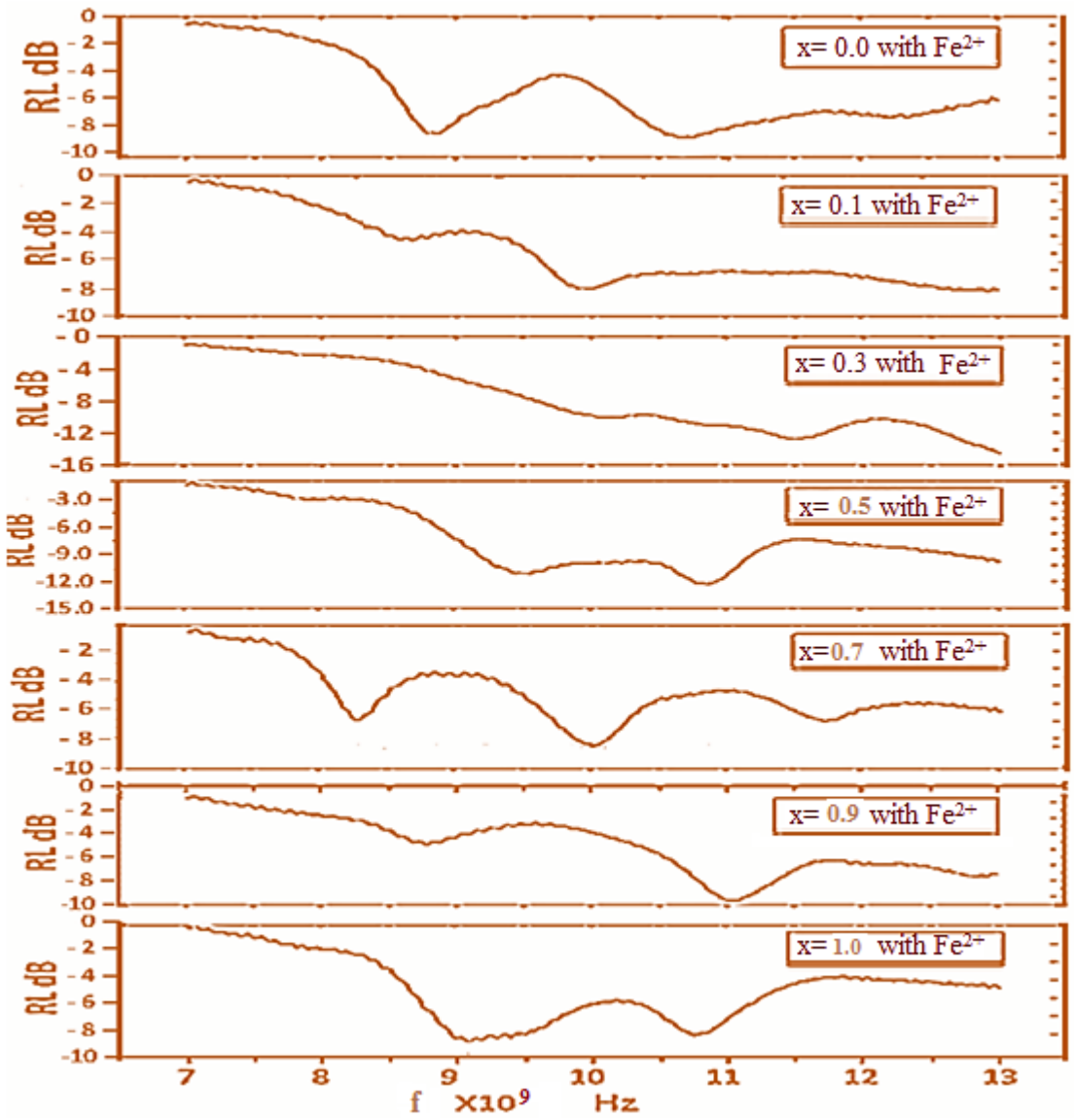

Fig.4.39. Return loss RL versus frequency in x-band for samples with Fe^{2+}.

The general comparison between the samples with and that without Fe^{2+} ions shows that the samples with Fe^{2+} have lower reflection than samples without Fe^{2+}. It is thought the reason behind this lower reflection (high absorption) is the losses due to absorption by hopping conductivity.

The effect of molar ratio (x) on insertion loss (IL) for the samples without $Fe^{2+}$is illustrated in Fig.4.40. Insertion loss expresses how much power is lost if material under test (MUT) is inserted in line. It is equivalent to S_{12} or S_{21}-parameter in dB, this is right if the material under test MUT has reasonable homogeneity. The best result for these samples is for

(x=0.5, 1.0) those are close to -6 dB with minimum transmission located at 10 GHz and 8.7 GHz respectively. The other compositions show comparable IL values, which are around -5 dB. It was observed that there is no distinguishable peaks and instead of that there are very broad bands.

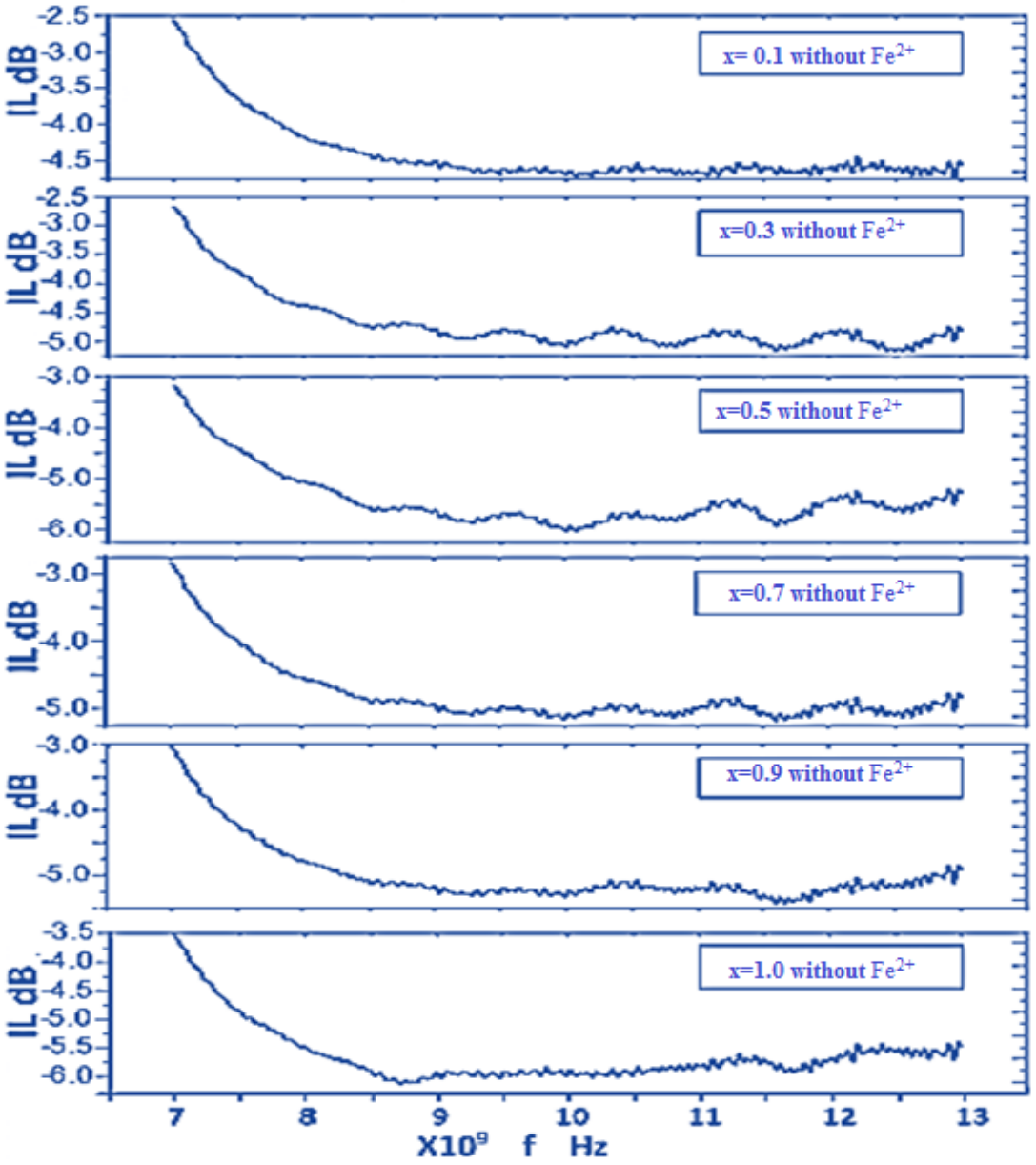

Fig.4.40. Insertion loss IL versus frequency in x-band for different compositions without Fe^{2+}.

It is good to mention here the small rippling on the spectrum is related to standing wave between sample surfaces and references planes of the set up. The insertion loss is exhibited for different compositions with Fe^{2+} and is demonstrated in Fig.4.41. One can find minimum IL equal to -7 dB at 9.8 GHz at x=0.7.

The composition (x=0) has minimum peak at 11GHz. The general behavior of samples with and without Fe^{2+} is similar except that the samples with Fe^{2+} have slightly larger loss. It should be mentioned that the smaller grain size encourages more multiple internal reflections and smaller crystallite size means more deformation. As a result of these reasons besides substitution and related magnetic properties effects, more absorption can occur. The most effective mechanisms of absorption at frequency more than 8GHz in dielectric and magnetic material are that due to dielectric and magnetic dipoles rotation. This may be attributed to give high absorption for nanoferrite samples compared to bulk ferrite one [142].

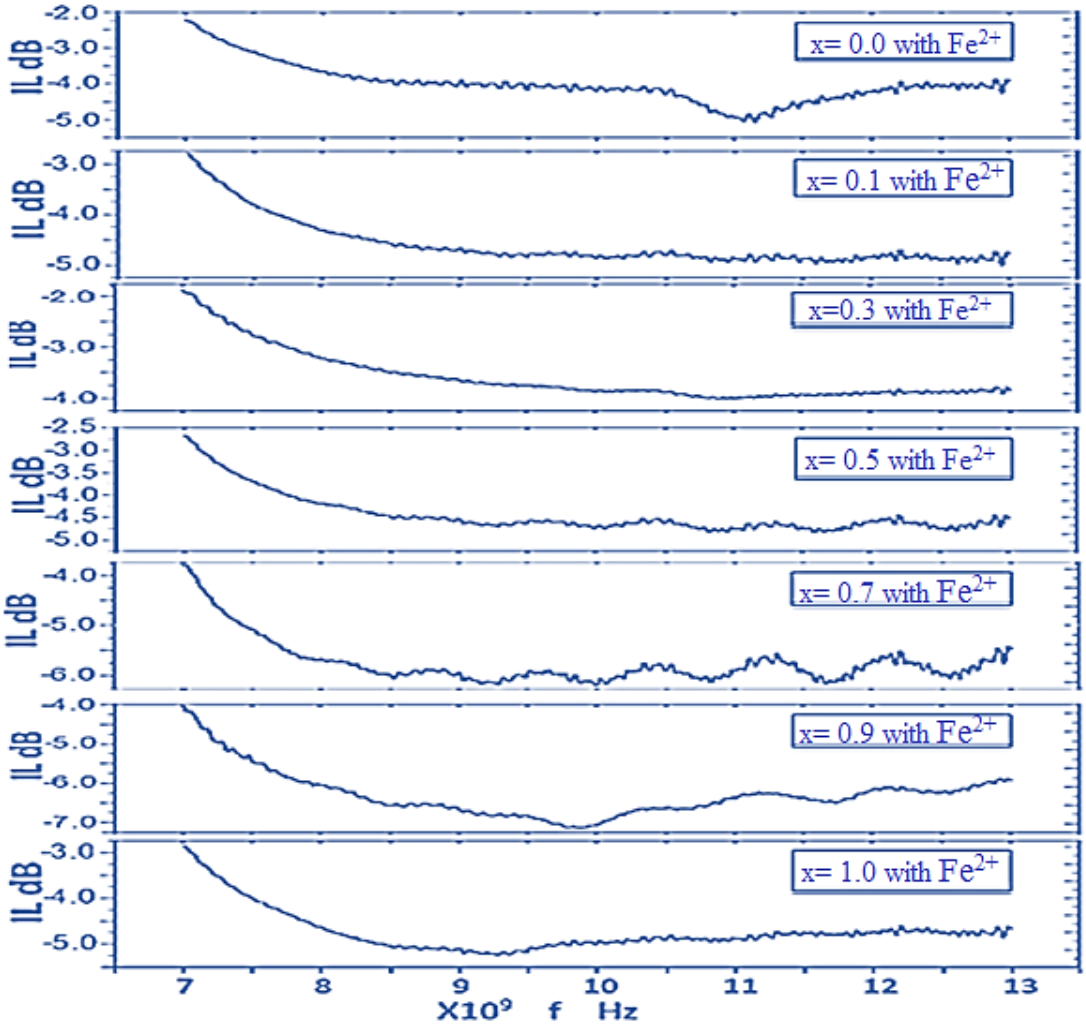

Fig.4.41. Insertion loss IL versus frequency in x-band for samples with Fe^{2+}.

The thickness is more effective if it is equal to ¼ of incident microwave wavelength. There are several researches showed that the product of

thickness and resonance frequency is constant in general at certain conditions [74,190].

4.4.3. Return Loss and Insertion Loss in Ku-Band

Many applications require efficient shield in Ku-band. So it was tried to extend the measurement of the RL and IL to cover the range up to 18 GHz. The results of return loss (RL) as a function of frequency of samples without Fe^{2+} as displayed by Fig.4.42. All samples showed same behavior and nearly same values of (RL) from 12.5 GHz to 15.25 GHz. There is a minimum (RL) appeared at 15.8 GHz at (x=0.1), and there is a minimum at 16.25 GHz reaching -18 dB at (x=0.5). The behavior beyond 16.9 GHz is also the same.

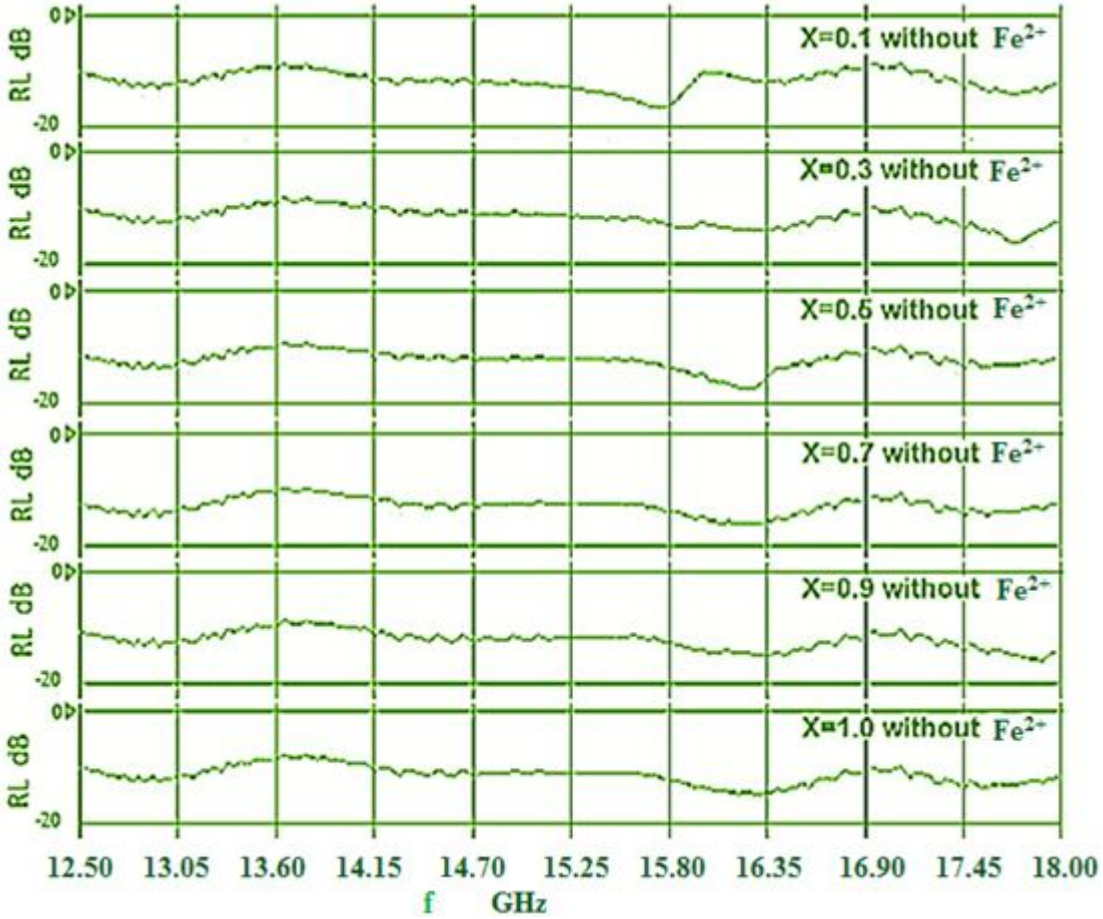

Fig.4.42. Return loss RL versus frequency in Ku-band for samples without Fe^{2+}.

The (RL) versus frequency for different composition with Fe^{2+} is shown in Fig.4.43. The samples also have the same behavior and the values of (RL) which, are around 9 dB. The general values of RL for samples without Fe^{2+} was near to the values of samples with Fe^{2+}.

The semi steady behavior of RL of samples with and without Fe^{2+} is in agreement with the results discussed before through Fig.4.36 and Fig.4.37. It is believed that the dielectric losses by electric dipole lagging and conduction hopping losses have comparable role contribution to magnetic losses in this range of microwave radiation. The resonance is not located in this range of frequency, so the losses are somewhat equal for most samples.

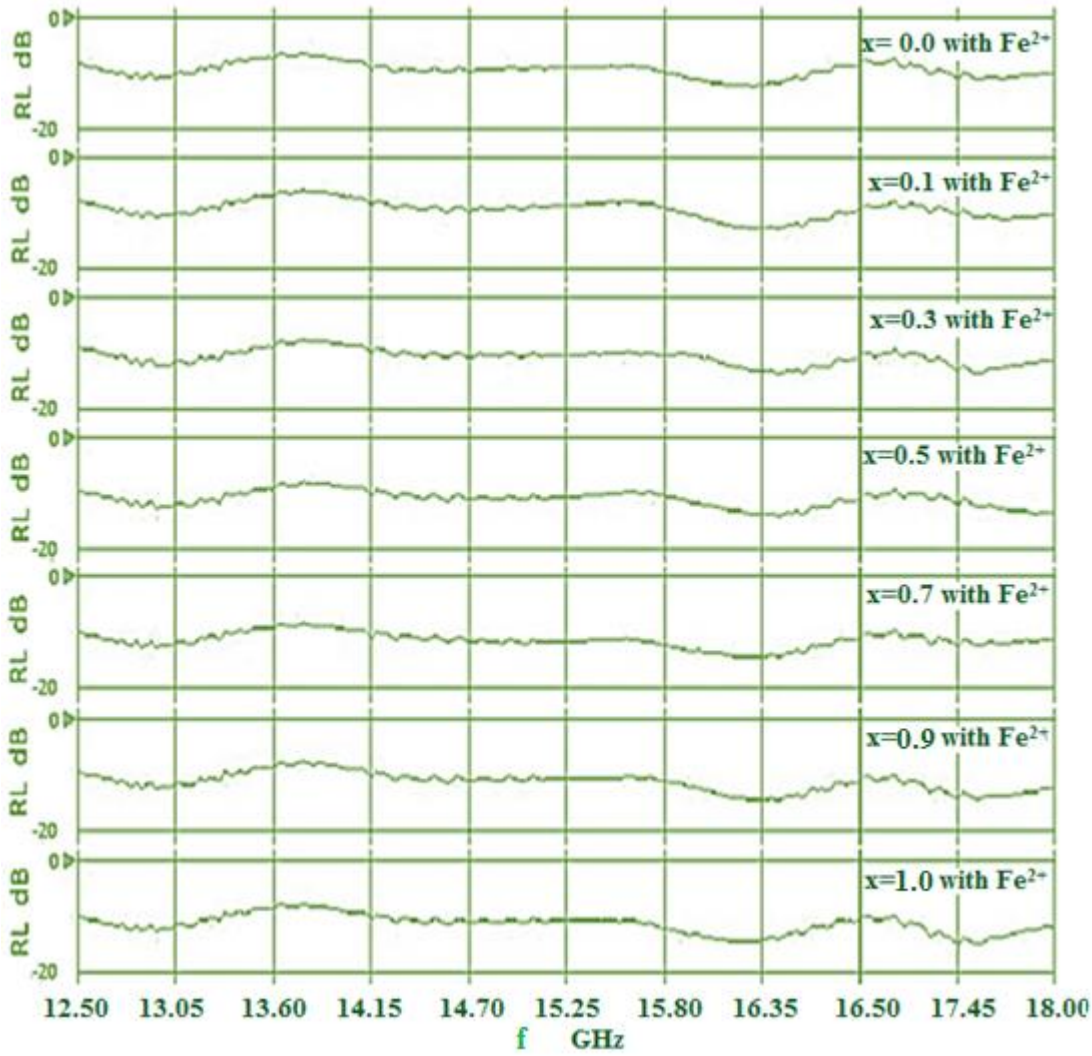

Fig.4.43. Return loss RL versus frequency in Ku-band for samples with Fe^{2+}.

Insertion losses IL in Ku-band are illustrated in Fig.4.44 for samples without Fe^{2+} ions. The behavior is repeated for all samples, with average losses at about -6 dB, while at x=0.1 a minimum in transmission goes to -12 dB, that supports our previous explanation of dielectric loss because this sample has composition containing hematite as mentioned before.

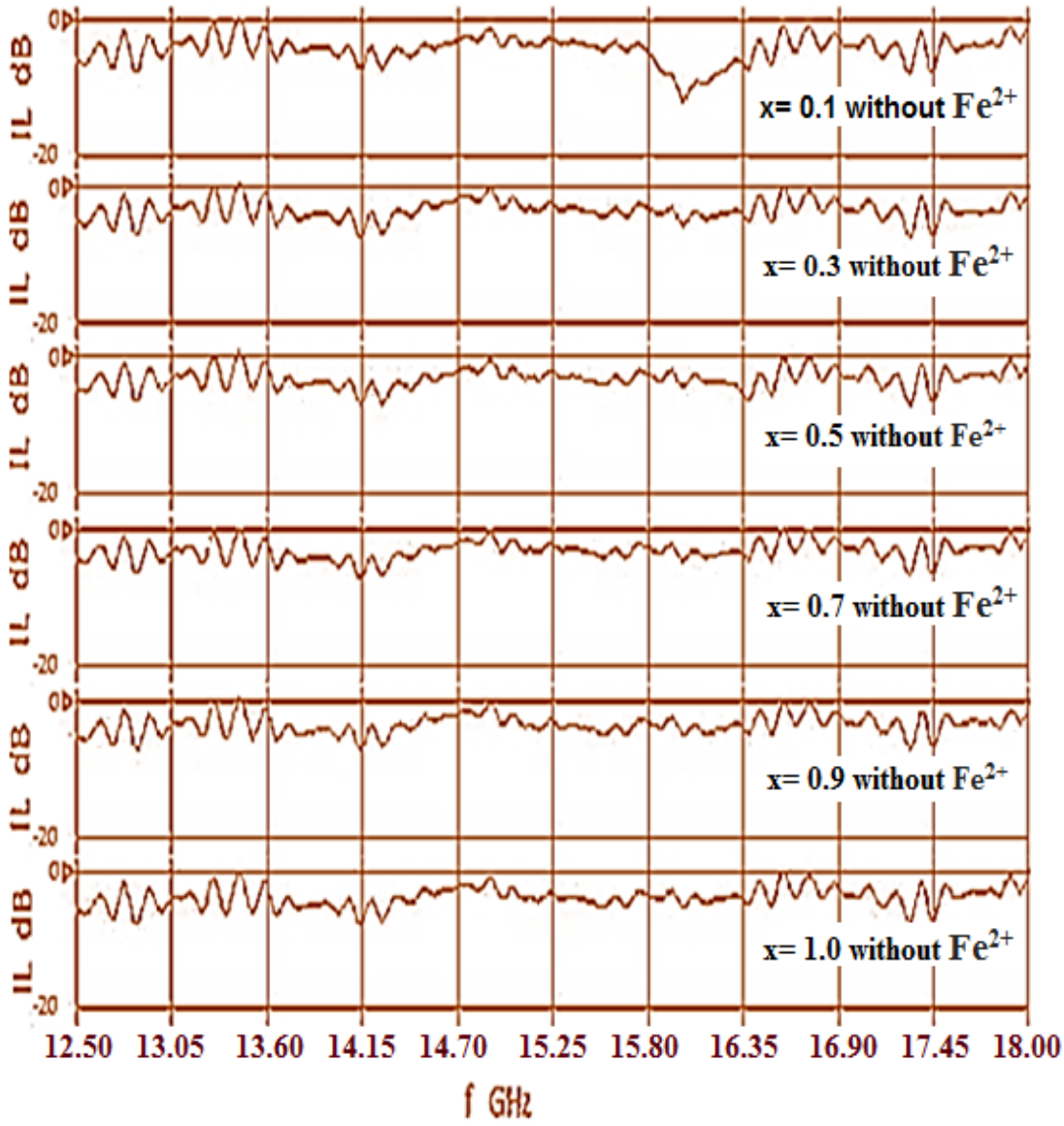

Fig.4.44. Insertion loss IL versus frequency in x-band for samples without Fe^{2+}.

The insertion losses (IL) versus frequency for samples with Fe^{2+} is shown in Fig 4.45 for suggested compositions. No difference appeared on insertion losses when using sample implemented Fe^{2+} in spite of the effect of conductivity of these samples should appear here. Which may be because of hopping of electrons from Fe^{2+} to Fe^{3+}.

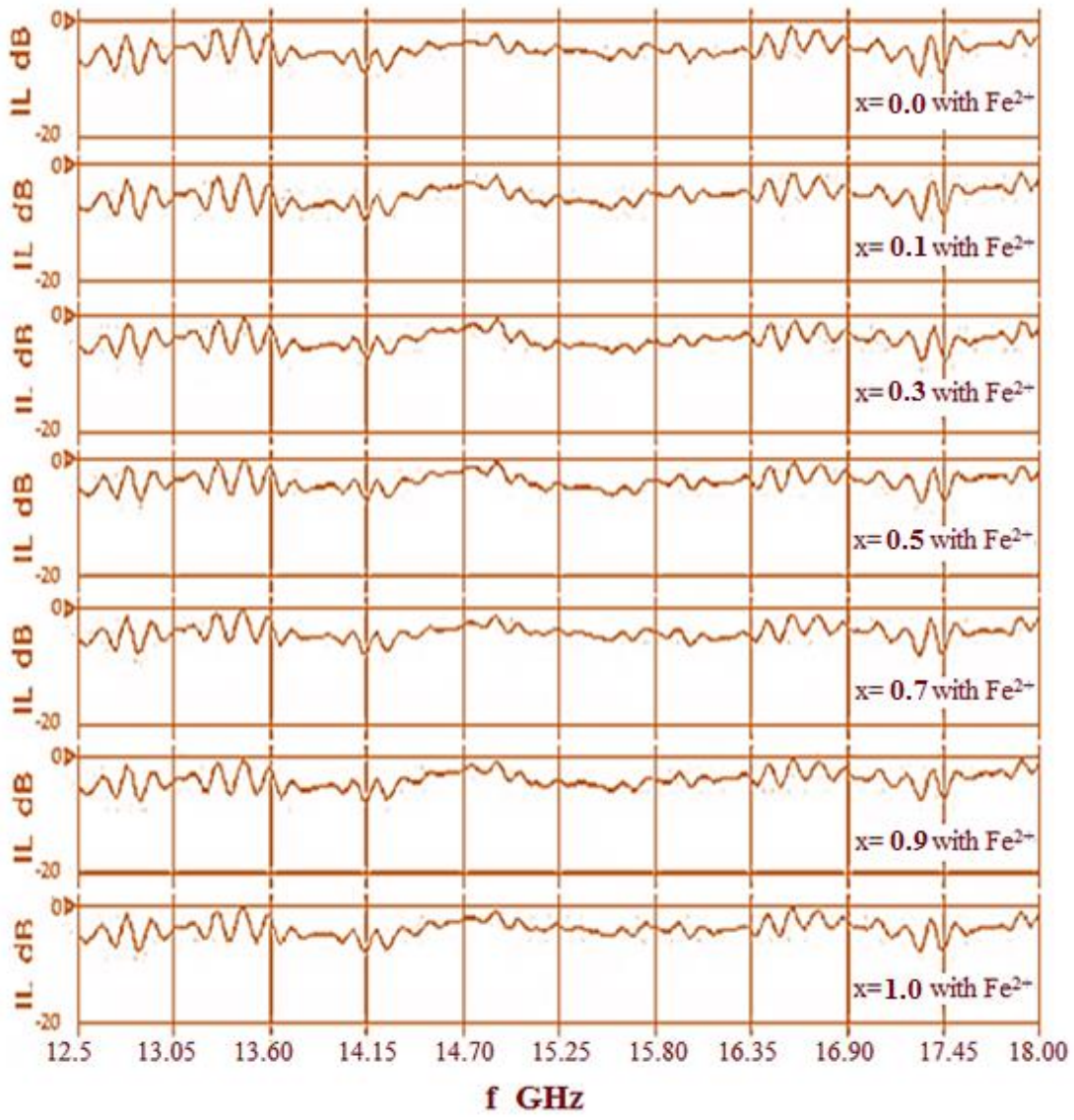

Fig.4.45. Insertion loss IL versus frequency in Ku-band for samples with Fe^{2+}.

There were previous works of measuring the insertion loss registered values such as -8 dB for polycrystalline hexaferrite at 50-75 GHz and 5mm thick [195], -4 dB for three layer of acrylic resin with magnetite and carbon as fillers in range from 12-16 GHz with the whole thickness of 0.5mm[196], IL values enhance from −40 dB to −48 dB for 30 wt% to 50 wt% graphite novolac phenolic resin 3.7 mm at 8-12 GHz[197], -32 dB for Li-Zn ferrite at0.1 GHz (toroid 9mm thick) [198], -17dB (2mm) Ni-ferrite in rubber 8-12 GHz which increased gradually to -35dB with adding carbon black [199]. The value of IL for most prepared samples is around -6 dB, this value is reasonable for thickness of 1mm compared with those mentioned above and taking into account the ratio of mixing with ferrite and the frequency range. All works having (IL) higher than that of in

previous figures for samples prepared in this work are related to using hexaferrite or thicker samples.

In general, it is better to say here the contribution of dielectric and conduction losses may have greater effect than magnetic losses in range of 8-18 GHz, depends on the SC-FMR results as discussed before. The effect of particle size and magnetic parameters contributes to shift magnetic loss peaks (resonance frequencies) above 19 GHz.

4.4.4. Thickness Effect on Reflection Loss and Insertion Loss

The return loss is experimentally equal to reflection loss if the short wave guide at one port of VNA is used [193], and that what was done in experimental part. When comparing the reflection loss results in literatures given in Table 4.2 with the results of this work samples, one can consider this work needs to study the thickness effect.

Table 4.2. Return (Reflection) loss results of different materials with corresponding research group, mixing ratio, thickness, frequency range.

No.	Researcher	Ref.	RL dB	Mixing ratio vol.%	Thickness mm	material	Freq. GHz
1	R. Dosoudil et al.	171	-50 to -30	30-60 PVC	3mm toroidal	MnZn:NiZn ferrite	0.1-1
2	Patrizia Savi et al.	191	-17.5	10 epoxy	3	MWCNT	8-13
3	M. Oyharçabal	192	-5	100	3.3	PANI	5-12
4	Liyana Zahid	149	-75 to -20	polyester	90-170	sugar cane bagasse pyramidal	1-20
5	S. Kirouane et al.	194	-22	(simulation)	0.1-0.015	Graphin- Ba ferrite	45-53
6	H. Bayrakdar	72	-59.6	5:1 wt% Acrylated epoxy	2	Co-Mn ferrite	8-16
7	Kazuaki Shimba	74	-20	72 polyethylene	1.5 toroidal	Ni-Zn ferrite	0.1-10
8	Chang Sun	78	-20	70%paraffin	1.5 toroidal	Li-Ce ferrite	2-18
9	Na Chen	142	-35 to -25	30% paraffin	3 toroidal	Ni-Zn-Y Ferrites	2-18
10	Xianming Qin	116	-40 to -10	8:3 wt paraffin	2-3.2	BaMnZnCo ferrite	2-18
11	Raj Kumar Jain	144	-30 to -10	50-90 % wt polyurethane resin	2mm	Barium titanate	11.4-13.6
12	R.C. Pullar	25	-35 to -10	Different (review)	1.4-2	Different hexaferrite	8-13
13	S.P. Gairola	195	-16 to -6	PVA as binder	2	BaCoMnTi ferrite	8-13

So three composite samples of Li-Ni ferrite with Fe^{2+} at molar ratio x=0.5 were prepared at thicknesses of 1.5 mm and 2 mm to measure

reflection loss and insertion loss for them. The effect of increasing sample thickness on reflection loss at x=0.5 with using Fe^{2+} is illustrated in Fig.4.46 and their insertion loss is given n Fig.4.47.

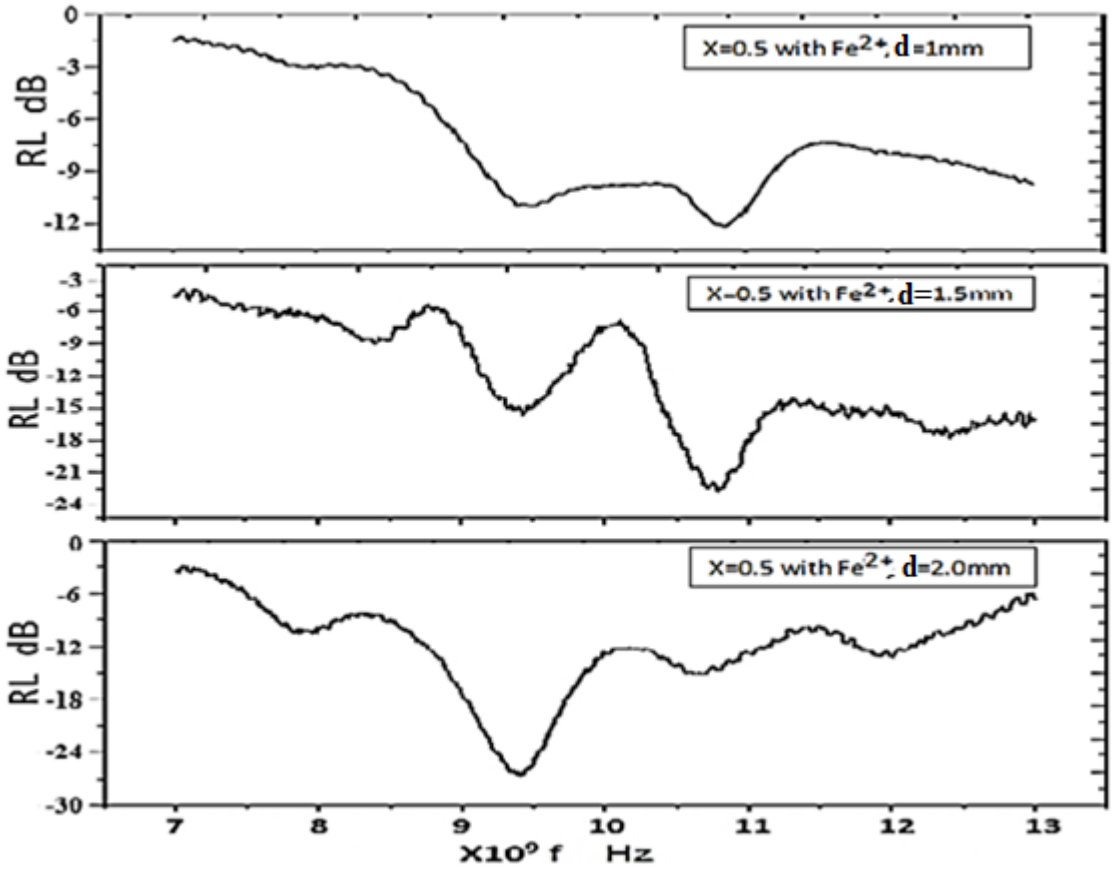

Fig.4.46. Return (reflection) loss as a function of frequency in x-band for x=0.5 with Fe^{2+} at different thicknesses 1mm, 1.5mm and 2.0mm.

It can be recognized that the minimum return loss gets lower as thickness increases, which is thought due to longer wave path in absorber. There is also a shift in absorbance peak to lower frequency which means the waves or photon of lower energy absorbs larger than higher one, in other words, the higher energy photons are stronger to transmit through the absorber. Satisfying return or reflection losses about -27 dB (less than 5%) of incident power is reflected from prepared sample with thickness of 2mm which is believed a good attenuation compared to other absorbers in Table 4.2. The IL minimum value is decreased as thickness increased and shifted to lower frequency, which is related to the same reasons mentioned for return loss.

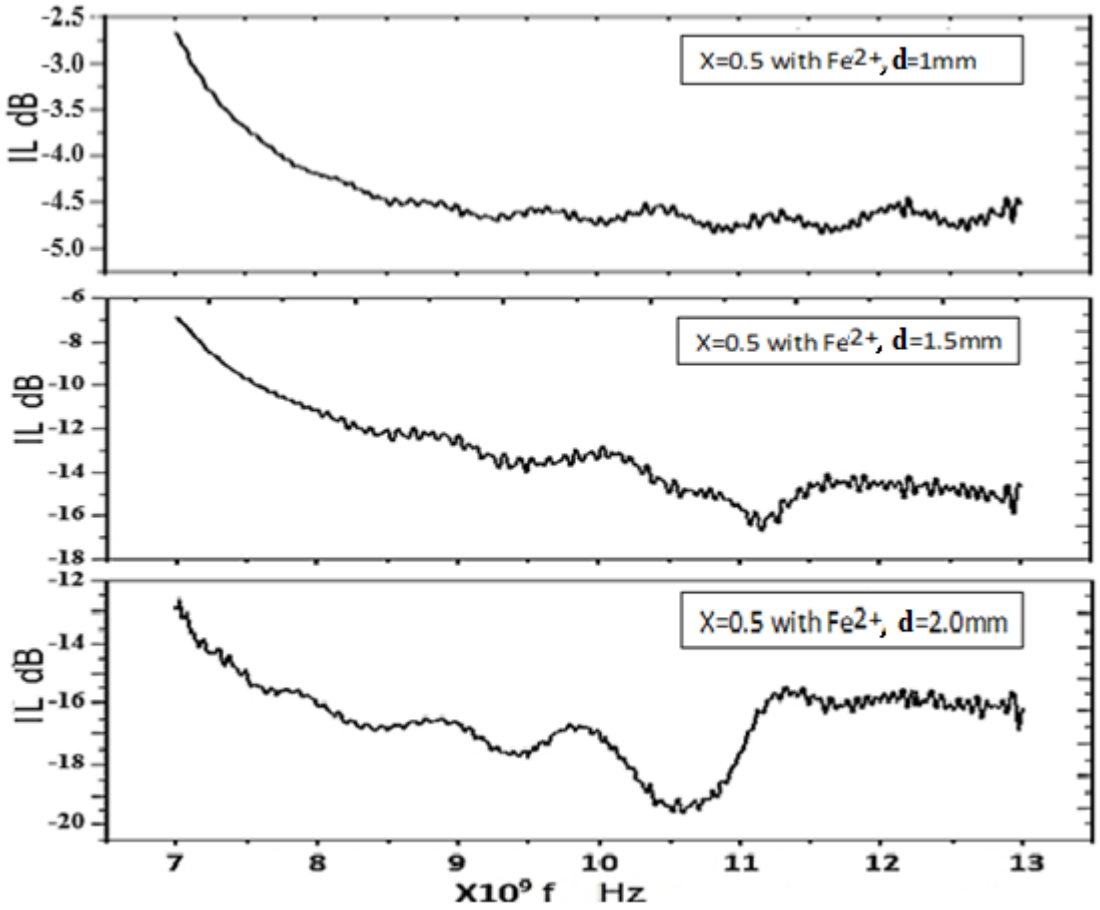

Fig.4.47. Insertion loss as a function of frequency in x-band for x=0.5 with Fe^{2+} at different thicknesses of 1mm, 1.5mm and 2.0mm.

The general shape of the spectrum of reflection or transmission (insertion) loss is nearly still the same with thickness increasing that means the main role of attenuation is related to composition. The role of thickness clearly appears in shifting the peak to minimum frequency, which may be explained by the dependence of thickness on wavelength to satisfy the condition of resonance which usually produces intensive sharp peak.

4.5. Composition Results

The prepared compositions were examined by EDX to ensure those samples have the same suggested composition. The used EDX technique was performed through SEM and TEM microscopy. The EDX has no ability to detect light elements have atomic number lower than 10, like lithium, as well as increasing of error percentage for short time detection, some element, and due to interference of elements at some energies. So Atomic Absorption technique is used also to check the concentrations of all elements per each tested sample. Fig. 4.48 show the EDX spectrum and associated analysis table of some sample.

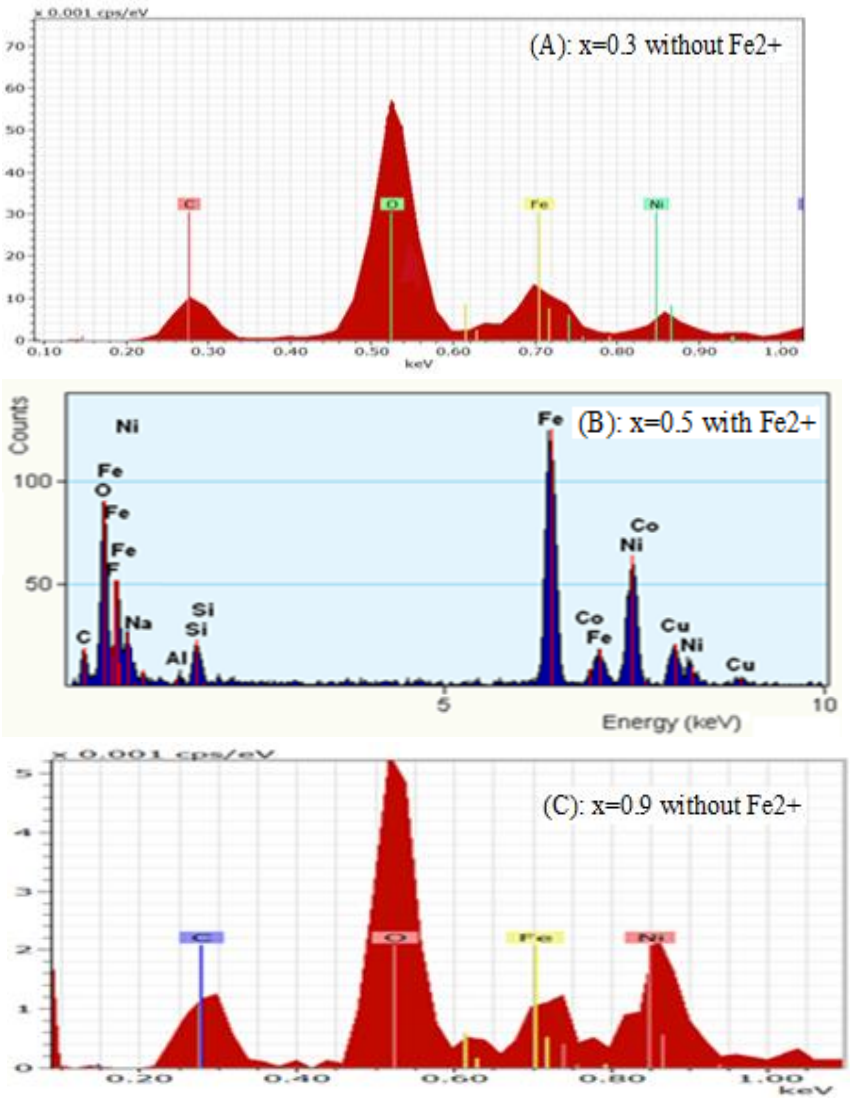

Ele.	Atomic No.	Ato. %
C	6	22.98
O	8	43.63
Na	11	0.983
Al	13	3.471
Fe	26	25.06
Ni	28	3.858
	Sum:	100

Ele.	Atomic No.	Ato. %
C	6	6.756
O	8	57.87
Na	11	1.198
Si	14	6.097
Fe	26	22.02
Co	27	1.413
Ni	28	4.635
	Sum:	100

Ele.	Atomic No.	Ato. %
C	6	30.760
O	8	55.291
Si	14	1.7001
Fe	26	5.7407
Ni	28	6.5069
	Sum:	100

Fig.4.48. SEM-EDX analysis. (A): x=0.3 without Fe^{2+}, (B): x=0.5 with Fe^{2+}, (C): x=0.9 without Fe^{2+}.

All elements are detected through characteristic x-ray of K-series. The measured concentrations of elements by EDX technique have slight difference for the mixed ones mentioned before. It is believed that the deviations related to relatively short time of measuring and interference of background and contamination elements but not to inhomogeneity of structure. The background in Fig.4.48 (A) is Aluminum whereas in Fig.4.48 (B) it is carbon tape. The sodium element is believed related to NaCl that is produced from reaction. The carbon in (A) and (C), Co in (B) and Si in (B) and (C) have unknown source but they may be due to interference of their energy with Li-Ni ferrite elements energies or due to contamination from silver paste or background or SEM chamber.

The atomic absorption results are shown in Fig.4.49. There is also no perfect match between concentrations measured by atomic absorption and that related to chemical prompt given in section 3.3.1 with error percentage does not exceed 7%.

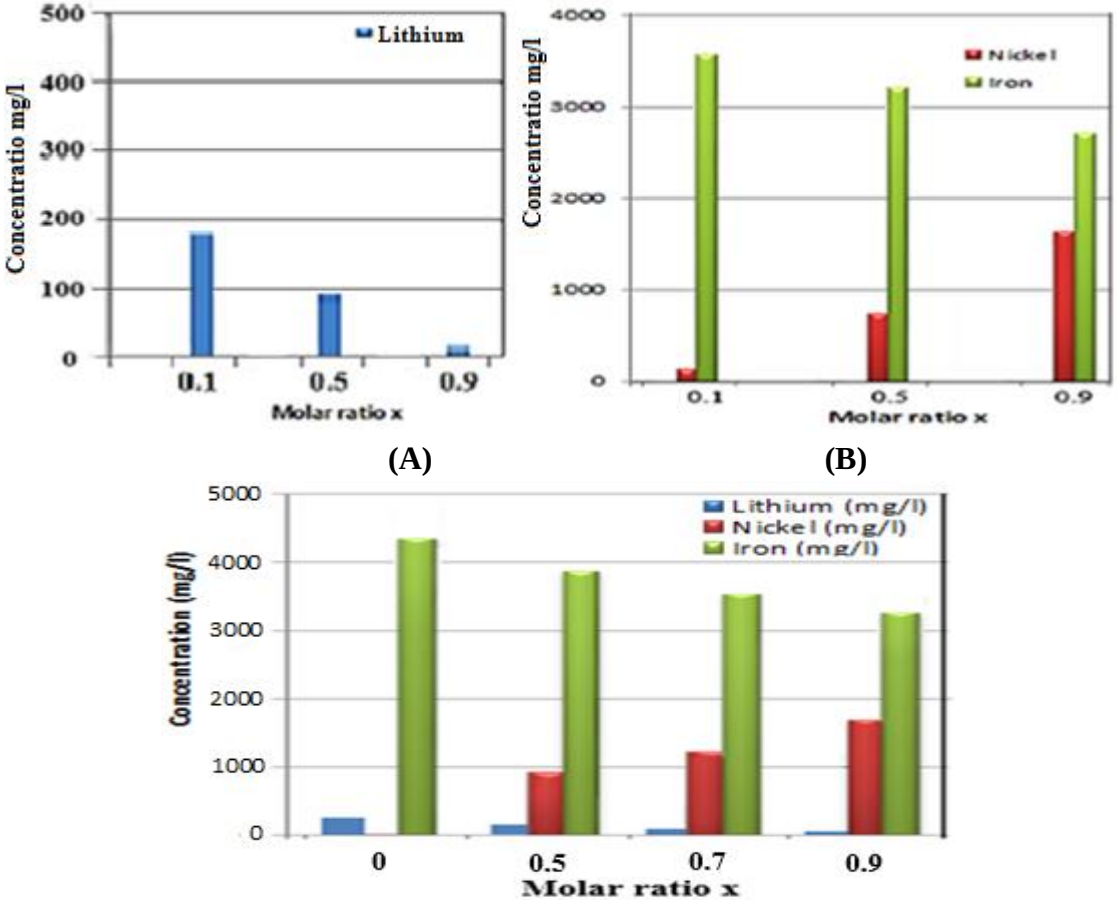

Fig.4.49. Atomic absorption analysis results. (A) and (B) Li, Fe and Ni concentrations versus x for some samples without Fe^{2+}. (C) Li, Fe and Ni concentrations versus x for some samples with Fe^{2+}.

Chapter 5: Conclusions and Future Works

5.1. Introduction

This chapter illustrate the conclusions that were extracted from experimental observations, the results and discussion. It is also reviewed the suggested future works and the references.

5.2. Conclusions

From previous results and our observatione and depending on literatures one can conclude the following points:

- Hydrothermal method is an attractive method for preparing nanoferrite especially Li-Ni ferrite by using metal chlorides and NaOH.
- Li ferrite cannot be prepared by hydrothermal method up to 200 ^{o}C, and hematite phase is constructed instead of spinel ferrite, which is believed due to no existence of divalent ion and low activation energy to form ferrite phase by just lithium and ferric cations.
- The increase of the Ni^{2+} enhances lattice constant and XRD density to be larger. Pure spinel phase can be prepared at molar ratio more than x=0.3.
- The Fe^{2+} encourages forming pure ferrite even at room temperature.
- The adding of Fe^{2+} fluctuate lattice constant with tendency to be increased.
- Influence of Ni substitution on crystallite size smoothly gets minimum at x=0.5 without using Fe^{2+}, but maximum with adding Fe^{2+}.
- The two characteristic main peaks of FTIR transmission appear with shift to higher wave number by Ni^{2+} and Fe^{2+} adding.
- Different shapes of nano particles can be produced by used hydrothermal conditions with dominant spherical one (≈20 nm) related to spinel ferrite. The effect of using Fe^{2+} shifts the particle to be larger to about 30 nm. The distribution of particles sizes was somewhat wide.
- The M-H loops shapes, particle size, and crystallite size leads to think that the samples have superparamagnetic behavior. Coercivety H_c is minimum at x=0.3. The general values are lower in literatures.
- The Ni^{2+} adding maximize Saturation magnetization (M_s) at x=0.5 due to cation distribution and magnetic moments of cations. Adding Fe^{2+} leads to to shift maximum of M_s to x=0.3 keeping some characteristic height at 0.7 as well as enlarges the maximum to higher value. The M_s values were higher than literature but lower than bulk one.
- Nickel substitution in Li ferrite by hydrothermally produces maximum susceptibility at x=0.5. Ferrous cation lowers slightly the maximum.

- Resonance microwave absorption through FMR test proves that the Fe^{2+} ions has the main role in microwave absorption in x-band at 9.7 GHz. The absorption is nearly doubled compared to samples without using Fe^{2+}. The Fe^{2+} presence shifted the maximum absorption from x=0.5 to x=0.9.
- Nickel content increases FMR line width to be max at x=0.7 without adding Fe^{2+}, but the max is at 0.9 with adding Fe^{2+}.
- Li-Ni ferrite appears to be more active absorber in range 20-26 GHz according to the relative absorption response to microwave radiation by SC-FMR. The Ni content has noticeable influence on the relative absorption intensity and got max at x=1.0 which matches H_c information. Adding ferrous cation enhances microwave absorbance considerably (1.5 times) and shifts the peak of nickel content to x=0.9, where is the highest linewidth and minimum initial susceptibility.
- The Ni^{2+}content decrease Reflection (return) loss RL to minimum at x=0.3 without Fe^{2+} because the contribution of dielectric absorption. The Fe^{2+} effect enlarges minimum at x=0.3 to be around -15dB. The Ni^{2+} content does not affect the behavior of insertion loss IL but just its magnitude. The best attenuation is at x=0.5 and x=1.0 around 10GHz.
- Effects of adding Ni^{2+} and Fe^{2+} cations on RL and IL in Ku-band have nearly flat value around -12dB for RL and around -6dB for IL.
- The dielectric losses and the conduction losses have comparable effect on magnetic losses in x-band and Ku-band.
- Increasing of ferrite-epoxy sample thickness to 2mm can leads to decreasing minimum to about -27dB for x=0.5 leading to produce comparable attenuation of other researcher values. That composite has considerable attenuation for microwave attenuation at resonance and out of resonance especially at molar ratio x=0.5 in x-band for 2mm thick. The absorption in Ku-band is moderate semi flat absorption. A very good absorption is in K-band (18-27) GHz.
- If lower thickness with moderate mixing ratio is to be applied as paint but with lower reflection loss of RL of about (-5dB or 56% for about 0.5mm thick) this may be enhanced with increasing mixing ratio and using other additive.

5.3. Suggested Future Works

Due to the limited time of the project and variety of many parameters that interfere in performance of the absorption composite, it is appropriate to suggest the following future work:

1- Studying the effect of changing Fe^{3+}/Fe^{2+} ratio on absorption in X, Ku, K bands.
2- Preparation of Li ferrite by hydrothermal method at higher temperature and by using different lithium compounds.
3- Study the effect of preparation parameters (like solution pH, preparation temperature, and concentrations) on structural and microwave properties.
4- Adding more than lossy known elements like Mg and heavy rare earth elements which is expected to broaden band width and enhance absorption of microwave.
5- Adding dielectric and conductive nano materials like nano carbon wire (or tube), nano metallic wires or particles, carbon black and conductive polymer like polyaniline.
6- Study the absorbance of multilayer with gradual impedance to reduce reflection loss
7- Make simulation study to specify which is better component and its quantity in the composite.
8- Study the effect of annealing on prepared samples to enhance crystallinity and conduction especially at low molar ratio.
9- Apply Li-Ni ferrite to some applications on nano particles in magnetic resonance imaging (MRI), drug delivery techniques and other medical and industrial applications.
10- Study nano Li-Ni microwave properties at MHz range and calculating the real and imaginary parts of permeability and permittivity.

References:

1- V.K. Saxena and U. Chandra, "Microwave Synthesis: a Physical Concept", Janeza Trdine, InTech Press, 2011, Rijeka/Croatia.

2- G. Vázquez, U. Salas and R. Valenzuela, "Microwave Absorption in Nanostructured Spinel Ferrites Magnetic Ceramics", Orhan Yalcin, InTech Publishing, 2013.

3- G. Skrotskii and L. Ktjrbatov, "Phenomenologcal Theory of Ferromagnetic Resoance", S. Vonsovskii, Pergamon Press, 1966, Oxford.

4- D.K. Cheng, "Fundamentals of Engineering Electromagnetics", Addison-Wesley Press, 1992, New York.

5- M. Getzlaff, "Fundamentals of Magnetism", Springer Berlin Heidelberg, 2008, Germany.

6- Ü. Özgüri, Journal of Materials Science Materials in Electronics. 20(10):911-952.

7- N. A. Spaldin, "Magnetic Materials Fundamentals and Applications", Second edition, Cambridge University Press, 2011, New York.

8- K.H.J. Buschow and F.R. Boer, "Physics of Magnetism and Magnetic Materials", Kluwer Academic Publishers, 2004, New York.

9- B.D. Cullity and C. D. Graham, "Introduction to Magnetic Materials", John Wiley & Sons Inc. Publication, New Jersy, 2009.

10- R. Valenzuela, "Novel Applications of Ferrites", Physics Research International, Vol. 2012, Article ID 591839, 9 pages.

11- N. Kanat, "Surface Properties and Catalytic Activity of Manganese Ferrospinels", PH.D Dissertation, Cochin University of Science and Technology, April- 2002, Kochi.

12- J. Hu, "Growth and Characterization of Zinc Ferrite Thin Films for High Frequency Applications", PhD Dissertation, Oregon State University, 2006, Oregon.

13- V.G. Harris, "Advances in Magnetics", IEEE Transactions on Magnetics, vol.4 8, no.3, March 2012.

14- H. Chang, "Magnetic Properties and Structure of Pulsed Laser Deposited Nickel Ferrite Films", Master Thesis, Northeastern University, 2008.

15- A. Goldman, "Modem Ferrite Technology", Second Edition, Springer Science and Business Media Inc., 2006, USA.

16- S. Somiya, "Handbook of Advanced Ceramics", Elsevier Inc., 2003, USA.
17- R. Valenzuela, "Magnetic Ceramics", Cambridge University Press, 2005, Cambridge.
18- U. Chhaya, B. Mistry, K. Bhavsar, M. Gadhvi, V. Lakhani, K. Modi, U. Joshi, Indian Journal of Pure and Applied Physics, Vol.49 December 2011 pp833-840.
19- M. Pardavi and Horvath, Journal of Magnetism and Magnetic Materials 215-216, p.171-183, (2001).
20- E. Wohlfarth, "Handbook of Magnetic Materials", Volume 2, North-Holland Publishing Company, 1980.
21- S. Horikoshi and T. Sumi, Journal of Microwave Power and Electromagnetic Energy, 46 (4), 2012, pp. 215-228.
22- E.D. Gignoux and T. Lacheissrie and M. Schlenker, "Magnetism Fundamentals", Springer Inc., 2005, Boston.
23- M. Hadi "A Study on Electrical and Magnetic Characterization of $Co_{87}Zr_5Nb_8$ Films for High-Q On-chip Inductors", Tokyo Institute of Technology, 2010, Tokyo.
24- K. Rozanov, Z. W. Li. Chen, M. Koledintseva, Journal of Applied Physics, 97, 013905 (2005).
25- R.C. Pullar, Progress in Materials Science, 57 (2012) 1191–1334.
26- D. Li, "Designing Functional Magnetic Nanoparticle with Flame Spray Pyrolysis for Bio-Application", PhD Dissertation, New South Wales University 2009.
27- M. Faraji, Y. Yamini, M. Rezaee, J. Iran. Chem. Soc., Vol. 7, No. 1, March 2010, pp. 1-37.
28- F.X. Qin, H.X. Peng, Progress in Materials Science 58 (2013) 183–259.
29- J. Jiang, Liangchao Li, Feng Xu, Materials Science and Engineering A 456 (2007) 300–304.
30- S.A. Mazen, and T.A. Elmosalami, ISRN Condensed Matter Physics, Vol. 2011 (2011), Article ID 820726, 9 pages.
31- M.F. Al-Hilli, Sean Li, K.S. Kassim, Materials Science and Engineering: B, Vol. 158, Issues 1–3, 2009, Pages 1–6.
32- M.F. Al-Hilli, Sean Li, K. S. Kassim, Journal of Magnetism and Magnetic Materials, 324, (2012) 873–879.

33- M. Al–Hilli Sean Li, K. S. Kassim ,, Materials Chemistry and Physics 128 (2011) 127–132
34- S.T. Assar, H.F. Abosheiasha, Journal of Magnetism and Magnetic Materials, Vol. 324, Issue 22, November 2012, Pages 3846–3852.
35- A. T. Pathan and A. M. Shaikh, International Journal of Computer Applications (0975 – 8887, Vol. 45– No.21, May 2012.
36- S.A. Saafan, S.T. Assar, Journal of Magnetism and Magnetic Materials 324 (2012) 2989–3001.
37- M. Maisnam, S. Phanjoubam, C. Prakash, Proceeding of International Conference on Microwave – 08, 978-1, 2008 IEEE.
38- M. Maisnam, S. Phanjoubam, H. Sarma, L.R. Devi, O.P. Thakur, C. Prakash, Physica B, 352, (2004), 86 – 90.
39- E. Chappel, G. Chouteau, G. Prado, C. Delmas, Solid State Ionics, 159 (2003) 273–278.
40- S.S. Bhatu, Lakhani, V.K. Tanna, A. R. Vasoya, N.H. Buch, J.U. Sharma, P.U. Trivedi, U.N. Joshi, H.H. Modi, K.B., Indian J. Pure & Appl. Phys., 45, 597 (2007).
41- R. G. Kharabe, R. S. Devan, C. M. Kanamadi, B. K. Chougule, Smart Material Structure, 15, (2006) 36-39.
42- R.G. Kharabe, R.S.Devan, B.K.Chougale, Journal of Alloys and compounds, 463, (2008) 67-72.
43- V.K. Sankaranarayanan, Om Prakash, R.P. Pant, M. Islam, Journal of Magnetism and Magnetic Material, 01/2002; 252(2002):7-9.
44- D.H. Ridgley, H. Lessoff, and J. D. Childress, J. Am. Ceram. Soc, 53, 304-311, 1970.
45- Y.C. Venudhar, K. Satya Mohan, Materials Letters, 54 (May 2002) 135–139.
46- Y. Pei Fua and Chin-Shang Hsu, Journal of Alloys and Compounds 395, 247–251 (2005).
47- Y. Pei Fua and Chin-Shang Hsu, Solid State Communications 134, 201–206, (2005).
48- Y. Pei Fua, Journal of Alloys and Compounds 395 272–276, (2005).
49- Y. Pei Fua, Materials Research Bulletin, 41, 809–816, (2006).
50- N. Li, "Chemical Vapor Deposition of Thin Film Materials for Electronic and Magnetic Applications", PhD Dissertation, University of Alabama, 2011.

51- S. Singhal, K. Chandra, Electromagnetic Analysis & Applications, 2: 51-55, 2010.
52- F.S. Tehrani, V. Daadmehr, A. T. Rezakhani, R. H. Akbarnejad, S. Gholipour, Journal of Superconductivity and Novel Magnetism October 2012, Vol. 25, Issue 7, pp 2443-2455, 2012.
53- M.A. Khan, M. ul Islam, M. A.Iqbal, M. Ahmad, M. F. Dinb, G. Murtaza, I. Ahmad, M.F. Warsi, Vol. 40, Issue 2, , Pages 3571–3577, March 2014.
54- D. Carta, M. F. Casula, A. Falqui, D. Loche,, G. Mountjoy, C. Sangregorio, and A. Corrias, J. Phys. Chem., 113, 8606–8615, 2009.
55- N. Singh, A. Agarwal, S. Sanghi, Current Applied Physics, 11 783-789, (2011).
56- J. Ho Lee and C. Kong Kim, Shunsaku Katoh, Riichi Murakami, Journal of Alloys and Compounds, 325, 276–280, (2001).
57- A. Faraz and A. Maqsood, J. Supercond. Nov. Magn., 25:1085–1091 (2012).
58- O. Obi, M. Liu, J. Lou, S. Stoute, X. Xing, N.X. Sun, J.Warzywoda, A. Sacco, D. E. Oates and G. F. Dionne3, Journal of Applied Physics, 109, 07E527 (2011).
59- R. B. Bhise, S. M. Rathod, A. K. Supekar, The International Journal of Engineering And Science (IJES), Vol. 1, Issue 1, Pages 57-63 , 2012.
60- A.N. Yusoff and M.H. Abdullah, Journal of Magnetism and Magnetic Materials, 269, 271 – 280(2004).
61- Nutan Gupta and S. C. Kashyap Journal of Magnetism and Magnetic Materials, Vol. 288, March 2005, Pages 307–31, 2005.
62- L. Folgueras, A. Alves and C. Rezende, Journal of Aerospace Technology and Management, Vol. 2, n. 1, Jan. – Apr., 2010.
63- E. De Fazio, P. Bercoff and S.E. Jacobo1, IV Euro-Asian Symposium "Trends in Magnetism": Nanospintronics, Ekaterinburg, Russia", June 28 – July 2, 2010.
64- S .A. Mazen and N.I. Abu-Elsaad, ISRN Condensed Matter Physics, Vol. 2012, Article I D 907257, 9 pages, 2012.
65- J. Cadieu, R. Raniet, W. Mendoza, B. Peng, S. A. Shaheenal, M. J. Hurben and C. E. Patton, J. Appl. Phys., Vol. 81, No. 8, 15 April 1997.
66- M.K. Rendale et al, Archives of Applied Science Research, 2011, 3 (5):491-497

67- W. H. Kwon , J.G. Lee, S.W. Lee and K. P. Chae, Journal of the Korean Physical Society, Vol. 56, No. 6, p.p. 1838 ~ 1842, June 2010.
68- H. M. Widatallah, C. Johnson, F. J. Berry, E. Jartych, Materials Letters 59 (2005) 1105-1109, 2005.
69- M. H. Al-Darub, Master Thesis, Al-Nahrain University, Baghdad 2002.
70- L. Gama, E. P. Hernandez, D. R. Cornejo, A. A. Costa, S. M. Rezende, R. H. G. A. Kiminami, A.C.F.M. Costa, J. Magn. Magn. Mater. 317, 29-33(2007).
71- L. Torres, M. Zazo, J. Iñiguez, C. de Francisco, J. M. Muñoz, Appl. Phys. A 60, 303-307 (1995).
72- H. Bayrakdar, Progress in Electromagnetics Research M, Vol. 25, 269–281, 2012.
73- H. Hsiang, W. Chen, Y. Chang, F. Hsu, F. Yen, American Journal of Materials Science. 2011; 1(1): 40-44, (2011).
74- K. Shimba,, K. Furuta, N. Morimoto, N. Tezuka and S. Sugimoto, Materials Transactions, Vol. 52, No. 4 (2011) pp. 740 to 745, (2011).
75- A. Šutka, "Physicl Properties of Structured Nickel Zinc Ferrites Synthesized by Sol-Gel Method", PhD Dissertation, Riga Technical University, 2012.
76- M. Tada, T. Abe, J. Miyasaka, N. Matsushita, and M. Abe, Journal of Applied Physics 97, 10G109, 2005.
77- A. Dias, N. D. Mohallem and R. L. Moreira, J. Phys. III France 6 (1996) 843-852.
78- C. Sun and K. Sun, Solid State Communications, Vol. 141, Issue 5, February 2007, Pages 258–261.
79- E. Allbers, J. Appl. Phys. 25, (1954l), 152-154.
80- J.H. Rowen, E.F. Kankowski, Proc. IRE 44 (10) (1956) 1294-1303.
81- D. Ravinder, P. Reddy, Materials Letters, 57, (2003) 4344-4350.
82- D. Ravinder, K. Vijaya Kumar, P. Balaya, Materials Letters, 48, (2001) 210-214.
83- N. Rezlescu, E. Rezlescu, C. Pasnicu, M. L. Craus, J. Phys. Condens. Matter 6 (1994) 5707-5716.
84- A. Sattar, S.A. Rahman, Phys. Stat. sol. (a), 200, (2) (2003) 415-422.
85- K. Vijaya Kumar, A. Reddy, D. Ravinder, Journal of Magnetism and Magnetic Materials, 263, (2003) 121-126.

86- L. J. Berchmans, R. K. Selvan, P. N. Kumar, C. O. Augustin, Journal of Magnetism and Magnetic Materials, 279, (2004) 103-110.
87- R. V. Mangalaraja, S. Ananthakumar, P. Manohar, F. D. Gnanam, M. Awano, Materials Letters, 58, (2004) 1593-1596.
88- B. Rao, K. Rao, G. Sankaranarayana, A. Paduraru, O. Caltun, Journal of Optoelectronics and Advanced Materials, 7, (2005) 697-700.
89- B. Rao, K. Rao, T.V. Rao, A. Paduraru, O. F. Caltun, Journal of Optoelectronics and Advanced Materials, 7, (2) (2005) 701-704.
90- B. Rao, O. caltun, I. Dumitru, Leonard Spinu, Journal Magnetism Magnetic Material. 304, (2006) e752-e754.
91- A.M. Abo El Ata, M.K. El Nimra, S.M. Attia, D. El Konya, A.H. Al-Hammad, Journal of Magnetism and Magnetic Materials, 297, (2006) 33–43.
92- M. Ajmal, A. Maqsood, Materials Science and Engineering B, 139, (2007) 164–170.
93- N. Sivakumar, A. Narayanasamy, N. Ponpandian, Journal of Applied Physics, 101, (2007) 084116-1_084116-6.
94- H. Su, H. Zhang, X. Tang, Yu Shi, Journal of Magnetism and Magnetic Materials, 320, (2008) 483–485.
95- N. Singh, A. Agarwal, S. Sanghi, Current Applied Physics 11 (2011) 783-789.
96- R. Raman, V. Murthy and B. Viswanathan, Journal of Magnetism and Magnetic Materials, 102, (1991) 181-183.
97- K. Tripathi, S. Abbas, P. Alegaonkar, R. Sharma, International Journal of Advanced Research in Science, Engineering and Technology, Vol. 2, Issue 2 , February 2015.
98- T. Giannakopoulou, L. Kompotiatis, A. Kontogeorgakos, and G. Kordas, Journal of Magnetism and Magnetic Materials, 246, (2002) 360 – 365.
99- J. Ramprecht, "Electromagnetic Waves in Media with Ferromagnetic Losses", Doctoral Thesis, Electromagnetic Theory, Royal Institute of Technology, Stockholm, Sweden, 2008.
100- H. Nejati, "Analysis of Physical Properties and Thermo –Mechanical Induced Fractures of Rocks Subjected to Microwave Radiation", PhD Dissertation, McGill University, April 2014, Montreal.
101- C. Tsipogiannis, "Microwave materials characterization using waveguides and coaxial probe", Master Thesis, Lund University, 2012, Lund /Sweden.

102- R.E. Newnham, J. Jang, M. Xu, and F. Jones, "Fundamental Interaction Mechanisms Between Microwaves and Matter", Proceedings of the Symposium on Microwave Theory and Application in Materials Processing Annual, Vol. 21, 1991.
103- W. Kuang, S. O. Nelson, American Society of Agricultural Engineers, vol. 41, 173-184, 1998.
104- S. O. Nelson, Cereal Chem., vol.58, No.6, P.487-492, 1981.
105- A. Loupy, "Microwaves in Organic Synthesis", Second Edition, WILEY- Verlag, 2008.
106- B. Fromme, "D-D Excitations in Transition-Metal Oxides", Springer, 2001.
107- J. Baker, M.D. Janezic, J.H. Grosvenor, R.G. Geyer "Transmission /Reflection and Short-Circuit Line Methods for Measuring Permeability and Permittivity, U.S. Government Printing Office, WASHINGTON, 1992.
108- D. Stuerga, Fundamentals of Microwave – Matter Interactions, Wiley, Vol. 1, 3rd Edition, 2012.
109- G.A. Nazri, J.M. Tarascon, Materials Research Society Symposium Proceedings, Solid State Ionics IV, Vol.369. 1994, Boston.
110- B. Minov, M.J. Konstantinovic and L. Dupre, Electrical Review, R. 87 No 9b/2011.
111- T. Galek, "Modeling of Microwave Absorption Mechanisms in Metallic Powders", Ph.D. Dissertation, Universitat Rostock, 2013, Rostock Germany.
112- S. Das, A. Mukhopadhyay, S. Datta and D. Basu, Bulletin of Materials Science, Vol. 32, No. 1, February 2009, pp. 1–13.
113- J.B. Jarvis, M. D. Janezic, B.F. Riddle, R.T. Johnk, P. Kabos, C.L. Holloway, R.G. Geyer, C.A. Grosvenor "Measuring the Permittivity and Permeability of Lossy Materials: Solids, Liquids, Metals, Building Materials and Negative Index", U.S. Government printing Office, 2005.
114- D. A. Jones, "Understanding Microwave Treatment of Ores", Ph.D Dissertation, University of Nottingham, 2004.
115- B. J. Goodenough, "Summary of Losses in Magnetic Materials", IEEE Vol.:38, Issue:5, 2002.
116- X. Qin, Y. Cheng, K. Zhou, S. Huang, X. Hui, Journal of Materials Science and Chemical Engineering, 2013, 1, 8-13.

117- T. Nakamura, "Study of High Frequency Permeability in Ferrite Ceramic and Ferrite Composite Material", PhD dissertation, Hiroshima University 1996.
118- J. Säily and A.V. Räisänen, "Studies on Specular and Non-Specular reflectivities of Radar Absorbing Materials (RAM) at Submillimeter Wavelengths", Helsinki University, 2003, Helsinki.
119- C. Anderson, "Design and Implementation of an Ultrabroadband Millimeter-Wavelength Vector Sliding Correlator Channel Sounder and In-Building Multipath Measurements at 2.5 & 60 GHz", Master Thesis, Electrical Dep. Baylor University, 2002, Blacksburg.
120- T. M. Perekalina, A. A. Askochiniskii, Soviet Physics JETP Vol.13, No.2 July, 1961.
121- M.T. Rahman, M. Vargas, C.V. Ramana, Journal of Alloys and Compounds, 617, (2014) 547–562.
122- C. Zollitsch, "Ferromagnetic Resonance at Low Temperatures", Diploma Thesis, Munchen university, 2011.
123- Y.N. Bataiev, "Ferromagnetic Resonance Study of Spintronics Materials", PhD Dissertation, Ohio State University, 2008.
124- N. Mo, J.J. Green, P. Krivosik and C. E. Patton, Journal of Applied Physics, 101, 023914, 2007.
125- M. Farle, T. Silva and G. Woltersdorf, "Magnetic Nanostructures: Spin Dynamic and Spin Transport", 2013, Springer.
126- M. Farle, Rep. Prog. Phys, 61, 755, 1998.
127- S. Beguhn, Ziyao Zhou, S Rand, X Yang, J Lou, NX Sun, Journal of Applied Physics, 111, 07A503, 2012.
128- C.P. Neo, Y.Yang, and J. Ding, Journal of Applied Physics, 107, 083906 2010.
129- D. M. Pozar, "Microwave Engineering", Addison Wesley Publishing Company, Reading, MA, 1996.
130- N.V. Reddy, "Coatings for Selective Microwave Absorption", USA Patent, No: DAALO2-91-C-0028, 1991.
131- D. Warin, J. C.Mage, and W. Simonet, J. Appl. Phys. 55, 2452 (1984).
132- Y. Chen, M.J. Nedoroscik, A.L. Geiler, C. Vittoria, and V. G. Harris, J. Am. Ceram. Soc., 91, [9] 2952–2956 (2008).
133- C. Srivastava, M. Patni, N. Nanadikar, Journal De Physique Colloque Cl, no 4, Tome 38, 1977, page Cl-267.

134- R. Biasi, T. Devezas, Journal of Applied Physics 1978; 49 2466-2470. 151.
135- V.G. Harris , A. Geiler, Y. Chen, S.D. Yoon, M. Wu, A. Yang , Z. Chen, P. He, P.V. Parimi, Xu Zuo, C.E. Pattonc, M. Abee, O. Acher, C. Vittoria, Journal of Magnetism and Magnetic Materials, 321, (2009) 2035–2047.
136- N. Song, H. Yang, H. Liu, X. Ren, H. Ding, X. Zhang & Z. Cheng, "Exceeding Natural Resonance Frequency Limit of Monodisperse Fe3O4 Nanoparticles via Superparamagnetic Relaxation", Scientific Reports, 3, Article number: 3161 (2013).
137- R.G. Martín, "Electromagnetic Field Theory for Physicists and Engineers: Fundamentals and Applications", University of Granada Publishing, 2009.
138- V.Verma, J.Kapil, N.Singh, International Journal of Engineering Research & Technology (IJERT), Vol. 3, Issue 12 (2014).
139- H.S. Nalwa, "Hand Book of Thin Film Materials", Acadimic Press, 2002, Florida.
140- R.C. Dorf, "The Engineering Handbook", Second Edition, CRC Press, 2004.
141- X.C. Tong, "Advanced Materials and Design for Electromagnetic Interference Shielding", CRC Press, 2008, New York.
142- N. Chen, M. Gu, Open Journal of Metal, 2, 2, 37-41, 2012.
143- Y. Wang, L. Wang, Materials 2013, 6, 1520-1529.
144- R.K. Jain, A. Dubey, A. Soni, S.K. Gupta, Processing and Application of Ceramics, 7 [4] (2013) 189–193.
145- H.A. Sulaiman and M.A.Othman, "Theory and Applications of Applied Electromagnetics", Springer, 2014, Switzerland.
146- C.H. Oxley, J. Williams, R. Hopper, H. Flora, D. Eibeck, C. Alabaster, IET Science, Measurement & Technology, 2007, Vol. 1, Issue 3, p.166 – 169.
147- J. Creech, "S-Parameters Allow High-Frequency Verification of RF Switch Models", Analog Device, Vol. 45 –2011.
148- J. M. Szepieniec, "Magneto Electric Thin Film Laminate Composites for Voltage-Controlled Tunable Nonreciprocal RF Devices", Master Thesis, University of Twente, 2012.

149- L. Zahid, F. Malek, H. Nornikman, N.A. Affendi, A. Ali, N. Hussin, B.H. Ahmad, and M. Abd Aziz, Progress in Electromagnetics Research, Vol. 137, 687–702, 2013.
150- H. Hayashi and Y. Hakuta, Materials, 2010, 3, 3794-3817.
151- B. Nakhjavan, "Designer Synthesis of Monodisperse Heterodimer and Ferrite Nanoparticles", PhD dissertation, Johannes Gutenberg-University, 2011, Mainz.
152- A. Dias, Journal Solution Chemistry, (2009) 38: 843–856.
153- J. Ortiz, C. Gómez, R. López, I. Dávalos, H. Pfeiffer, "Synthesis of Advanced Ceramics by Hydrothermal Crystallization and Modified Related Methods", J. of Advanced Ceramics, 2012, 1(3): 204-220.
154- K. Marie, "Particle Formation and Growth in Hydrothermal Synthesis", PhD dissertation, Aarhus University, 2013.
155- K. Byrappa and M. Yoshimura, "Handbook of Hydrothermal Technology A Technology for Crystal Growth and Materials Processing", William Andrew Inc., 2001.
156- B.F. Drive, "Fundamentals of Vector Network Analysis", Version 1.1, Published by Rohde & Schwarz USA, Inc. 6821, Columbia.
157- J. Dunsmore, Network Analyzer Basics, Agilent Technology, 2007.
158- E.H. Masood "Accessible Broadband Network Analysis", Master Thesis, Massachusetts Institute of Technology, 2002.
159- A.R. Denton and N. W. Ashcroft, "Vegard's law", Phys. Rev., A 43, 3161 – Published 1 March 1991.
160- W. Marwat, J Material Sci. Eng., 2014, 3:3.
161- A.Monshi, M.R. Foroughi, M.R. Monshi, World Journal of Nano Science and Engineering, 2012, 2, 154-160.
162- G.Aravind, D.Ravinder, and V.Nathanial, Hindawi Publishing Corporation, Physics Research International, Vol. 2014, Article ID 672739, 11 pages
163- S.A.Mazen and T.A.Elmosalami, ISRN Condensed Matter Physics, Vol. 2011 (2011), Article ID 820726, 9 pages
164- R. S. Puche1, M. J. T. Fernandez, Bol. Soc. Esp. Ceram. V.47, 3, 133-137 (2008).
165- A.Aimable et al., Powder Technology 190 (2009) 99–106.
166- D.N. Bakoyannakis, 2004 Kluwer Academic Publishers. Printed in the Netherlands, Nanoengineered Nanofibrous Materials, 495-500.

167- J. H. Lee , C. K. Kim, S. Katoh and R. J. Murakami,Journal of Alloys and Compounds 325 (2001) 276–280.
168- S. Verma and P. A. Joy, J. Appl. Phys. 98, 124312, 2005.
169- A. Ahniyaz, T. Fujiwara, Solid State Ionics 151 (2002) 419– 423.
170- X. Wang and L. Gao, Nanotechnology Vol. 16 Number 11, 2005.
171- R. Dosoudil, M. Usáková, IEEE Transactions on Magnetics, Vol. 46, No. 2, 2010.
172- E. F. Chagas, G. C. Leite and R. Pereira, Journal of Magnetism and Magnetic Materials. 09/2012; 324(18):2711–2716.
173- A. Jagminas M. Kurtinaitien, and K. Mažeika, ChEMIJA, 2013. vol. 24. No. 2. P. 103–110, 2013.
174- A. Baykali, N.Kasapoglu, H. Kavas, Z. Durmus, S. Özden, and M. Toprak, Turk J. Chem., 33 (2009), 33 – 45.
175- M. Abdullah Dar, J. Shah, W. A. Siddiqui, R. K. Kotnala, Appl. Nanosci., (2014) 4:675–682.
176- L. Nalbandian, A. Delimitis, V.T. Zaspalis, E.A. Deliyanni, D.N. Bakoyannakis and E.N. Peleka, Microporous and Mesoporous Materials114 (2008) 465–473.
177- K. Nejati and R. Zabihi, Chemistry Central Journal, 2012, 6:23
178- P.S. Neelakanta, "Handbook of Electromagnetic Materials: Monolithic and Composite Versions and Their Applications", CRC press, 1995.
179- B.K. Rai, S.R. Mishraa and W. Nguyen, Journal of Alloys and Compounds, 550 (2013) 198–203.
180- N. Singh and A. Agarwal, Journal of Magnetism and Magnetic Materials, 36-Vol. 323, Issue 5, March 2011, Pages 486–492.
181- M. Rahman and B. Sonia, M. Kumar Das1, F. Ahmed, Md. Abul Hossain, D. K. Saha, S. Akhter, International Journal of Physics, V1, issue5, 128-132, 2013.
182- Neha Pachauri, "Fabrication and Ferromagnetic Resonance Study of Epitaxial Spinel Ferrite Films for Microwave Device Applications, PhD Dissertation", the University of Alabama ALABAMA, 2014.
183- G. Nabiyouni1, M. Jafari Fesharaki1, Chin. Phys. Lett. Vol. 27, No. 12 (2010) 126401.
184- I. Ahmad, T. Abbas, A.B. Ziya, Asghari Maqsood, Ceramics International, Vol. 40, Issue 6, July 2014, Pages 7941–7945

185- M. Naveen, International Journal for Research in Applied Science and Engineering Technology (IJRASET), Vol. 1 Issue I, August 2013.
186- R. Mitra, R. K. Puri, R. G. Mendiratta, Journal of Materials Science, March 1992, Vol. 27, Issue 5, pp 1275-1279.
187- S. J. Azhagushanmugam, N. Suriyanarayanan, and R. Jayaprakash, Advances in Materials Science and Engineering, Vol. 2013 (2013), 5 pages.
188- M.I. Sukur, "Design A Compination of Radial Line Slot Array (RLSA) Anttena and Patch Anttena That Operates at Both 2.4 GHz and 5.8 GHz", Bachelor Thesis, University of Technology, Malaysia, 2012.
189- K. Chang, "RF and Microwave Wireless Systems", John Wiley & Sons, Inc, 2000.
190- P. Singh, A. Razdan, A. Razdan, T. Goel, S.Srivastava, Indian Journal of Pure and Applied Physics, V.42. March 2004, p.p.221-228.
191- Patrizia Savi1 and Mario Miscuglio1, Progress In Electromagnetics Research Letters, Vol. 44, 63-69, 2014.
192- M. Oyharçabal, T. Olinga, M.P. Foulc, S. Lacomme, Composites Science and Technology 74 (2013) 107–112.
193- K. Naishadham and P. Chandrasekhar, Microwave Symposium Digest Conference, 1998 IEEE MTT-S International, Vol. 3, pp.1353 – 1356.
194- S. Kirouane, E. Verney, D. Vincent, and A. Chaabi, Progress In Electromagnetics Research Letters, Vol. 8, 161–170, 2009.
195- S.P. Gairola, V. Verma, L. Kumar, M. Dar, S. Annapoorni, and R. Kotnala, Solid State Communications 150 (2010) 147-151.
196- I. Nedkov and S. Stavrev, 27th International Seminar on Electronic Technology. 2004 IEEE. vol.3, P.577- 579.
197- J. Prasad and N. S. Bhattacharyya, PIERS Proceedings, Kuala Lumpur, MALAYSIA, March 27–30, 2012, pp. 132-135. 57.
198- N.C. Joshi, S.S. Islam and A. Verma, Ferrites – Journal of Interface Technology, 136, 2007.
199- G. Nabiyouni, M. J. Fesharaki, M. Mozafari; J. Amighian, Chinese Phys. Lett., 27 126 (2010) 401.

Appendix 1

A History of RAM Development

The development of Radar absorbing materials has been reviewed in several papers [1-6] and Books [7-9]. Exploitation of radar absorbing materials started in the 1930's shortly after the advent of radar. Absorber design has incorporated materials with different loss mechanisms and has made use of physical optics to optimize absorption over wide bandwidths. Absorbers therefore come with many different shapes and structures, ranging from thick pyramidal structures, to multilayers and single coatings. Microwave absorbing materials have been used in commercial settings, for anechoic chambers and for reducing the reflected signals from buildings and superstructures around radar installations. Current communication technologies at microwave frequencies are driving the development of absorbers and frequency selective surfaces. This section gives a brief review of the historical development of RAM, and referral to subsequent sections will help illustrate the devices, materials and structures being discussed here. Also due to the secret nature of RAM development some details are sketchy or not published.

Research into electromagnetic wave absorbers started in the 1930's,[2,8] with the first patent appearing in 1936 in the Netherlands [10]. This absorber was a quarter-wave resonant type using carbon black as a lossy resistive material and Titanium dioxide for its high permittivity to reduce the thickness.

During World War II, Germany, concerned with radar camouflage for submarines, developed "Wesch" material, a carbonyl iron powder loaded rubber sheet about 0.3 inches thick and a resonant frequency at 3 GHz. The front surface of this material was waffled to produce a larger bandwidth. They also produced the Jaumann Absorber, a multilayer device of alternating resistive sheets and rigid plastic. This device was about 3 inches thick with resistances decreasing exponentially from the front to the back. This device achieved a reduction in the reflectivity of –20 dB over 2-15 GHz. America, during this period, led by Halpern at MIT Radiation Laboratory developed materials known as "HARP" for Halpern Anti Radiation Paint. The airborne version, known as MX-410, had a thickness of 0.025 inches for X-band resonance. The base dielectric had a high permittivity of 150 due to loading with highly oriented disk shaped aluminum flakes suspended in a rubber matrix and carbon black for loss. This material offered a 15-20 dB reduction in reflectivity. Shipborne absorbers were 0.07 inch thick (X-band) iron particle loaded rubber with a permittivity of 20 and enough permeability to produce resonance broadening [11, 12]. At the same time the resonant Salisbury Screen was developed with about 25% bandwidth at resonance [13]. Production of Salisbury screens was aided by the US Rubber Company marketing a resistive cloth called Uskon. Another absorber design that arose at this time was a long pyramidal structure with the inside coated with Salisbury Screen and the apex in the direction of propagation. The multiple reflections from the absorber resulted in high attenuation [14]. The importance of ferrites was known. With the exceptions of the Jaumann device and the inverted pyramid, these devices are typically narrow band.

The postwar period (1945-1950) was characterized by the development of broadband absorbers using sharp pointed geometric shapes that produce a gradual transition into the absorbing material. These materials found application in anechoic chambers [15-18].

Materials investigated for microwave attenuation include carbon loaded plaster of paris, graphite, iron oxide, powdered iron, powdered aluminium and copper, steel wool, water, powdered “Advance” and “Constantin” and metal wires [19]. Binders included various plastics and ceramics, while supports with a lot of air at the interface included foams, fibers and “excelsior”. More functional lossy broadband materials were created with a flat surface by using patterned flat layered resistive sheets that reproduced the pyramidal, or conical structures of above [12].

The1950’s saw the commercial production of RAM called “Spongex”, based on carbon coated animal hair, by the Sponge Products Company, (later to become a division of B.F. Goodrich Company). This material, 2 inches thick, resulted in –20 dB attenuation in the reflectivity over 2.4-10 GHz for normal incidence. 4 and 8 inch versions also produced for lower frequencies. This company was later joined by, Emerson and Cuming Inc. and McMillan Industrial Corporation, in the manufacture of absorbers. Research into circuit analog devices was started by Severin and Meyer during this decade [1 ,2,20,21] . The term circuit analog comes from the use of circuit theory to represent the components/processes occurring in the absorber, and hence to model the reflectivity. This technique was adopted from research programs on acoustical absorbers. Severin and Meyer made experimental absorbers based on resistance loaded loops, slots in resistive foil, resistance loaded dipoles, strips of resistive material with various orientations, strips of magnetic material with various orientations, surface shaping and magnetic loading of resonant materials. This started a new field of research into frequency selective surfaces (FSS) [22].

The 60’s and 70’s saw continuing work on circuit analog materials,[9] and significant absorber thickness reductions were demonstrated using ferrite underlayers [23]. Pyramidal shaped absorbers were being used for anechoic chambers achieving –60 dB at near normal incidence. Control of the fabrication of Jaumann layers was demonstrated by screen printing,[24] and absorbers were being made from foams, netlike structures, knitted structures, or honeycomb and coated with a paint containing particulate or fibrous carbon, evaporated metal or nickel chromium alloy [25]. Interesting, though not practical one patent describes an absorbers that employing a plasma to absorb the microwaves. The plasma was generated by a radioactive substance requiring about 10 Curies/cm2 [26].

The 1980’s. The absorber design process is improved by optimization techniques [27-29]. Bandwidth improvement of Jaumann absorbers was evaluated by using graded layers [6,30] and different resistive profiles to achieve maximum bandwidths. Computers and transmission line models were used to calculate reflectivity from material properties, and for frequency selective surfaces which can be represented as equivalent circuits, the transmission line model are applied [5]. Circuit analog materials are designed [31] and the scattering of these materials is analysed based on the Floquet theorem.[32] Materials continue to use carbon black or graphite, carbonyl iron and ferrites, though now artificial dielectrics are being made by adding inclusions such as rods, wires, disc and spheres.[6] Helical inclusions are found to improve absorption and resulted in research into chiral materials[33]. Mixing theory is used to calculate the desired permittivity and permeability of these new materials. Conducting polymers appear as potential radar absorbing materials.

The 1990's and on to today has seen more optimisation techniques for Jaumann structures including genetic algorithm optimization [34-40]. Circuit analog and frequency selective surfaces continue to big in the literature [20, 31, 32, 35, 40-49]. Conducting polymers and composite materials with these are found along with conducting polymer coated fibres and fabrics for creating devices [50-84]. A new class of absorbers that find their roots in conducting polymers is that of dynamic RAM [85-89] where the resonant frequency of the absorber is tunable through variation of resistive and capacitive elements in the absorber.

Reference:

Paul Saville, Review of Radar Absorbing Materials, Defence R&D Canada – Atlantic, DRDC Atlantic TM 2005-003 January 2005.

Web address: http. dtic.mil/dtic/tr/fulltext/u2/a436262.pdf

Appendix 2

Magnetic Units Conversion

Quantity	Symbol	Gaussian & cgs emu [a]	Conversion factor, C [b]	SI & rationalized mks [c]
Magnetic flux density, magnetic induction	B	gauss (G) [d]	10^{-4}	tesla (T), Wb/m^2
Magnetic flux	Φ	maxwell (Mx), G⊙cm^2	10^{-8}	weber (Wb), volt second (V⊙s)
Magnetic potential difference,magnetomotive force	U, F	gilbert (Gb)	$10/4\pi$	ampere (A)
Magnetic field strength, magnetizing force	H	oersted (Oe), [e] Gb/cm	$10^3/4\pi$	A/m [f]
(Volume) magnetization [g]	M	emu/cm^3 [h]	10^3	A/m
(Volume) magnetization	$4\pi M$	G	$10^3/4\pi$	A/m
Magnetic polarization, intensity of magnetization	J, I	emu/cm^3	$4\pi \times 10^{-4}$	T, Wb/m^2 [i]
(Mass) magnetization	σ, M	emu/g	1 $4\pi \times 10^{-7}$	A⊙m^2/kg Wb⊙m/kg
Magnetic moment	m	emu, erg/G	10^{-3}	A⊙m^2, joule per tesla (J/T)
Magnetic dipole moment	j	emu, erg/G	$4\pi \times 10^{-10}$	Wb⊙m [i]
(Volume) susceptibility	χ, κ	dimensionless, emu/cm	4π $(4\pi)^2 \times 10^{-7}$	dimensionless henry per meter (H/m), Wb/(A⊙m)
(Mass) susceptibility	χ_ρ, κ_ρ	cm^3/g, emu/g	$4\pi \times 10^{-3}$ $(4\pi)^2 \times 10^{-10}$	m^3/kg H⊙m^2/kg
(Molar) susceptibility	χ_m, κ_{mol}	cm^3/mol, emu/mol	$4\pi \times 10^{-6}$ $(4\pi)^2 \times 10^{-13}$	m^3/mol H⊙m^2/mol
Permeability	μ	dimensionless	$4\pi \times 10^{-7}$	H/m, Wb/(A⊙m)
Relative permeability [j]	μ_r	not defined	-	dimensionless
(Volume) energy density, energy product [k]	W	erg/cm^3	10^{-1}	J/m^3
Demagnetization factor	D, N	dimensionless	$1/4\pi$	dimensionless

a. Gaussian units and cgs emu are the same for magnetic properties. The defining relation is B=H+4πM.
b. Multiply a number in Gaussian units by C to convert it to SI (e.g., 1 G x 10-4 T/G = 10-4 T).
c. SI (System International d'Unitès) has been adopted by the National Bureau of Standards. Where to conversion factors are given, the upper one is recognized under, or consistent with, SI and is based on the definition B = μo (H + M), where μo = 4π x 10-7 H/m. The lower one is not recognized under SI and is based on the definition B = μoH + J, where the symbol I is often used in place of J.
d. 1 gauss = 105 gamma (γ).
e. Both oersted and gauss are expressed as cm-1/2⊙g1/2⊙s-1 in terms of base units.
f. A/m was often expressed as "ampere-turn per meter" when used for magnetic field strength.
g. Magnetic moment per unit volume.
h. The designation "emu" is not a unit.
i. Recognized under SI, even though based on the definition B = μoH + J. See footnote c.
j. μr = μ/μo = 1 + χ, all in SI. μr is equal to Gaussian μ.
k. B⊙H and μo M⊙H have SI units J/m3; M⊙H and B⊙H/4π have Gaussian units erg/cm3.

This information was taken with permission from R. B. Goldfarb and F. R. Fickett, U.S. Department of Commerce, National Bureau of Standards, Boulder, Colorado 80303, March 1985, NBS Special Publication 696.

Reference:

http://www.ieeemagnetics.org/index.php?option=com_content&view=article&id=118&Itemid=107

Appendix 3

Some Properties of Starting Material

	$FeCl_3$	$LiCl.H_2O$	$NiCl_2.6H2O$	NaOH	$FeSO4.7H2O$
Solubility in water	92 g/100 mL (hexahydrate, 20 °C)	H2O 100 grams of 67 grams (0 ° C),	254 g/100 mL (20 °C)	111 g/100 mL (20 °C)	29.51 g/100mL (25 °C)
appearance	green-black	white solid	green crystals	White	Blue-green crystals
density	2.898 g/cm^3	2.068 g/cm^3	1.92 g/cm^3	2.13 g/cm^3	1.895 g/cm^3
melting	306 °C	605–614 °C	140 °C	318 °C	60–64 °C
Molar mass	162.2 g/mol	42.39 $g{\cdot}mol^{-1}$	237.69 g/mol	39.9971 g mol^{-1}	278.015 g mol^{-1}

Reference:WIKIPEDIA

Web address: http://en.wikipedia.org/wiki

Appendix 4

Conversion from VSWR to Normal Ratio and dB

r [VSWR]	r	r [dB]
1,002	0,001	60
1,004	0,002	54
1,006	0,003	50
1,008	0,004	48
1,01	0,005	46
1,02	0,01	40
1,04	0,02	34
1,1	0,05	26
1,2	0,1	20
1,3	0,13	18
1,4	0,16	15
1,5	0,2	14

Reference: http://www.markimicrowave.com/

Appendix 5

Methods of Ferrites powder preparation

method	***Brief Description***
Ceramic	Metal salts compounds mixing and fired in high temperature.
Double sintering	Two stage of firing metal salts compounds (lower than ceramic method)
Sol-Gel	Preparation gelatin of sol by hydrolysis of metal salts compound solution and intensifying by heating.
Citrate	Metal salts compounds solution mixed with citric acid to precipitate the powder with low heating.
Co-precipitation	Metal salts compounds solution mixed with base to precipitate the powder with at atmospheric.
Hydrothermal	Metal salts compounds solution mixed with base to precipitate the powder with at high pressure and temperature.
Auto combustion	Metal salts compounds dense solution mixed with liquid fuel and then fired.
Spray pyrolysis (Flame spray)	Metal salts compounds solution mixture is sprayed on hotplate or with flame.
Thermal decomposition	Thermal decomposition of organometallic compounds in a boiling organic solvents containing stabilizing surfactants.
Microemulsion	Isotropic liquid mixtures of oil, salts water and surfactant with a co-surfactant.
Sonochemical	Induced reactions by using ultrasonic waves causing acoustic cavitation

Reference: collected from WIKIPEDIA. Web address: http://en.wikipedia.org/wiki

---

Appendix 6

Triple phase diagram of Li-Ni ferrite $Li_{0.5-0.5x}Ni_xFe_{2.5-0.5x}O_4$

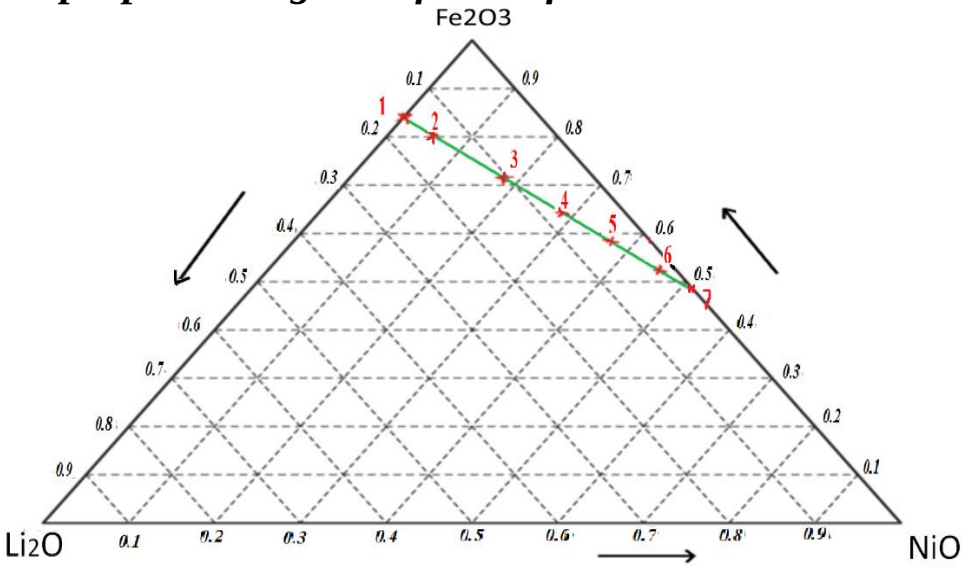

The green line represent the stoichiometric of x values for Li-Ni ferrite. Red numbers represent the prepared compositions.

الملخص

حَّضر فيرايت الليثيوم-نيكل النانوي ذو التركيب $Li_{0.5-0.5x}Ni_xFe_{2.-0.5x}O_4$ بطريقة الهايدروحرارية وبمجموعتين من كلوريدات المعادن وكبريتات الحديدوز وهيدروكسيد الصوديوم. كل مجموعة تتصمن تغيير x بالقيم 0.1 و 0.3 وحتى 1.0. المجموعة واحد بدون Fe^{2+} والمجموعة اثنين مع اضافة Fe^{2+} . النسبة Fe^{3+}/Fe^{2+} أبقيت ثابتة بمقدار 1.7، درجة حرارة التحضير كانت 155ºC والدالة الحامضية مساوية لقيمة 11.

كل التراكيب حّضرت باستثناء المركب عند x=0 بدون اضافة Fe^{2+} والتي لم يتمكن من تحضيرها بهذه الطريقة تحت الظروف التجريبية المستخدمة. أظهرت النماذج سيادة طور سبنل فيررات بعد x=0.3 للمجموعة واحد وطور نقي عند x=0.3 باستخدام Fe^{2+} . ثابت الشبيكة للمجموعة اثنين اقل مما للمجموعة واحد. الحجم البلوري يصل لادنى قيمة عند x=0.5 للمجموعة واحد وتقريبا أعظم ما يمكن للمجموعة اثنين عند x=0.

قمم أطياف تحت الحمراء لرباعي السطوح تزاح نحو الترددات الاعلى مع زيادة تركيز +Ni2. أشكال الجسيمات كانت: قضبان (غالبا للهمتايت) بمعدل قطر 40nm، وكروية(اصلها مكعبات فيرايت نانوية) بحجم حوالي 20nm.

حلقات M-H امتلكت شكل الحرف S مماثلة للتي للسوبربارامغناطيسية. عموما فالنماذج المحضرة تمتلك اقل قاهرية (coercivity)، واعلى تمغنط اشباع (saturation magnetization) من الادبيات المنشورة. كلا المجموعتين امتلكت اعلى تأثرية عند x=0.5. وقد فسرت هذه النتائج على اساس التركيب وتوزيع الايونات الموجبة والتفاعل بينها وحجم الجسيمات.

الامتصاص الرنيني للأشعة المايكروية باستخدام اختبار FMR أظهر ان القيمة الأعظم للتأثرية الخيالية χ'' هي عند x=0.5 للمجموعة وقيم عليا عند x=0.7 و x=0.9، وأكبر عرض خط حوالي 950G عند x=0.7 . المجموعة الثانية أظهرت اعظم امتصاص(χ'') وعرض خط عند x=0.9 . بعدها تم الخلط مع ايبوكسي النوفالاك بنسبة وزنية 39.7 %. أختبار دائرة القصر-لقياس الرنين المغناطيسي بانعدام المجال قد أظهرت أمتصاص للاشعة المايكروية لترددات اكبر من 19GHz. تفسير ان نماذج المجموعة أثنين تمتلك امتصاص اكبر من المجموعة واحد أعتمد على الموصلية التنقلية hopping وعلى تغير المعلمات المغناطيسية (Ms وHc).

طريقة خط النفاذ باستخدام VNA في الحزمة-X والحزمة-Ku أظهرت أن خسائر العودة او الانعكاس RL تكون اقل ما يمكن عند x=0.3 للمجموعة واحد في الحزمة-X بينما ذلك عند x=0.3 و x=0.5 للمجموعة أثنين. اضافة Fe^{2+} يقلل القيمة الدنيا بعامل اكبر من 1.5. خسائر الادراج IL في الحزمة-X تتراوح بين 4.5dB- الى 7dB- . أن RL و IL في الحزمة-Ku تمتلك سلوك متشابه ولكن قيمها اقل. أن RL تصبح اقل ما يمكن عند x=0.5 وبقيمة 18dB- بينما كانت حوالي 12dB- باضافة Fe^{2+} . ومعدل قيمة IL في حزمة - Ku هي 6dB-. يلخص تأثير السمك بتحسين قيم RL وIL ولكن مع ازاحة القمم الدنيا الى تردد اقل. سمك بمقدار 2mm يمتلك RL<-27dB وIL<-19dB.

جمهورية العراق
وزارة التعليم العالي والبحث العلمي
جامعة النهرين
كلية العلوم
قسم الفيزياء

تحضير مادة طلأء من فررايت الليثيوم-النيكل بالتعويض المتكافيء

أطروحة

مقدمة الى كلية العلوم /جامعة النهرين

كجزء من متطلبات نيل درجة الدكتوراه فلسفة في علوم الفيزياء

من قبل

صادق هاني لفته

ماجستير فيزياء تطبيقية 1998

أشراف

الاستاذ الدكتور
عماد خضير عباس

الاستاذ الكتور
علي مطشر موسى

صفر 1437هـ

كانون الثاني 2016 م